Compounds for Investigating Photosynthetic Pathways and Solar Energy Conversion

by

Chelsea L. Brown

A Dissertation Presented in Partial Fulfillment
of the Requirements for the Degree
Doctor of Philosophy

Approved November 2015 by the
Graduate Supervisory Committee:

Ana Moore, Chair
Devens Gust
Neal Woodbury

ARIZONA STATE UNIVERSITY

December 2015

ABSTRACT

Humanity's demand for energy is increasing exponentially and the dependence on fossil fuels is both unsustainable and detrimental to the environment. To provide a solution to the impending energy crisis, it is reasonable to look toward utilizing solar energy, which is abundant and renewable. One approach to harvesting solar irradiation for fuel purposes is through mimicking the processes of natural photosynthesis in an artificial design to use sunlight and water to store energy in chemical bonds for later use. Thus, in order to design an efficient energy conversion device, the underlying processes of the natural system must be understood. An artificial photosynthetic device has many components and each can be optimized separately. This work deals with the design, construction and study of some of those components. The first chapter provides an introduction to this work. The second chapter shows a proof of concept for a water splitting dye sensitized photoelectrochemical cell followed by the presentation of a new p-type semiconductor, the design of a modular cluster binding protein that can be used for incorporating catalysts, and a new anchoring group for semiconducting oxides with high electron injection efficiency. The third chapter investigates the role of electronic coupling and thermodynamics for photoprotection in artificial systems by triplet-triplet energy transfer from tetrapyrroles to carotenoids. The fourth chapter describes a mimic of the proton-coupled electron transfer in photosystem II and confirms that in the artificial system a concerted mechanism operates. In the fifth chapter, a microbial system is designed to work in tandem with a photovoltaic device to produce high energy fuels. A variety of quinone redox mediators have been synthesized to shuttle electrons from an electron donor to the microbial system. Lastly, the synthesis of a variety of photosensitizers is detailed for possible future use in artificial systems. The results of this work helps with the understanding of the processes of natural photosynthesis and suggests ways to design artificial photosynthetic devices that can contribute to solving the renewable energy challenge.

DEDICATION

I would like to dedicate this dissertation to my wonderful fiancé, Abraham, and my family.

ACKNOWLEDGMENTS

There is a multitude of people who have helped me to reach this point in my academic career. I would like to start by thanking my advisor, Professor Ana Moore. I am so thankful that, although you were not looking for a student, you chose to accept me into the group anyways and allowed me to pursue my own interests. Your patience, knowledge, and guidance have allowed me to be successful as a chemist. You have kept me motivated to be successful in the lab and in the real world. Thank you. I would also like to thank Professor Tom Moore and Professor Devens Gust for being additional advisors to me, helping my guide me research and making me look at the big picture. I would also like to acknowledge my supervisory committee member, Professor Neal Woodbury for all of your advice and assistance with my dissertation projects.

I would like to thank my undergraduate advisor, Jeffery Carney, for your enormous help in assisting me with the graduate school process and encouraging me to pursue a Ph.D. I would never have made it to Arizona State University without your help and I never would have even considered graduate school before taking your class.

I must give a special thank you to Jesse Bergkamp for taking me under your wing even though I was a clueless first year who broke all of your glassware. Everything I know about organic synthesis I learned from you and without your guidance I never would have survived past my second year. Thank you for being patient with me, giving me advice when I need it, and thank you for your awesome friendship.

A special thank you to my lab mate and friend, Marely Estefania Tejeda Ferrari. You have been my partner throughout graduate school. You have been there when I wanted to quit and you have been there when I was happy something finally worked. You have

helped me scientifically, emotionally, and even physically when I was down with one of my many injuries. I do not know what I would have done without you.

I must thank Paul Liddel for your help with synthetic issues, your assistance around the lab, and for the interesting conversations. I would also like to thank Gerdenis Kodis, Manuel Llansola Portolés, and Antonio Arrigo for their help with gathering and interpreting spectroscopic data. Also, a big thanks to Smitha Pillai for her great help with carotenoids and dyads synthesis!

A huge thanks to Benjamin Sherman, Anindya Roy, Michael Vaughn, Robert Schmitz, Matthieu Koepf, Jim Bridgewater, Rafael Alcala-Torano, and Dayn Sommer for their collaboration and advice throughout graduate school. Each of you has taught me a lot and I appreciate your friendships. I would also like to thank Steve Davidowski for helping me with NMR when I would randomly ask you questions after finding you at one of the other instruments, thank you for always being willing to help!

I must also thank all the friends I have made in the department, you have all made school fun. Thank you to the current and past Gust/Moore/Moore group members, specifically Antaeres, Jeff, Ian, Dalvin, Jaro, Katie, John, Max, and Graeme. Special thanks to my undergraduate research assistants, Elena, Tony, Ghabriel, Gabriella, and Daniel for assisting me with projects, allowing me to practice my teaching skills, and making chemistry fun.

Lastly, I would like to thank my family, friends, and fiancé. You have all supported me throughout this journey, through the ups and the downs, and I cannot thank you enough. Especially Abraham who was there with me through it all. I could not have done it without you.

TABLE OF CONTENTS

LIST OF TABLES

LIST OF FIGURES

Figure Page

Figure Page

Figure Page

Figure Page

LIST OF SCHEMES

Chapter 1

BACKGOUND

Over forty years ago it was predicted that by the early 21st century, global resources would begin to show limitations.[1] With the mounting environmental concerns, it is becoming evident that there is an urgent need for change, specifically in the fuel industry. Fossil fuels are the predominant source of energy today and with the energy demand projected to grow exponentially, fossil fuels are expected to make up 80% of the energy demand by 2040.[2,3] It is largely understood that our dependence on fossil fuels has led to the monumental increase in atmospheric pollutants, like carbon dioxide and nitrous oxide, which has spiked since the start of the industrial revolution.[4-6] In addition to the issues of environmental damage and carbon pollution, the fact that fossil fuels are not renewable will continue to increase their cost and drive geopolitical unrest. The need for a renewable, abundant, and clean form of energy has become vital. Solar energy is the most abundant natural resource, with $4.3\text{x}10^{20}$ J of energy reaching the Earth's surface in one hour, and is a resource that will not run out in the foreseeable future.[7,8] Considering mankind annually uses 4.1×10^{20} J of energy, the sun provides more energy in one hour than humans utilize in one year. The main complication with harnessing this solar radiation is that there is not adequate technology at present for converting solar radiation to electricity and fuels to support global energy needs.

Silicon-based solar cells are effective for small scale electricity during daylight hours but they are expensive and cannot support human activities after dusk. To combat the expensive silicon required for conventional photovoltaics, organic pigments and earth abundant inorganic materials are being used to capture sunlight and shuttle electrons in dye-sensitized solar cells (DSSCs) (Figure 1).[9,10] DSSCs have low production costs, are light weight, and are more flexible in shape and color than silicon-based photovoltaics.[9,11,12] A DSSC is composed of a nanoporous semiconducting oxide spread onto conductive glass. A photosensitizer is adsorbed onto the semiconductor surface and that makes up the photoanode. The cathode is usually platinum electrode and the cell is completed by an electrolyte with a redox mediator to shuttle the electrodes between the cathode and the photoanode. The photosensitizer absorbs sunlight and the excited electron is injected into the conduction band of the semiconductor. The electron travels to the cathode through an external wire where it reduces the mediator. The mediator is then able to regenerate the oxidized dye, therefore completing the electrical circuit. Expanding on the functionality of a DSSCs and finding a way to store the electrons in the form of high-energy chemical bonds for fuel storage, would provide a solution to the global energy crisis; this is where the area of artificial photosynthesis becomes an important factor.

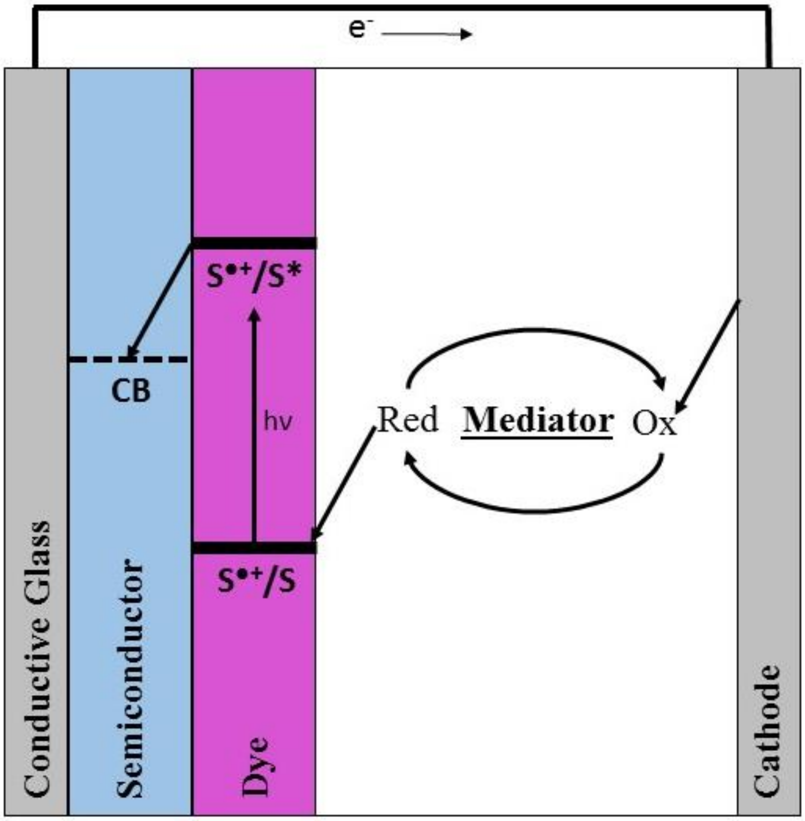

Figure 1. A general schematic of a DSSC where S stands for the photosensitizer and CB stands for the conduction band of the semiconductor.

Artificial photosynthesis aims to mimic natural photosynthesis by converting incident solar energy into chemical potential energy by carrying out photo-induced electron transfer to drive the production of a fuel from water. Photosynthesis is the reason we have coal, petroleum, and natural gas for our current energy economy because they are formed from plant material over time.[13] In photosynthetic organisms, there are two main enzymes that drive these photo-induced electron transfer processes, Photosystem I (PSI) and Photosystem II (PSII). These enzymes are made up of multiple subunits that form the framework for the reaction centers in PSI and PSII. In PSI, antennas made up of mostly chlorophylls absorb sunlight and undergo charge separation by transferring electrons to nearby electron acceptors. These electrons continue down the electron transport chain to be stored in chemical bonds as carbohydrates, fuel for the plant. The oxidized chlorophyll in PSI is then reduced by an electron from PSII which comes from the oxidation of water by the oxygen evolving complex. Therefore, photosynthetic organisms are able to produce a fuel for their survival by harvesting solar energy and using electrons from water. The problem with natural photosynthesis is that it has very low efficiency, around 1% in terms of biomass production.[14] Understanding and mimicking these two enzymes which have evolved into ecologically neutral fuel producing systems and improving upon their basic principles to develop an efficient solar fuel device is the main goal of this thesis.

This work discusses a variety of artificial photosynthetic systems, ranging from basic DSSCs to photoelectrochemical fuel cells (PECFC)[15,16] in Chapter 2 to microbial artificial photosynthetic systems[17-19] in Chapter 5. PECFCs are an extension of DSSCs by adding in catalysts for water oxidation and proton reduction.[20,21] Tandem systems have been designed to use two photosynthetic cells in series in order to increase efficiency (Figure 2). The first cell is designed to absorb blue light in order to generate holes capable of driving the water oxidation catalyst, while the second cell absorbs green and red light to produce enough reducing potential to generate the desired fuel, usually hydrogen gas, by the reduction catalyst from the protons and electrons generated in the water oxidation cell. The device employs two different semiconductors and increases the amount of the solar spectrum that is being utilized because two different chromophores can be used, therefore increasing the maximum theoretical photoconversion efficiency from 31% in a single junction cell to 42% in a tandem junction cell.[22]

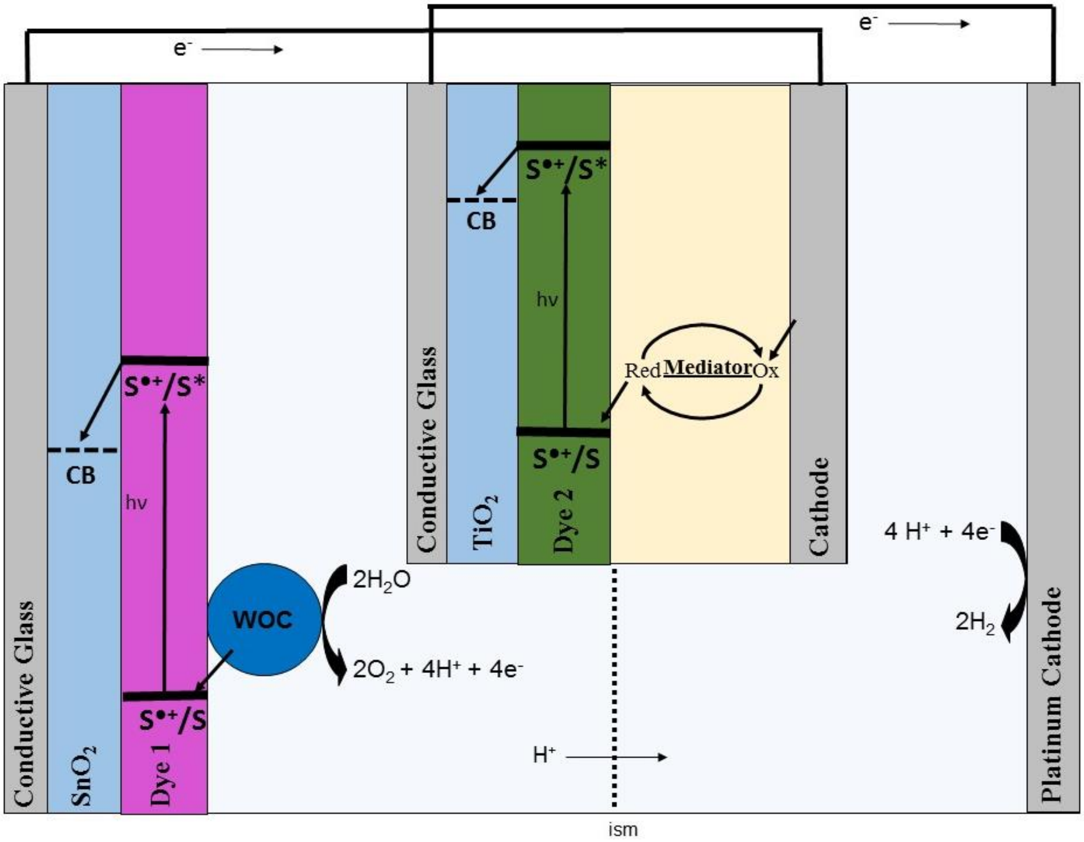

Figure 2. A general schematic of a PECFC where WOC is the water oxidation catalyst and ism is an ion selective membrane.

Microbial systems use engineered organisms to produce a fuel. Modified cyanobacteria and green algae can be used to produce a simple fuel like hydrogen[17] or they can be used to fix CO_2 and produce more complex fuels like methane and butanol.[18,19] By using a microbial systems in tandem with a photovoltaic, as discussed in Chapter 5, we aim to improve the efficiency of microbial systems.

Each system is made up of modular components that can be optimized separately to eventually incorporate into the final device. DSSCs and PECFCs are each composed of electrodes with semiconductors spread on the surface. These semiconductors can be either

N-type or P-type[23,24] and are sensitized with a light-absorbing chromophore, typically a porphyrin, phthalocyanine, or ruthenium dye.[11,16,25] The dyes are attached to the semiconductor via an anchoring group (Figure 3). PECFCs require catalysts for both water oxidation and proton reduction.

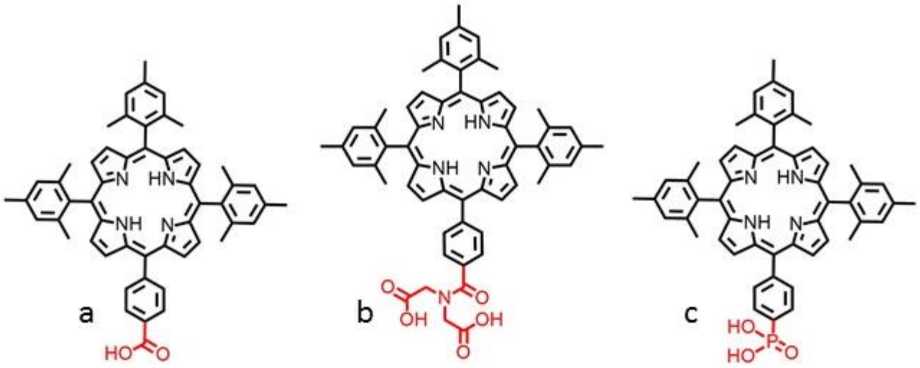

Figure 3. Examples of the different anchoring groups (red) discussed in this thesis: a) carboxylic acid, b) imidodiacetic acid, and c) phosphonic acid.

To create devices that are efficient enough to meet humanities energy demands, one must improve upon the natural system.[26] Understanding how the natural system works is crucial to mimicking and improving it. Two components of the natural system that this thesis discusses is photoprotection by carotenoids, Chapter 3, and charge separation in PSII, Chapter 4. Photoprotection is essential because when excess solar radiation is absorbed, the photosystems can be overloaded with excitation energy leading to the sensitization of singlet oxygen, a deleterious reactive oxygen species capable of destroying cellular structures and photosynthetic devices. When the overloaded situation is produced the tetrapyrroles undergo intersystem crossing to the triplet state, which has the potential to sensitize singlet oxygen. Carotenoids are able to perform photoprotection in a few ways, one of them being through triplet-triplet energy transfer from the tetrapyrrole to the carotenoid, where the carotenoid triplet cannot sensitize singlet oxygen and the energy instead decays rapidly to the ground state (Figure 4).[27-30] Understanding this triplet-triplet energy transfer is important for being able to reproduce and optimize the principles in artificial devices as protection from overwhelming solar irradiation.

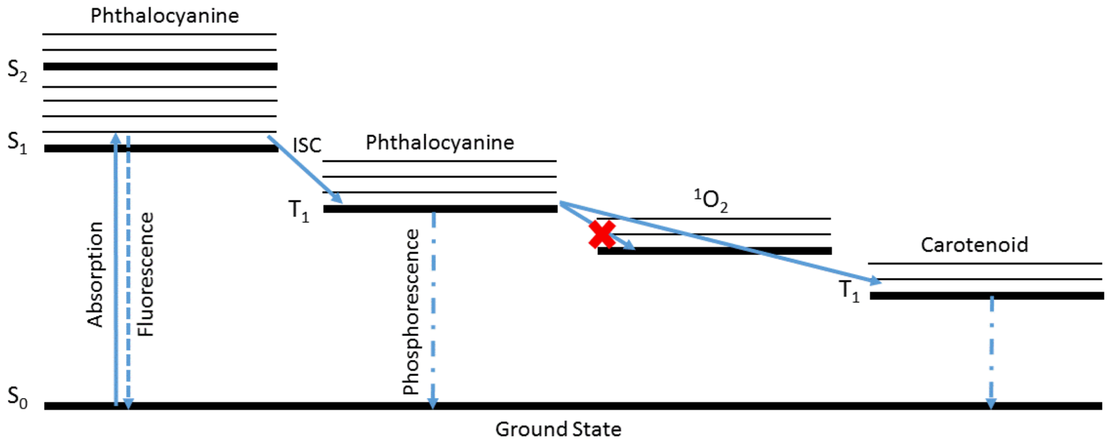

Figure 4. Illustration of the energy states involved in photoprotection by carotenoids. ISC is for intersystem crossing.

The other component of photosynthesis that this thesis addresses in Chapter 4 is charge separation in PSII. In PSII, it is known that $P680^{\bullet+}$ (the oxidized photoactive species of PSII) is relatively short lived (on the hundreds of nanoseconds timescale) and the process of water oxidation at the OEC is quite slow (on the millisecond time scale). To achieve a kinetic match in the electron transfer reaction between these two redox centers a redox relay consistent of a tyrosine-histidine pair is situated between P680 and the OEC. It is thought that the relay function through a proton-coupled electron transfer (PCET) mechanism.[31,32] To understand the PCET mechanism, it is necessary to design model systems to study the characteristics of this process and for implementation into artificial devices with the purpose of increasing overall efficiencies.

Lastly, Chapter 7 details the synthesis of other novel compounds that can be used for developing artificial photosynthetic devices.

Chapter 2

PORPHYRINS FOR ARTIFICIAL PHOTOSYNTHETIC SYSTEMS

Chapter 2.1

A tandem dye sensitized photoelectrochemical system for light driven hydrogen production

Benjamin D. Sherman, Jesse J. Bergkamp, Chelsea L. Brown, Ana L Moore, Devens Gust, and Thomas A. Moore

A manuscript with the subject of this chapter is presently in preparation.

My contribution to this work is assisting with synthesis of the porphyrin, gathering data, and helping with the editing process.

Abstract

Combining a dye sensitized photoelectrochemical cell in series with a dye sensitized solar cell establishes a tandem system for the generation of H2 from hydroquinone with only light energy. To target distinct portions of the spectrum, a more-blue absorbing freebase porphyrin and more-red absorbing Si inserted phthalocyanine chromophores are used at the two photoelectrodes. With incorporation of a suitable water oxidation catalyst, this approach could enable tandem photochemical water splitting without the need for p-type semiconductors.

Introduction

Through the conversion of abundant precursors (H_2O and CO_2) to fuel using only energy from sunlight, photosynthesis supports nearly all life on the planet.[33] In the process of oxygenic photosynthesis, the net conversion of water and carbon dioxide to oxygen and reduced carbon compounds is driven by the absorbed energy of two photons per electron involved in the process. Although photosynthesis does use two photons per electron, because the two photosystems have essentially the same bandgap, the tandem junction advantage is not realized.[26,34] A detailed thermodynamic accounting for artificial photosynthesis shows that a tandem junction approach is essential to maximize the efficiency of using solar energy to split water to hydrogen and oxygen (essentially the same thermodynamics apply to photosynthesis in which CO_2 is reduced to carbohydrates).[26,35,36]

Tandem photoelectrochemical systems capable of generating hydrogen from water with sunlight at efficiencies greater than 12% have been known for over 15 years.[37] Unfortunately, the high cost in materials and manufacturing, as well as long term stability of some of these systems, makes large scale implementation unlikely.[38] One strategy for potentially decreasing the cost of a tandem water splitting system centers on the development of photoelectrodes based on those used in dye sensitized solar cells (DSSC).[39] In the context of solar water splitting, a dye sensitized photoelectrode would function analogously to that in a DSSC,[9] with the distinction that a catalyst to carry out one half reaction of water splitting be incorporated at the electrode interface. This approach offers cost savings by avoiding the need for high purity, defect free crystalline semiconducting materials and through the the incorporation of organic chromophores. In addition, the system embodies a compartmental design, allowing for the interchange of different components, for instance the dye or catalyst as improved versions become available, while maintaining the integrity of the overall design.

Our group in collaboration with Mallouk's group at Penn. State University,[15,16] along with several others[40-43] have studied photoanodes for use in water splitting dye sensitized photoelectrochemical cells (DSPEC). A ubiquitous feature in these single junction systems is the need for applied bias to carry out the net conversion of water to O_2 and H_2. With the advantages of a tandem junction system as outlined above, a logical step in the progress of DSPEC systems involves the incorporation of a second light absorbing junction, for instance a DSSC, a semiconductor based photovoltaic (PV), or DSPEC photocathode, to satisfy the need for added bias to split water with the only energy input from light. In this vein, Sun et al. have reported a dye sensitized photoanode/photocathode system capable of supporting a steady state photocurrent without applied bias.[44]

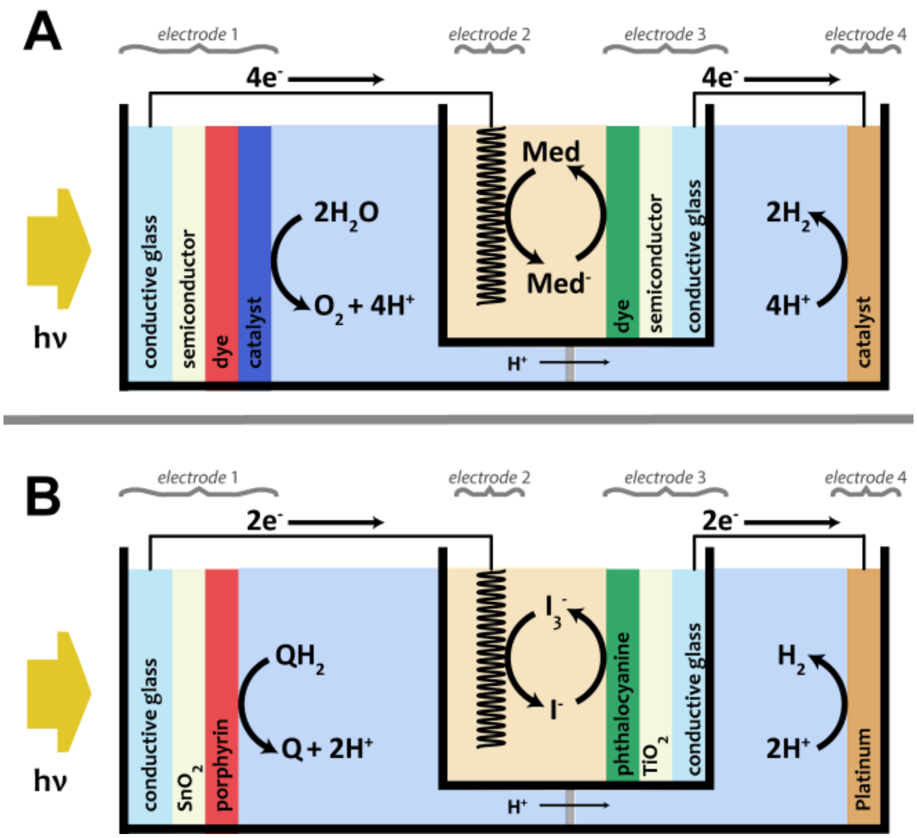

Figure 5. Schematics of (A) a tandem DSPEC and DSSC system connected in series for the light driven conversion of water to O_2 and H_2 and (B) the comparative tandem system studied here for the light driven production of H_2 from hydroquinone with the only energy input from light.

Figure 5 presents a design of a tandem system for light driven water splitting (panel A) and the specific tandem system used in this study (panel B). The system consists of four electrodes, two dye sensitized photoanodes and two dark cathodes comprising a DSPEC wired in series with a DSSC. Photoanode *1* absorbs bluer wavelengths of the incident light and carries out the light driven oxidation of the electron source. The second photoanode in the system, *3*, absorbs light of longer wavelength and caries out the oxidation of a redox mediator. The photoanodes are parallel to each other and perpendicular to the path of illumination, and, as such, the shorter wavelength absorbing junction is positioned in front of the longer wavelength absorbing junction. Electrode *2* serves as the cathode of the DSSC and carries out the reduction of the mediator. The production of the high energy reduced fuel occurs at *4,* the cathode of the DSPEC. A proton permeable membrane (PEM) allows proton movement between *1* and *4* while preventing diffusion of the oxidized product at *1* or reduced product at *4* across the cell and thereby prevents short circuiting of the system.

Simply stated, the system shown in Figure 5 represents an artificial Z-scheme. While sharing design elements with natural photosynthesis, tuning the spectral (band gap) and redox properties of the dyes used as well as the choice of semiconductor materials in the system can, in theory, lead to overall efficiencies much greater than that observed in nature.[26] This study focuses on the development of a tandem DSPEC system incorporating two distinct chromophores with disparate spectral and redox properties, a porphyrin (at *1*) and a phthalocyanine (at *3*), as well as utilizing both tin(IV) oxide (SnO_2) and titanium(IV) oxide (TiO_2) as semiconducting materials at *1* and *3* respectively to facilitate current flow in the system with the only energy input from light.

Results and Discussion

As seen in Figure 5, the design of the tandem photoelectrochemical cell used in this study incorporates two n-type semiconductor based photocells wired in series. Considering the two photocells in isolation, the electrodes *1* and *4* comprise a standalone DSPEC while *2* and *3* comprise a DSSC. This tandem cell design contrasts with that of a two electrode tandem cell that incorporates a photoanode and photocathode.[44-46] The advantage of a four electrode system over the two electrode system lies in avoiding the use of a dye-sensitized photocathode based on a p-type semiconductor.[46-48] Typical p-type semiconductors used in such applications, generally NiO and CuO, exhibit poor photoconversion efficiencies as compared to systems using n-type semiconductors (TiO_2 or SnO_2 e.g.). Incorporating n-type materials at both photojunctions should therefore avoid the loss in efficiency due to charge recombination that would otherwise occur at the p-type interface.[49]

Although overall water splitting is not demonstrated herein, this study does elaborate on a multipanel water splitting device design first described by Bard et al.[50] and demonstrates a route to improving the overall efficiency of a tandem dye sensitized photoelectrochemical system. Here the photoanodes incorporate different semiconductor materials, SnO_2 and TiO_2, with the conduction band levels chosen to support the chemistry at each interface. In addition, two distinct chromophores allow each junction to target separate portions of the solar spectrum enabling higher theoretical efficiency.[26,36]

Taken together, the redox and spectral properties of the chromophores predicate their position in the tandem system. Incident irradiation would first interact with electrode *1* containing **1** (Figure 6). At this interface, the absorption of higher energy, more blue light ultimately drives the oxidation of the electron source in the system. The potential of the porphyrin radical cation formed after excitation and subsequent sensitization of the SnO_2 must be sufficiently positive to carry out the oxidation of the electron source, in this case QH_2. On a thermodynamic basis, the reduction potential of the $\mathbf{1}^{\bullet+}/\mathbf{1}$ couple (1.03 V vs. Ag/AgCl)[51] is 150 mV positive of water oxidation at pH 5.8, the conditions used here, and, with a suitable catalyst, might be sufficient in a water splitting device.

Dye selection and synthesis

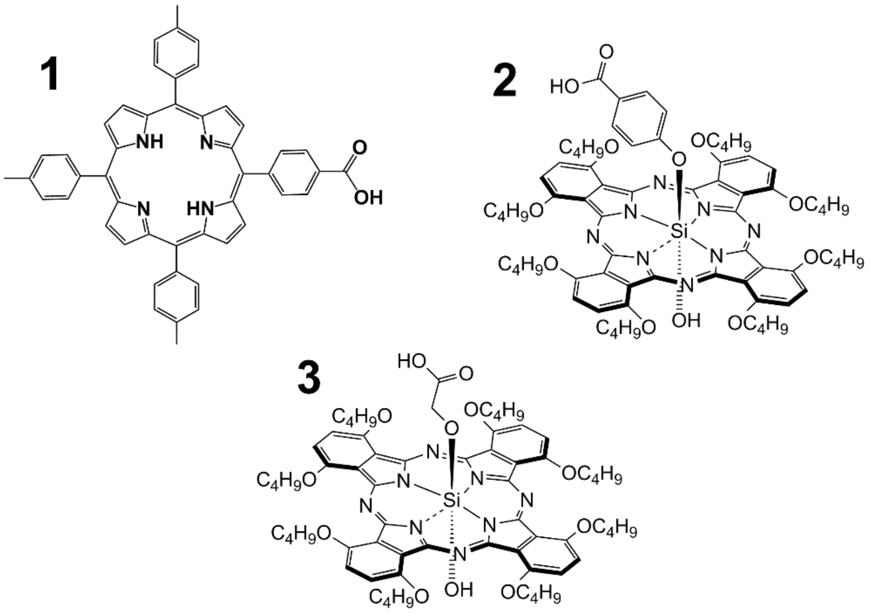

Figure 6. Structures of dyes used in this study.

Figure 6 shows the chemical structures for dyes **1**, **2**, and **3** used in this study. Both the spectral and redox properties of these chromophores led to their selection for this study. Tritolyl porphyrin **1** contains a carboxylate anchoring group for attachment to a metal oxide surface and was prepared using established protocols.[52] As a class, porphyrins absorb strongly in the higher energy portion of the visible spectrum, with Q-bands extending to ~650 nm. In addition the reduction potential for the oxidized radical cation form of **1** is sufficiently positive to oxidize the sacrificial mediator (hydroquinone, HQ_2 used in this study). In addition, the reduction potential for forming the radical cation from the excited state of **1** is also sufficiently negative for sensitizing SnO_2.

The second photojunction in this system incorporates phthalocyanine **2** bearing an axial carboxylic moiety, again for anchoring the dye to a TiO_2 semiconducting electrode. This dye was selected for its strong absorption from 650-750 nm. Though absorbing more to the low energy portion of the visible spectrum and extending to the near-infrared, the reduction potential for the $Pc^{\bullet+}/Pc^*$ couple still lies sufficiently negative for sensitizing TiO_2. The electron donating nature of the alkoxy moieties at the 1,4 positions (non-peripheral) of the macrocycle cause both a bathochromic shift in the Q-band and negative shift in the redox potentials as compared to unsubstituted phthalocyanines.[53]

A new method was developed for the synthesis of **3**. Li et al.[54] have demonstrated the formation of ether groups attached to the central silicon atom in phthalocyanines starting with triflate, chloride, or isopropyl groups. We have used similar chemistry but started from the bis-hydroxy silicon phthalocyanine (SiPc). It's worth noting that under the conditions used here, one can obtain mono substituted phthalocyanines without the need of protecting one of the reactive ligands.

The generation of **3** bearing an axial glycolic ether ligand to Si first demonstrated the viability of this method. The synthesis of **3** was done at room temperature with bis-hydroxy SiPc in dichloromethane using pyridine as base, followed by the addition of glycolic acid. By controlling the equivalents of glycolic acid, the mono-substituted Pc can be obtained. Compound **3** was characterized by ^1H NMR and MALDI-TOF mass spectrometry (see SI) The ^1H NMR shows a signal at ca. -1.5 ppm, which can be attributed to the methylene protons. The upfield chemical shift of the CH_2 protons axial to the plane of the macrocycle is in agreement with reported values.[55,56] DSSCs based on SiPc **3** gave little photocurrent presumably due to insufficient dye loadings on the TiO_2 surface. This could be due to the close proximity of the anchoring group to the large macrocycle, which sterically hindered **3** from attaching to the TiO_2 surface. Because of such complications, compound **3** was not used in a tandem cell application. Compound **2** bears an axial carboxy group separated by a phenyl spacer to the ether group that provides the link to the central Si of the macrocycle. Our group previously reported the synthesis of SiPc with axial substitution, starting with *para*-phenol esters.[53] Here we introduce a method to directly modify the axial position of a SiPc with a free carboxylic acid, thereby eliminating the need for deprotection steps.

Photochemical results

In the absence of sufficiently rapid and stable water oxidation catalysts, sacrificial donors were used to determine the functionality of the other components comprising the photoanode.[14] Previous work has shown that NADH is an adequate electron donor in solution to support the photogeneration of hydrogen in a single threshold TiO_2 dye-sensitized photoelectrochemical system.[57,58] An extension of that work also explored the use of hydroquinone (QH_2) as a sacrificial electron donor, though NADH gave far superior photoelectrochemical performance in the system.[59,60] Comparing the same TiO_2-porphyrin electrodes, the use of QH_2 gave both overall lower photocurrent densities as well as a more positive potential for the point of zero current under illumination. The influence of charge recombination to the oxidized form of the electron donor (NAD^+ or 1,4-benzoquinone), with recombination occurring more readily to benzoquinone, largely explains the difference in performance between the two sacrificial donors.[60] Given these results, a single junction system with NADH can produce H_2 spontaneously under illumination whereas the same system with QH_2 cannot.

Although a SnO_2-porphyrin photoanode in the presence of QH_2 does not sustain photocurrent without applied bias (dashed trace Figure 7, upper panel), stable photocurrent does flow with sufficient forward bias. Similarly, a TiO_2 based photoanode prepared with a $Ru(bpy)_3^{2+}$ chromophore and IrO_2 water oxidation catalyst requires a forward bias to carry out light driven water oxidation, largely attributed to unfavourable recombination dynamics.[15] In place of an electrical bias, non-actinic wavelengths to the SnO_2-dye electrode can be utilized at a second light absorbing junction to generate the needed applied voltage. In this report, we constructed a DSSC using phthalocyanine **2** to generate sufficient photoelectrical bias to sustain photocurrent in the tandem system with the only energy input from incident light.

Overall, the tandem system described here carries out the net conversion of hydroquinone to H_2 with only light energy. This of course represents less overall solar energy conversion than water splitting (1.23 V) yet still entails the conversion of some solar energy to chemical potential, with, in the case of QH_2 at pH 7 of around 0.7 V ($E_{H+/H2} = –0.44$ V vs. NHE; $E_{Q/QH2} = 0.3$ V vs. NHE).[61] Any sustainable solar energy conversion must consume a renewable electron source with water the ideal choice. Although this work relies on a non-regenerative process (a closed loop would require energy production from a fuel cell burning H_2 and reducing Q) the study of QH_2 does illustrate the benefit of the tandem junction system.

With the presence of a sacrificial donor in the anodic side of the photoelectrochemical cell, illumination of the tandem cell produces a stable photocurrent response without any bias applied to the system as shown in Figure 7. As controls, in the absence of a sacrificial donor, the system produces negligible photocurrent and with a sacrificial donor present, but without the DSSC connected in the circuit, negligible photocurrent is generated during illumination (dotted trace). Observation of the potential reached at the platinum cathode of the photoelectrochemical cell versus a reference electrode in the same solution shows that, upon illumination of the tandem system, the Pt polarizes negative of the H^+/H_2 couple, indicating the photochemical production of H_2 (Figure 7) with H_2 production verified by GC (Figure 9).

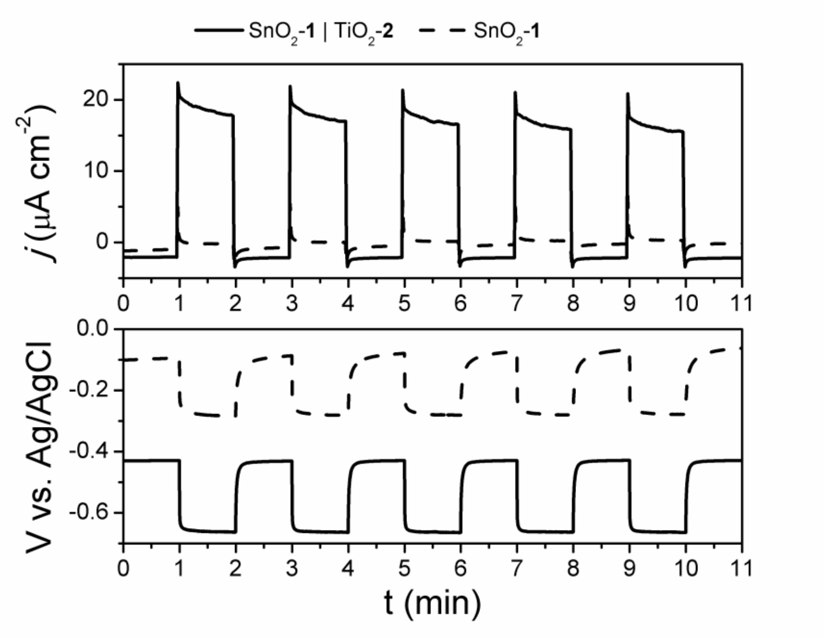

Figure 7. Photocurrent trace (upper frame) and voltage vs. time trace (lower frame) as measured at the platinum cathode (electrode *4* in Figure 5). Solid trace shows the result using a tandem configuration and the dashed trace shows the result for the DSPEC cell alone (electrode *1* directly wired to *4*, i.e. no DSSC in series). The electrolyte conditions for the DSPEC shown consisted of 25 mM Na_2SiF_6 buffer at pH 5.8 with 100 mM Na_2SO_4 supporting electrolyte. The DSSC electrolyte consisted of 1:1 acetonitrile:valeronitrile with 0.2 M LiI, 0.05 M I_2, 0.2 M TBAI, and 0.5 M 4-t-butylpyridine.

The photochemical performance of the phthalocyanine DSSC as measured in the same context as in the assembled tandem cell (DSPEC not connected in series) is shown in Figure 8. Although modest in terms of overall performance compared with state of the art DSSCS,[62] the principal objective for the DSSC here is to supply sufficient photovoltage to support photocurrent in the DSPEC with incident light that goes unabsorbed at the photoanode of the DSPEC. The photocurrent density of the TiO_2-**2** DSSC (~300 uA cm^{-2}) exceeds that of the SnO_2-**1** even at high applied bias. With the two cells wired in series, the cell with the lower photocurrent will dictate the maximum photocurrent obtainable by the tandem system. In the case explored here, the phthalocyanine based DSSC generates sufficiently high photocurrent and photovoltage to sustain the generation of H_2 by the tandem system without the application of any applied bias.

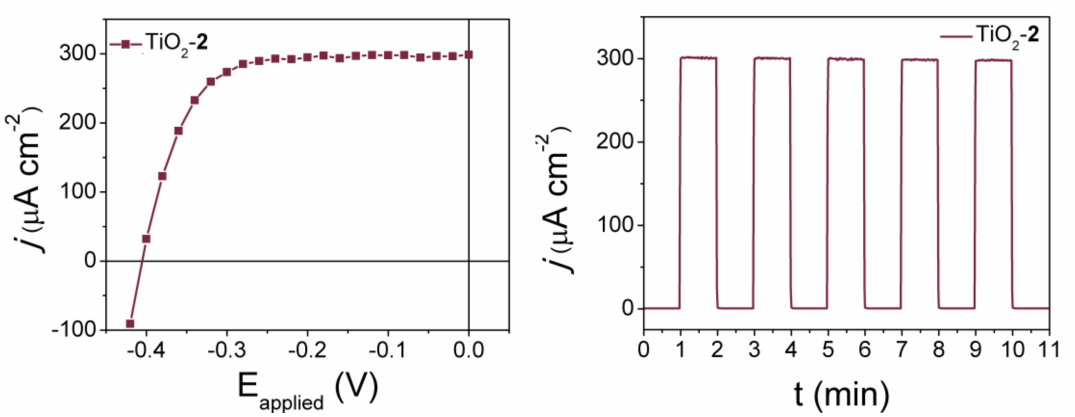

Figure 8. Current vs. applied voltage (left) and current vs. time (right) for the TiO_2-**2** based DSSC measured in the same orientation as used in the tandem configuration.

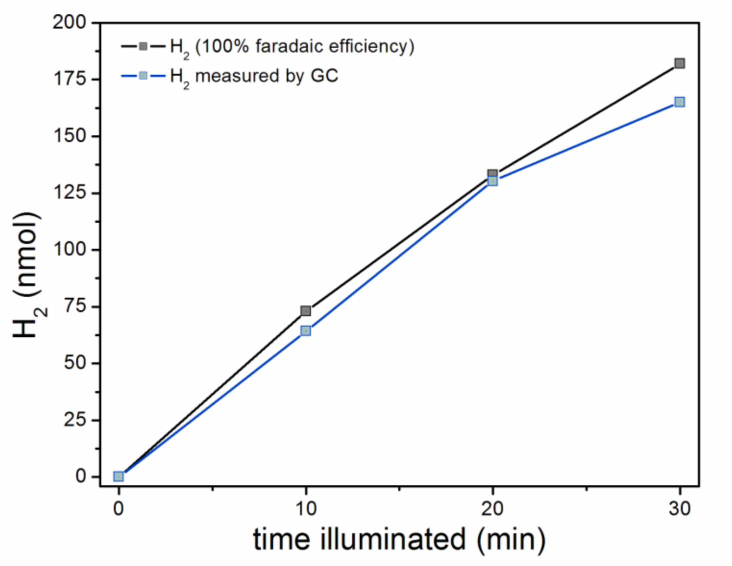

Figure 9. H_2 produced vs. time as measured by gas chromatography (blue trace) and as calculated from the charge passed in the experiment.

The results with QH_2 demonstrate that the second, more-red absorbing junction in this system can supply the added bias to overcome kinetic limitation at the first junction. To demonstrate the net production of H_2 with light by the tandem cell, gas samples collected above the Pt counter electrode were measured by gas chromatography. As shown in Figure 9, the light driven conversion of QH_2 to H_2 occurs with approximately 100% faradaic efficiency while no H_2 is produced when the DSSC is removed from the circuit. In previous work applied electric voltage was needed, here all the energy input in the system comes directly from light. This has important implication with comparable systems designed for overall water splitting. Single junction dye-sensitized photoelectrochemical systems for light driven water splitting almost exclusively use TiO_2 at the photoanode and require applied bias to carry out the net production of H_2.[15,16,40-43]

Conclusions

The tandem configuration presented here is akin to running the single junction cell with an applied bias, however, in place of an electrical bias, incident light unused at the first photojunction generates the needed bias at the second photoanode in the cell. Despite the use of sacrificial donor, this system presents an effective means for both eliminating the need for electrical bias and, by the incorporation of SnO_2, it allows for the utilization of higher potential, more strongly oxidizing dyes to drive water oxidation. Employing SnO_2 at this interface opens the possibility of integrating higher potential porphyrin chromophores, such as those containing pentafluorophenyl groups at the *meso*-positions or cyano moieties at the *beta*-position. Paired with a suitable water oxidation catalyst, such a surface could enable H_2 production from water as shown here with QH_2.

Supplemental Information

Experimental Details

All materials used in this study were used as received unless otherwise stated and purchased from either Sigma Aldrich or Alpha Aesar. Fluorine doped tin oxide (FTO) was purchased from Hartford Glass.

Photoelectrode preparation

Colloidal TiO_2[63] and SnO_2[64]sol-gel pastes were prepared using literature protocols. For the FTO-TiO_2 electrodes, a compact TiO_2 blocking layer was first prepared. The blocking layer was formed via spray pyrolysis of 0.2 M titanium diisopropoxide bis(acetylacetonate) in ethanol onto the conductive face of the FTO electrodes that were heated to and maintained at 400 °C during the deposition. The FTO was then heated at 450 °C for 30 min after deposition of the blocking layer, and prior to the application of the sol-gel paste. The colloidal paste was applied to the FTO electrodes using a doctor-blade method with tape spacers used to set the thickness of the sol-gel layer. Once spread, the films were allowed to dry in air and then annealed at 450 °C for 45 min. After annealing, the electrodes underwent an overnight soak in a 40 mM solution of $TiCl_4$ in water. Finally they were dried and cured for an addition 30 min at 450 °C. For the FTO-SnO_2 electrodes, a compact SnO_2 blocking layer was first established by spin coating (2000 rpm, 1 min) a solution of 15 wt% SnO_2 in water on the FTO face, followed by heat treatment at 450 °C in air for 45 min. The SnO_2 sol-gel paste was then applied, again using the doctor blade method. Finally, the FTO-SnO_2 were soaked in a 40 mM solution of $TiCl_4$ in water overnight to introduce an TiO_2 surface coating which has been shown to improve device performance.[65] The FTO-TiO_2 electrode were soaked in a 400 µM solution of **2** or **3** in ethanol and the FTO-SnO_2 electrodes in a 400 µM solution of **1** in ethyl acetate overnight, and rinsed with ethanol for the former or ethyl acetate for the latter to form the fully prepared photoelectrodes used in this study.

Photochemical experiments

A custom made photoelectrochemical cell was used to prepare the dye sensitized photoelectrochemical cell (DSPEC) with a nafion membrane separating the anodic and cathodic sides of the cell. Each side of the cell consisted of a threaded glass opening (acethred #15, Ace Glass) with custom machined Delrin bushing. Each bushing contained three drilled and taped ports allowing introduction of electrode leads or gas lines which could be secured using threaded nuts (IDEX Health and Science) allowing for a complete gas-tight seal on either side of the cell. Unless otherwise noted, the electrolyte for the DSPEC consisted of 0.1 mM Na_2SO_4 and 25 mM SiF_6 buffer with the pH adjusted to 5.8 using a concentrated solution of $NaHCO_3$. Additionally the anodic solution of the DSPEC contained 20 mM hydroquinone. To form the dye sensitized solar cells (DSSCs) used here, the FTO-TiO_2 photoanode described above was attached to a FTO-Pt cathode using a heat shrink gasket (Solaronix). The Pt coating was applied to the FTO by applying a solution of chloroplatinic acid in ethanol and heating to 450 °C for 30 min. The electrolyte used for the DSSC consisted of 1:1 acetonitrile:valeronitrile with 0.2 M lithium iodide, 0.05 M iodine, 0.2 M tetrabutylammonium iodide, and 0.5 M 4-*tert*butylpyridine. The electrolyte was introduced inside the DSSC via ports drilled through the FTO-Pt cathode after assembling the cell.

For the light driven experiments, a 350 W Xe light source (Osram) was used with a 400 nm long pass filter (Thor Labs) as well as an AM 1.5 filter (Oriel) with the DSPEC photoanode placed to receive 100 mW cm^{-2} light intensity. For the tandem cell photocurrent measurements, a Keithely 2400 source meter was connected between the photoanode of the DSPEC and the FTO-Pt cathode of the DSSC to monitor the current flow in the cell. A separate wire connected the DSSC photoanode to the Pt cathode of the DSSC to complete the series connection. The DSSC was placed directly behind the DSPEC photoanode for the tandem configuration to receive light that had passed through the DSPEC photoanode. For the voltage vs. time traces, a fresh prepared silver/silver chloride reference (in saturated KCl) was prepared and placed in the cathodic chamber of the DSPEC. A CH Instruments 650C potentiostat was used to monitor the opencircuit voltage between the Pt counter and the Ag/AgCl reference during the course of the experiment. The incident photon to current efficiency (IPCE) measurement used a Jobin-Yvon monochromator and a Keithely 2400 source meter and custom written software (LabVIEW). The light intensity at each wavelength was calibrated using a photodiode (Newport).

Hydrogen measurements

An SRI Instruments 310C gas chromatograph was used for detection of photogenerated hydrogen. In order to measure the evolved hydrogen gas, a Pt cathode assembly was constructed in order to both minimize the headspace volume above the cathode (1.2 mL) and seal off the headspace from the atmosphere with a septa port for extracting samples for GC analysis. The assembly consisted of an insulated wire lead placed inside a 1/8’’ Teflon tube with a Pt wire soldered to the end of the lead, extruding from the end of the tube. The Pt wire end was then place inside a piece of glass cylinder (internal diameter 3.5 mm) with an epoxy seal applied between the tube and the top of the glass cylinder. A second piece of glass cylinder was epoxied to the top of the Teflon tube with the wire and a second piece of tubing extending out the top through an epoxy seal. Completing the assembly, the end of the second tube was connected to one side of a ¼’’-28 threaded union (IDEX Health and Science) with a ferrule and nut with the opposite side of the union containing a ¼’’-28 threaded to female Luer fitting. A Luer cap with a drilled hole through the top and a septa placed inside the cap was fastened over the female Luer fitting. To measure a gas sample, a 100 µL syringe was filled with Ar, inserted through the septa, mixed with the head space gas by plunging (causing noise in the current trace of the measurement due to electrolyte flow across the Pt counter as the syringe was moved back and forth), extracted from the septa, and injected into the GC.

Synthesis

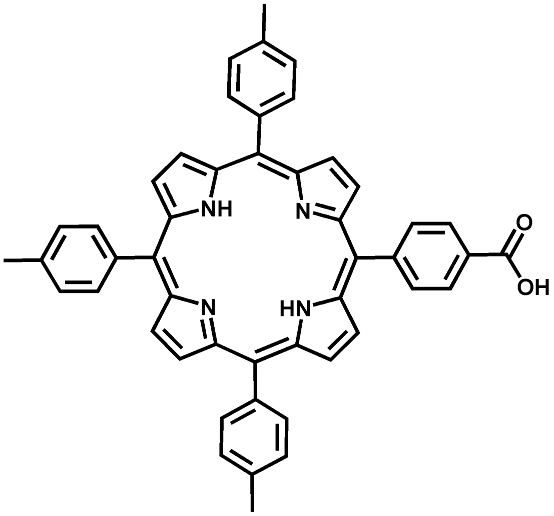

5-(4-carboxyphenyl)10,15,20-tri(4-methylphenyl)- 29,31-H2 Porphyrin (1). Porphyrin **1** was prepared by the Adler-Longo porphyrin condensation method.[52] By adjusting the stoichiometry of the two aldehydes one can change the ratio of different substituted porphyrins formed from the condensation. Using a stoichiometry of 1, 5, and 6 of methyl 4-formylbenzoate, 4-methylbenzaldehyde and pyrrole respectively, compound **1** is preferentially formed. After treatment with potassium hydroxide, followed by washing with water the target mono-carboxyphenyl porphyrin is obtained. Characterization of compound **1** was achieved by using ^{1}H NMR and MALDI-TOF-MS. All values were consistent with literary values.

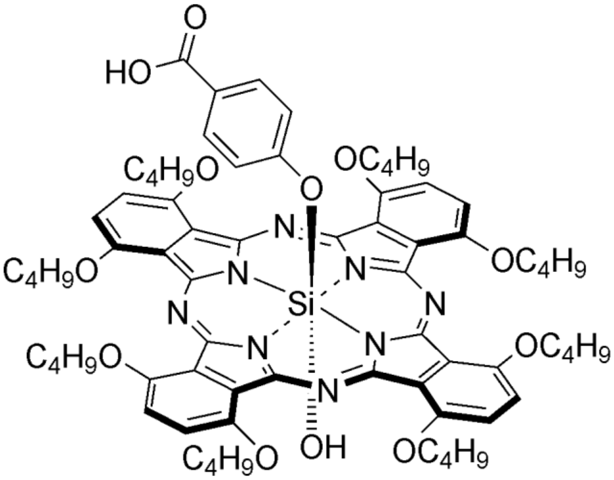

4-(Oxybenzoic acid)hydroxy-1,4,8,11,15,18,22,25-octabutoxyphthalocyaninatosilicon(IV) (2): Into a dry 10 ml round bottom flask was placed SiPc(OH)$_2$ (20 mg, 0.017 mmol), 4-hydroxybenzoic acid (12 mg, 0.087 mmol), dry dichloromethane (4 ml), and pyridine (4 drops). This solution was allowed to stir at room temperature for 4 days. The solution was evaporated under reduced pressure and the crude solid was taken up in dichloromethane and washed with deionized water, dried with sodium sulfate and concentrated. The crude product was purified via silica gel column chromatography using toluene/ethyl acetate (65:35) as eluent to afford a green solid. Yield 5.3 mg (24%). ^{1}H-NMR (400 MHz; CDCl$_3$; 0.03% Me$_4$Si): δ_H, ppm 7.63 (s, 8H) ppm 6.40 (d, 2H, J=8.8Hz) ppm 4.78 (m, 16H) ppm 2.86 (d, 2H, J=8.8Hz) ppm 2.14 (p, 16H) ppm 1.63 (sex, 16H) ppm 1.04 (t, 24H, J=7.4Hz). MS (MALDI-TOF): *m/z* calcd. for $C_{71}H_{86}N_8O_{12}Si$ 1271.57, obsd. 1272.43 (M+H), 1149.58 (M-benzoic acid).

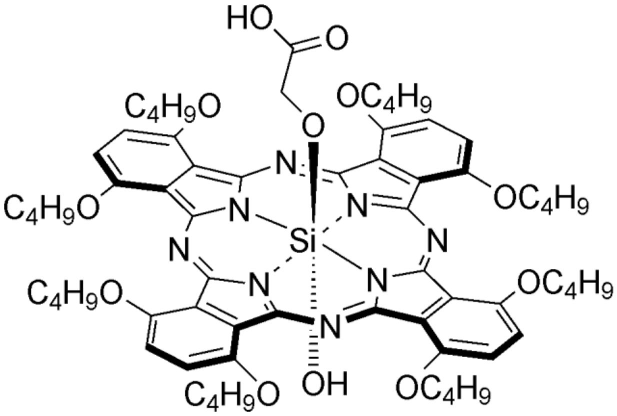

2-(Oxyacetic acid)hydroxy-1,4,8,11,15,18,22,25-octabutoxyphthalocyaninatosilicon(IV) (3). A portion of SiPc(OH)$_2$ (30 mg, 0.026 mmol) was dissolved in dry pyridine and the solution was degassed for 5 min with argon. Glycolic acid (9.8 mg, 0.13 mmol) was added and the resulting solution was stirred at 55 ^{o}C, under argon for 3 days. The pyridine was evaporated under reduced pressure and the resulting residue was taken up in dichloromethane and washed with deionized water (20 mL). The organic phase was dried over sodium sulfate and evaporated under reduced pressure. Column chromatography was done using silica gel in two purification steps; first, toluene/ethyl acetate/methanol (60:38:2) was used as eluent followed by a second column using chloroform/ethyl acetate/methanol (78:20:2) as eluent, which afforded a green solid. Yield 7 mg (22%), ^{1}H-NMR (400 MHz; CDCl$_3$; 0.03% Me$_4$Si): δ_H, ppm 7.63 (s, 8H, Pc-H) ppm 4.86 (t, 16H, -C*H$_2$*-CH$_2$-CH$_2$-CH$_3$, J=7.4Hz) ppm 2.20 (p, 16H, -CH$_2$-C*H$_2$*-CH$_2$-CH$_3$) ppm 1.66 (sex, 16H, -CH$_2$-CH$_2$-C*H$_2$*-CH$_3$) ppm 1.08 (t, 24H, -CH$_2$-CH$_2$-CH$_2$-C*H$_3$*) ppm -1.40 (s, 2H, CH$_2$-Glycolic acid). MS (MALDI-TOF): *m/z* calcd. for $C_{66}H_{84}N_8O_{12}Si$ 1209.50, obsd. 1209.49, 1149.58 (M-Glycolic acid).

Supplemental Figures

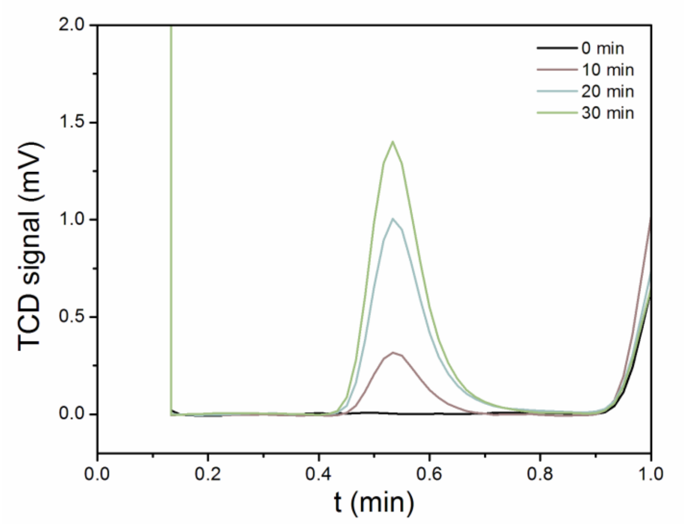

Figure S 1. GC traces used for determination of the amount of light generated H_2 as shown in Figure 4 of the paper. The peaks starting at 0.4 min and centered at 0.55 min of the trace were assigned to H_2 and verified using a hydrogen standard.

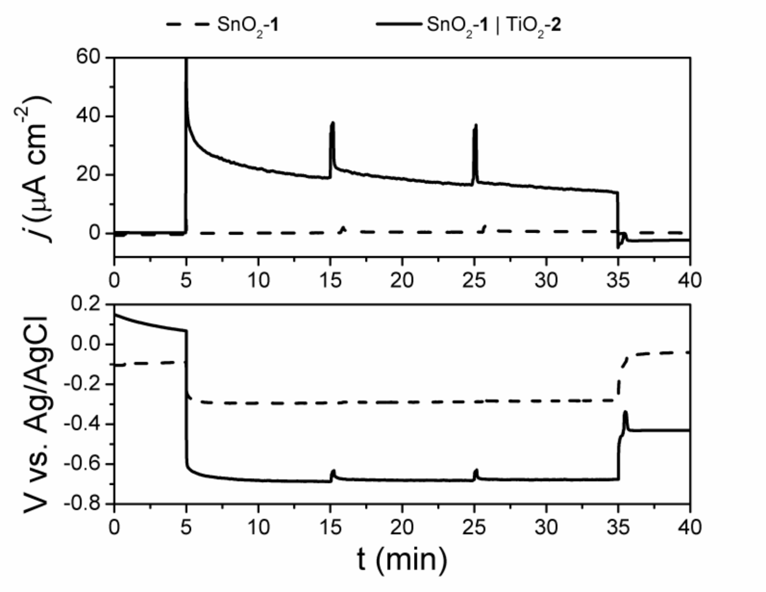

Figure S 2. Photocurrent (upper) and voltage vs. time (lower) as measured at the platinum cathode for a tandem cell (solid trace, same as Figure 7 of the paper) consisting of (electrode *1*) SnO_2-**1**, (electrode *2*) Pt, (electrode *3*) TiO_2-**2**, and (electrode *4*) Pt and DSPEC cell (dashed trace) without the DSSC wired in series (electrode *1* directly connected to electrode *4*). No H_2 is observed in the case of the PEC by GC consistent with the lack of photocurrent and insufficiently negative potential observed at the Pt cathode (dashed traces).

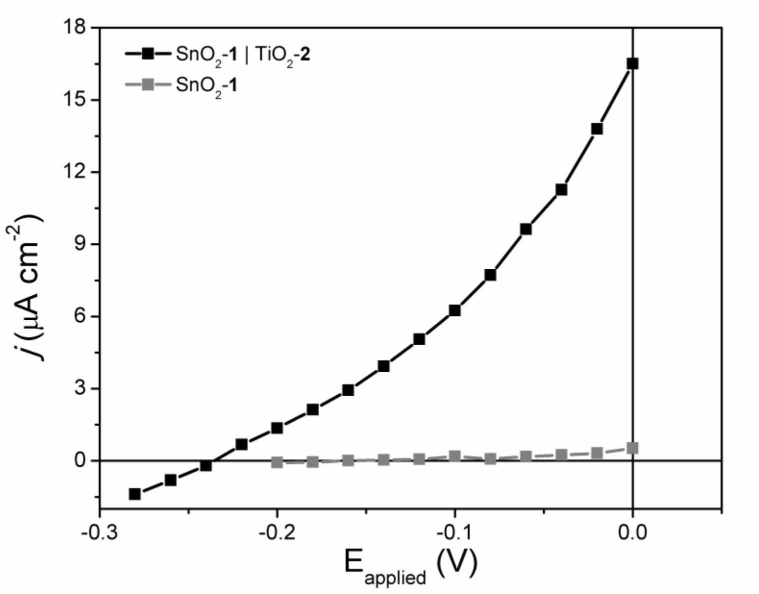

Figure S 3. Photocurrent vs. applied bias for the tandem cell (black trace) and DSPEC without the DSSC connected in series (grey trace).

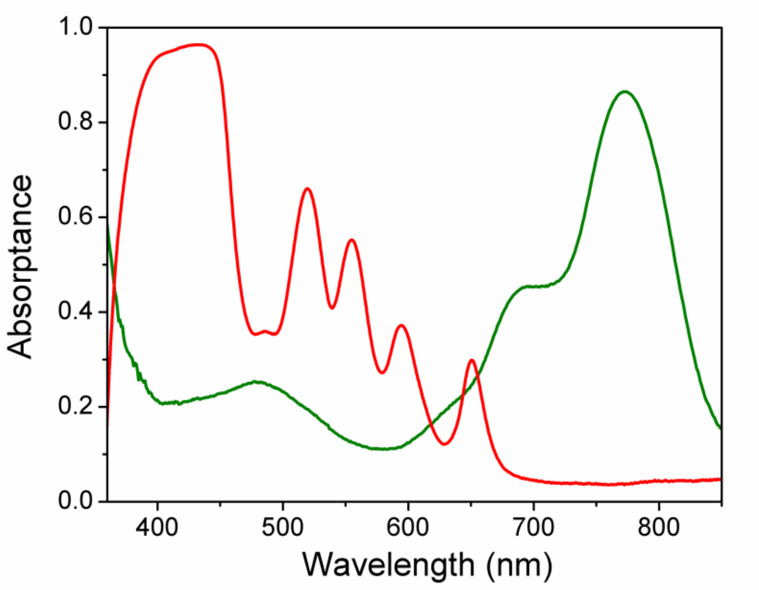

Figure S 4. Absorbance spectra of (red) SnO_2-**1** and (green) TiO_2-**2**.

Chapter 2.2 Journal of Physical Chemistry C Paper

Photo-injection of High Potential Holes into $Cu_5Ta_{11}O_{30}$ Nanoparticles by Porphyrin Dyes

Ian Sullivan,[†] Chelsea Brown,[‡] Manuel J. Llansola-Portoles,[‡] Miguel Gervaldo,[§] Gerdenis Kodis,[‡] Thomas A. Moore,[‡] Devens Gust,[‡] Ana Moore,[‡] Paul Maggard[†*]

[†] *Department of Chemistry, North Carolina State University, Raleigh, NC 27695-8204 USA*

[‡] *Department of Chemistry and Biochemistry, Arizona State University, Tempe, AZ 85287-1604 USA*

§ Departamento de Química, Universidad Nacional de Río Cuarto. Agencia Postal Nro. 3, X5804BYA Río Cuarto, Córdoba, Argentina

Citation:

Ian Sullivan, Chelsea L. Brown, Manuel J. Llansola-Portoles, Miguel Gervaldo, Gerdenis Kodis, Thomas A. Moore, Devens Gust, Ana L. Moore, and Paul A. Maggard. *The Journal of Physical Chemistry C* **2015**, *119*, 21294-21303.

My contribution to this work was synthesis of the porphyrin chromophores, preparing the synthetic write-ups, and aiding in the editing process.

KEYWORDS: $Cu_5Ta_{11}O_{30}$ nanoparticles, porphyrin, hole injection, p-type semiconductors, dye-sensitized solar cell, optical properties.

ABSTRACT

Excited-state hole injection into the valence band of $Cu_5Ta_{11}O_{30}$ nanoparticles (NP-$Cu_5Ta_{11}O_{30}$) was investigated through sensitization with zinc porphyrin dyes using simulated solar irradiance. The $Cu_5Ta_{11}O_{30}$ nanoparticles were prepared by a flux-mediated synthesis and found to have an average particle size of ~10–15 nm by DLS and TEM. The zinc 4-(10,15,20-tris(4-pyridinyl)-porphin-5-yl)phenylphosphonic acid (**D1**) and its analog in which the pyridine groups are methylated (**D2**) were synthesized and found to have excited state reduction potentials appropriate for *p*-type dye sensitization of the nanoparticles. The dye-sensitized NP-$Cu_5Ta_{11}O_{30}$ exhibited fluorescence quenching consistent with electron transfer from the NP-$Cu_5Ta_{11}O_{30}$ to the dye; forward and recombination rates were obtained by transient absorption measurements. Hole injection times of 8 ps and <100 fs were observed for **D1** and **D2,** respectively. Nanoparticulate films of $Cu_5Ta_{11}O_{30}$ were prepared and evaluated in dye sensitized solar cells (DSSC) under simulated solar irradiance (AM 1.5 G, 100 mW/cm^2). Measureable photocurrents with open circuit potentials (V_{oc}) of 200 mV and 110 mV were observed using **D1** and **D2**, respectively.

INTRODUCTION

Anthropogenic activity and especially the massive burning of fossil fuels has a deleterious effect on the global ecosystem.[66] Due to the magnitude of the solar energy reaching the earth, developing a technology capable of efficiently converting sunlight into electricity or highly energetic fuels is an appealing prospect.[33] In this connection, photoelectrochemical dye-sensitized solar cells (DSSCs) have attracted growing interest since the seminal contribution by Grätzel and O'Regan in 1991.[67] Currently, two general classes of DSSC designs can be distinguished. The first (n-DSSC) is based on the sensitization of a wide-band-gap n-type semiconductor oxide (e.g. TiO_2, SnO_2 or ZnO). Photoinduced electron injection from the excited photosensitizer into the oxide conduction band is followed by electron transmission by a conductor through the load and to a non-photochemically active cathode. A mediator in solution transports electrons from the cathode to regenerate the oxidized dye at the photoanode. So far photoconversion efficiencies up to 13% have been achieved.[68] The second class of DSSC uses a p-type metal oxide such as NiO, Cu(I)-containing oxides or doped diamond (p-DSSC). In these devices, photoinduced hole injection into the valence band (VB) of the semiconductor of a photocathode initiates the overall electron flow. Thus far, they have achieved a maximum energy conversion efficiency of only around 1.3%.[24]

These same concepts may be used in the design of photoelectrosynthetic systems that use visible light to split water into oxygen and hydrogen, or that produce other fuels or chemicals. Such systems are generally inefficient because of the great challenge of generating the necessary photopotential.[15] However, if both efficient photocatalytic n-DSSC type anodes and p-DSSC type photocatalytic cathodes were available, one can envision their use in a tandem-type photoelectrosynthetic cell for water splitting. Such a cell would be based on two-step photoexcitation,[69,70] wherein water is oxidized by catalysts at the photoanode and hydrogen is produced by catalysts at the photocathode. In principle, such cells could be very efficient because the overall power conversion efficiency of a tandem cell is higher than the Shockley-Queisser limitation for a single junction cell.[71] In a tandem photoelectrosynthetic cell, electron flow is analogous to that in the Z scheme of natural oxygenic photosynthesis, but the thermodynamics are fundamentally different in that a properly designed tandem cell better matches the absorption spectra of the sensitizers to the solar spectrum, thereby nearly doubling the rate of light absorption. Optimally designed sensitizers would cover the solar spectrum from the near UV to about 750 nm for one photoelectrode and from 750 nm to about 1100 nm for the second photoelectrode.[36]

The principle of operation of a p-type semiconductor sensitized by organic dyes is illustrated in Figure 10a. Light excitation (step 1) of the sensitizer (S), forms the excited state (S*), which decays by hole injection into the valence band of the p-type semiconductor to form the charge separated state (step 2). In this case, because there is no "wiring" to take the hole or electron away from the interface, they must recombine following step 3. Figure 10b illustrates the pathway followed by a hole in a p-DSSC photoelectrochemical cell. Upon light absorption (step 1), the sensitizer excited state (S*) injects a hole into the valence band of the semiconductor, leading to the reduction of the sensitizer ($S^{\bullet -}$) (step 2). The injected holes diffuse to the back side of the transparent conducting electrode, pass into the external circuit and reach the counter electrode where they oxidize the redox mediator (M/M^-) (step 4). This mediator reacts with the reduced sensitizer to restore the ground state of the sensitizer (step 5).[72] In a photoelectrosynthetic application, a catalyst may be linked to or otherwise associated with the sensitizer so that useful synthetic chemistry is carried out at each electrode. In this case, an alternative pathway at the photocathode is reduction of the catalyst by the sensitizer excited state followed by hole injection into the semiconductor by the oxidized sensitizer.

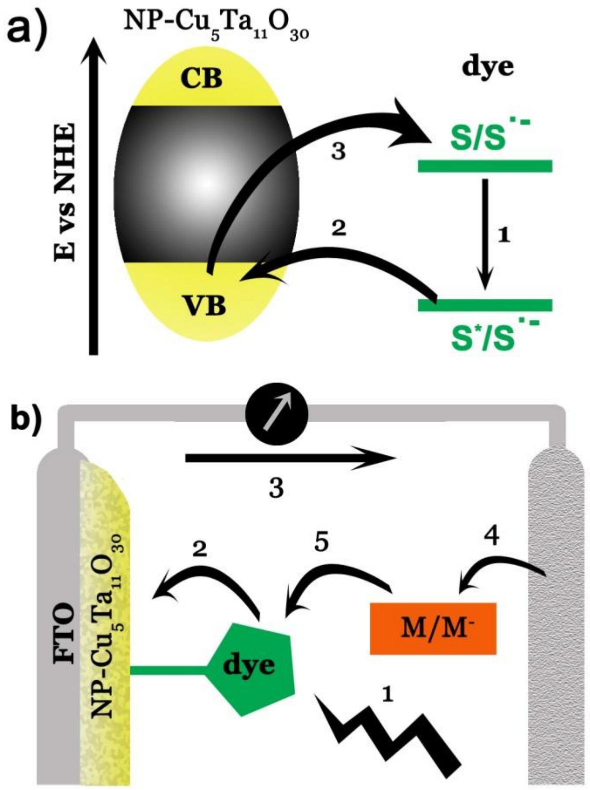

Figure 10. a) Schematic of the processes involved in hole photo-injection in a system of a chromophore and a p-type semiconductor. The numbers on the arrows represent the order in which the processes occur; 1 – light absorption, 2 – hole injection, 3 – electron recombination. b) Schematic of a p-DSSC showing the electron transfer processes involved in the operation of the photoelectrochemical cell, as described in the text.

In this work, we describe the synthesis and characterization of $Cu_5Ta_{11}O_{30}$ nanoparticles (NP–$Cu_5Ta_{11}O_{30}$) and their ability to accept high-potential holes into their valence band from a photoexcited porphyrin. Such nanoparticles may be suitable candidates for construction of tandem cells. In these cells, the photocathode would take advantage of the well-known high hole mobility of the copper(I)-based semiconductors like Cu_2O[73] and

$CuNb_3O_8$,[74] as compared to the significantly lower charge carrier mobility in the commonly used NiO.[75]

EXPERIMENTAL SECTION

Materials. Dichloromethane (anhydrous, 99.5%), anhydrous methanol (99.8%), propionic acid, 4-pyridinecarboxaldehyde, 4-bromobenzaldehyde, triethylamine, diethyl phosphite, zinc acetate dihydrate, iodomethane, bromotrimethylsilane, tetrakis(triphenylphosphine)palladium (0), and ammonium hexafluorophosphate were purchased from Sigma-Aldrich and used without further purification. Pyrrole was purchased from Sigma-Aldrich and distilled prior to use. Silica gel (SiliaFlash F60 40–63 μm) used for column chromatography was purchased from SiliCycle. Dichloromethane, hexane, ethyl acetate, methanol, acetone, tetrahydrofuran, acetonitrile, and chloroform for synthesis and column chromatography were distilled. Toluene and dimethylformamide for synthesis were dried over activated 4 Å molecular sieves. Copper sulfate (anhydrous, 99%), ascorbic acid (99.9%), tantalum pentachloride (99.9%), and copper chloride (99%) were purchased from Alfa Aesar and used without further purification.

Structural Characterization. Mass spectra were obtained with a Bruker Microflex LRF matrix-assisted laser desorption/ionization time-of-flight spectrometer (MALDI-TOF), equipped with a 60 Hz laser, using α–cyano-4-hydroxycinnamic acid (αCN), sinapinic acid (SA), or (1E, 3E)-1,4-diphenylbuta-1,3-diene (DPB) as a matrix. The reported mass is the most abundant isotope observed. Calculated values are listed after the experimental result for comparison. The ^{1}H-NMR spectra were taken on a Varian spectrometer at 400 MHz.

Samples were prepared using deuterated solvents and with 0.03% tetramethylsilane as an internal standard.

Synthesis of Dyes. Scheme S 1shows the synthetic strategy followed for the preparation of the porphyrin sensitizers.

5-(4-Pyridinyl)dipyrromethane (**1**). Compound **1** was synthesized following a published procedure.[76] Portions of 4-pyridinecarboxaldehyde (2.0 g, 18.7 mmol, 1.8 mL) and pyrrole (18.8 g, 281 mmol, 20 mL) were added to a 100 mL round-bottom flask equipped with an air-cooled condenser. The mixture was purged with argon for 20 min and heated at 85 ºC under argon and stirred for 24 h. The resulting dark red solution was first purified using silica gel column chromatography (hexane:ethyl acetate 1:1) and further purified by crystallization from hexane:dichloromethane (DCM). The first crop of crystals was light brown (1.0 g) and the second was brown (1.2 g), giving an overall yield of 2.2 g (1.0 mmol, 53% yield). ^{1}H-NMR δ ppm ($CDCl_3$): 8.48 (d, *J* = 6.0 Hz, 2H), 8.16 (s, 2H), 7.12 (d, *J* = 6.0 Hz, 2H), 6.73 (m, 2H), 6.17 (dd, *J* = 2.9, 5.8 Hz, 2H), 5.89 (m, 2H), 5.45 (s, 1H).

5,10,15-Tris(4-pyridinyl)-20-(4-bromophenyl)-porphyrin (**2**). In a 250 mL round bottom flask was placed **1** (2.0 g, 8.58 mmol), 4-pyridinecaboxaldehyde (0.46 g, 4.29 mmol), and 4-bromobenzaldehyde (0.79 g, 4.29 mmol). Propionic acid (70 mL) was added and the flask was equipped with a condenser. The reaction was refluxed at 140 ºC for 45 min and then cooled to room temperature. The propionic acid was removed by distillation under reduced pressure and the mixture was dissolved in DCM. The organic solution was washed with a saturated sodium bicarbonate solution (× 4) to neutralize any remaining acid. The organic layer was dried over Na_2SO_4. The solvent was removed under reduced pressure and the mixture was purified by silica gel column chromatography (4%

MeOH:DCM) to yield a purple solid (175 mg, 0.252 mmol, 5.5% yield). ^{1}H-NMR δ ppm ($CDCl_3$): 8.99 (d, *J* = 4.0 Hz, 6H), 8.83 (d, *J* = 4.8 Hz, 2H) 8.77 (m, 6H) 8.08 (d, *J* = 4.0 Hz, 6H), 7.99 (d, *J* = 8.2 Hz, 2H), 7.84 (d, *J* = 8.2 Hz, 2H), -2.96 (s, 2H). MALDI-TOF: *m/z* obsd. 695.14 calc. for $C_{41}H_{26}BrN_7$ 695.14.

4-(10,15,20-Tris(4-pyridinyl)-porphin-5-yl)phenylphosphonic acid diethyl ester (**3**). Compound **2** (160 mg, 0.23 mmol) was dissolved in dry toluene (100 mL), triethylamine (20 mL), and diethyl phosphite (0.65 g, 4.60 mmol, 0.6 mL). The solution was purged with argon for 20 min and tetrakis(triphenylphosphine)palladium(0) (53 mg, 0.046 mmol) was added quickly. The reaction was stirred under argon at 80 ºC for 18 h. The solvent was removed by distillation under reduced pressure and the mixture was purified using silica gel column chromatography (2% MeOH:18% acetone:DCM). Compound **3** was obtained in 23% yield (40 mg, 0.053 mmol). ^{1}H-NMR δ ppm ($CDCl_3$): 9.06 (d, *J* = 5.6 Hz, 6H), 8.85 (m, 8H), 8.33 (dd, *J* = 4.0, 7.9 Hz, 2H), 8.24 (dd, *J* = 7.9, 13.1 Hz, 2H) 8.16 (d, *J* = 5.6 Hz, 6H), 4.40 (m, 4H), 1.53 (t, *J* = 7.1, 7.1 Hz, 6H) -2.89 (s, 2H). MALDI-TOF: *m/z* obsd. 753.27 calc. for $C_{45}H_{36}N_7O_3P$ 753.26.

Zinc 4-(10,15,20-tris(4-pyridinyl)-porphin-5-yl)phenylphosphonic acid diethyl ester (**D1E**). In a 100 mL round bottom flask compound **3** (40 mg, 0.053 mmol) and $ZnOAc{\cdot}2H_2O$ (117 mg, 0.53 mmol) were dissolved in THF (20 mL) and DCM (20 mL). The round bottom flask was equipped with a condenser and the reaction mixture was refluxed at 60 ºC for 12 h. The solvent was removed by distillation under reduced pressure. The mixture was redissolved in DCM and washed with H_2O three times. The organic solution was dried over Na_2SO_4 and filtered, and the solvent was removed under reduced pressure. The mixture was purified using silica gel column chromatography (10%

MeOH:DCM) to yield a purple solid (14.1 mg, 0.0173 mmol, 32% yield). ^{1}H-NMR δ ppm (DMSO): 9.01 (d, *J* = 5.6 Hz, 6H), 8.81 (m, 8H), 8.35 (dd, *J* = 3.8, 8.0 Hz, 2H) 8.21 (d, *J* = 5.6 Hz, 6H), 8.14 (dd, *J* = 8.0, 13.0 Hz, 2H) 4.28 (m, 4H), 1.42 (t, *J* = 7.1, 7.1 Hz, 6H). MALDI-TOF: *m/z* obsd. 815.18 calc. for $C_{45}H_{34}N_7O_3PZn$ 815.18.

Zinc 4-(10,15,20-tris(4-pyridinyl)-porphin-5-yl)phenylphosphonic acid (**D1**). **D1E** (5 mg, 6.1 μmol) was dissolved in chloroform (10 mL) and triethylamine (17 μL). The solution was heated at 60 °C in a flask bearing a condenser and trimethylsilyl bromide (TMS-Br) (14.1 mg, 92.1 μmol, 12 μL) was added. The reaction mixture was refluxed for 18 h. The solvent was removed under reduced pressure and the product was extracted using DCM:H_2O. The organic layer was dried over Na_2SO_4 and filtered, and the solvent was removed by distillation under reduced pressure. The final product was obtained in a 100% yield (5 mg, 6.14 μmol). ^{1}H-NMR δ ppm (DMSO): 9.14 (s, 6H), 8.90 (m, 4 H), 8.87 (d, *J* = 4.7 Hz, 2H), 8.83 (d, *J* = 4.7 Hz, 2H), 8.43 (s, 6H), 8.28 (dd, *J* = 3.3, 8.0 Hz, 2H), 8.12 (dd, *J* = 7.9, 12.8 Hz, 2H). MALDI-TOF: *m/z* obsd. 759.15 calc. for $C_{41}H_{26}N_7O_3PZn$ 759.11.

Zinc 4-(10,15,20-tris(4-(N-methylpyridiniumyl)-porphin-5-yl)phenylphosphonic acid diethyl ester (**D2E**). **D1E** (20 mg, 0.025 mmol) was dissolved in dry dimethylformamide (DMF) (10 mL) and the solution was purged with argon for 10 min. Methyl iodide (5.2 mg, 0.037 mmol, 2.3 μL) was added and the reaction mixture was heated at 100 ºC for 1 h, and then cooled to room temperature and stirred for 12 h. The solvent was removed by distillation under reduced pressure and the mixture was extracted using DCM:H_2O. The aqueous layer was removed and concentrated by distillation of the solvent under reduced pressure. Anion exchange with NH_4PF_6 yielded porphyrin with hexafluorophosphate counterions, thus, increasing the solubility of the porphyrin in organic solvents. The mixture was cooled to 0 ºC and the product precipitated out of solution. The water was removed by filtration to give a purple solid (21.5 mg, 0.0349 mmol, 100%). ^{1}H-NMR δ ppm (DMSO): 9.42 (d, *J* = 6.3 Hz, 6H), 9.04 (m, 4H), 8.98 (d, *J* = 4.7 Hz, 2H), 8.92 (m, 8H), 8.35 (dd, *J* = 3.7, 7.7 Hz, 2H), 8.18 (dd, *J* = 7.8, 13.0 Hz, 2H), 4.71 (s, 9H), 4.30 (m, 4H), 1.43 (t, *J* = 7.0, 7.0 Hz, 6H). MALDI-TOF: *m/z* obsd. 860.42 calc. for $C_{48}H_{43}N_7O_3PZn^{3+}$ 860.24.

4-(10,15,20-Tris(4-(N-methylpyridiniumyl)-porphin-5-yl)phenylphosphonic acid (**7**). **D2E** (5 mg, 5.8 μmol) was dissolved in acetonitrile (10 mL) and triethylamine (0.02 mL) and heated to 65 ºC. TMS-Br (13.3 mg, 0.087 mmol, 15 μL) was added and the reaction mixture was refluxed for 12 h. The reaction conditions both cleaved the phosphonate esters and removed the zinc from the macrocycle. A green solid precipitated and the solvent was removed under reduced pressure. The solid was resuspended in H_2O and washed with DCM. The H_2O was then removed under reduced pressure to yield a green solid (5 mg, 5.8 μmol, 100%). Compound **7** was used immediately to reintroduce the zinc without further purification. MALDI-TOF: *m/z* obsd. 742.30 calc. for $C_{44}H_{37}N_7O_3P^{3+}$ 742.27.

Zinc 4-(10,15,20-tris(4-(N-methylpyridiniumyl)-porphin-5-yl)phenylphosphonic acid (**D2**). In a 50 mL round bottom flask compound **7** (5 mg, 6 μmol) was dissolved in H_2O (5 mL) and THF (10 mL). $ZnOAc \cdot 2H_2O$ (26 mg, 0.119 mmol) was added and the flask was equipped with a condenser. The reaction was refluxed for 2 h. The solvent was removed by distillation under reduced pressure and the mixture was crystallized in H_2O/acetone. The crystals were filtered and rinsed with cold acetone to yield a green solid (5 mg, 6 μmol, 100%). ^{1}H-NMR δ ppm (DMSO/D_2O): 9.22 (s, 6H), 9.01 (d, *J* = 19.2 Hz, 8H), 8.80 (s, 6H), 8.20 (m, 4H), 4.65 (s, 9H). MALDI-TOF: *m/z* obsd. 804.34 calc. for $C_{44}H_{35}N_7O_3PZn^{3+}$ 804.18.

High Resolution Transmission Electron Microscopy. TEM micrographs were collected using a Philips CM200 TEM at 200kV, Cs 1.2 mm, PTP Resolution: 0.25nm Focused Probe: 0.5nm and Imaging Modes: TEM/STEM. TEM micrographs were analyzed using Digital Micrograph™ software.[77]

Dynamic Light Scattering. Dynamic light scattering (DLS) data were taken on a Malvern Zetasizer Nano S with the detector 173° from the incident beam and a laser wavelength of 633 nm. Intensity by number was used for expressing the particle size distribution of the dispersion of nanoparticles. The particle size is determined using the velocity of Brownian motion and the Stokes-Einstein equation.

$$d = \frac{kT}{3\pi\eta D} \tag{1}$$

Where d is the hydrodynamic diameter, k is Boltzmann's constant, T is absolute temperature, η is viscosity and D is the translational diffusion coefficient. These measurements were done by placing 5 mL of a dispersion of nanoparticles in ethanol into a disposable plastic cuvette with a path length of 1 cm. The refractive index of Cu_2O (2.94) was used as an approximation of the refractive index of $Cu_5Ta_{11}O_{30}$, which has not been determined in the literature.[78]

Mott-Schottky Measurements. Electrochemical impedance spectroscopy was used to measure the flat-band potentials of nanoparticles of $Cu_5Ta_{11}O_{30}$, using a frequency of 30 KHz and ac amplitude of 5 mV. Measurements were carried out using a Parstat-2263 potentiostat from Princeton Applied Research. A three necked flask filled with 0.5 M

Na_2SO_4 solution (pH 6.5) was purged with N_2 gas 30 min prior to the experiment. A flow of N_2 gas was kept over the headspace to purge any oxygen during the experiment. A film of NP-$Cu_5Ta_{11}O_{30}$ deposited on fluorine doped tin oxide (FTO, Pilkington TEC-15) served as the working electrode, Pt foil as a counter electrode and a saturated calomel electrode (SCE sat. KCl) as the reference electrode. The working electrode was made by depositing an ethanol solution of the nanoparticles onto the FTO slides at 70°C in air.

Current-voltage measurements (i-v curves) were performed using a CH-Instruments CH620a potentiostat under simulated AM 1.5 G irradiation at 100 mW/cm^2 (Oriel) using a scan rate of 10 mVs^{-1}. Scans were started negative of the open circuit voltage (V_{oc}) and scanned towards the short circuit condition (I_{sc}, V=0). The sensitized film served as the working electrode and platinized FTO served as counter and reference electrode.

Steady state absorption. Spectra were recorded in 1 cm path length cuvettes with the following spectrophotometers: diode array HP 8452, Shimadzu - UV-IR (2041PC), and Hitachi double beam UV/Vis spectrophotometer (U-2800).

Electrochemical and Spectroelectrochemical experiments. The voltammetric characterization of the redox processes was performed with an Autolab potentiostat-galvanostat (Electrochemical Instruments) in a conventional three-electrode cell. Electrochemical and spectroelectrochemical studies of porphyrins were carried out in anhydrous N,N-dimethylformamide (DMF) deoxygenated solution (argon bubbling), with 0.10 M tetra-n-butylammonium perchlorate ($TBAClO_4$) as supporting electrolyte. For cyclic voltammetry a Pt working electrode, a Pt counter electrode, and a silver wire quasi-reference electrode were used, while for spectroelectrochemistry a Pt mesh was used as working electrode. Absorption spectra of the dyes in the reduced state were obtained by applying a fixed potential at the redox potential of the first cathodic wave. After each voltammetric experiment, ferrocene was added as an internal standard (Fc/Fc+= 0.72 V vs Normal Hydrogen Electrode), and the potential axis was calibrated against the formal potential for the NHE. The Pt working electrode was cleaned between experiments by polishing with 0.3 µm alumina paste followed by solvent rinses.

Time resolved absorption. Transient absorption measurements in the femtosecond to nanosecond window were acquired with a kilohertz pulsed laser source and a pump-probe optical setup. Laser pulses of ca. 100 fs at 800 nm were generated from an amplified, mode-locked titanium sapphire kilohertz laser system (Millennia/Tsunami/Spitfire, Spectra Physics). The laser pulse was divided and part was sent through an optical delay line and focused onto a 3 mm sapphire plate to generate a white light continuum for the probe beam. The rest of the pulse was used to pump an optical parametric amplifier to generate excitation pulses selected using a mechanical chopper. Polarization of the pump beam was set to the magic angle (54.7°) relative to the probe beam and its intensity was adjusted using a continuously variable neutral density filter. White light generated was compressed by prism pairs (CVI) before passing through the sample. The white light probe was dispersed by a spectrograph (300 line grating) onto a charge-coupled device (CCD) camera (DU420, Andor Tech.). The final spectral resolution was about 2.3 nm for over a nearly 300 nm spectral region. Decay-associated spectra (DAS) were obtained by globally fitting the transient absorption kinetic traces over a selected wavelength region using a parallel kinetic model, equation (2),[79]

$$\Delta A(\lambda,t)=\sum_{i=1}^{n} A_i(\lambda)\exp(-t/\tau_i) \tag{2}$$

where $\Delta A(\lambda,t)$ is the observed absorption change at a given wavelength at time delay t and n is the number of kinetic components used in the fitting. A plot of $A_i(\lambda)$ versus wavelength is called a DAS and represents the amplitude spectrum of the i^{th} kinetic component, which has a lifetime of τ_i.

RESULTS AND DISCUSSION

Synthesis and Characterization of NP–$Cu_5Ta_{11}O_{30}$. Nanoparticulate (NP)–$Cu_5Ta_{11}O_{30}$ was prepared by a flux-mediated synthesis using Cu_2O nanoparticles, Ta_2O_5 nanoparticles and CuCl, following procedures similar to those used for nanoparticles of the Cu(I)-niobate phases such as $Cu_2Nb_8O_{21}$.[80] The Cu_2O and Ta_2O_5 nanoparticles were synthesized following methods reported elsewhere.[81,82] These two compounds were used as reactants to obtain the final NP–$Cu_5Ta_{11}O_{30}$. Both Cu_2O nanoparticles (0.109 g) and Ta_2O_5 nanoparticles (0.390 g) were ground together with a mortar and pestle inside a glove box, along with 0.250 g of CuCl as the flux.[83] In flux synthesis, the inorganic salt is heated to above its melting point and functions as a relatively low-temperature reaction medium for the dissolution of the reactant metal oxides and the formation of high-quality crystals of the product phase. The metal oxide nanoparticles were allowed to react within the molten CuCl flux at this temperature, yielding a better dispersion of the nanoparticles during the reaction. This mixture was placed under vacuum in a fused-silica reaction vessel and then heated at 900°C for 24 h. Afterwards, the powder obtained, which is a mixture of bulk and NP–$Cu_5Ta_{11}O_{30}$, was sonicated in absolute ethanol for 30 min and the larger particles were removed from the nanoparticle solution by centrifugation via sedimentation at 3000 rpm for 20 min. The yellow supernatant, consisting of the nanoparticles suspended in ethanol, was decanted to produce a yield on the order of ~1% in mass.

The NP–$Cu_5Ta_{11}O_{30}$ product was characterized by UV-Vis, DLS and HR-TEM. Figure 11 shows a representative HR-TEM micrograph of NP–$Cu_5Ta_{11}O_{30}$ with a narrow size distribution (15 ± 5 nm) having quasi-spherical morphologies, as measured from 50 nanoparticles (Supporting Information, Figure S 5). It is noteworthy that the NP–$Cu_5Ta_{11}O_{30}$ product does not exhibit crystallinity detectable by powder XRD, suggesting either very small crystalline domains or a high amount of amorphous content. Although the nanoparticles show a slight tendency for agglomeration when they are dried, they are stable and remain dispersed for months in an ethanol solution. In order to gain insight into their behavior in ethanol solution, DLS measurements were performed.[84,85] A size distribution centered on 12 nm (Figure 11, inset) was observed. Within the experimental error, the size and distribution of NP–$Cu_5Ta_{11}O_{30}$ measured by DLS is in good agreement with the HR-TEM images.

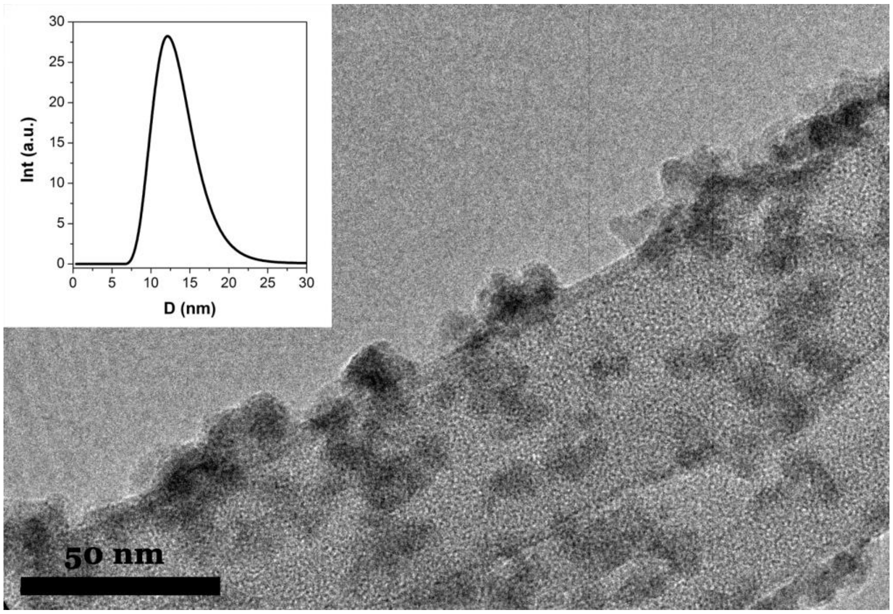

Figure 11. Representative HR-TEM of NP–$Cu_5Ta_{11}O_{30}$ where a quasi-spherical distribution of particles with sizes of (15 ± 5) nm can be observed. **Inset:** Size distribution obtained by DLS of NP–$Cu_5Ta_{11}O_{30}$ dispersed in an ethanol solution.

The UV-Vis absorption spectrum was recorded in order to compare the absorption of NP–$Cu_5Ta_{11}O_{30}$ to that of bulk $Cu_5Ta_{11}O_{30}$. Figure 12a shows the UV-Vis absorption spectrum of $Cu_5Ta_{11}O_{30}$ at a concentration of 0.75 mg/mL in ethanol. The energy gap for NP–$Cu_5Ta_{11}O_{30}$ was determined using a Tauc plot, (equation (3)[86] and inset in Figure 12a), where α is the absorption coefficient, h is Planck's constant, υ represents the frequency of incident light, k is a proportionality constant and E_g is the energy gap.

$$(\alpha h\upsilon)^2 = k(h\upsilon - E_g) \tag{3}$$

The energy gap obtained for these NP–$Cu_5Ta_{11}O_{30}$ is (3.1 ± 0.2) eV, which is significantly larger than the $Cu_5Ta_{11}O_{30}$ bulk band gap situated at 2.6 eV.[87] This result suggests that in NP–$Cu_5Ta_{11}O_{30}$ the Bohr radius is larger than 7.5 nm; hence our sample is in the quantum confinement regime and the potentials of the conduction and valence bands are shifted from the bulk potentials. In order to determine the new positions of the semiconductor energy levels, Mott-Schottky analyses were performed. In this case, for *p*-type semiconductors the capacitance is related to the flat-band potential (V_{fb}) as given in equation (4),[88]

$$\frac{1}{c^2} = \left(\frac{2}{e\varepsilon_r \varepsilon_0 N_A A^2} \right) \bullet \left(-V_0 + V_{fb} - \frac{KT}{e} \right) \tag{4}$$

where *c* is the capacitance, *e* is the charge of the electron, ε_r is the dielectric constant of the material, ε_o is the permittivity of free space, N_A is the acceptor density, *A* is the geometrical area of the working electrode, *K* is Boltzmann's constant, and *T* is temperature in Kelvin. Plotting the inverse square of capacitance against applied bias yields a straight line, which can be extrapolated to the *x*-ordinate (V_o) using equation (5).

$$V_0 = V_{fb} - \frac{KT}{e} \tag{5}$$

These data are plotted in Figure 12b; the negative slope indicates that the semiconductor is *p*-type. The value obtained for V_o is 0.625 V, and hence V_{fb} is 0.652 V vs. SCE. Converting from SCE to NHE, the V_{fb} is 0.896 V vs. NHE. The valence band energy, E_v, can be obtained from equation (6),

$$E_v = V_{fb} - kT \bullet \ln(\frac{N_A}{N_V}) \tag{6}$$

where N_A and N_V are the acceptor level and the densities of states, respectively. The acceptor level, N_A, can be calculated using the second term of the Mott-Schottky equation where:

$$Slope = \frac{-2}{e\varepsilon_0 \varepsilon N_A A^2} \qquad (7)$$

Using an N_A of ~10^{16} and densities of states of ~10^{19}, E_v is calculated to be 1.07 V vs. NHE. Thus, the valence band is ~200 mV more positive than the oxidation potential of water at pH of 6.5. [74,87,88]

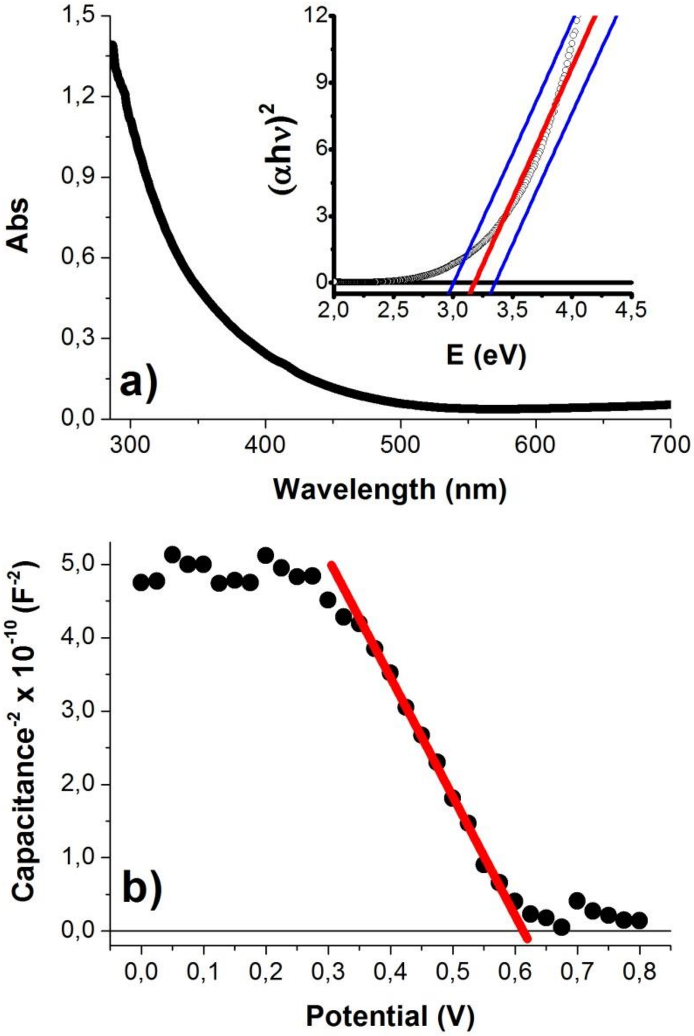

Figure 12. **a)** Absorption spectrum of NP–$Cu_5Ta_{11}O_{30}$ in ethanol at a concentration of 0.75 mg/mL. **Inset:** Absorption onset value of the first direct allowed transition for NP–$Cu_5Ta_{11}O_{30}$ (red line) and 99% confident bands (blue line). **b)** Mott-Schottky plot of NP–$Cu_5Ta_{11}O_{30}$.

Synthesis of dyes The structures of the dyes used for these studies are shown in Figure 13. They were prepared using variations of methods reported in the literature and characterized using NMR, mass spectrometry, and UV-Visible spectroscopy. Details are given in the Experimental Section.

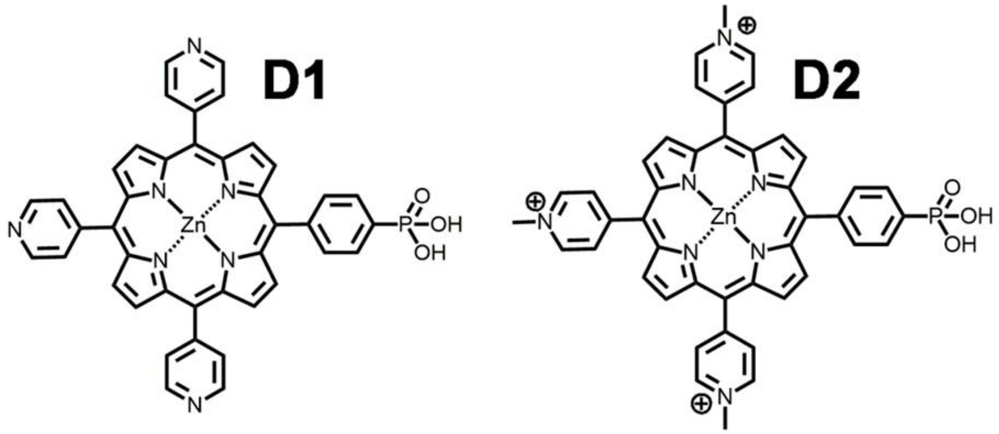

Figure 13. Molecular structures of the dyes **D1** and **D2** in their acid forms. Molecular structures of dyes **D1E** and **D2E**, in their ester forms, are shown in the Supporting Information.

Electrochemical experiments. Cyclic voltammograms for **D1E** and **D2E** in were obtained in dimethylformamide containing tetrabutylammonium perchlorate (DMF/ClO_4TBA) as the supporting electrolyte with a Pt working electrode, a Pt counter electrode and an Ag wire as a reference electrode. Both dyes were expected to have the reduction potential of their first singlet excited state more positive than the valence band of NP–$Cu_5Ta_{11}O_{30}$.[89,90] Figure 14 shows the CV for a) **D1E** where a reversible porphyrin reduction is observed at -0.41 V vs NHE and b) **D2E** having a quasi-reversible porphyrin reduction at -0.23 V vs NHE. The porphyrin reduction potential of **D2E** is less negative than that of **D1E** due to the presence of the electron withdrawing alkylated pyridyl groups.

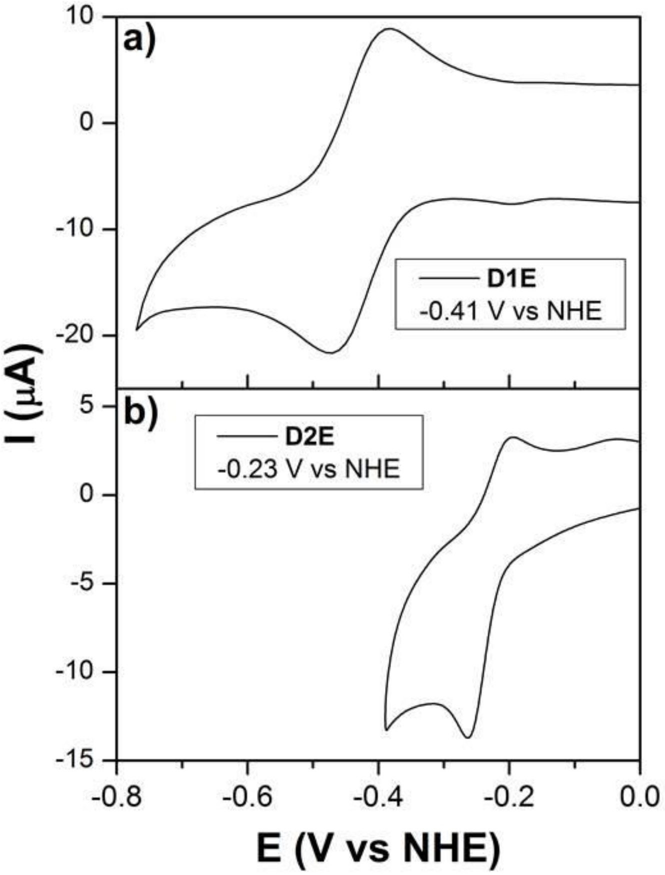

Figure 14. Cyclic voltammogram of **a) D1E** and **b) D2E** in DMF/ClO_4TBA with a Pt working electrode, a Pt counter electrode and an Ag wire as the reference electrode.

Based on the reduction potentials obtained for the nanoparticles and the dyes, Figure 15 depicts the relative energetics of the ground and excited states of the dyes and the conduction band edge (CB) and valence band edge (VB) of NP–$Cu_5Ta_{11}O_{30}$. The potential for the first reduction ($D/ D^{\bullet-}$) of the dye was measured electrochemically as discussed above and the potential for the reduction of the excited state ($D^*/D^{\bullet-}$) was calculated using the equation $D^*/D^{\bullet-} = D/D^{\bullet-} + E_{00}$, where E_{00}, 2.06 eV, is the zero-zero optical excitation energy estimated from the intersection of the normalized absorption and emission spectra in ethanol for porphyrin **D1** and **D2** (Supporting Information, Figure S 14). As depicted in Figure 15, the excited singlets of **D1** and **D2** are thermodynamically capable of photoinjecting a hole into the VB because the position of the VB of NP–$Cu_5Ta_{11}O_{30}$ is at less positive potentials than the porphyrin dye *D*/D*$^{\bullet-}$ levels. In contrast, the conduction band potential of NP–$Cu_5Ta_{11}O_{30}$ is more negative than the oxidation potential of the excited states of the porphyrins by 1.12 V and 1.30 V for **D1** and **D2**, respectively and thus electron injection from the excited dye into the conduction band of the semiconductor is not thermodynamically possible.

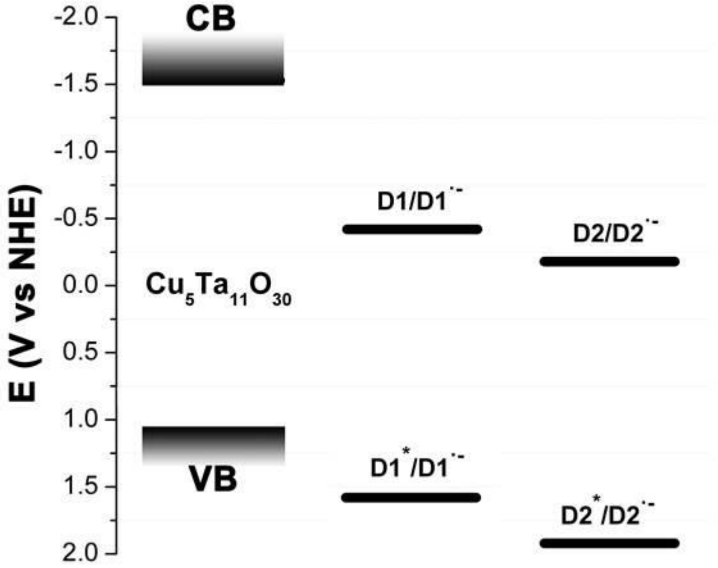

Figure 15. Diagram depicting the reduction potentials for the ground and the lowest excited singlet states of **D1** and **D2**, the NP–$Cu_5Ta_{11}O_{30}$ conduction band energy (CB), and the NP–$Cu_5Ta_{11}O_{30}$ valence band energy (VB).

In order to study the photophysical behavior of the systems **D1**- NP–$Cu_5Ta_{11}O_{30}$ and **D2**-NP–$Cu_5Ta_{11}O_{30}$, the dyes were attached to the nanoparticles as follows. The dye (**D1** or **D2** in acid form) dissolved in methanol ([dye] ~ 10^{-3} M) was added dropwise into an ethanol suspension of $Cu_5Ta_{11}O_{30}$ until the mixture reached an absorbance of 0.4 at 560 nm ([dye] ~ 10^{-5} M). The suspension was stirred for 24 h at 40 ºC to reach equilibrium conditions. UV-vis absorption spectra of **D1**, **D1**-NP–$Cu_5Ta_{11}O_{30}$, **D2**, and **D2**-NP–$Cu_5Ta_{11}O_{30}$ in ethanol were recorded (Figure 16). After the dyes were attached to the nanoparticles, a broadening and shifting to longer wavelengths of the Soret and Q-bands was observed for both dyes. This phenomenon is more significant for **D2** than **D1**. Since the experimental conditions are the same, this may be explained by taking into account that **D2** has three positive charges on the methylpyridinium groups and it is possible that (instead of, or in addition to, attaching to the nanoparticles through the phosphonic moiety) **D2** associates with the nanoparticles in a different way. Emission spectra of **D1**, **D1**–NP–$Cu_5Ta_{11}O_{30}$, **D2**, and **D2**–NP–$Cu_5Ta_{11}O_{30}$ in ethanol were taken with excitation at 540 nm. Figure 16 shows a complete quenching of fluorescence for both dyes when they are attached to NP–$Cu_5Ta_{11}O_{30}$. This fluorescence quenching is consistent with the first excited singlet state of the porphyrins being deactivated by means of electron transfer from the NP–$Cu_5Ta_{11}O_{30}$ VB to the excited dye (hole injection into the VB).

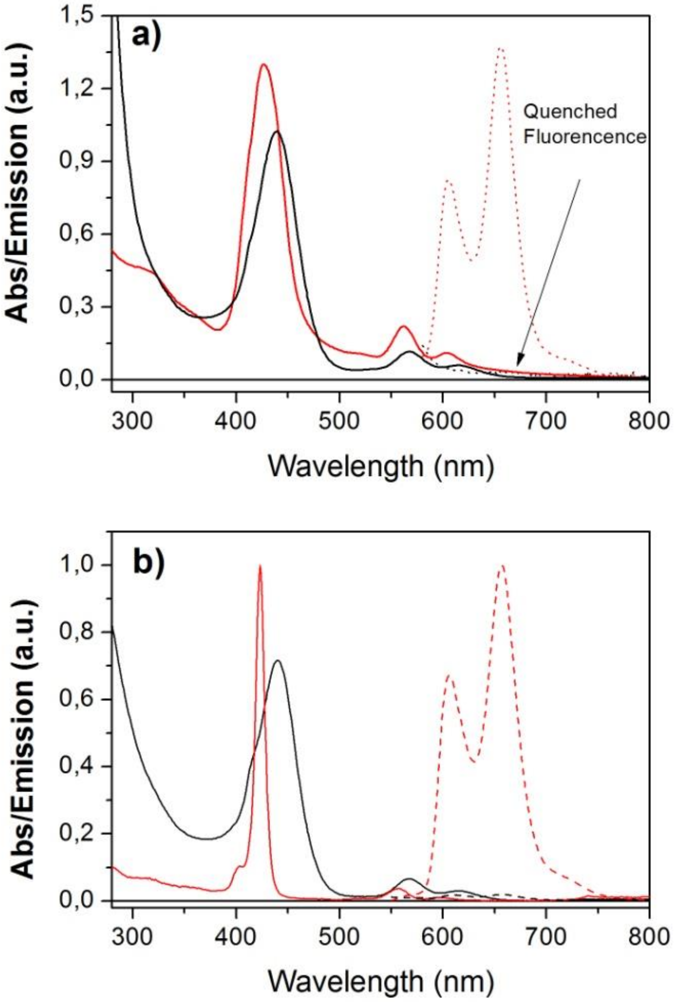

Figure 16. Absorption (solid lines) and emission (dashed lines) spectra of **D1** (panel a) and **D2** (panel b) before (red line) and after (black line) attachment to the NP–$Cu_5Ta_{11}O_{30}$ nanoparticles. Emission spectra were taken with excitation at 540 nm.

Transient absorption measurements. Transient absorption measurements were done in both systems to investigate the hole injection into the VB of NP–$Cu_5Ta_{11}O_{30}$ by the excited dyes and to determine the injection and recombination rates. The absorption signatures of the reduced dyes $D1^{\bullet-}$ and $D2^{\bullet-}$ were obtained by spectroelectrochemistry, as is shown in

Figure 17a and 17c, respectively. The difference absorption spectrum for D1$^{\bullet-}$shows ground-state bleaching of the Q-bands at 560 nm and 610 nm. There is also a broad absorption band at 620–760 nm. The difference absorption spectrum for D2$^{\bullet-}$ presents a well-defined ground state bleaching of Q-bands at 560 nm and 610 nm and a broad band at ~620–770 nm.

The decay-associated-spectra (DAS) for **D1**–NP–$Cu_5Ta_{11}O_{30}$ and **D2**–NP–$Cu_5Ta_{11}O_{30}$ in ethanol solution measured by fs transient absorption after excitation at 428 nm are shown in Figure 17b and 17d, respectively. For **D1**–NP–$Cu_5Ta_{11}O_{30}$, global analysis of the transient absorption gives a satisfactory fit with three decay lifetimes of 0.7 ps, 8 ps and 190 ps (Figure 17b). The 0.7 ps DAS shows a characteristic induced absorption at ~640–740 nm, which corresponds to the **D1** radical anion and therefore can be associated with the decay of the **D1**$^{\bullet-}$–NP–$Cu_5Ta_{11}O_{30}$(+) transient. The 8 ps DAS can be attributed to the formation of the **D1**$^{\bullet-}$–NP–$Cu_5Ta_{11}O_{30}$(+) state since it shows ground state bleaching of Q-bands and stimulated emission at ~670 nm. The bleaching maxima of the Q-bands are red shifted, probably due to the attachment of **D1** to the nanoparticles. Thus, the rate of decay of the charge-separated species is greater than the rate of formation. The 190 ps DAS features ground state bleaching of the Q-band maxima that is blue shifted compared to the 0.7 DAS and 8 ps DAS, and therefore can be associated with **D1** molecules that are aggregated and/or not directly attached to the nanoparticles.

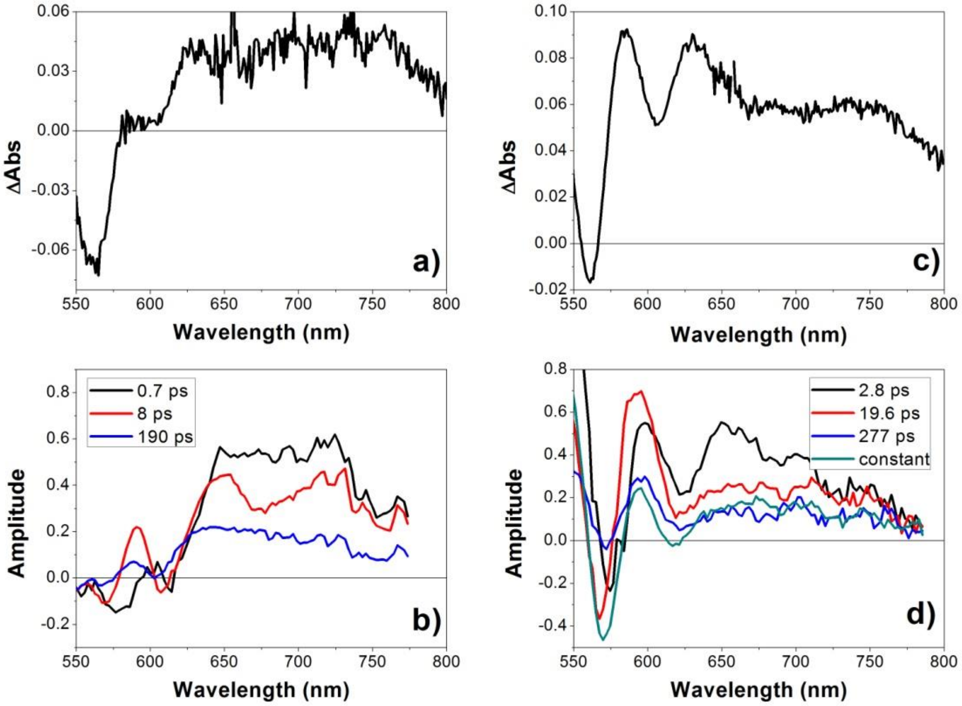

Figure 17. Difference absorption spectra **a)** ($D1^{\bullet-}$- D1) and **c)** ($D2^{\bullet-}$- D2) obtained by spectroelectrochemistry. Decay-associated-spectra in ethanol solution measured by fs transient absorption after excitation at 428 nm for **b)** D1–NP–$Cu_5Ta_{11}O_{30}$ and **d)** D2–NP–$Cu_5Ta_{11}O_{30}$.

For the system **D2**–NP–$Cu_5Ta_{11}O_{30}$ the global analysis of the transient absorption gives a satisfactory fit with four decay lifetimes of 2.8 ps, 19.6 ps, 277 ps and a nondecaying lifetime on a 1 ns time scale (Figure 17d). The 2.8 ps DAS does not show stimulated emission and instead shows **D2** radical-anion induced absorption at ~580–700, and can therefore be associated with the decay of the species $\mathbf{D2^{\bullet-}}$–NP–$Cu_5Ta_{11}O_{30}$(+). The charge separated species is formed in <100 fs, and its rise time is too fast to observe. The other three DAS show ground state bleaching of Q band maxima that is blue shifted compared to the 2.8 ps DAS, and which therefore can be attributed to **D2** that is aggregated and/or not directly attached to the semiconductor surface**.**

In thermodynamic terms, the more rapid hole injection observed for the **D2** system (as compared to the **D1** case) may be ascribed to the larger energetic driving force for the process, i.e., as shown in Figure 15. Alternatively, the driving force for charge recombination is greater for the **D1** system, and thus this rate constant is larger than that for the **D2** case.

DSSC measurements. $Cu_5Ta_{11}O_{30}$ nanoparticle films were deposited on fluorine-doped tin oxide (FTO) slides by a drop cast method and annealed under vacuum at 200 °C for 2 h. The films were then immersed in a 0.1 mM solution of **D1** (methanol) or **D2** (1% methanol in water) overnight, rinsed with ethanol and dried in air. Pt counter electrodes were fabricated by applying a 6 mM solution of H_2PtCl_6 in ethanol to FTO on a glass substrate (1 drop/cm^2) and heating to 350 °C in air for 30 min. The working and counter electrodes were sandwiched together with a Parafilm gasket and the redox electrolyte (0.2 M KI and 0.02 M I_2 in ethylene glycol) was introduced by capillary diffusion. Current-potential scans were performed in the dark and under AM 1.5 G irradiation at a scan rate of 10 mV·s^{-1}, starting from negative applied potentials and continuing to the I_{sc} condition. The results are shown in Figure 18.

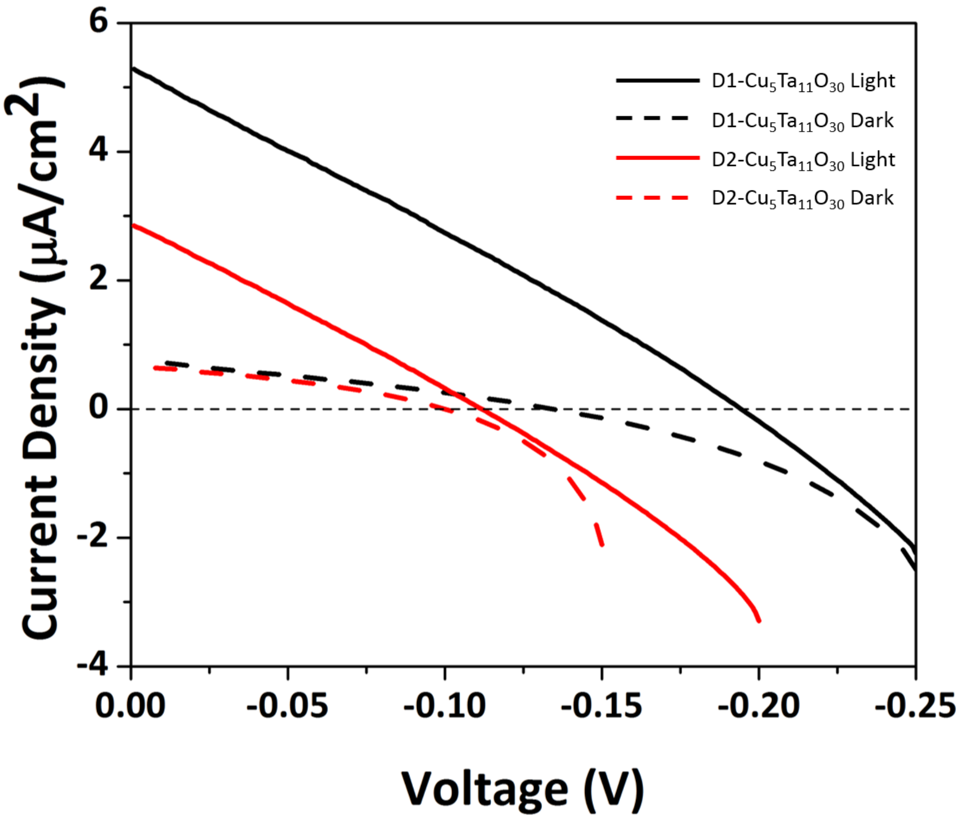

Figure 18. Linear sweep voltammograms of **D1** (black lines) and **D2** (red lines) in dark (dotted lines) and under AM 1.5 G irradiation (solid lines) with sweep rate of 10 mV·s^{-1}.

In Figure 18, positive current indicates hole injection into the photocathode. In the dark, both dye-nanoparticle systems show negligible current as no hole injection occurs. At suitably negative applied potentials, somewhat larger currents in the opposite direction are observed. These are likely due to reduction of the redox mediator by the semiconductor. In fact, when no dye is present, much larger currents of this type are observed, and are similar under both dark and light conditions (see Supplementary Information). When light is applied to the electrodes bearing the dye-nanoparticle composites, photoinjection of holes from the dye molecules into the nanoparticles and thence into the circuit is observed

(Figure 18). As summarized in Table 1, open circuit voltages (V_{OC}) of 110 mV and 200 mV were observed for nanoparticles bearing **D2** and **D1**, respectively. Such V_{OC} values are comparable to those observed for NiO (~100 mV)[75] and other Cu(I) based p-DSSCs (~150–300 mV)[91,92] using the I^-/I_3^- redox mediator. Short circuit currents (I_{SC}) were on the order of a few μA per cm^2. Table 1 also reports the fill factors (ff) and light conversion efficiencies (η), calculated as discussed in the Supporting Information. These results indicate that the dye-nanoparticle composites are indeed capable of light-driven hole injection into an external circuit. The low current densities may be due in part to the lack of a suitable blocking layer[93] to slow charge recombination.

Table 1. Contains short circuit current, open circuit voltage, fill factor and light conversion efficiency for D1 and D2.

Dye	I_{sc} (μA/cm^2)	V_{oc} (mV)	ff	η (%)
D1	5.28	200	0.260	$2.75 \cdot 10^{-4}$
D2	2.85	110	0.265	$8.31 \cdot 10^{-5}$

CONCLUSIONS

The preparation of p-type semiconductor $Cu_5Ta_{11}O_{30}$ nanoparticles (NP–$Cu_5Ta_{11}O_{30}$) with a valence band edge suitable for water oxidation has been described. Two sensitizers, zinc 4-(10,15,20-tris(4-pyridinyl)-porphin-5-yl)phenylphosphonic acid (**D1**) and its analog in which the pyridine groups are methylated (**D2**), were shown to have excited state reduction potentials that were thermodynamically capable of photoinjecting a hole into the VB of the NP-$Cu_5Ta_{11}O_{30}$. These sensitizers are not thermodynamically capable of photoinjecting electrons into the CB of the NP–$Cu_5Ta_{11}O_{30}$. Transient absorption measurements of the **D1**–NP–$Cu_5Ta_{11}O_{30}$ system show hole injection in 8 ps and very fast recombination in ~700 fs. The **D2**–NP–$Cu_5Ta_{11}O_{30}$ system shows very fast injection, <100 fs, and slower recombination on the 2.8 ps time scale. DSSC measurements on the NP-$Cu_5Ta_{11}O_{30}$ sensitized with **D1** and **D2** show significant photocurrent responses under simulated solar irradiance. Taken together, the thermodynamic, spectroscopic, and cathodic i-v measurements lead us to conclude that these systems function by a photoinduced hole injection mechanism. Investigating the use of NP–$Cu_5Ta_{11}O_{30}$ as a new p-type semiconductor with a VB more positive than the water oxidation potential and extremely negative CB (> -1.5V vs NHE) is a step in the development of new materials for p-DSSCs, which could lead to more efficient ways to carry out solar water splitting.

SUPPORTING INFORMATION: Includes HR-TEM images, schematic and details of dye synthesis, ^{1}H-NMR results**,** absorption and transient absorption spectra, power-voltage curves and control experiments, and fill factor and efficiency calculations. This material is available free of charge via the Internet at http://pubs.acs.org.

ACKNOWLEDGEMENTS

The work at ASU was supported by the Center for Bio-Inspired Solar Fuel Production, an Energy Frontier Research Center funded by the U.S. Department of Energy, Office of

Science, Office of Basic Energy Sciences under Award Number DE-SC0001016 and the Office of Basic Energy Sciences, Division of Chemical Sciences, Geosciences, and Energy Biosciences, Department of Energy under contract DE-FG02-03ER15393. The work at NCSU was supported by the Research Corporation for Science Advancement (P.M. is a Scialog awardee) and the Department of Chemistry. M.G. gratefully acknowledges financial support from Secyt-UNRC, CONICET and ANPCYT.

AUTHOR INFORMATION

Corresponding Author: *Prof. Paul Maggard*, Department of Chemistry, North Carolina State University, Raleigh, NC 27695-8204 USA. E-mail: pamaggar@ncsu.edu

Author Contributions: The manuscript was written jointly with contributions from all authors. All authors have given approval to the final version of the manuscript.

Note: The authors declare no competing financial interests.

SUPPORTING INFORMATION

Figure S 5. Representative HR-TEM images of NP-$Cu_5Ta_{11}O_{30}$.

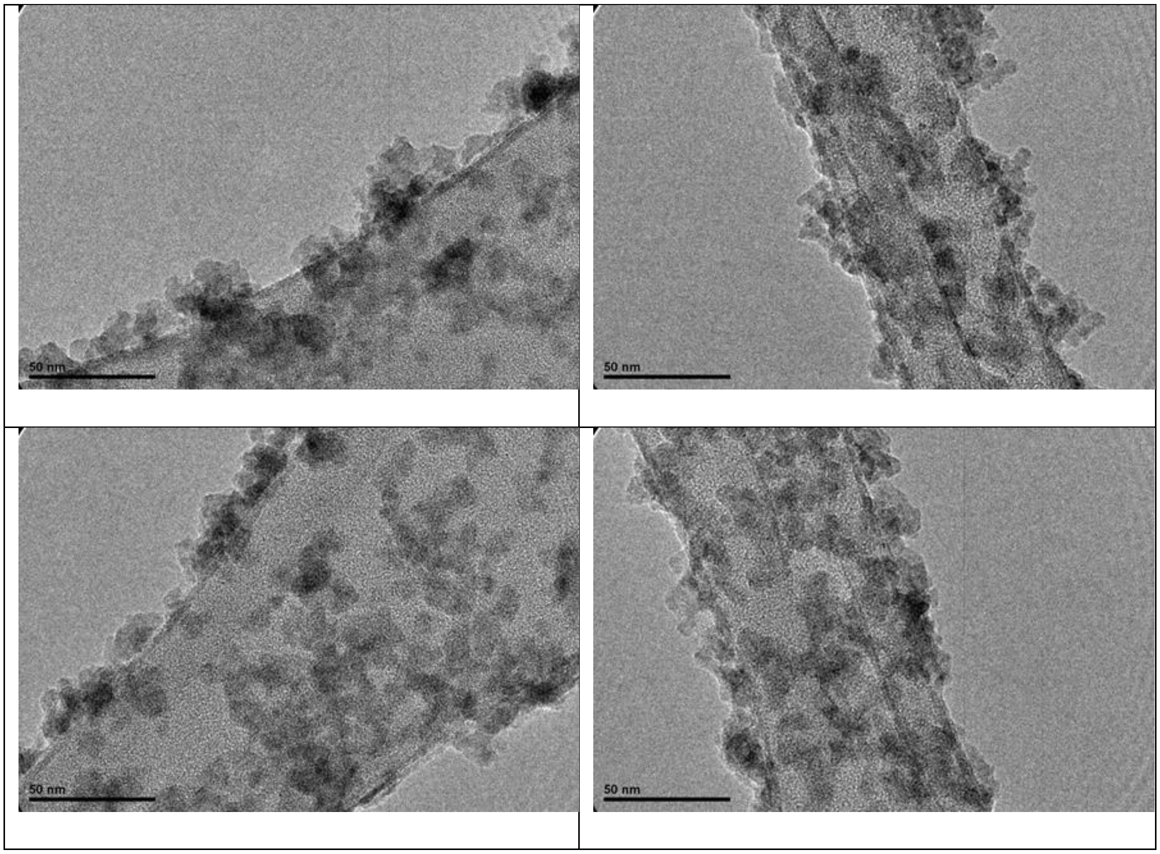

Dye synthesis

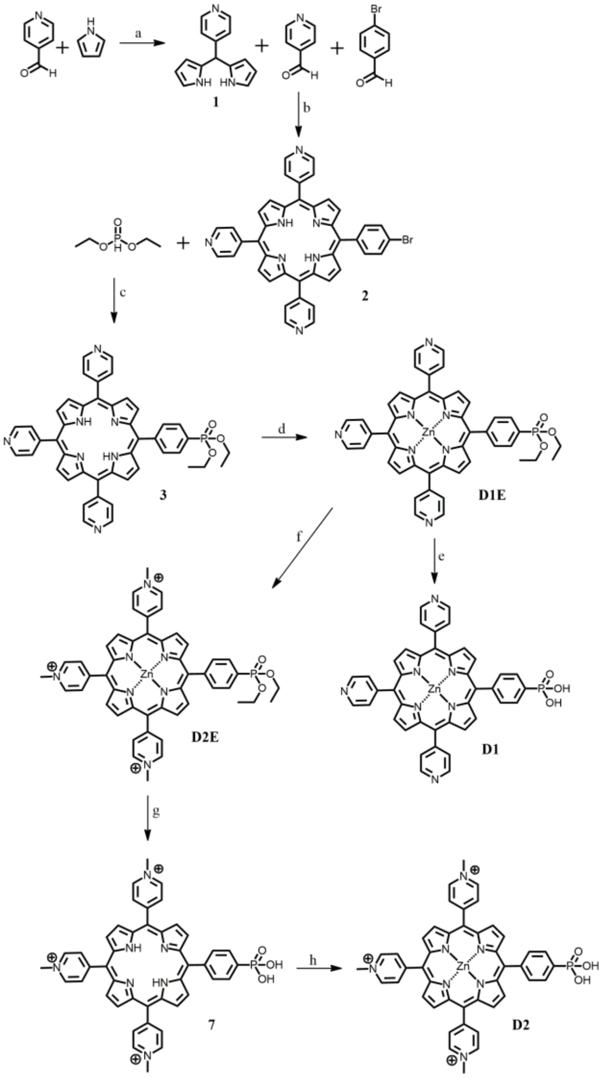

Scheme S 1. Reagents and conditions: (a) Ar/85 ºC/24 h, 53% yield; (b) propionic acid, reflux/45 min, 5.5% yield; (c) diethyl phosphite/Pd(PPh_3)$_4$/toluene/TEA, Ar/80 ºC/18 h, 23% yield; (d) ZnOAc•2H_2O/THF/DCM, 60 ºC/12 h, 32 % yield; (e) TMS-Br/$CHCl_3$/TEA, 60 ºC/18 h, 100% yield; (f) MeI/DMF, Ar/100 ºC/1 h then room temperature/12 h, 100% yield; (g) TMS-Br/ACN/TEA, 65 ºC/12 h, 100 % yield; (h) ZnOAc•2H_2O/THF/H_2O, 60 ºC/2 h, 100% yield.

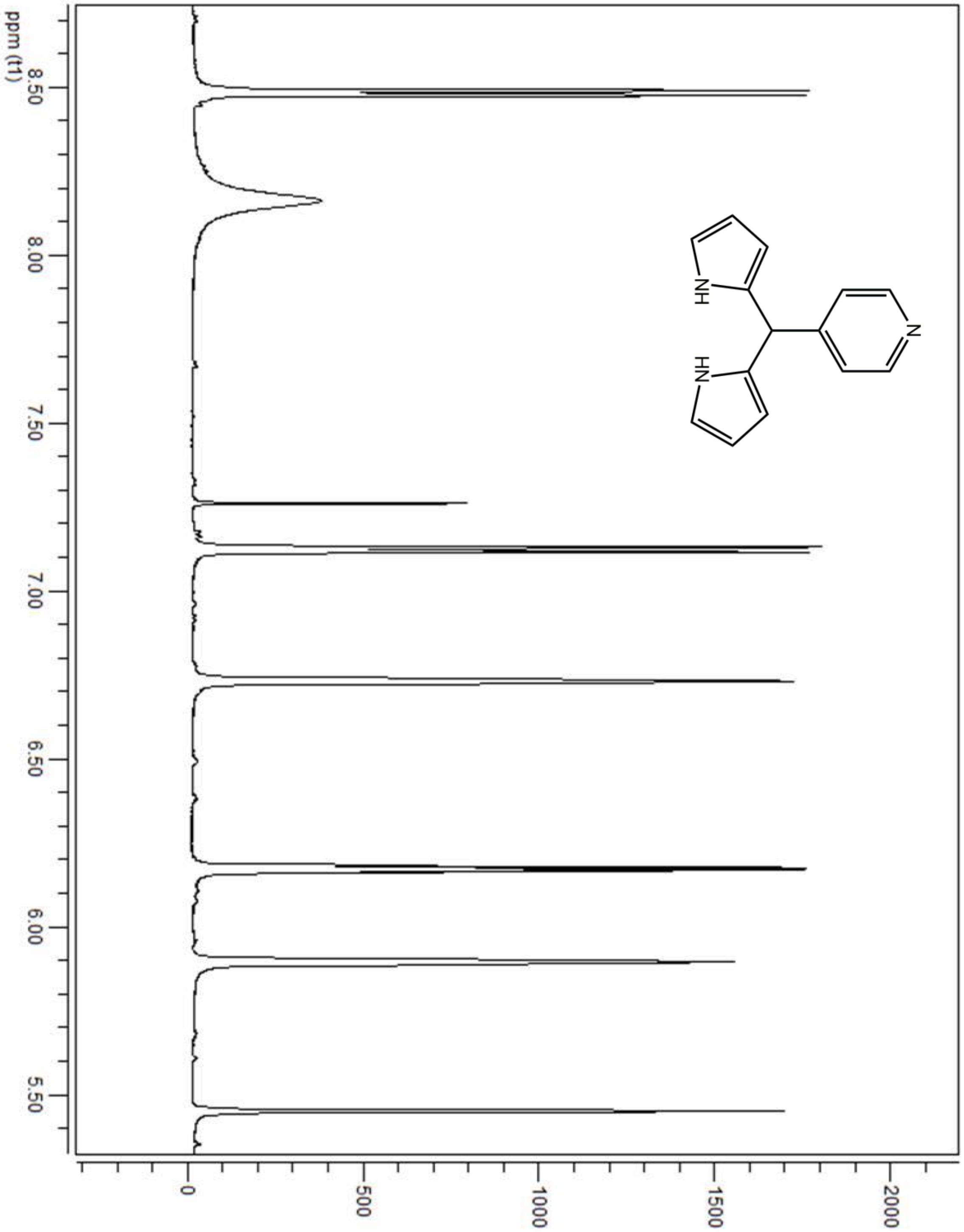

Figure S 6. ^{1}H-NMR of **1** in $CDCl_3$.

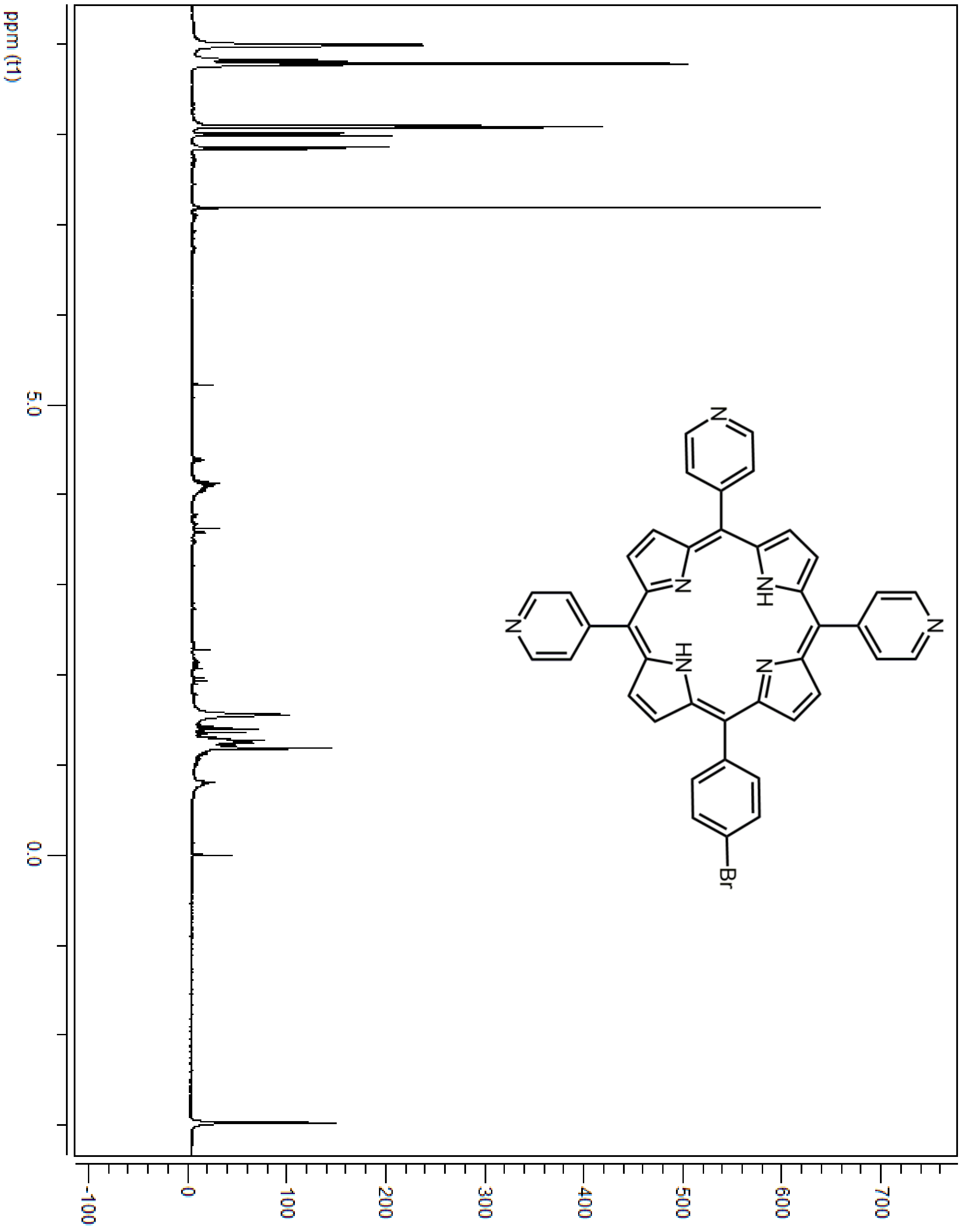

Figure S 7. ^{1}H-NMR of **2** in $CDCl_3$.

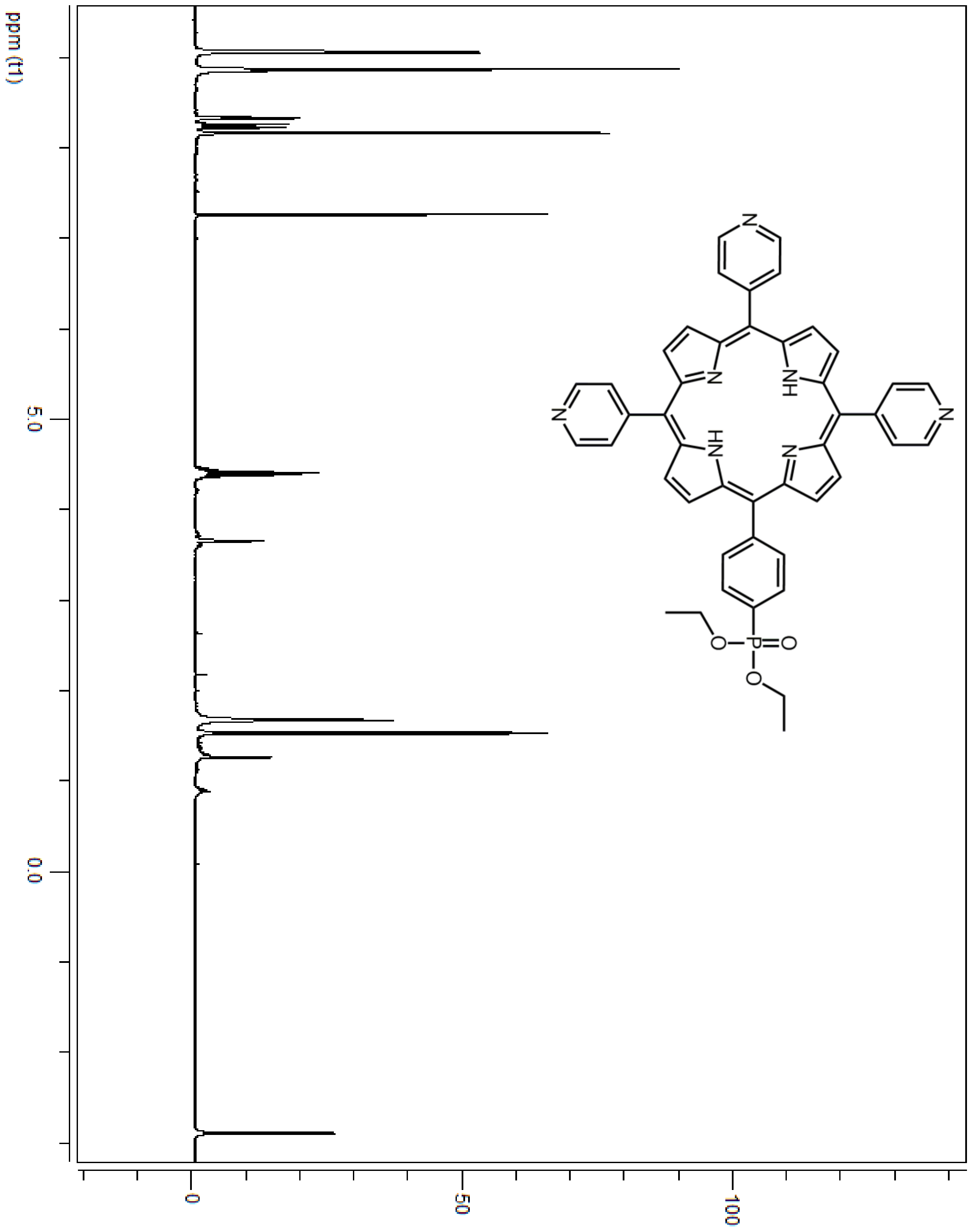

Figure S 8. ^{1}H-NMR of **3** in $CDCl_3$.

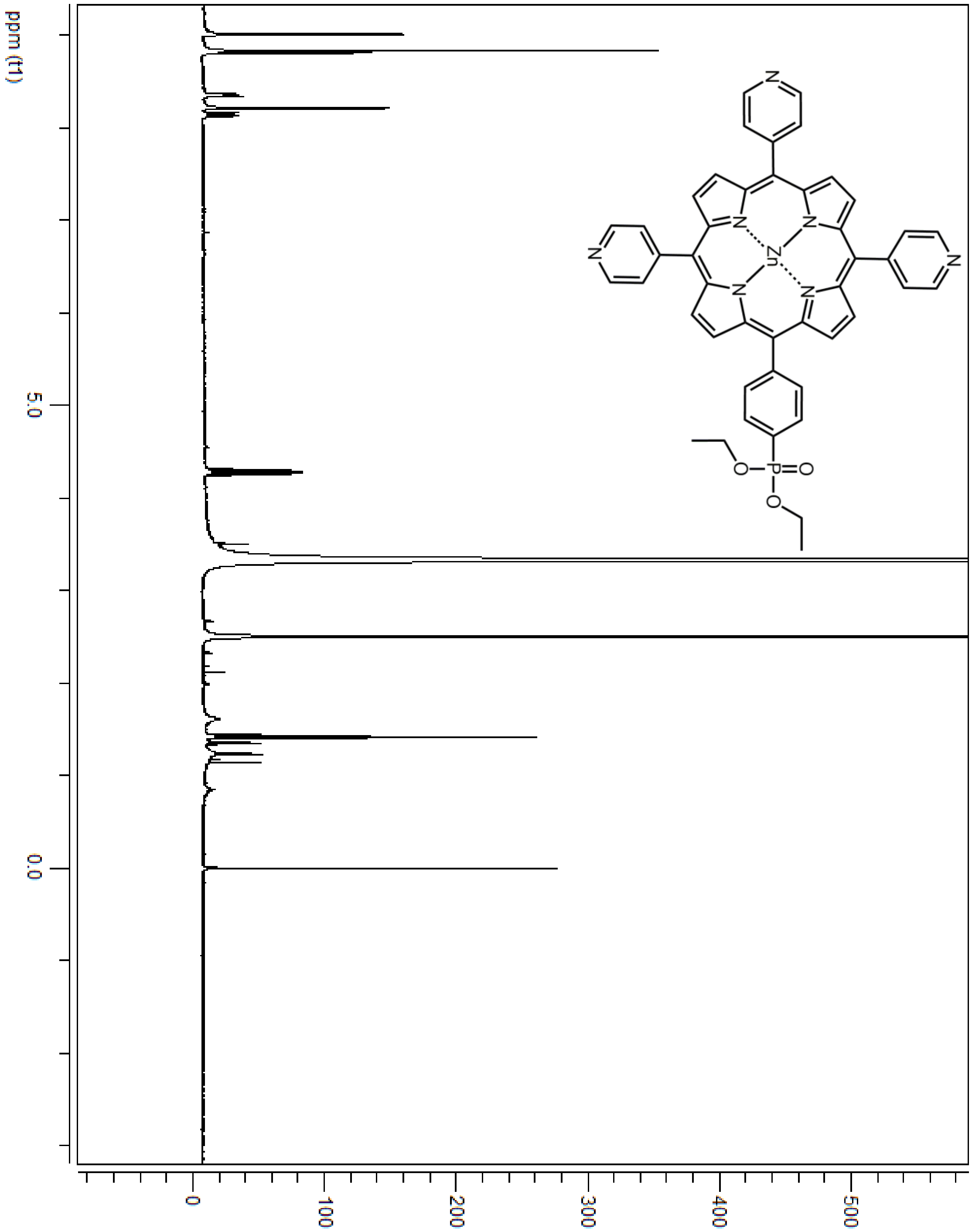

Figure S 9. ^{1}H-NMR of **D1E** in DMSO-d$_6$.

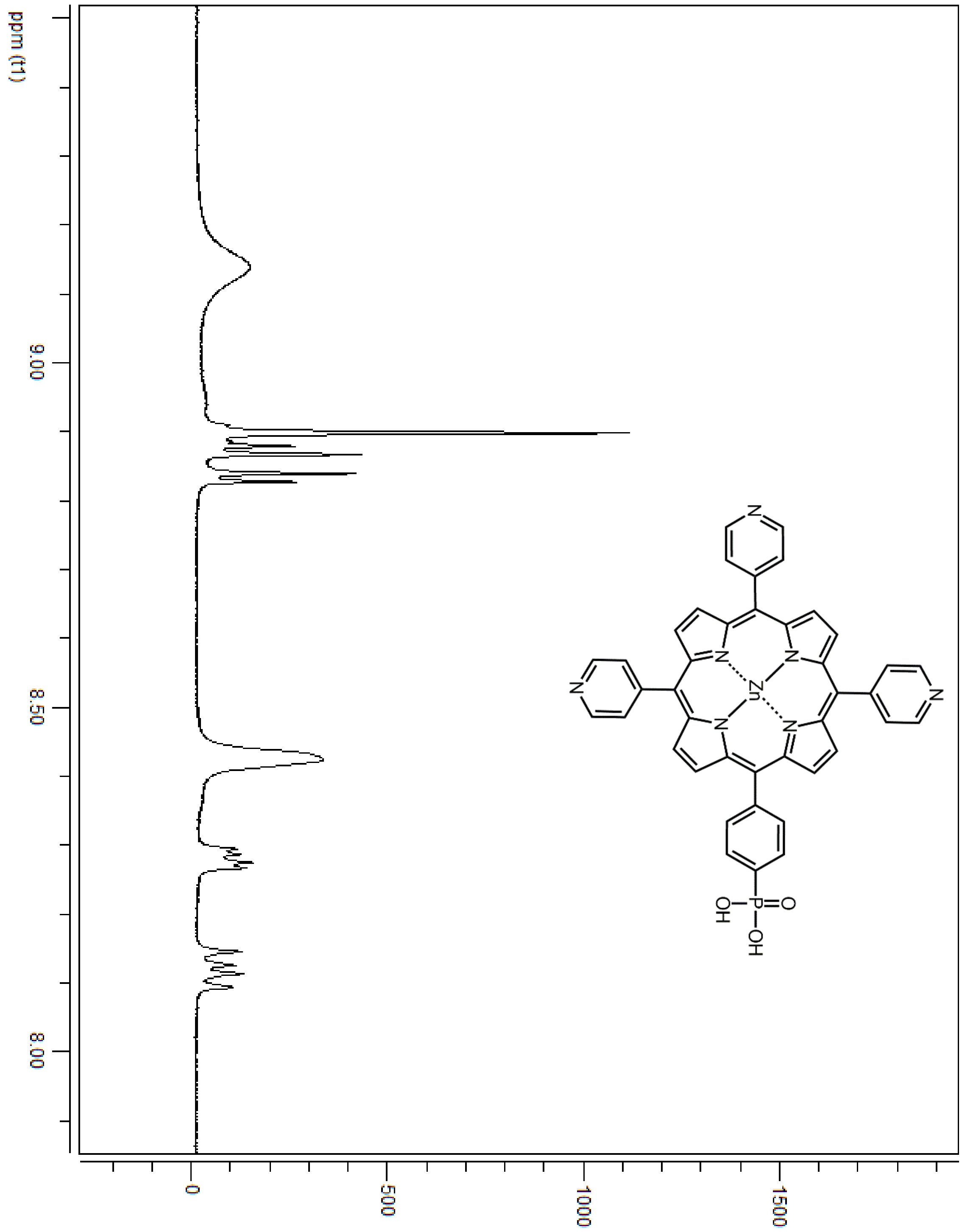

Figure S 10. ^{1}H-NMR of **D1** in DMSO-d_6.

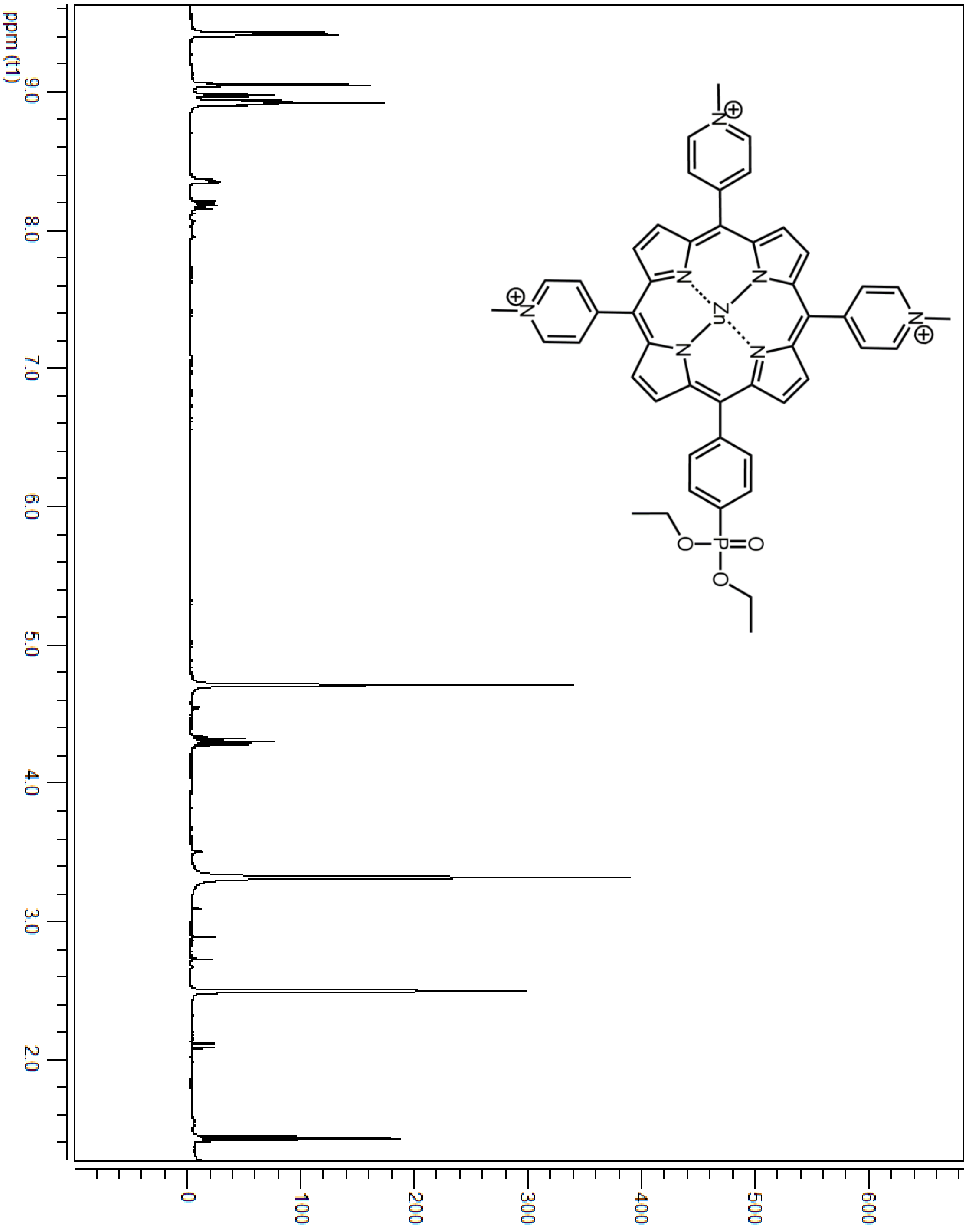

Figure S 11. ^{1}H-NMR of **D2E** in DMSO-d_6.

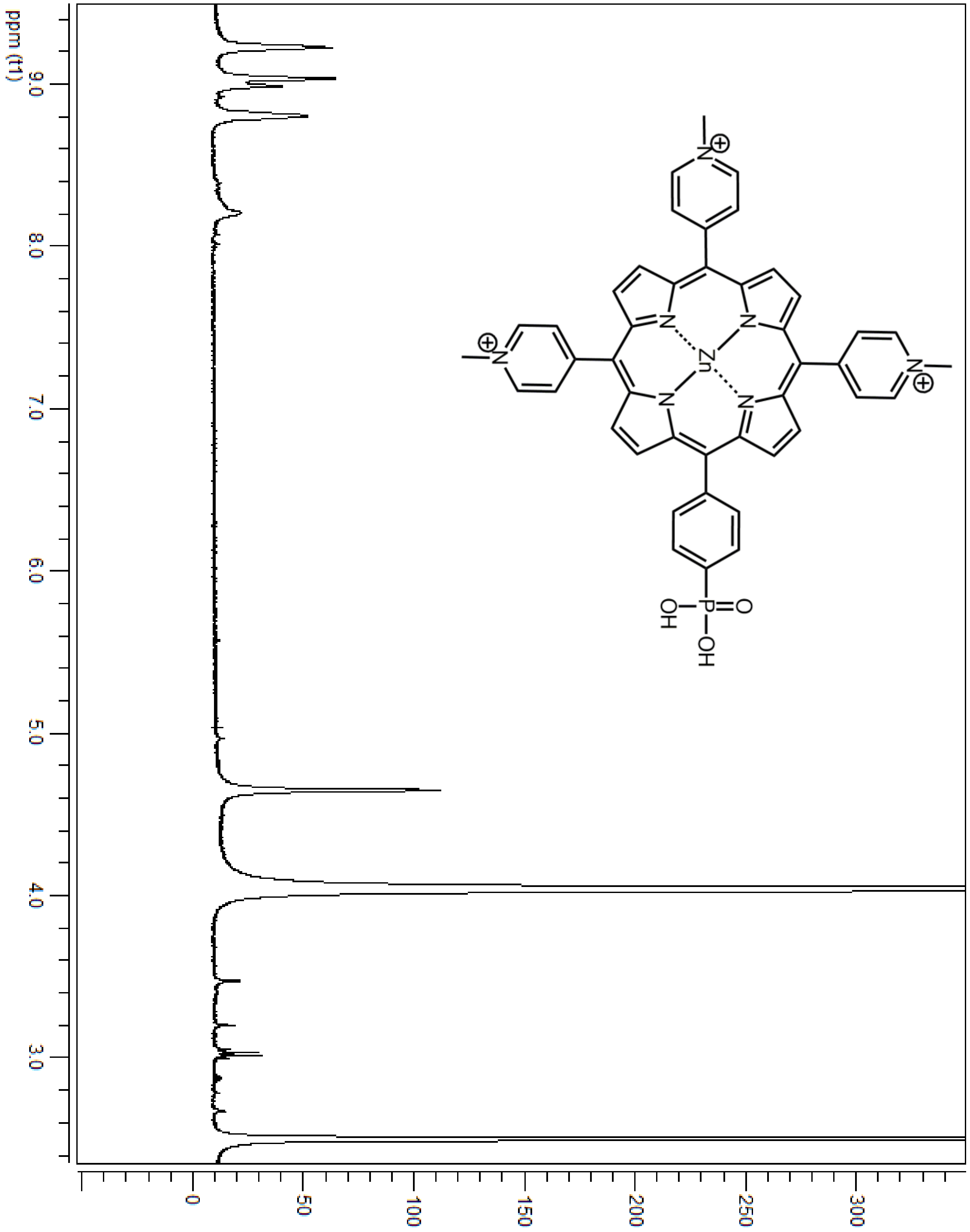

Figure S 12. ^{1}H-NMR of **D2** in DMSO-d_6/D_2O.

Determination of E_{00} of D1 and D2

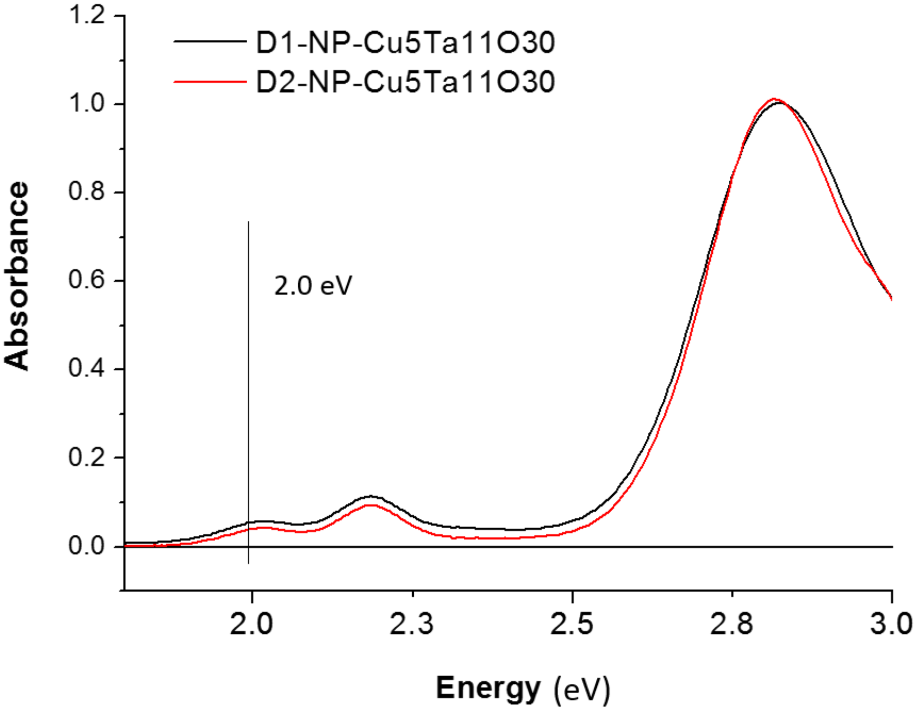

Figure S 13. *Absorption spectra in ethanol for: a)* ***D1****-$Cu_5Ta_{11}O_{30}$ (black line) and b)* ***D2****–NP-$Cu_5Ta_{11}O_{30}$ (red line).*

Photophysics of **D1** in its ester form attached to NP-$Cu_5Ta_{11}O_{30}$.

Following the same procedure described on the main manuscript, **D1** in ester form (**D1E**) was attached to NP-$Cu_5Ta_{11}O_{30}$. Figure S 14 shows how the Soret Q bands of attached **D1E** shift toward the red and the emission of the dye is completely quenched presumably because the hole injection into the semiconductor.

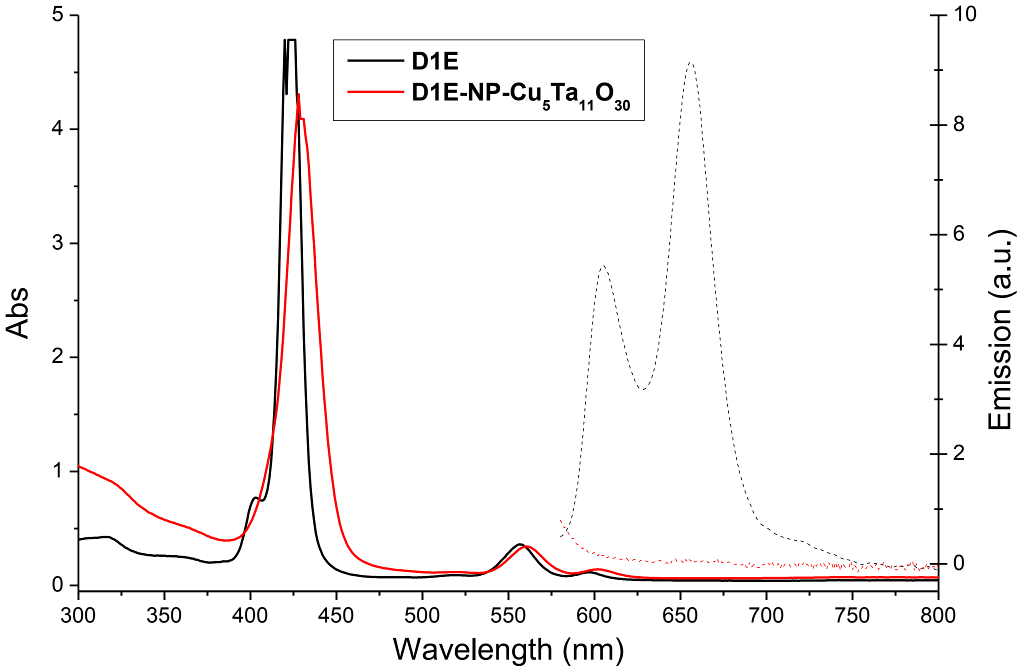

Figure S 14. *Absorption spectra (solid lines) and emission spectra upon 560 nm excitation (dash lines) in ethanol for* ***D1E****–NP-$Cu_5Ta_{11}O_{30}$ (red) and* ***D1E*** *(black).*

Femtosecond transient absorption experiments were performed to establish the kinetics of the photoinduced hole transfer reactions in **D1E**–NP-$Cu_5Ta_{11}O_{30}$, in ethanol solution. Global analysis of the transient absorption data for **D1E**–NP-$Cu_5Ta_{11}O_{30}$ (Figure S 15) reveals three lifetimes of 800 fs, 15.6 ps, 758 ps and a nondecaying component (not shown) upon excitation at 426 nm (Figure S 15a) and 560 nm (Figure S 15b). Since some NP–$Cu_5Ta_{11}O_{30}$ band gap absorption can be registered at 426 nm, spectra with excitation at 560 nm excitation were recorded finding the same overall features and confirming that the small band gap absorption at 426 nm can be neglected in front of the huge Soret band absorption. The 800 fs DAS can be attributed to the recombination of the charge separated state of the

D1E$^{\bullet-}$–NP-$Cu_5Ta_{11}O_{30}$(e+) (inverted kinetics), showing ground state bleaching around 560 and 610 nm and induced absorption associated with D1E$^{\bullet-}$ between 620 nm and 700 nm. The 15.6 ps DAS can be attributed to the hole injection from D1E* to the valence band of the $Cu_5Ta_{11}O_{30}$ showing ground state bleaching around 560 and 610 nm and decay of the stimulated emission around 620 and 670 nm. The 758 ps DAS can be attributed to decay of the singlet excited state of the non-attached(physisorbed)/aggregated dye, which is not involved in the hole injection process, ground state bleaching and stimulated emission bands are slightly blue shifted. Due to the high nonhomogeneity (heterogeneity) of the system, obtained lifetimes do not correspond to single species. These lifetimes represent an average of the decay of several slightly different species. For D1E–NP–$Cu_5Ta_{11}O_{30}$ there is likely some population with very fast formation of charge separate state (<100 fs), this would explain high amplitude of 0.8 ps DAS in such inverted kinetics case, but overall the rate of decay of the charge-separated species is greater than the average effective rate of formation.

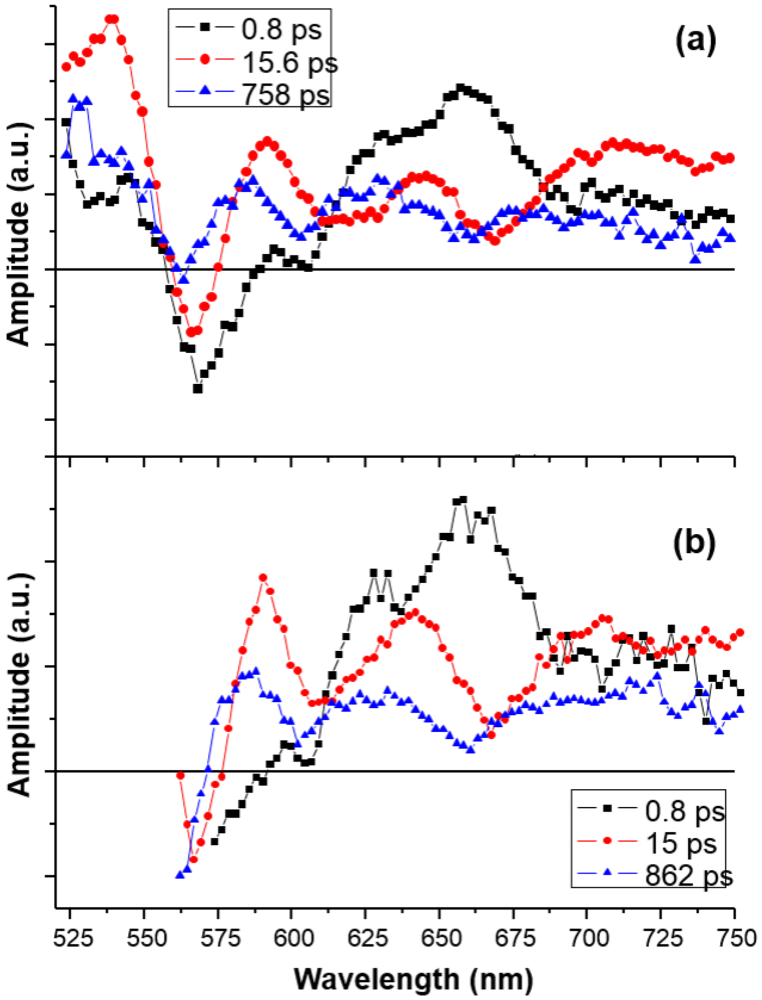

Figure S 15. *Decay-associated-spectra in ethanol measured by fs transient absorption upon excitation at a) 426 nm and b) 560 nm for **D1E**–NP-*$Cu_5Ta_{11}O_{30}$.

DSSC Efficiency Calculations

Fill factor and efficiency for the DSSCs were calculated by using Equations S1 and S2:

$$\boldsymbol{ff} = \frac{\boldsymbol{I_{mp}V_{mp}}}{\boldsymbol{I_{sc}V_{oc}}} = \frac{\boldsymbol{Area\ B}}{\boldsymbol{Area\ A}} \qquad \text{(S1)}$$

$$\boldsymbol{\eta} = \boldsymbol{I_{sc}V_{oc}}\left(\frac{\boldsymbol{ff}}{\boldsymbol{I_c}}\right) \qquad \text{(S2)}$$

Where ff is the fill factor, I_{mp} is maximum power current, V_{mp} is maximum power voltage, I_{sc} is the short circuit current, V_{oc} is the open circuit potential, I_c is incident power from the light source (100 mW/cm^2) and η is the photo-conversion efficiency (PCE) [24] and is graphically shown in Figure S 16. Current-potential scans were performed on a CH-Instruments CH-620a potentiostat under simulated solar irradiance using an AM 1.5 G filter (Oriel). Scans were started near the open circuit voltage and scanned towards the short circuit condition (0.0 V) at a scan rate of 10 mV s^{-1}. The semiconducting film served as the working electrode, while the Pt deposited FTO served as the counter and reference electrode. Power curves were made by multiplying the voltage and currents obtained and plotting against the voltage range used, shown in Figure S 16. Shown in Figure S 17 are the i-v curves for the control experiments in the absence of sensitizing dye. Currents from the control are negligible and do not show any large changes between dark and light conditions, indicating that the dye must be present for any photoinjection to occur.

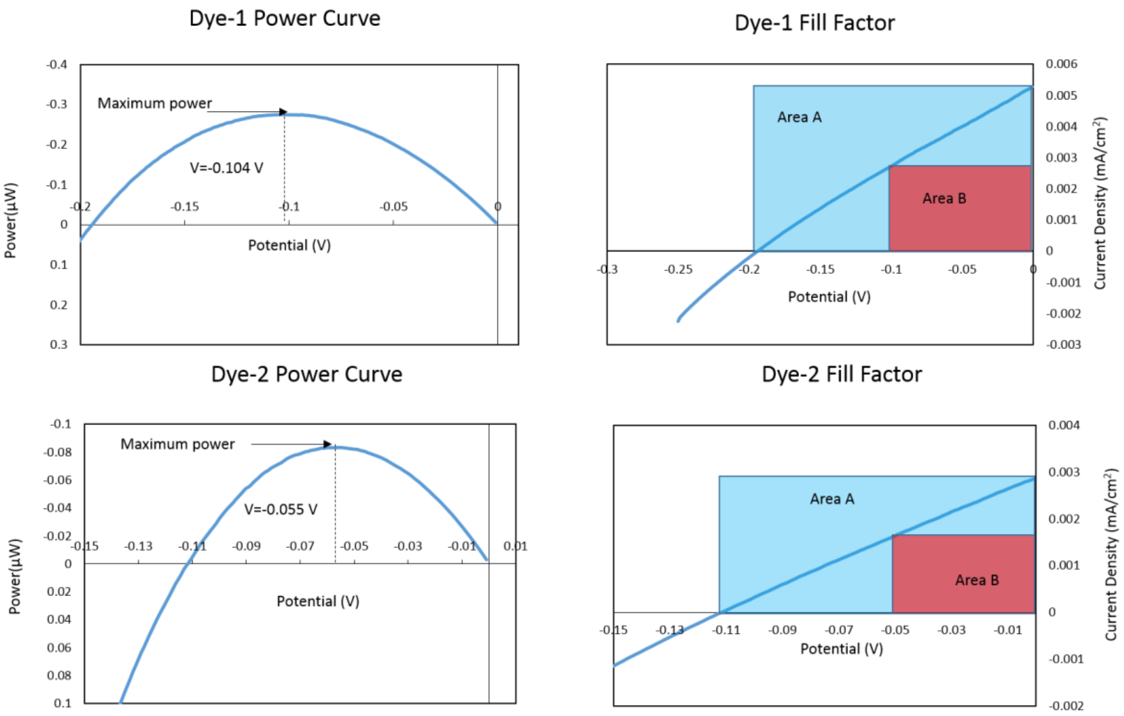

Figure S 16*: Power-voltage (P-V) curves and fill factor (ff) plots for Dye-1 (top) and Dye-2 (bottom) on nanoparticle $Cu_5Ta_{11}O_{30}$ films.*

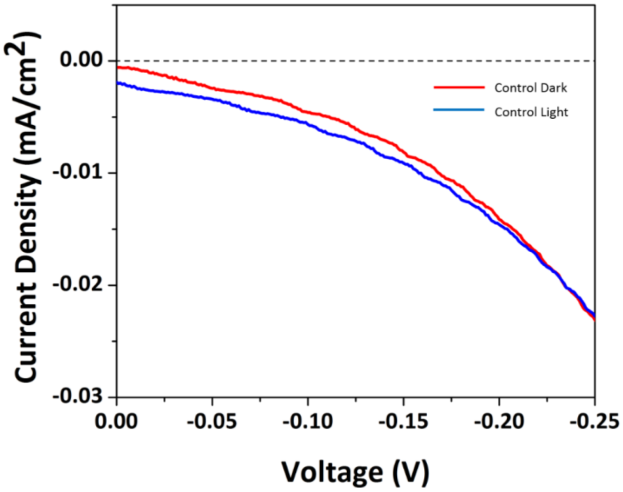

Figure S 17. *Control i-v curves for $Cu_5Ta_{11}O_{30}$ nanoparticle films without dye.*

	Dye-1	Dye-2
V_{oc} (V)	0.2	0.11
I_{sc} (A)	5.28E-06	2.85E-06
I_{mp}	2.64E-06	1.51E-06
V_{mp}	0.104	0.055
FF	2.60E-01	2.65E-01
η	2.75E-04	8.31E-05

Table S 1. *Table of Parameters Determined in the Efficiency Calculations.*

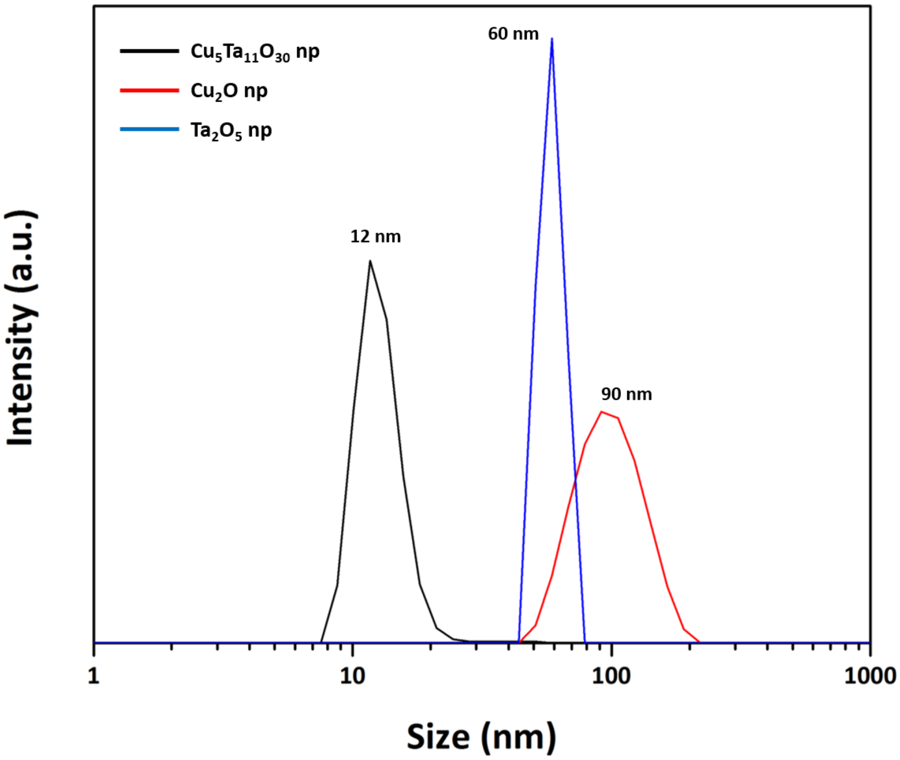

Figure S 18. *Particle size distributions of Cu_2O (red) and Ta_2O_5 (blue) nanoparticle precursors and $Cu_5Ta_{11}O_{30}$ nanoparticle product (black).*

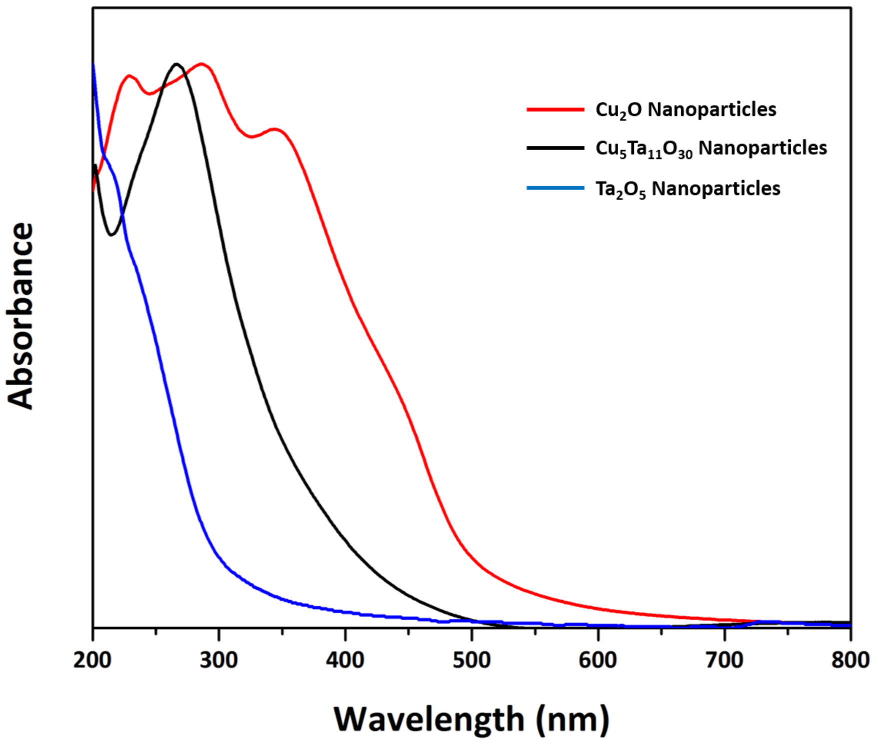

Figure S 19. *UV-Vis of suspended* Cu_2O *(red),* Ta_2O_5 *(green) and* $Cu_5Ta_{11}O_{30}$ *(black) nanoparticles.*

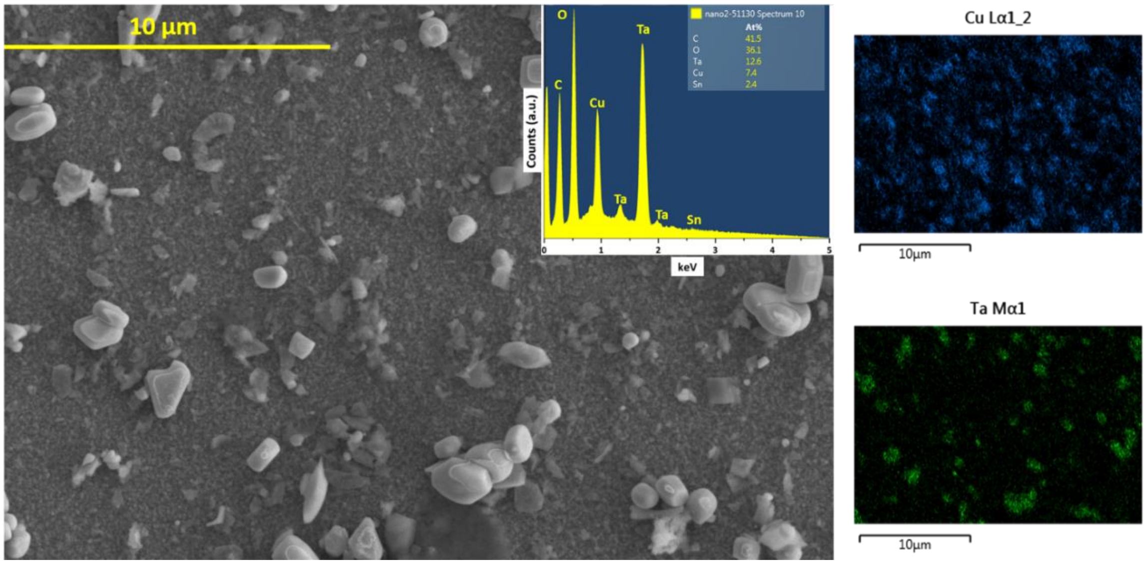

Figure S 20. *FESEM image of an annealed film of* $Cu_5Ta_{11}O_{30}$ *nanoparticles in solution with elemental mapping of Cu and Ta (right). Inset: EDS spectrum of the area.*

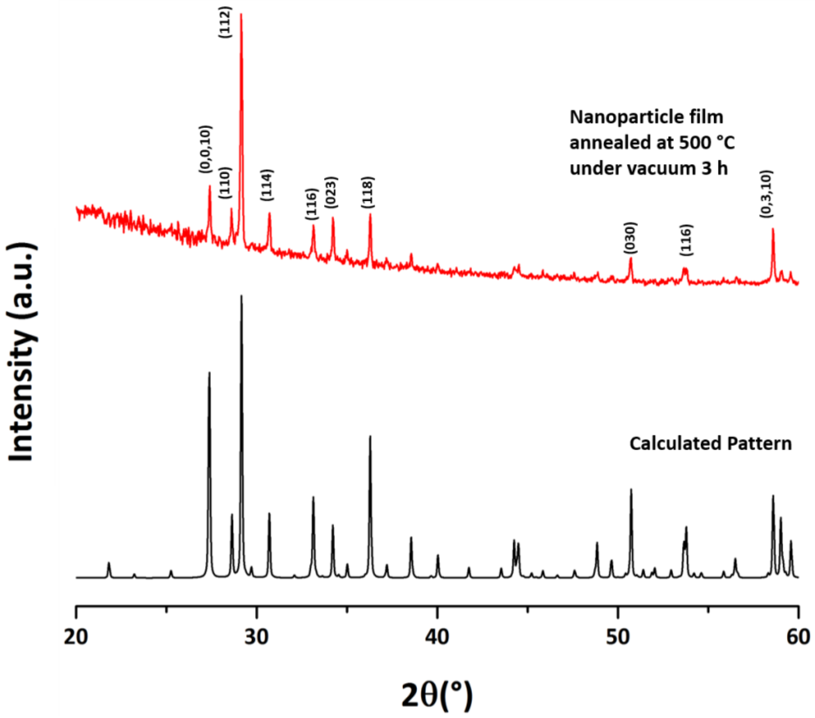

Figure S 21. *Powder X-ray diffraction pattern of the* $Cu_5Ta_{11}O_{30}$ *film (upper), and comparison to a calculated pattern based on the known crystalline structure of* $Cu_5Ta_{11}O_{30}$ *(lower).*

EXPERIMENTAL SECTION

Materials. For the $Cu_5Ta_{11}O_{30}$ nanoparticles: copper sulfate (anhydrous, 99%), tantalum pentachloride (99.9%), ascorbic acid (anhydrous, 99.9%), sodium hydroxide (99%) and copper(I) chloride (anhydrous, 99.9%) were all purchased from Alfa Aeasar. 200 proof anhydrous ethanol was purchased from Koptek.

High Resolution Transmission Electron Microscopy. TEM micrographs were collected using a Philips CM200 TEM at 200kV, Cs 1.2 mm, PTP Resolution: 0.25nm Focused

Probe: 0.5nm and Imaging Modes: TEM/STEM. TEM micrographs were analyzed using *Digital Micrograph*™ software [77].

Powder X-ray Diffraction. The $Cu_5Ta_{11}O_{30}$ products were characterized by powder X-ray diffraction using an Inel X-ray diffractometer and Cu $K\alpha_1$ radiation (λ=1.54056 Å) from a sealed tube X-ray generator (30 mA, 35 kV). A curved position sensitive detector (CPS-120) was used in transmission mode.

Steady State Absorption and Fluorescence. Spectra were recorded in 1 cm path length cuvettes with the following spectrophotometers: diode array HP 8452, Shimadzu - UV-IR (2041PC), and Hitachi double beam UV/Vis spectrophotometer (U-2800). Steady-state fluorescence spectra were measured using a Photon Technology International MP-1 spectrometer and corrected for detection system response and excitation source intensity as a function of wavelength. Excitation was provided by a 75 W xenon-arc lamp and single-grating monochromator. Fluorescence was detected at 90° to the excitation beam via a single-grating monochromator and an R928 photomultiplier tube having S-20 spectral response and operating in the single photon counting mode.

Time Resolved Absorption. Femtosecond to nanosecond transient absorption measurements were acquired with a kilohertz pulsed laser source and a pump-probe optical setup. Laser pulses of 100 fs at 800 nm were generated from an amplified, mode-locked titanium sapphire kilohertz laser system (Millennia/Tsunami/Spitfire, Spectra Physics). Part of the laser pulse energy was sent through an optical delay line and focused onto a 3 mm sapphire plate to generate a white light continuum for the probe beam. The remainder of the pulse energy was used to pump an optical parametric amplifier (Spectra Physics) to generate excitation pulses, which were selected using a mechanical chopper. The white light generated was then compressed by prism pairs (CVI) before passing through the sample. The polarization of the pump beam was set to the magic angle (54.7°) relative to the probe beam and its intensity was adjusted using a continuously variable neutral density filter. The white light probe was dispersed by a spectrograph (300 line grating) onto a charge-coupled device (CCD) camera (DU420, Andor Tech.). The final spectral resolution was about 2.3 nm for over a nearly 300 nm spectral region. The instrument response function was ca. 100 fs. The decay-associated spectra (DAS) were obtained by fitting globally the transient absorption kinetic traces over a selected wavelength region simultaneously as described by equation (1) (parallel kinetic model).[79]

$$\Delta A(\lambda,t)=\sum_{i=1}^{n}A_i(\lambda)\exp(-t/\tau_i) \tag{1}$$

where $\Delta A(\lambda,t)$ is the observed absorption change at a given wavelength at time delay t and n is the number of kinetic components used in the fitting. A plot of $A_i(\lambda)$ versus wavelength is called a DAS and represents the amplitude spectrum of the i^{th} kinetic component, which has a lifetime of τ_i. Random errors associated with the reported lifetimes obtained from transient absorption measurements were typically $\leq 5\%$. Rigorous analysis of time resolved emission and absorption data in a non-homogeneous system requires the use of a model which considers a distribution of multi-exponential decays to describe the kinetics of each transient species and thus accounts for the distribution of available environments in the heterogeneous system. In our analysis we used the minimum number of exponential components that adequately fitted the experimental data within the experimental error. Thus it is likely that the reported decay components correspond to a weighted mean value of the actual distribution of constants associated with each species.

Dynamic Light Scattering Measurements. Dynamic light scattering measurements were performed on a Malvern Zetasizer Nano S with detector 173° from the incident beam and a laser wavelength of 633 nm. Nanoparticles of $Cu_5Ta_{11}O_{30}$, Cu_2O and Ta_2O_5 were separately suspended in ethanol and measurements were taken at a temperature of 25° C, with single size distributions observed for each sample. Ta_2O_5 and Cu_2O precursor nanoparticles have size distributions centered around 60 nm and 90 nm, respectively, with $Cu_5Ta_{11}O_{30}$ nanoparticles having a lower size distribution centered around 12 nm. This is due to the dissolution of the precursors in the CuCl flux and then re-crystallization at a smaller size.

Electronic Absorption Spectroscopy of Nanoparticle Solutions. Electronic absorption spectra were taken of suspended particles in ethanol using a Shimadzu UV 3600. The suspensions of Cu_2O, Ta_2O_5 and $Cu_5Ta_{11}O_{30}$ show different absorption profiles shown in Figure S 19. Cu_2O absorbs around 2.3 eV, Ta_2O_5 absorbs around 4.0 eV and $Cu_5Ta_{11}O_{30}$ absorbs around 3.0 eV.

Field Emission Scanning Electron Microscopy and Energy Dispersive Spectroscopy (FESEM/EDS). FESEM/EDS measurements were taken on an FEI Verios 460L field emission scanning electron microscope. Nanoparticle films were deposited from an ethanol solution, then annealed at 200 °C for 2 h under dynamic vacuum. Images show nanoparticle films on fluorine doped tine oxide (FTO) with a Cu-Ta ratio of 2:1, in agreement with the Cu-Ta ratio in $Cu_5Ta_{11}O_{30}$. Small amounts of Sn are also detected from the FTO substrate. Elemental mapping shows the coverage of Cu and Ta across the entier area of the film.

X-ray Diffraction of Annealed Films. Suspended nanoparticles in ethanol were deposited on fluorine doped tin oxide (FTO) and allowed to dry in air leaving a film of the nanoparticles. The film was heated to 500 °C for 3 h under dynamic vacuum and allowed to cool to room temperature before removing from the tube furnace. Scotch tape was then used to remove the film from the FTO and taken for X-ray diffraction (XRD). Diffraction patterns of the material match the calculated pattern for $Cu_5Ta_{11}O_{30}$, with peaks indexed in Figure S 21. Preferential orientation is observed for the thin films with dominant diffraction on the (112) reflection.

Chapter 2.3 Journal of the American Chemical Society Paper

A De Novo Designed 2[4Fe-4S] Ferredoxin Mimic Mediates Electron Transfer

Anindya Roy[‡†#], Dayn Joseph Sommer[‡†], Robert A. Schmitz[†], Chelsea Brown[†], Devens Gust[†], Andrei Astashkin[‡], and Giovanna Ghirlanda[†]*

[†]*Department of Chemistry and Biochemistry, Arizona State University, Tempe, Arizona 85287-1604, United States* [‡]*Department of Chemistry and Biochemistry, University of Arizona, Tucson, Arizona 85721, United States*

[#]*Current Address: Department of Biochemistry, Molecular Engineering and Sciences, University of Washington, Seattle, WA-98195, USA.*

Citation:

Anindya Roy, Dayn Joseph Sommer, Robert Arthur Schmitz, Chelsea Lynn Brown, Devens Gust, Andrei Astashkin, and Giovanna Ghirlanda. *Journal of the American Chemical Society* **2014**, *136*, 17343-17349.

My contributions to this work involved the preparation of the porphyrin dye and the synthetic write-up, as well as aiding in the editing process.

KEYWORDS. Iron-sulfur proteins, de novo design, metalloproteins, EPR, electron transfer

ABSTRACT: [Fe-S] clusters, nature's modular electron transfer units, are often arranged in chains that support long-range electron transfer. Despite considerable interest, the design of biomimetic artificial systems emulating multicluster-binding proteins, with the final goal

of integrating them in man-made oxidoreductases, remains elusive. Here, we report a novel bis-[4Fe-4S] cluster binding protein, DSD-Fdm, in which the two clusters are positioned within a distance of 12 Å, compatible with the electronic coupling necessary for efficient electron transfer. The design exploits the structural repeat of coiled coils as well as the symmetry of the starting scaffold, a homo-dimeric helical protein (DSD). In total, eight hydrophobic residues in the core of DSD were replaced by eight cystine residues that serve as ligands to the [4Fe-4S] clusters. Incorporation of two [4Fe-4S] clusters proceeds with high yield. The two [4Fe-4S] clusters are located in the hydrophobic core of the helical bundle as characterized by various biophysical techniques. The secondary structure of the apo and holo proteins is conserved; further, the incorporation of clusters results in stabilization of the protein with respect to chemical denaturation. Most importantly, this de novo designed protein can mimic the function of natural ferredoxins: we show here that reduced DSD-Fdm transfers electrons to cytochrome c, thus generating the reduced cyt c stoichiometrically.

INTRODUCTION

Ferredoxins are nature's electron transfer modules, supporting crucial processes such as photosynthesis and respiration.[94-98] The so-called bacterial type consists of small proteins containing two cubane-like [4Fe-4S] clusters within sequences of 50-60 amino acids. Each cluster is coordinated by four cysteine residues and ensconced in one of two pseudo-symmetric domains thought to derive from a gene duplication event.[97,99] Ferredoxins function as one-electron shuttles and couple oxidation of several substrates with reduction of cofactors or final acceptors such as H^+ or $NADP^+$.[95,100-102] The ferredoxin fold has also been coopted as a separate subunit (e.g. PsaC) or as an integral domain within complex enzymes, such as Photosystem I and the hydrogenases.[103-109] In these redox proteins, chains of [4Fe-4S] clusters transfer electrons produced or consumed at a buried active site to the protein surface, allowing interaction with soluble partners. To optimize the rates of electron transfer, the clusters are typically separated by up to 12-14 Å.

A substantial amount of work in the field of de novo design has sought to incorporate the clusters into peptide-based model systems, to elucidate the properties of the natural cluster environment, and eventually to include these model peptides in engineered redox enzymes.[100,103,110-117] Most of these peptides, however, have been designed to bind a single electronically isolated cluster, which limits their usefulness as electron conduits in vitro. To address this problem, we have recently developed a general method to design bis-[4Fe-4S] cluster binding peptides by exploiting the symmetry of coiled coils. Using this approach, we have shown that two [4Fe-4S] clusters can be incorporated inside the hydrophobic core of a three-helix bundle.[118] However, the distance separating the two clusters in our prototype was 36 Å, which did not provide a useful platform for studying efficient electron transfer. Here, we present a second generation design, DSD-Fdm, in which the two clusters are located within 12 Å of each other, a biologically relevant distance for effective electron transfer. The redox potential of DSD-Fdm falls within the range observed for natural ferredoxins, suggesting that this artificial protein could engage in electron transfer with external redox active species. We show that DSD-Fdm is capable of transferring electrons to cytochrome c in a stoichiometric manner. Further, DSD-Fdm undergoes energy transfer in the presence of a photosensitizer, suggesting a possible use in solar fuel cell applications.

METHODS

Peptide Synthesis and Purification. All peptides were synthesized by automated microwave-assisted solid phase peptide synthesis on a Liberty instrument (CEM). The synthesis was carried out using standard Fmoc protection procedures. Briefly, Rink Amide resin was doubly deprotected using 0.1 M hydroxybenzotriazole (HOBt) in a 20% piperidine in DMF solution. Amino acid couplings were achieved using appropriate amounts of 0.45 M HBTU in DMF, 2 M ethyl-diisopropylamine (DIEA) in N-methyl-2-pyrrolidone (NMP), and 0.2 M Fmoc protected amino acid (Novabiochem), followed by irradiation with microwaves to pre-established temperatures according to CEM protocols. Peptides were acetylated at the N-terminus via addition of acetic anhydride under coupling conditions. The peptides were cleaved from the resin using 94% trifluoroacetic acid (TFA), 2.5% H_2O, 2.5% 1,2-ethanedithiol (EDT), and 1% triisopropylsilane (TIS) for 3 h. The solution was then evaporated under a stream of N_2, and the peptide was precipitated with cold ether. Crude, lyophilized peptides were purified using preparatory-scale HPLC on a C18 reverse-phase column, with a linear gradient of Solvent A (99.9% water with 0.1% TFA) and Solvent B (95% acetonitrile, 4.9% water, and 0.1% TFA) at a flow rate of 10 mL/min. Peptide identity was confirmed by MALDI-TOF-MS; peptides were >99% pure as assessed by C18 analytical HPLC.

Cluster Incorporation and quantification. Iron-sulfur clusters were incorporated into peptide variants by adapting well-established methodologies.[111,119] All reactions were performed in an anaerobic chamber (Coy Scientific), with a 95% N_2 and 5% H_2 environment. To a solution of 150 μM peptide in 100 mM Tris-HCl, pH 8.5, the following reagents were added sequentially at 20 min intervals to a final concentration: 0.8% (v/v) β-mercaptoethanol, 3 mM ferric chloride ($FeCl_3$), and 3 mM sodium sulfide (Na_2S). The mixture was incubated overnight at 4 °C. The resulting dark brown solution was subjected to desalting with a PD10 G25 column (GE Healthcare) that was pre-equilibrated with 100 mM Tris at pH 7.5 to obtain the holo protein.

Cluster quantification. Cluster incorporation was assessed quantitatively by measuring independently the concentration of iron and of peptide in identical samples.[118] DSD-Fdm samples were further purified using anion exchange chromatography on a Q-Sepharose FF column (GE Healthcare), using 100 mM Tris at pH 8.5 as equilibration buffer, and 100mM NaCl, 100 mM Tris at pH 8.5 as elution buffer. The DSD-Fdm samples were split in two portions: one was used to measure peptide concentration (Bradford assay), and the second was used to determine iron concentration using a ferrozine assay.[120,121] EPR spin quantification was used to assess the amount of reduced clusters in concentrated EPR samples. The double integral of the CW EPR spectrum of $[4Fe\text{-}4S]^{1+}$ recorded at 7 K was compared with the spectrum of 5 mM Cu(II) nitrate recorded at 21 K (at lower temperatures the Cu(II) EPR signal saturated even at the lowest accessible mw power of 0.2 μW). The estimated concentration of $[4Fe\text{-}4S]^{+}$ was then compared with the DSD-Fdm protein concentration evaluated by Bradford assay.

Gel Filtration. Size exclusion chromatography was performed on a G-25 gel filtration column fit to an Agilent Technologies 1260 Insight FPLC system. The column was pre-equilibrated in 100 mM Tris-HCl, pH 7.5, and 200 μL of 150 μM apo or holo peptide were used for each injection. The apo peptide was pre-treated with tris(2-

carboxyethyl)phosphine (TCEP) for 30 min before injection to reduce any disulfides resulting from air oxidation.

Circular Dichroism Spectroscopy. Spectra were recorded on a JASCO J-815 spectropolarimeter in the range of 260-190 nm. Data were recorded every 1 nm and averaged over 3 scans. The concentration of apo and holo-peptides were kept at 50 μM in 100 mM Tris, pH 7.5, while the measurements of the apo-peptide were carried out in the presence of an excess of TCEP. Holo peptide was measured under anaerobic conditions in an airtight CD cuvette. Chemical denaturation titrations were carried out through addition of an 8 M stock solution of guanidinium-HCl (Gdn·HCl), followed by mixing and incubation for 5 min to allow for equilibration. Holo peptide was titrated under anaerobic conditions. Spectra were normalized to protein concentration in the sample and converted to fraction folded relative to the apo or holo protein signal, which lacked Gdn·HCl.

Electron Paramagnetic Resonance Spectroscopy. Holo-protein obtained from PD10 desalting was concentrated in a 3000 MWCO centrifuge concentrator to approximately 1 mM peptide concentration. Reduced samples were prepared by addition of 100 mM sodium dithionite in 1 M glycine buffer, pH 10, to a final concentration of 20 mM dithionite. EPR samples were prepared by addition of 10% (v/v) glycerol as a cryoprotectant and placed in quartz EPR tubes, after which the samples were flash frozen and stored under liquid N_2 until measurements. Continuous wave (CW) EPR experiments were carried out on a X-band EPR spectrometer Elexsys E500 (Bruker) equipped with the ESR900 flow cryostat (Oxford Instruments).

Synthesis of water-soluble porphyrin analogue. The 5,10,15,20-tetrakis(4-diethyl 2-benzylmalonate) porphyrin was synthesized following published procedures for related compounds.[100,122] Zinc insertion was achieved using $Zn(O_2CCH_3)_2(H_2O)_2$ in THF for 12 h at 60 ºC by modifying a literature procedure (Figure S 22),[123-125] and the esters were cleaved as reported for related compounds.[103,111,126,127] The resulting water-soluble, malonate-functionalized porphyrin was characterized by mass spectrometry and NMR in D_2O. (Figure S 23, S 24)

Transient Absorption Spectroscopy. Nanosecond transient absorption measurements were performed on a flash photolysis apparatus using a pulsed laser source and a pump-probe optical setup. The samples contained 10 mM Tris-HCl at pH 7.5, with 30 μM holo or apo peptide in a 1 cm fluorescence cuvette. Malonate-porphyrin was added to a final absorbance of 0.25 at the first Q-band (560 nm). Excitation was provided by an optical parametric oscillator pumped by the third harmonic (352 nm) of a Nd:YAG laser (Ekspla NT 342B). The pulse width was 4-5 ns, and the repetition rate was 10 Hz. The signal was detected by a Proteus spectrometer (Ultrafast Systems). The instrument response function was 4-5 ns. Transient data analysis was carried out using the in-house program ASUFIT. Simple exponentials were fit one for wavelength at a time.

Cytochrome C_{550} Reduction Assay. DSD-Fdm was reduced via slow addition of dithionite, monitoring the loss of signal at 410 nm. Once the absorption at 410 nm had stabilized and a slight dithionite signal had arisen at 300 nm, the holo-peptide was subjected to two successive PD10 columns to exclude any unreacted dithionite. The first 1.5 mL of the total 3.5 mL elution volume was concentrated to a protein concentration of 300 μM. The reduced DSD-Fdm was added in 1 μL increments to 500μL of a solution of cytochome c_{550} isolated from Thermosynechococcus elongatus (7 μM protein concentration as assayed by absorbance at 550 nm, $\varepsilon_{550} = 21000\ M^{-1}\ cm^{-1}$). After each addition, UV-Vis spectra were obtained with an Ocean Optics USB4000 detector fitted with a USB-ISS-UV-Vis light source. Data were fit by a linear regression model before and after saturation in order to determine the mole equivalents required to obtain full reduction of the cytochome c_{550} heme cofactor.

RESULTS AND DISCUSSION

Protein Design and Synthesis. We used the heptad repeat pattern of coiled coils, which is reflected in a regular structural motif, to design two [4Fe4S] binding sites into the core of DSD-Fdm starting from DSD-bis[4Fe4S].[118,119,128,129] Each site was translated by one heptad towards the center of DSD along the longitudinal axis (PDB Code 1G6U) by moving the two cysteine side chains arranged at the i, i+3 positions within the same helix. Locations for the two remaining cysteines, one per helix, in positions compatible with chelating the cluster were determined by manually docking a [4Fe-4S] cluster binding site from Thermotoga maritima (PDB ID 2G36)[94-98] inside the core (Figure 1). Taking into account the pseudo two-fold symmetry of DSD, we replicated the site onto the other half of DSD by inserting appropriate mutations into the peptide sequence. DSD-Fdm thus incorporates two [4Fe-4S] clusters in the hydrophobic core, at a distance of 12 Å as measured between their centers, in an arrangement reminiscent of the symmetry observed in the natural ferredoxin fold. Mutation of eight core leucine side chains to cysteines causes the formation of a 62 Å polar cavity within the core of the apo peptide, which is completely filled upon incorporation of the cluster (Figure 19).[97,99]

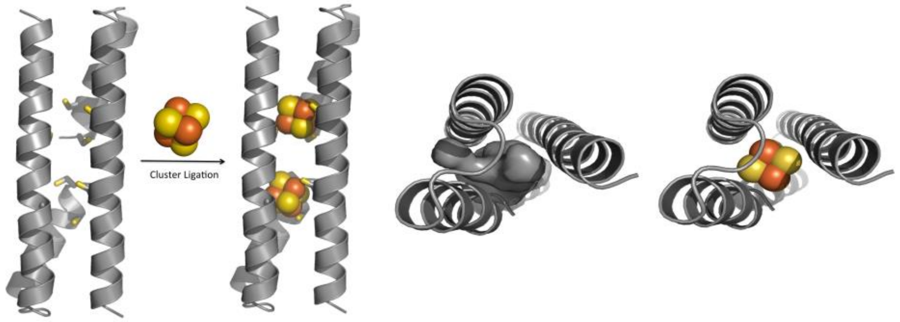

DSD: S**L**AA**L**KSELQALKKEGFSPEELAALESE**L**QALEKK**L**AALKSKLQALGW

DSD-Fdm: S**C**AA**C**KSELQALKKEGFSPEELAALESE**C**QALEKK**C**AALKSKLQALKG

Figure 19**.** Design strategy for DSD-Fdm (Top panel); Sequences of DSD, DSD-2[4Fe4S], and DSD-Fdm (bottom panel)

Cluster Incorporation. The [4Fe-4S] clusters were formed and incorporated in situ from inorganic precursors and mercaptoethanol using established protocols,[95,100-102] and holo DSD-Fdm was purified by gel filtration chromatography.

The UV-vis spectrum of DSD-Fdm shows a broad feature with maxima at 415 and 360 nm, characteristic of sulfur to iron charge transfer excitations in $[4Fe\text{-}4S]^{2+}$ clusters; the absorbance at 415 nm was reduced to below 50% of its initial value upon reduction to $[4Fe\text{-}4S]^{1+}$ (Figure 20) with dithionite. This behavior is typical of cuboidal [4Fe-4S] clusters.[103-109] The position of the bands, red-shifted compared to inorganic [4Fe-4S] clusters, suggests that the clusters are surrounded by a hydrophobic environment.[100,103,110-117]

We investigated the oligomeric state of apo and holo DSD-Fdm by analytical ultracentrifugation and size exclusion chromatography. When analyzed by gel filtration, both apo and holo DSD-Fdm elute at comparable volumes of elution buffer, which is consistent with a single species with the apparent molecular mass of a dimer (

Figure S **25**). The elution profiles of the holo DSD-Fdm monitored at 220, 280 nm and at 410 nm are identical, indicating the presence of the [4Fe-4S] cluster in the dimer. Analytical ultracentrifugation of the apo DSD-Fdm at ~100 mM loading concentration reveals an apparent molecular weight in solution of approximately 13.3 kDa, consistent with a dimeric form in solution (Figure S 26), confirming the results of the size exclusion chromatography.

We evaluated the level of cluster incorporation in the dimer by independently assessing Fe and protein concentrations as described in Methods. We found that the ratio of iron per monomer is 4.3 ± 0.9, corresponding to two [4Fe-4S] clusters per dimer. These data indicate that incorporation is approximately 100%.

Protein Structure and Stability. We investigated the secondary structure of both apo and holo DSD-Fdm using far-UV circular dichroism (CD) spectroscopy. The spectra of each of the two proteins are similar to that of the parent peptide, and display two minima centered at 208 nm and 222 nm, indicative of helical structures (Figure S 27). Cluster incorporation is well tolerated by the peptide, which is reflected by the similar molar ellipticity value of the holo peptide as compared to the apo peptide.

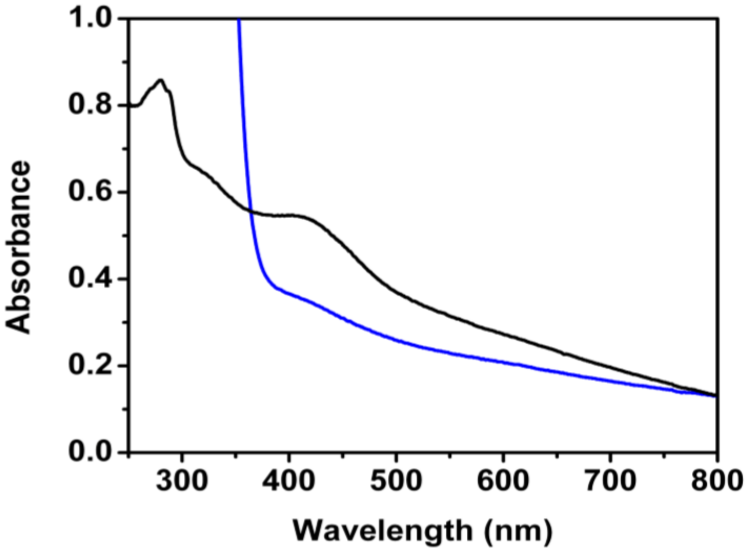

Figure 20. UV-Vis spectra of holo DSD-Fdm before (black trace) and after (blue trace) dithionite reduction.

To assess the effect of mutations on the DSD framework, we measured the stability of the apo and holo peptide towards chemical denaturation by monitoring the loss of secondary structure as a function of increasing concentration of a chaotropic agent, guanidine-hydrochloride (Gdn·HCl). The denaturation curves in Figure 21 report fraction folded, as monitored at 222 nm, versus denaturant concentration for each peptide, showing that holo DSD-Fdm is significantly more stable to chemical denaturants than is the apo version. The midpoint of denaturation for the apo peptide is at 2.1 M Gdn·HCl , while for the holo DSD-Fdm it is at 4.4 M Gdn·HCl. This behavior mirrors what is observed for DSD-bis[4Fe-4S], for which a large increase in stability resulted from the cluster incorporation.[118] The starting scaffold for both constructs, DSD, is exceptionally stable to thermal and chemical denaturation.[111,119] In both DSD-bis[4Fe-4S] and DSD-Fdm, substituting hydrophobic leucine residues in the core with polar, smaller cysteine results in the formation of a polar cavity, which in the case of DSD-Fdm has a volume of 62 Å. This volume is compatible with the dimensions of a [4Fe-4S] cluster; when modeled in the peptide core, the [4Fe-4S] cluster completely fills the cavity, thus restoring a well-packed core.

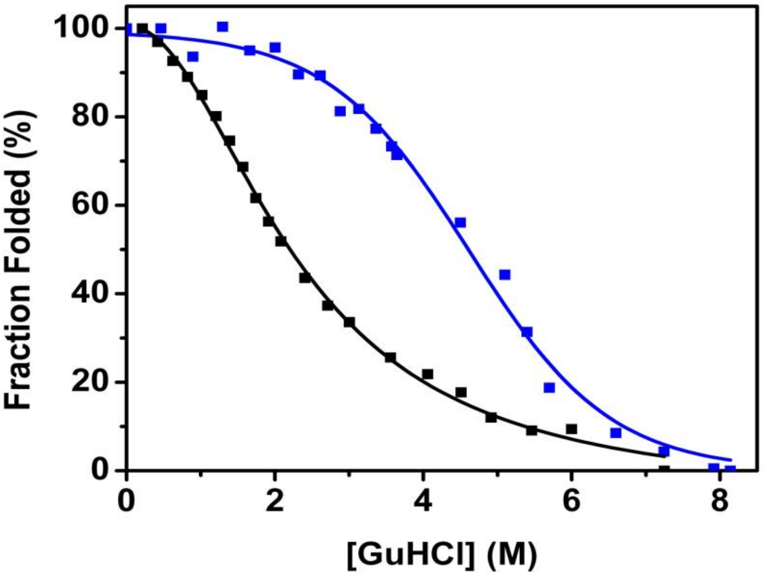

Figure 21. Chemical denaturation profile of apo and holo DSD-Fdm monitored by CD at 222 nm. The midpoint of the transition is at 2.1 M Gdn·HCl (black line) for the apo peptide, and at 4.4 M Gdn.HCl (blue line) for holo DSD-Fdm.

EPR Spectroscopy and redox properties of the cluster. The electronic properties of holo DSD-Fdm were explored by CW EPR spectroscopy. As expected, in vitro reconstitution of the iron-sulfur cluster into the designed protein results in formation of an EPR silent [4Fe-4S]$^{2+}$ resting state. Upon dithionite reduction, an EPR signal corresponding to intact [4Fe-4S]$^{1+}$ clusters arises, with typical principal g-values of 1.89, 1.94, and 2.06, and an isotropic g-value of about 1.96 (Figure 22). The temperature dependence of this signal is similar (if not identical) to that obtained earlier for DSD-bis[4Fe-4S] and indicative of the presence of low-lying (~60 K) excited states. (Figure S 28) The spin quantification of this signal and the comparison of the spin count with the protein concentration reveals a yield of reduced cluster per dimer of DSD-Fdm close to 0.6, similar to what has been observed for DSD-bis[4Fe-4S].[118] This value contrasts with complete cluster incorporation yields calculated by iron quantification based on resting state (i.e., oxidized) samples. The discrepancy is caused by difficulties in achieving complete reduction of the cluster in concentrated samples.

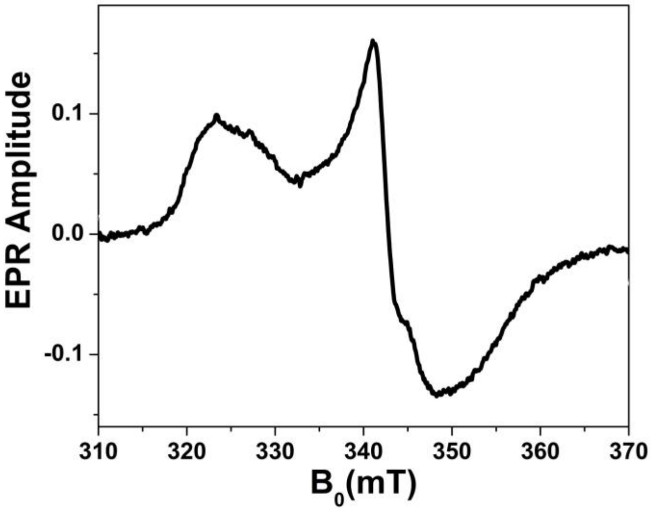

Figure 22. CW EPR spectrum of dithionite-reduced holo DSD-Fdm. Experimental conditions: microwave frequency, 9.337 GHz; microwave power, 20 mW; field modulation amplitude, 0.5 mT; temperature, 12 K.

Ferredoxin-type proteins containing two $[4Fe\text{-}4S]^{1+}$ within 10-15 Å of each other sometimes exhibit features in the EPR spectra attributable to a spin-spin interaction between the clusters.[120,121] Despite repeated attempts, these features were not observed in the spectra of DSD-Fdm. However, the lack of cluster interaction effects in the CW EPR spectra of dicluster ferredoxins is relatively common, for two main reasons.[100,122] First, the magnitude of the dipole and exchange interactions between two clusters strongly depends on their relative orientation, because of the mixed valence nature of the clusters.[123-125] For example, the dipole interaction constant estimated for DSD-Fdm as a function of the relative orientation of the clusters can be anywhere between ~ 300 and -25 MHz (in magnetic field units, ~ 11 and <1 mT, respectively) or distributed within these limits. The smaller of these couplings would probably not be detectable because it is much smaller even than the EPR linewidth at the intermediate turning point (> 3 mT). The larger of these couplings could in principle be resolvable, but the relatively flexible nature of DSD-Fdm may result in a significant broadening and the lack of pronounced features in the EPR spectrum of the pair. The second reason, which compounds the first one, is the relatively low yield of reduced cluster.

The redox properties of DSD-Fdm were probed using cyclic voltammetry (CV). Solution CV experiments showed no observable redox processes in the range from 0 to -1 V vs SHE, presumably because of the absence of interaction between the electrode surface and the electroactive species. Addition of 3.5 mM neomycin, which is known to stabilize and enhance the interaction of ferredoxin type proteins with electrode surfaces, resulted in the observation of a quasi-reversible process with cathodic and anodic waves centered around -0.438 and -0.521 V vs SHE respectively (Figure 23). We estimated a redox potential of -0.479 V vs SHE, consistent with the presence of a $[4Fe\text{-}4S]^{2+/1+}$ couple. This value falls within the window expected for low potential [4Fe-4S] clusters in proteins, and is very close to those observed for the PsaC subunit of Photosystem I.[103,111,126,127]

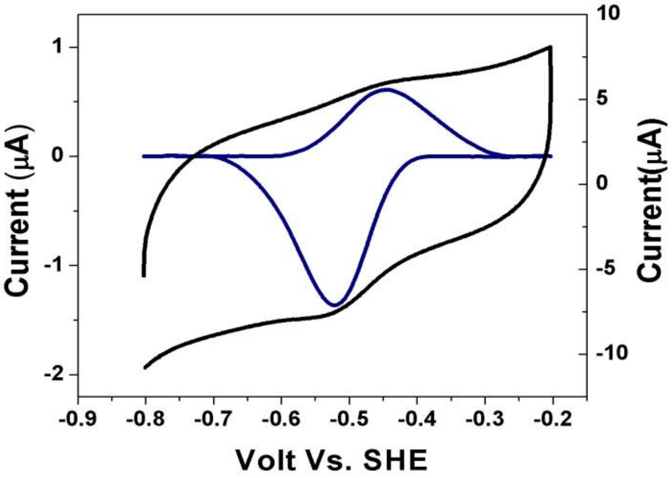

Figure 23. Cyclic voltammogram of DSD-Fdm in a 3.5 mM neomycin, 100 mM TRIS, 100 mM sodium chloride, pH 7.5, solution at 100 mV/s scan rate with a Ag/AgCl reference electrode, glassy carbon working electrode and a platinum mesh counter electrode.

Electron transfer properties of DSD-Fdm.

Because the redox potential of DSD-Fdm is comparable to that of natural ferredoxins, we tested the ability of DSD-Fdm to transfer an electron to a natural protein, oxidized cytochrome c. DSD-Fdm was reduced by sequential addition of sodium dithionite, monitoring the loss of absorbance at 410 nm, and stopping addition as soon as the signal stabilized.

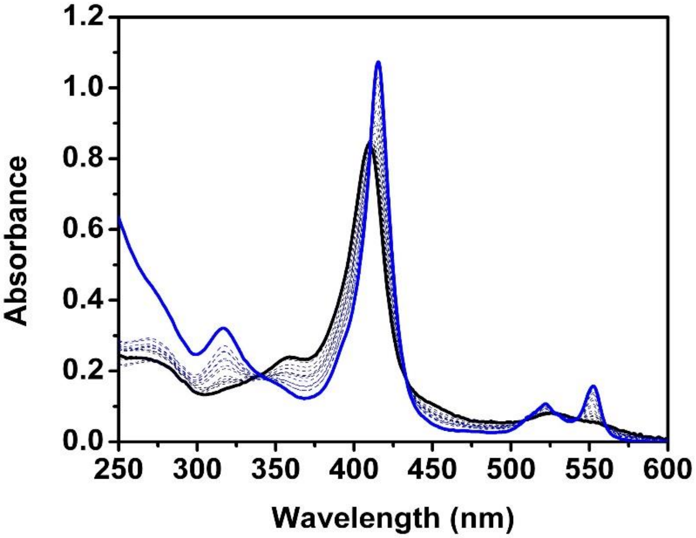

Figure 24. Reduction of cyt c550 by DS.-Fdm: UV-Vis monitored titration of reduced DSD-Fdm to a solution of air oxidized Cyt-C.

The reduced peptide was further purified to remove all excess dithionite, and titrated into an air-oxidized sample of Thermosynechococcus elongatus cytochrome c_{550}, while monitoring the reaction by UV-vis spectroscopy. We observed shifts of the Soret band (410 nm to 415 nm) and of the Q-bands (526 nm to 520 nm and 550 nm) that indicate reduction of the protein-bound heme (Figure 24). A plot of the change of absorbance at 415 nm as a function of molar equivalents of holo DSD-Fdm reveals that full reduction of the heme was achieved at a 0.74:1 molar ratio of DSD-Fdm/cyt c_{550}. (Figure S 29) This stoichiometry is reminiscent of the one-electron reduction processes typically mediated by natural bis-[4Fe-4S] cluster ferredoxins, and is consistent with the EPR spin quantification results, as incomplete reduction of the clusters would result in deviation of the ideal, 0.5:1 molar ratio for a 2 electron-carrying ferredoxin that mediates 1 electron reductions.[118,119,128,129]

Together with the similarity in redox potential, these results show that artificial proteins can interface effectively with natural ones to support redox reactivity.

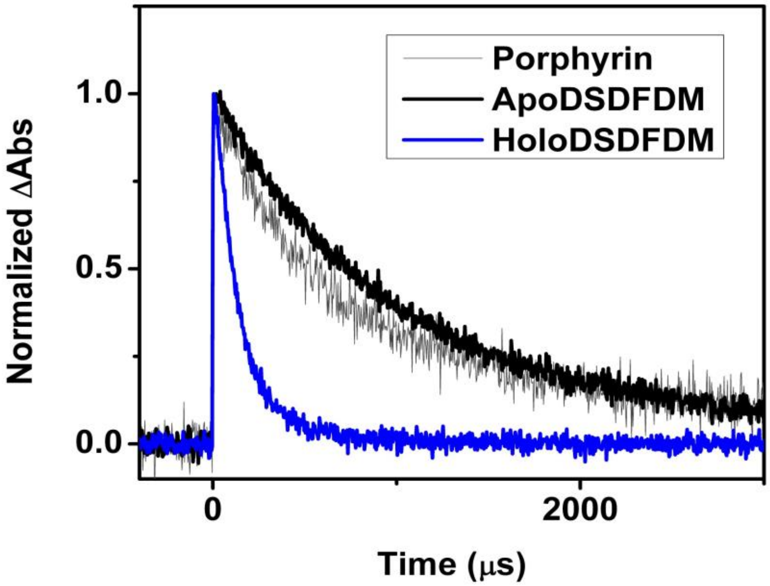

Figure 25**.** Normalized transient absorption kinetics of Zn-P alone (grey), with apo-protein (black), or holoprotein (blue) solutions. The porphyrin was excited at the 560 nm Q-band and probed at 450 nm.

De novo designed redox proteins have been proposed as functional parts of energy harvesting devices.[130-134] To investigate whether holo-DSD-Fdm could be used for this application, we investigated the interaction of a porphyrin photosensitizer with the oxidized cluster using laser flash photolysis. Ca. 15 μM solutions of zinc 5,10,15,20-tetrakis(4-diethyl 2-benzylmalonate) porphyrin (Zn-P) (Figure S 22) in deoxygenated buffer were excited at a Q-band (560 nm), and the triplet state lifetimes were probed via the transient absorption at 450 nm. We observed that samples containing either Zn-P only or Zn-P and apo-DSD-Fdm had similar triplet lifetimes, ca. 1400 μs, while in the presence of holo-DSD-Fdm the triplet lifetime of Zn-P was significantly shorter, ca. 100 μs (Figure 25). This quenching by a factor of ca. 14 signals electronic interactions between the zinc porphyrin and the iron-sulfur clusters. No signal for oxidized zinc porphyrin was detected at 650 nm.

The Zn-P triplet excited state quenching could occur via three mechanisms; triplet-triplet energy transfer, enhanced intersystem crossing (ISC), or photoinduced electron transfer. Photoinduced electron transfer is exergonic by only about 70 meV, based on the reduction potential for the cluster given above (-0.479 V vs SHE), the first oxidation potential of zinc tetraphenylporphyrin (1.04 V vs SHE), and the energy of the zinc tetraphenylporphyrin triplet state (1.59 eV).[135] Although no porphyrin radical cation was detected, photoinduced electron transfer cannot be completely ruled out because no porphyrin radical cation absorption would be detected if charge recombination were substantially more rapid than charge separation. Although the available data do not allow us to assign a mechanism for the quenching, all these possibilities require electronic interaction between the porphyrin and the cluster, which necessitates separations of only a few Å. Thus, the results show that external reagents can approach the clusters within the peptide closely enough for interesting and potentially useful energy and electron transfer interactions.

CONCLUSIONS

In summary, we designed a protein, DSD-Fdm, in which two [4Fe-4S] clusters are within 12 Å of one another, a distance biologically relevant for effective electron transfer. Both apo and holo-DSD-Fdm fold into stable dimers with high helical content. Cofactor binding induces a significant amount of stability towards chemical denaturation, as often seen in designed metalloproteins.[136,137] The redox potential of DSD-Fdm, -0.479 V vs SHE for the $[4Fe\text{-}4S]^{2+/1+}$ couple, is within the range typical of low-potential ferredoxins. We showed that DSD-Fdm can interface functionally with natural redox proteins by demonstrating stoichiometric electron transfer from reduced DSD-Fdm to oxidized cytochrome c. Further, we demonstrated that DSD-Fdm can interact electronically with a photoexcited dye. Compared to their natural counterparts, de novo designed proteins can be specifically tailored in terms of their redox potentials, stability, catalytic properties, protein-protein interactions and small molecule binding depending on the application desired.[138-146]

The results presented here support the use of de novo designed proteins as redox modules in various applications, ranging from components of artificial redox pathways in synthetic biology to parts of light-driven devices.

ASSOCIATED CONTENT

AUTHOR INFORMATION

Corresponding Author

* Giovanna Ghirlanda. Email: gghirlanda@asu.edu Tel.: (480)-965-6645.

Author Contributions

The manuscript was written through contributions of all authors. ‡These authors contributed equally.

ACKNOWLEDGMENT

No competing financial interests have been declared. This work was supported by the Center for Bio-Inspired Solar Fuel Production, an Energy Frontier Research Center funded by the U.S. Department of Energy, Office of Science, Office of Basic Energy Sciences under award Number DE-SC0001016.

ABBREVIATIONS

HBTU: *N,N,N′,N′*-Tetramethyl-*O*-(1*H*-benzotriazol-1-yl)uronium hexafluorophosphate, *O*-(Benzotriazol-1-yl)-*N,N,N′,N′*-tetramethyluronium hexafluorophosphate

Fmoc: Fluorenylmethyloxycarbonyl

HPLC: High performance liquid chromatography

MALDI-TOF-MS: Matrix-assisted laser desorption ionization time-of-flight mass spectrometry

SUPPORTING INFORMATION

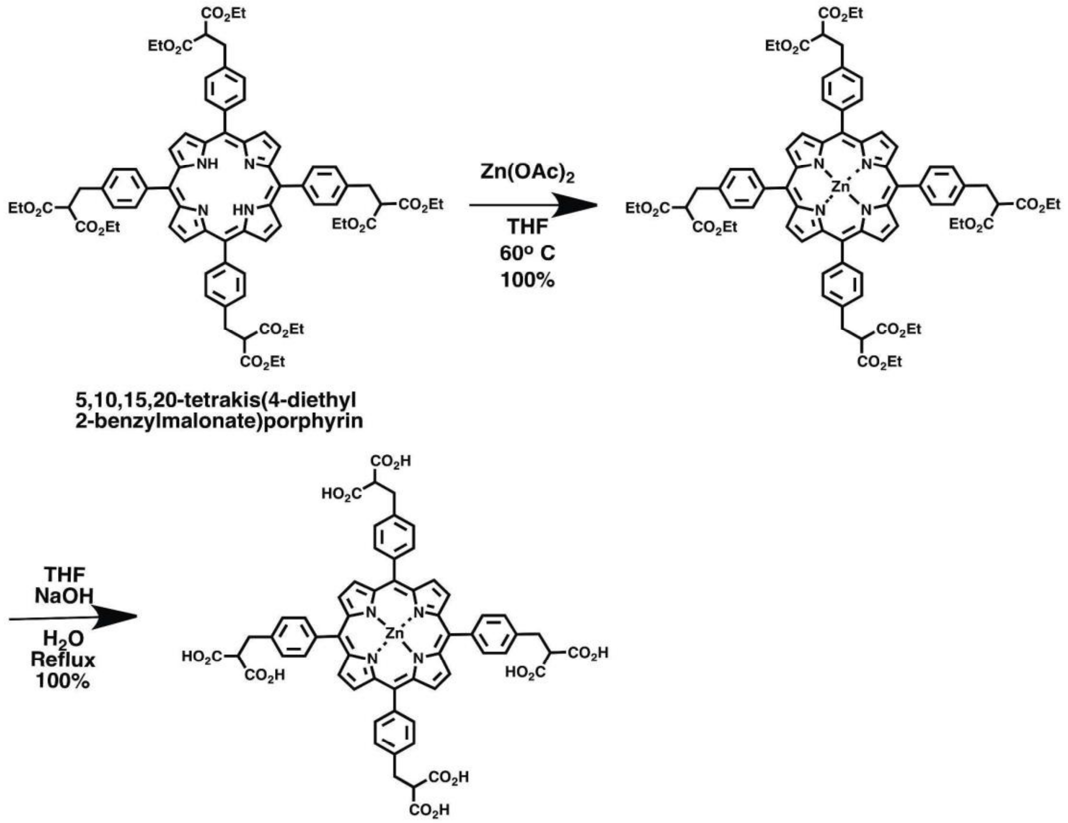

Figure S 22. Synthetic scheme for water-soluble porphyrin

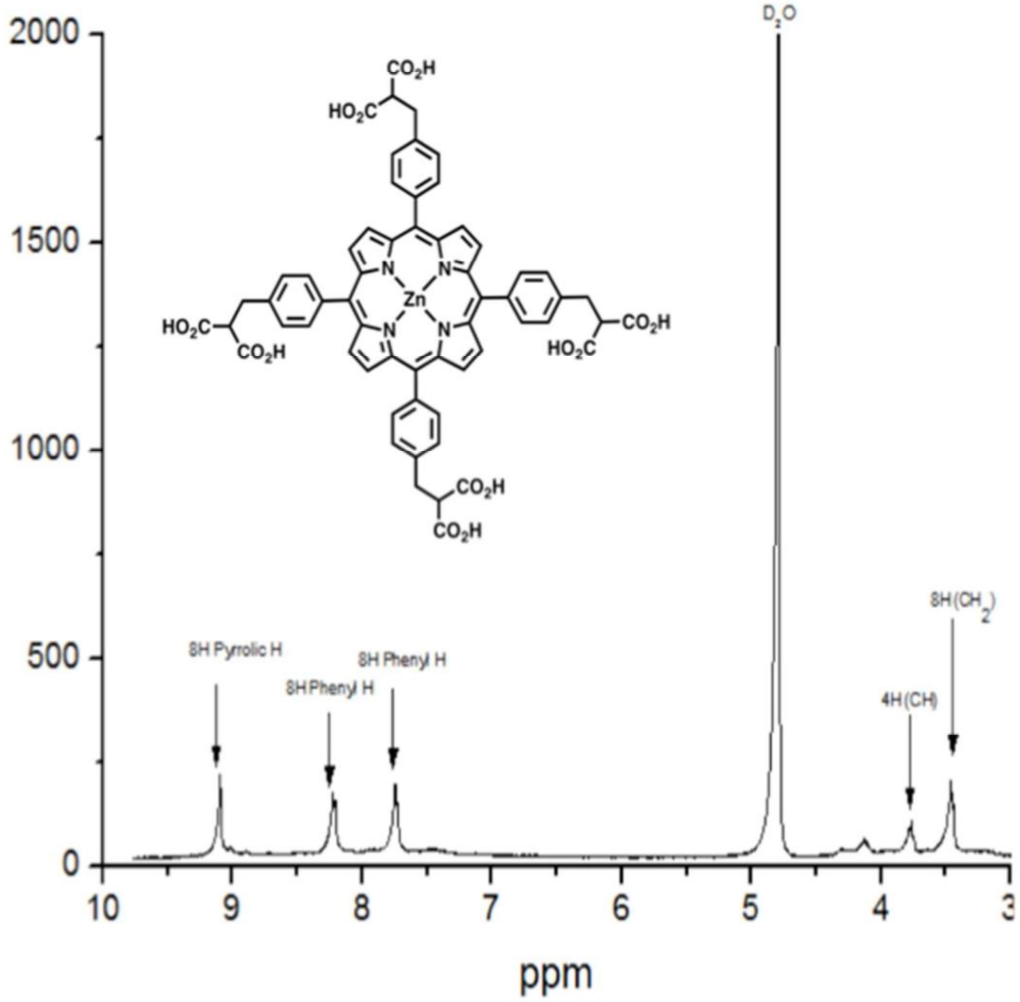

Figure S 23. ^{1}HNMR spectrum of the Zn(II)-5,10,15,20-tetrakis(2-benzylmalonic acid) porphyrin in D_2O. Spectra were obtained at 25 °C on a 400 MHz Varian spectrometer.

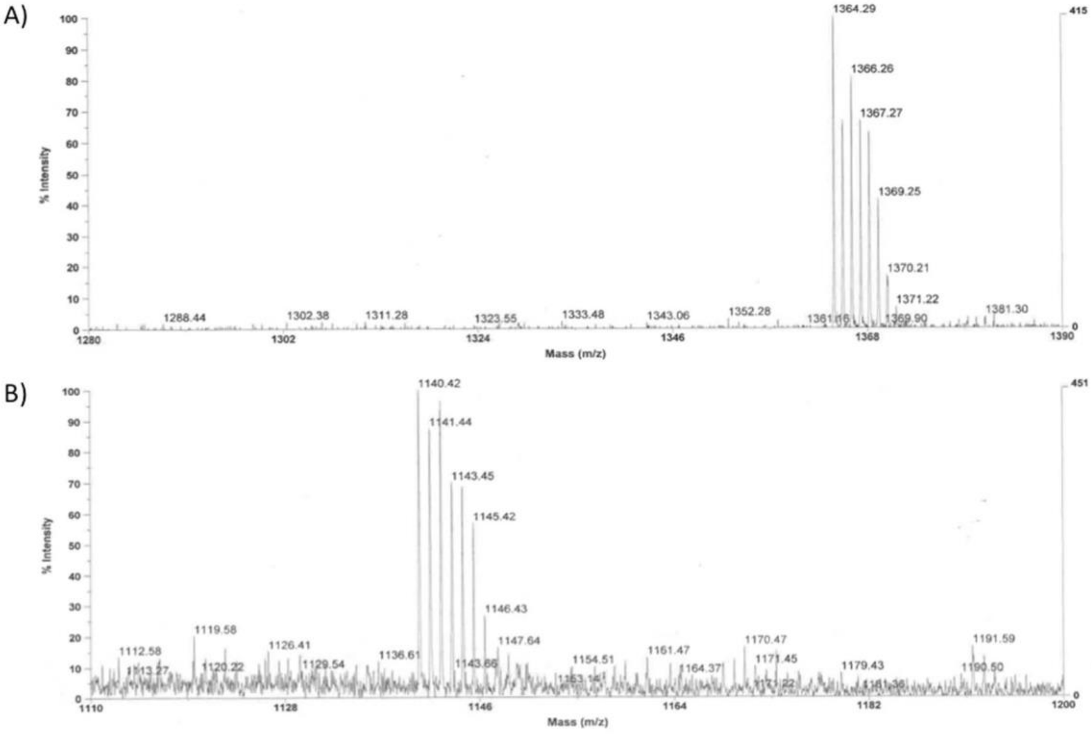

Figure S 24. MALDI-TOF spectra of Zn(II)-5,10,15,20-tetrakis(4-diethyl 2benzylmalonate) porphyrin before (A) and after (B) ester cleavage. Spectra were obtained utilizing α-cyano-4-hydroxycinnamic acid as a matrix with delayed extraction in positive reflector mode.

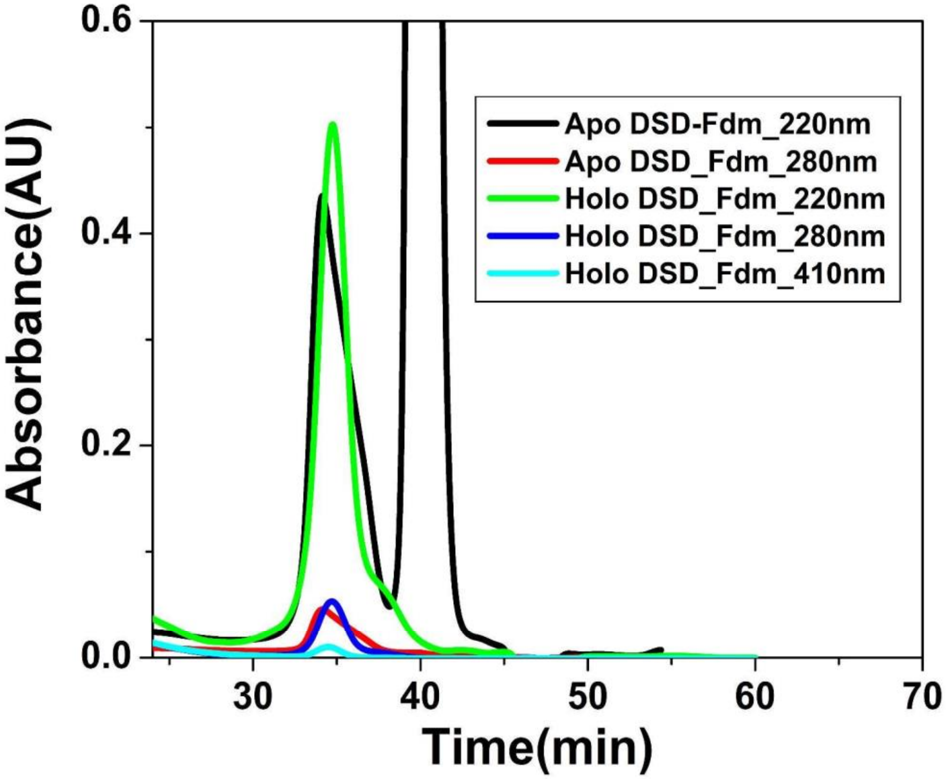

Figure S 25. Gel filtration chromatograms of apo DSD-Fdm and holo DSD-Fdm, with corresponding wavelengths in legend. Data were obtained on a G-25 gel filtration column in 100 mM Tris-HCl, pH 7.5. Apo peptide samples contained 50 molar excess of TCEP, which elutes in a large peak centered around 40 minutes (black trace).

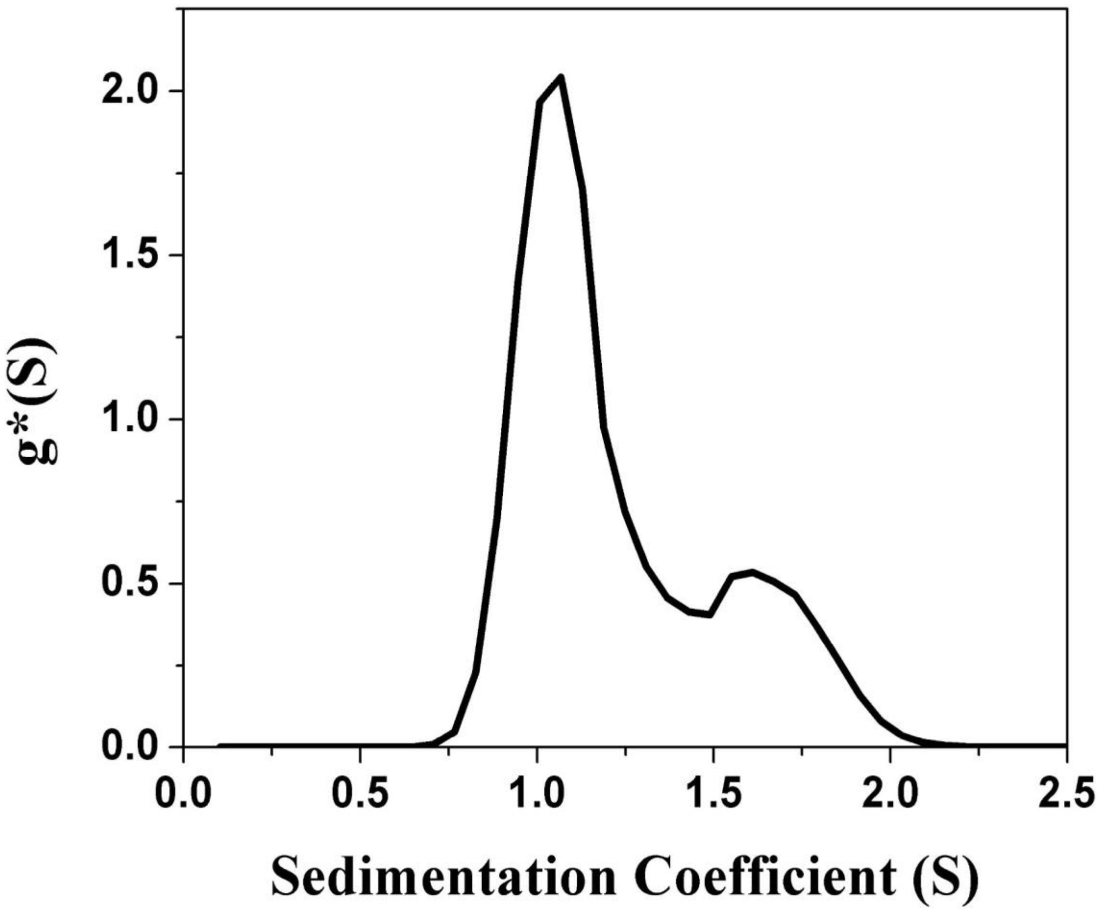

Figure S 26. Analytical ultracentrifugation of 100 µM apo DSD-Fdm, indicating a majority species with a MW of 13.3 KDa.

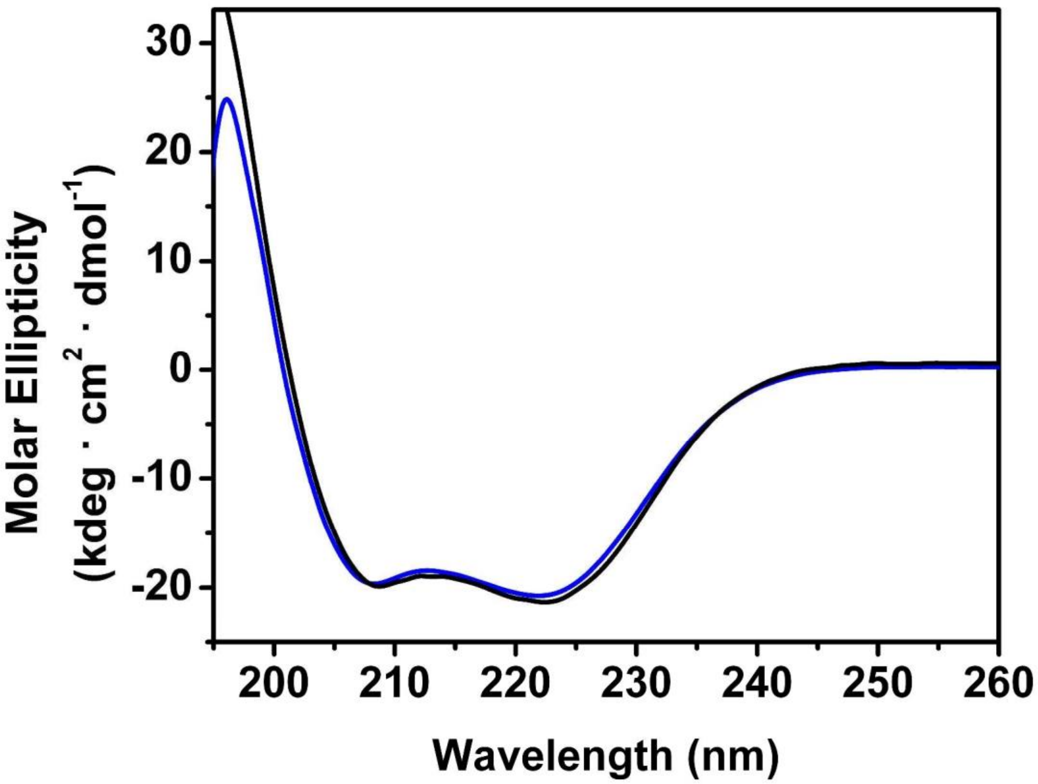

Figure S 27. CD spectra of apo (black) and holo (blue) DSD-Fdm in the far-UV range showing two minima at 222nm and 208nm. Proteins were at 50 µM in 10 mM TrisHCl, pH 7.5. Apo peptide contained a 50 molar excess of TCEP.

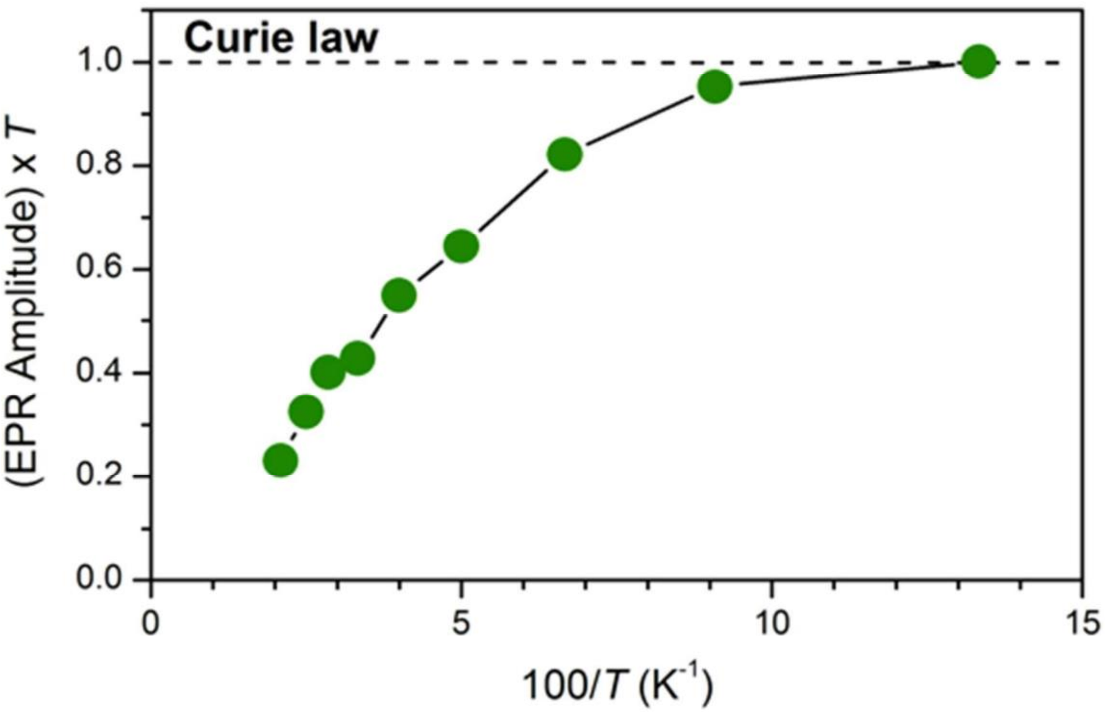

Figure S 28. Temperature dependence of the EPR amplitude under non-saturating conditions (mw power, 0.2 μW). The horizontal line corresponds to the temperature dependence described by the Curie Law (no low-lying excited states).

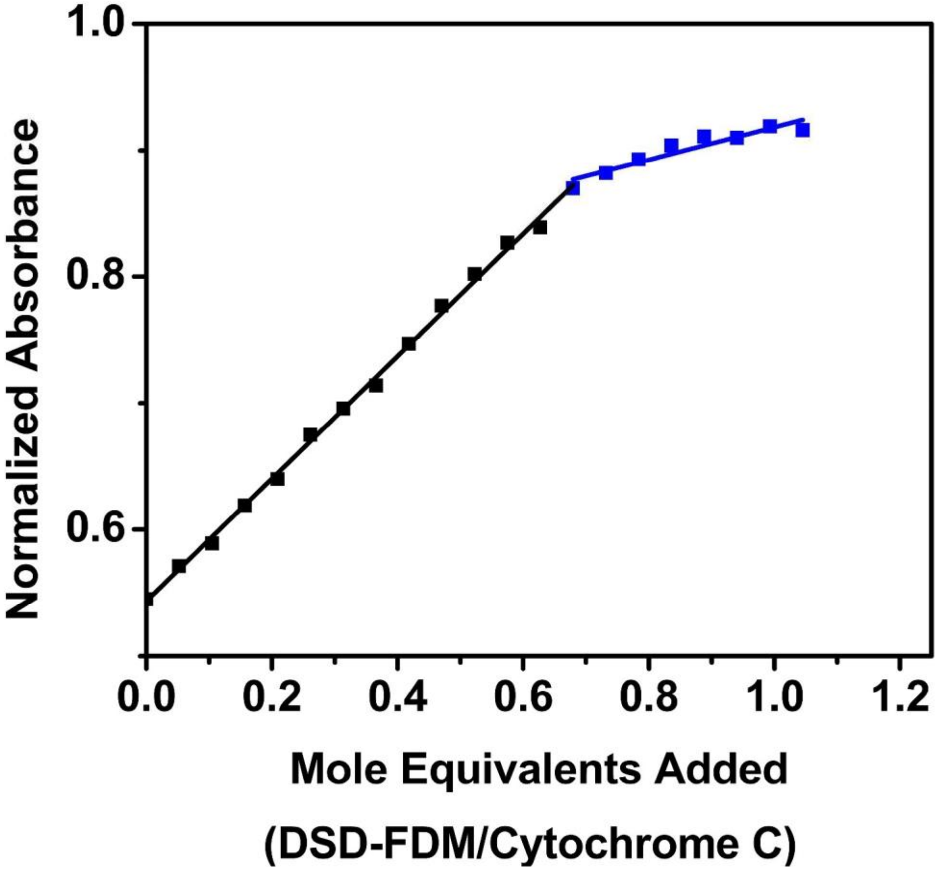

Figure S 29. Change in absorbance at 415 nm as a function of molar equivalents DSDFdm added during the reduction of cytochrome c_{550}. Values were normalized to isobestic point of the titration.

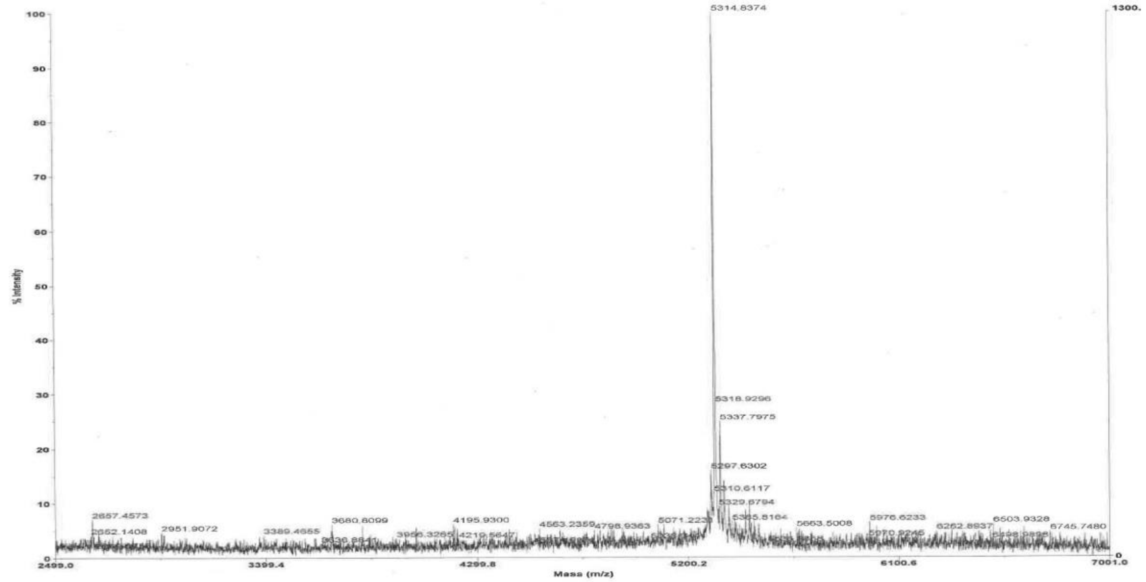

Figure S 30. MALDI-TOF spectra of apo DSD-Fdm, utilizing α-cyano-4hydroxycinnamic acid as matrix with delayed extraction in positive reflector mode. Calculated mass for the peptide was 5310.

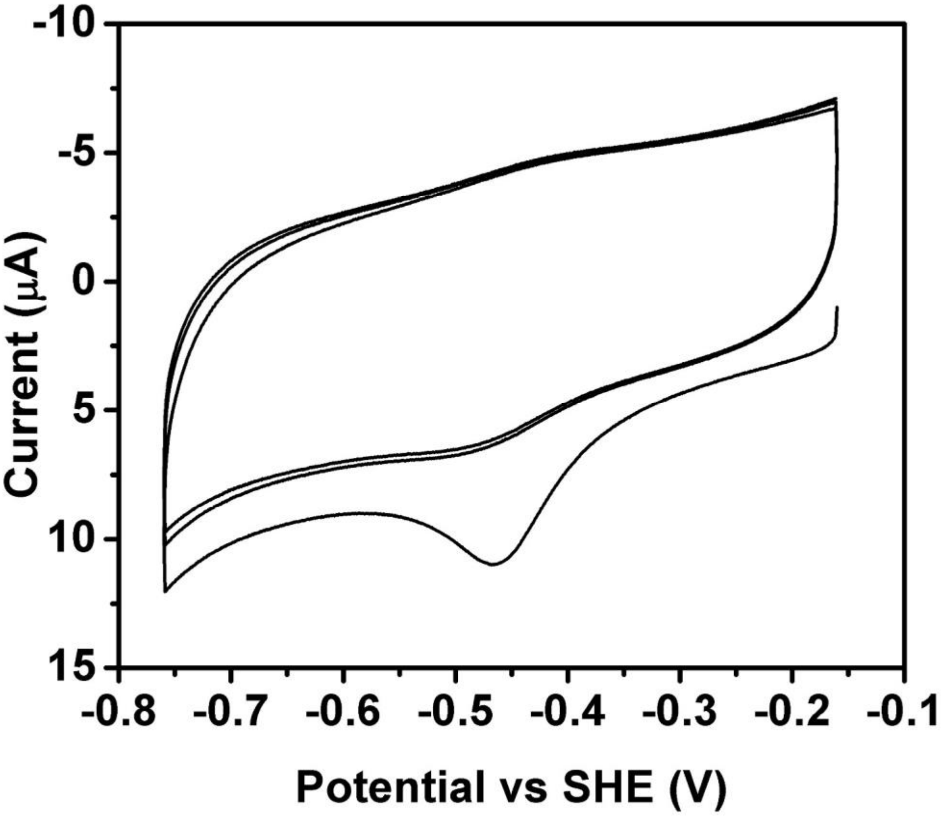

Figure S 31. DSD-Fdm response to multiple cyclic voltammetry sweeps. Scan 1 exhibits a large magnitude reduction, followed by equilibration to quasi-reversible behavior. Conditons are 3.5 mM neomycin, 100 mM Tris-HCl, 100 mM sodium chloride, pH 7.5, solution at 100 mV/s scan rate with a Ag/AgCl reference electrode, glassy carbon working electrode and a platinum mesh counter electrode.

Chapter 2.4 A NEW ANCHORING GROUP FOR SEMICONDUCTING OXIDES

Imidodiacetic Acid: An Effective Anchoring Group for Metal Oxides

Chelsea L. Brown, Manuel J. Llansola-Portoles, Antonio Arrigo, Gerdenis Kodis, Jesse J. Bergkamp, Thomas A. Moore, Devens Gust, Ana L. Moore

A manuscript with the subject of this chapter is presently in preparation.

> My contribution to this work is the synthesis of the porphyrins, gathering data, writing the manuscript, and assisting with the editing process.

Introduction

Human energy needs are projected to triple by 2100,[7] meaning there is an imminent need for alternative, clean energy sources. The abundance of solar energy has led to dominance of photovoltaics on the alternative energy market.[9] Unfortunately, presently photovoltaics are costly and, although they produce electricity, they are unable to directly store energy for future use.[147] Development of solar-to-fuel photoelectrochemical tandem cells may be one way to remedy this problem by storing energy in chemical bonds for future use.[9,37] Solar-to-fuel photoelectrochemical tandem cells are often referred to as artificial photosynthetic devices. Artificial photosynthesis aims to mimic the underlying principles of natural photosynthesis to utilize sunlight to produce a storable fuel, such as hydrogen gas.[148] There are two components to these devices, a water splitting cell and a dye-sensitized solar cell (DSSC). DSSCs are similar to photovoltaics, but use organic dyes to sensitize nanoparticulate semiconductor thin films, making them more cost effective.[10]

DSSCs are used in tandem with a water splitting cell in order to help increase the amount of the solar spectrum that is used to drive the redox process, increasing the efficiency of the device. The advantage of artificial photosynthesis over biofuels is that the energy demand could be met without interfering with the bioavailable net primary production.[21] These devices could be placed in areas that have already been developed, therefore leaving the global ecosystem untouched. However, over the last two decades, solar-to-electric conversion efficiencies of DSSCs have only improved from 10% to 13%.[23,39,149,150]

Artificial photosynthetic devices and DSSCs both require photoanodes that absorb photons, generating electrons in the system. The efficiency of the photoanode is related to (i) the nature of the chromophore linked, and (ii) to the electronic communication between the chromophore and the electrode. Concerning chromophores, a broad range of species have been investigated.[16,148,151-157] Porphyrins are good candidates because the aromaticity of the macrocycle provides a stable organic molecule that absorbs a broad spectrum of visible light and does not degrade in aqueous solutions. The electronic communication between chromophore and electrode influences the forward and backward electron transfer processes between them and the electron-transfer efficiency of a photoanode is highly dependent on the attachment of the chromophore to the underlying semiconductor.[158]

The attachment of dyes to the metal oxide surface is a key step in the constructions of hybrid systems.[159] Creating strong covalent bonds between the sensitizers (dyes) and the surface of the metal oxide offer several advantages, namely: increasing the surface coverage, improving electronic coupling between the excited dye’s occupied orbitals and the conduction band of the metal oxide, enhancing stability and raising the performance.[160] Suitable anchors for a DSSC and water-splitting photoanodes must provide strong chemical bonding between the molecular species and the bulk surface and should also be stable under both aqueous and oxidative conditions. While many linkers have been studied, carboxylic acids are the most common anchoring group due to their ease of synthesis, effective attachment to semiconductors, and fast electron injection rates.[151-153,158,160-167]

The carboxylic acid anchoring group is proposed to attach to metal oxides via a monodentate or bidentate linkage[153] and promote electronic coupling between the excited dye and the conduction band of the semiconductor.[152] Unfortunately, over time, carboxylic acids leech from the surface, and the stability is limited to a small pH range in aqueous media. Phosphonic acids are more stable in aqueous media than carboxylic acids, but have slower electron injection rates.[165-167] Other linkers that have been explored include silanes, malonates, acetylacetonates, catecholate, and recently, hydroxamates,[122,152,166] [168] none have proven to be both stable on the surface of metal oxides and capable of high efficiency electron transfer.

In this paper, a new anchoring group, imidodiacetic acid (IDAA), has been utilized on porphyrins with widely disparate reduction potentials (Figure 26). Iminodiacetic acid is commonly used as a chelating agent for metal ions,[169-173] and recently, graphene oxide,[174] thus it was thought that an analog, IDAA, could be used to chelate metal oxides. We studied the ability of IDAA as an anchoring group for the electron injection into metal oxides, under electrochemical and photophysical investigations. The IDAA porphyrins are directly compared to the same porphyrins bearing carboxylic acid anchoring groups (Figure 26). All four porphyrin compounds have been attached to SnO_2 nanoparticles for the photophysical measurements. The direct comparison of IDAA with simple carboxylic acids shows that IDAA could in principle improve the efficiency of DSSCs and other artificial photosynthetic devices.

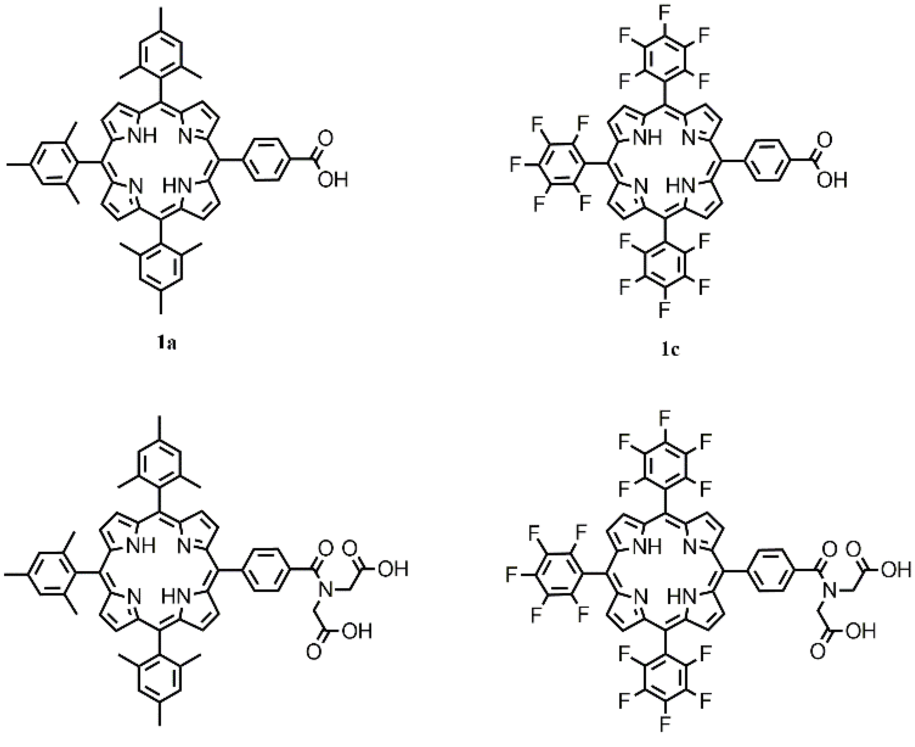
1a

1c

1b

1d

Figure 26. The structures of the four porphyrins examined in this study. Compounds **1b** and **1d** contain the new imidodiacetic acid anchoring group and compounds **1a** and **1c** contain the common carboxylic acid anchoring group.

Methods

Materials. Reagents were used as received. Anhydrous thionyl chloride, benzene, pyridine, tetrahydrofuran (THF), methanol (MeOH), and oxalyl chloride were all purchased from Sigma Aldrich. Pyrrole was freshly distilled under vacuum. Thin layer chromatography plates (250 μm) were purchased from Analtech, Inc. Silica gel (SiliaFlash

F60 40-63 μm) used for column chromatography was purchased from SILICYCLE. Tin tetrachloride (≥97.0%) and ethyl acetate (99.5%) were purchased from Sigma-Aldrich and used as received. All solvents used for column chromatography were distilled before use.

Instruments and Measurements. *Structural Characterization.* Mass spectra were obtained with a Voyager DE-STR matrix-assisted laser desorption/ionization time-of-flight spectrometer (MALDI-TOF), equipped with a 60 Hz laser,using α–cyano-4-hydroxycinnamic acid (αCN), sinapinic acid (SA), or (1E, 3E)-1,4-diphenylbuta-1,3-diene (DPB) as a matrix. The reported mass is the most abundant isotope observed. Calculated values are listed after the experimental result for comparison. The ^{1}H-NMR spectra were taken on a Varian spectrometer at 400 MHz. Samples were prepared using deuterated solvents and with 0.03% tetramethylsilane as an internal standard.

UV-Vis Spectroscopy. UV-vis absorption spectra were acquired on a Shimadzu UV2100U UV-visible spectrometer using a 1 cm quartz cuvette. Measurements were taken at ambient temperature in methanol. Steady-state fluorescence was measured using a Photon Technology International MP-1 spectrometer and was corrected for detection system response. Excitation wavelength was 425 nm, with 1.5 mm slits.

Electrochemical Measurements. Cyclic voltammetry was performed using a CH Instruments 760D potentiostat with the software provided by the company. A glassy carbon working electrode, a Ag+/Ag quasi-reference, and a Pt wire counter electrode were used for the measurements. Ferrocene was used to calibrate the quasi-reference. Dichloromethane was used as the solvent with 0.1 M tetrabutylammoniumhexafluorophosphate as the supporting electrolyte.

*High Resolution Transmission Electron Microscopy***.** TEM micrographs were collected using a Philips CM200 TEM at 200kV, Cs 1.2 mm, PTP Resolution: 0.25nm Focused Probe: 0.5nm and Imaging Modes: TEM/STEM. TEM micrographs were analyzed using Digital Micrograph™ software.[77]

Time resolved absorption. Femtosecond to nanosecond transient absorption measurements were acquired with a kilohertz pulsed laser source and a pump-probe optical setup. Laser pulses of 100 fs at 800 nm were generated from an amplified, mode-locked titanium sapphire kilohertz laser system (Millennia/Tsunami/Spitfire, Spectra Physics). Part of the laser pulse energy was sent through an optical delay line and focused onto a 3 mm sapphire plate to generate a white light continuum for the probe beam. The remainder of the pulse energy was used to pump an optical parametric amplifier (Spectra Physics) to generate excitation pulses, which were selected using a mechanical chopper. The white light generated was then compressed by prism pairs (CVI) before passing through the sample. The polarization of the pump beam was set to the magic angle (54.7°) relative to the probe beam and its intensity was adjusted using a continuously variable neutral density filter. The white light probe was dispersed by a spectrograph (300 line grating) onto a charge-coupled device (CCD) camera (DU420, Andor Tech.). The final spectral resolution was about 2.3 nm for over a nearly 300 nm spectral region. The instrument response function was ca. 100 fs. The decay-associated spectra (DAS) were obtained by fitting globally the transient absorption kinetic traces over a selected wavelength region simultaneously as described by equation (1) (parallel kinetic model).[79]

$$\Delta A(\lambda,t) = \sum_{i=1}^{n} A_i(\lambda)\exp(-t/\tau_i) \qquad (1)$$

where $\Delta A(\lambda,t)$ is the observed absorption change at a given wavelength at time delay t and n is the number of kinetic components used in the fitting. A plot of $A_i(\lambda)$ versus wavelength is called a DAS and represents the amplitude spectrum of the ith kinetic component, which has a lifetime of τ_i. Random errors associated with the reported lifetimes obtained from transient absorption measurements were typically ≤ 5%. Rigorous analysis of time resolved emission and absorption data in a non-homogeneous system requires the use of a model which considers a distribution of multi-exponential decays to describe the kinetics of each transient species and thus accounts for the distribution of available environments in the heterogeneous system. In our analysis we used the minimum number of exponential components that adequately fitted the experimental data within the experimental error. Thus it is likely that the reported decay components correspond to a weighted mean value of the actual distribution of constants associated with each species.

Synthesis.

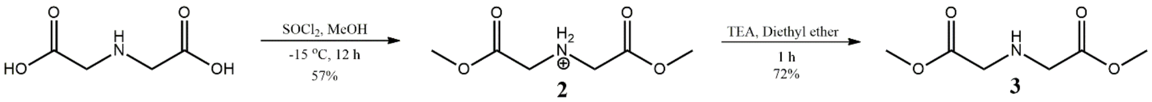

Scheme 1. Synthesis of the iminodimethylester compound.

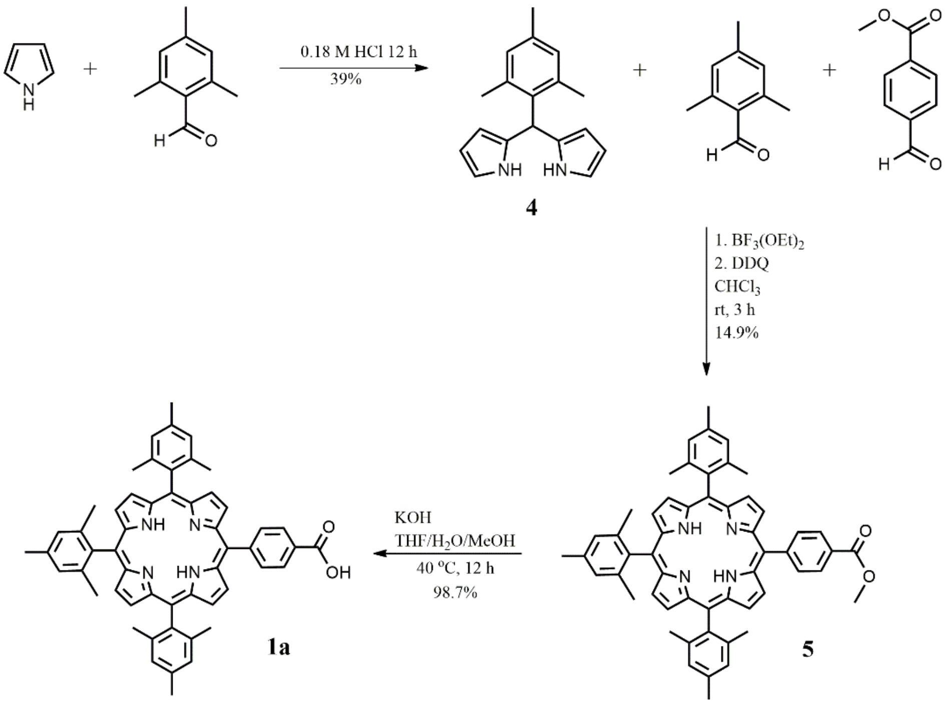

Scheme 2. Synthesis of compound **1a**.

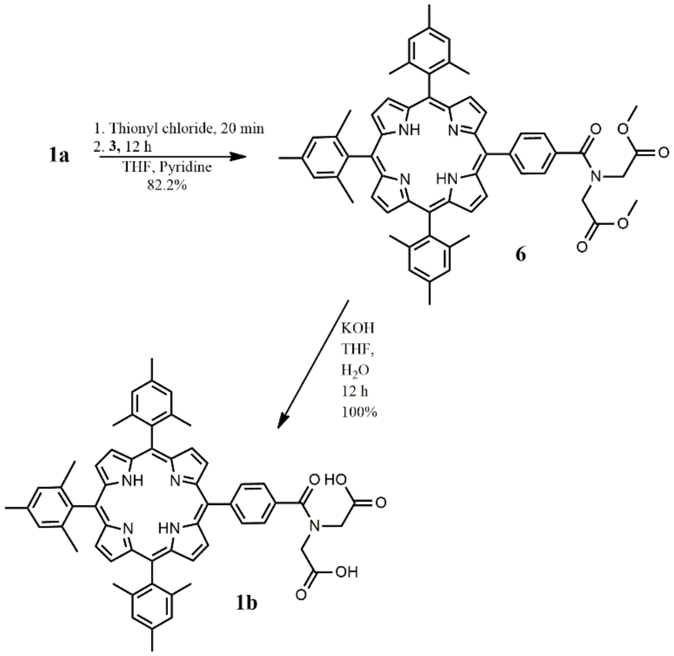

Scheme 3. Synthesis of compound **1b** from compound **1a**.

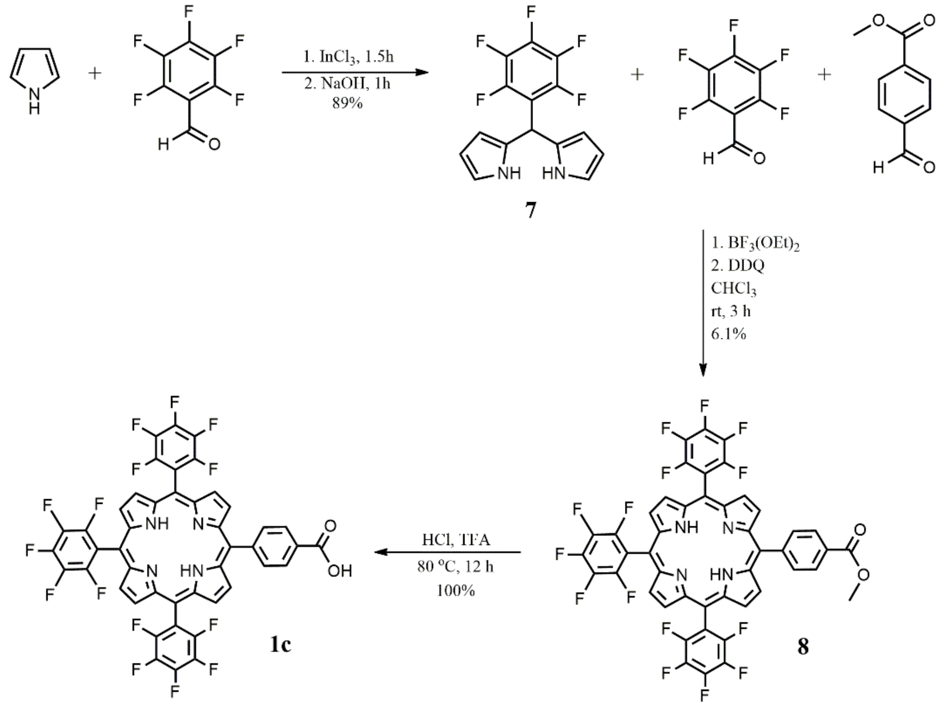

Scheme 4. Synthetic scheme for compound **1c**.

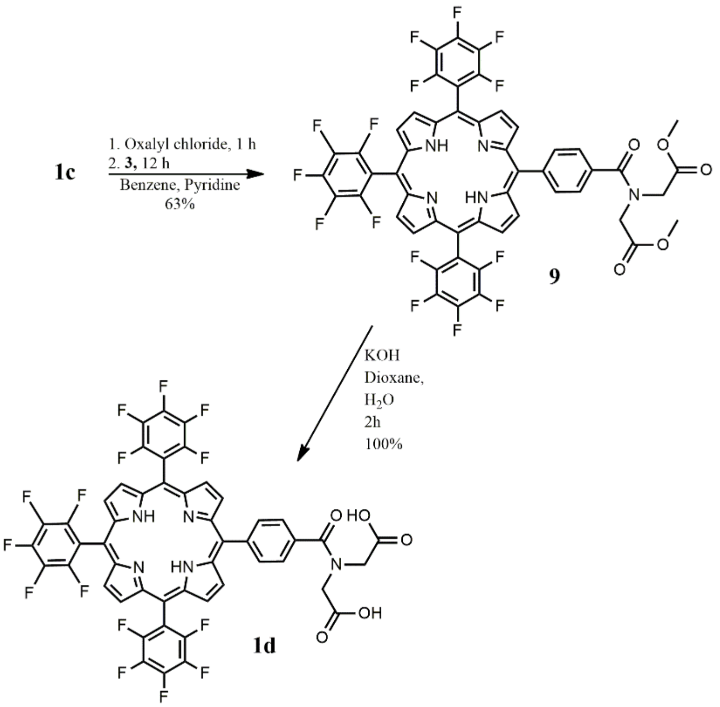

Scheme 5. Synthetic scheme for compound **1d**.

Bis(2-methoxy-2-oxoethyl)ammonium chloride (**2**). The iminodimethylester salt was prepared by dissolving iminodiacetic acid (50 g, 0.38 mol) in methanol (500 mL). The solution was cooled down to -15 ºC and thionyl chloride (115 mL, 1.13 mol) was added drop-wise along with vigorous stirring. The reaction mixture was allowed to warm to room temperature overnight. The precipitate was filtered and rinsed with ice cold acetone. The resulting white solid (35 g, 0.22 mol, yield 57%) was stored in a desiccator. ^{1}H-NMR δ ppm (D_2O): 4.58 (s, 2H), 4.14 (s, 4H), 3.84 (s, 6H).

Iminodimethylester or **dimethyl-2,2`-azanediylacetate** (**3**). Compound **3** was prepared by dissolving **2** (10 g, 0.062 mol) in diethyl ether (100 mL) and adding triethylamine (TEA) (20 mL). The reaction was stirred at room temperature for 1 hour and filtered to remove TEA salts. The filtrate was concentrated to yield a yellow oil (7.5 g, 0.047 mol, yield 76%): ^{1}H-NMR δ ppm ($CDCl_3$): 3.72 (s, 6H), 3.47 (s, 4H).

5-(Mesityl)dipyrromethane (**4**). Mesiyl-DPM was synthesized by modifying a previously published procedure. [175] Freshly distilled pyrrole (14.04 mL, 0.202 mol) and mesitaldehyde (10 g, 0.067 mol) was added to HCl (100 mL of 0.18 M). The reaction was stirred at room temperature for 12 h. The mixture was initially purified using column chromatography (hexanes/DCM 1:1) then further purified by crystallization in ethanol/water (4:1). The first crop of crystals gave a white solid (1.97 g, 7.45 mmol), the second crop gave a yellow solid (3.56 g, 13.4 mmol), and the third crop gave a brown solid (1.45 g, 5.49 mmol). Yield of pure compound was 11.1%. ^{1}H-NMR δ ppm ($CDCl_3$): 7.94 (s, 2H), 6.87 (s, 2H), 6.67 (m, 2H), 6.18 (m, 2H), 6.01 (m, 2H), 5.93 (s, 1H), 2.28 (s, 3H), 2.07 (s, 6H).

5-(Methyl-4-carboxyphenyl)-10,15,20-tris(2,4,5-trimethylphenyl)porphyrin (**5**). In a 1000 mL round-bottom flask, **4** (2.0 g, 7.6 mmol), mesitaldehyde (0.562 g, 3.79 mmol), and methyl 4-formylbenzoate (0.622 g, 3.79 mmol) were dissolved in chloroform (750 mL) with 1.0% ethanol by volume. The solution was purged with argon for 30 min and then BF_3OEt_2 (0.35 mL) was added and the mixture was allowed to stir for 2 h. Next, 2,3-dichloro-5,6-dicyano-1,4-benzoquinone (DDQ) (2.32 g, 10.23 mmol) was added and the reaction stirred for 12 h. This mixture was concentrated under reduced pressure to yield a crude purple solid. The mixture was extracted using ethyl acetate and water. The organic layer was dried over sodium sulfate, filtered, and concentrated. Silica gel column chromatography was used to purify the mixture using hexane/DCM (2:3) as the eluent yielding compound **5** (450 mg, 0.563 mmol, yield 14.9%). ^{1}H-NMR δ ppm ($CDCl_3$): 8.71 (m, 4H), 8.64 (s, 4H), 8.42 (d, 2H), 8.29 (d, 2H), 7.38 (s, 6H), 4.11 (s, 3H), 2.63 (s, 9H), 1.85 (s, 18H), -2.61 (s, 2H). MALDI-TOF: *m/z* obsd 798.56 calc for $C_{55}H_{50}N_4O_2$ 798.39.

5-(4-Carboxyphenyl)-10,15,20-tris(2,4,5-trimethylphenyl)porphyrin (**1a**). In a 500 mL round-bottom flask, compound **5** (250 mg, 0.313 mmol) was dissolved in THF (200 mL). Separately, KOH (26 mg, 0.47 mmol) was dissolved in methanol (10 mL) and water (2 mL). The basic solution was added to the round-bottom flask and the reaction was allowed to stir at 40 ºC for 12 h. The THF was evaporated and water was acidified with citric acid. The product was extracted with DCM and the organic layer was dried over sodium sulfate, filtered, and concentrated under reduced pressure. The compound was purified by silica gel column chromatography (hexane/DCM 2:3) yielding compound **1a** (242 mg, 0.309 mmol, yield 98.7%). ^{1}H-NMR δ ppm ($CDCl_3$): 8.65 (m, 6H), 8.57 (d, 2H), 8.44 (d, 2H), 8.26 (d, 2H), 7.21 (s, 6H), 2.55 (s, 9H), 1.78 (s, 18H) -2.62 (s, 2H). MALDI-TOF: *m/z* obsd 784.36 calc for $C_{54}H_{48}N_4O_2$ 784.38.

5-(4-(Dimethyl-2,2'-(formylazanediyl)diacetate)phenyl)-10,15,20-tris(2,4,5-trimethylphenyl)porphyrin (**6**). In a dry, two-neck flask, compound **1a** (150 mg, 0.191 mmol) was dissolved in anhydrous THF (50 mL) and anhydrous pyridine (10 mL). The solution was purged with argon for 20 min and then thionyl chloride (0.03 mL, 45.5 mg, 0.382mmol) was added. The reaction stirred at room temperature for one hour then evaporated to dryness while under argon. Compound **3** (154 mg, 0.955 mmol), dissolved in THF (30 mL) and pyridine (10 mL), was added to the reaction through a syringe. The reaction was left stirring under an argon atmosphere to stir for 12 h. The solvents were removed under reduced pressure and the product was extracted using ethyl acetate and water. The organic phase was dried over sodium sulfate, filtered, and the solvent was evaporated. The mixture was purified using silica gel column chromatography (ethyl acetate/DCM 1:10). The isolated product was a purple solid (152 mg, 0.157 mmol, yield 82.2%). ^{1}H-NMR δ ppm ($CDCl_3$): 8.83 (d, 2H), 8.65 (d, 2H), 8.61 (s, 4H), 8.30 (d, 2H), 7.76 (d, 2H), 7.36 (m, 6H), 4.49 (d, 4H), 3.78 (d, 6H), 2.52 (s, 9H), 1.78 (s, 18), -2.67 (s, 2H). MALDI-TOF: *m/z* obsd 927.45 calc for $C_{60}H_{57}N_5O_5$ 927.44.

5-(4-(2,2'-(Formylazanediyl)diacetic acid)phenyl)-10,15,20-tris(2,4,5-trimethylphenyl)porphyrin (**1b**). Compound **1b** was prepared by dissolving compound **6** (100 mg, 0.11 mmol) in THF (100 mL). Separately, KOH (30 mg, 0.310 mmol) was dissolved in water (8 mL) and then added to the porphyrin solution. The reaction was allowed to stir overnight for 12 h. The product was extracted with ethyl acetate and water acidified with citric acid. The organic layer was dried over sodium sulfate, filtered, and the solvent was evaporated under reduced pressure, yielding a purple solid. (97 mg, 0.108 mmol, yield 100%). MALDI-TOF: *m/z* obsd 899.63 calc for $C_{58}H_{53}N_5O_5$ 899.40.

5-(Pentafluorophenyl)dipyrromethane (**7**). 5-(Pentafluorophenyl)dipyrromethane was synthesized by modifying a previously published procedure.[175] In a dry 500 mL three-neck round bottom flask, pentafluorobenzaldehyde (10 g, 0.05 mol) was dissolved in freshly distilled pyrrole (210 mL, 3.02 mol). The solution was purged with argon for 20 min, and $InCl_3$ (1.12 g, 0.0051 mol) was added. After the reaction stirred in the dark for 1.5 h, NaOH (10 g, 0.25 mol) was added and the solution stirred for additional hour. The mixture was filtered through celite and rinsed with fresh pyrrole. The excess pyrrole was distilled off and collected for future use. The resulting gray solid was purified using silica gel column chromatography (hexane/DCM/ethyl acetate 10:2:1). The compound was further purified by crystallization in ethanol/water (4:1). The first crop produced white crystals (6.65 g, 0.0213 mol). The second crop gave light brown crystals (3.2 g, 0.0102 mol). The final crop gave brown crystals (4.6 g, 0.0147 mol). The total yield for this step was 14.15 g of compound **7** (0.0453 mol, yield 89%). ^{1}H-NMR δ ppm ($CDCl_3$): 8.14 (s, 2H), 6.73 (q, 2H), 6.16 (q, 2H), 6.02 (s, 2H), 5.90 (s, 1H).

5-(Methyl-4-formylphenyl)-10,15,20-tris(pentafluorophenyl)porphyrin (**8**). Compound **8** was prepared by dissolving compound **7** (2.0 g, 6.4 mmol), methyl-4-formyl benzaldehyde (0.525 g, 3.2 mmol) and pentafluorobenzaldehyde (0.627 g, 3.2 mmol) in chloroform (750 mL) with 1.0% ethanol by volume. The solution was purged with argon for 30 min, then BF_3OEt_2 (0.35 mL) was added and the reaction was allowed to stir at room temperature for 2 h. The color changed from clear to pink and 2,3-dichloro-5,6-dicyano-1,4-benzoquinone (1.96 g, 8.6 mmol) was added. The reaction proceeded for 12 h. The solvent was removed under reduced pressure and the product was extracted with DCM and water. The organic layer was dried over sodium sulfate, filtered, and concentrated under reduced pressure. The compound was purified using silica gel column chromatography (hexanes/DCM 2:3), to yield the final product (0.184 g, 0.195 mmol, yield 6.1%). ^{1}H-NMR δ ppm ($CDCl_3$): 8.90 (m, 6H), 8.84 (d, 2H), 8.48 (d, 2H), 8.30 (d, 2H), 4.13 (s, 3H), -2.86 (s, 2H). MALDI-TOF: *m/z* obsd 942.75 calc for $C_{46}H_{17}F_{15}N_4O_2$ 942.11.

5-(4-Carboxyphenyl)-10,15,20-tris(pentafluorophenyl)porphyrin (**1c**). The acid porphyrin was prepared by dissolving compound **8** (100 mg, 0.106 mmol) in TFA (20 mL) and then adding HCl (40 mL of 12 M). The reaction was refluxed at 80 ºC for 12 h, then neutralized with a saturated solution of sodium bicarbonate in water. The product was extracted with ethyl acetate and the organic layer was dried over sodium sulfate, filtered, and concentrated under reduced pressure to yield a purple solid (97.5 mg, 0.105 mmol, yield 99%). ^{1}H-NMR δ ppm ($CDCl_3$): 8.86 (m, 6H), 8.77 (s, 2H), 8.51 (d, 2H), 8.30 (d, 2H), -2.92 (s, 2H). MALDI-TOF: *m/z* obsd 928.49 calc for $C_{45}H_{15}F_{15}N_4O_2$ 928.10.

5-(4-(Dimethyl-2,2'-(formylazanediyl)diacetate)phenyl)-10,15,20-tris(pentafluorophenyl)porphyrin (**9**). In a dry, 250 mL round-bottom flask, compound **1c** (80 mg, 0.086 mmol) was dissolved in anhydrous benzene (100 mL) and anhydrous pyridine (10 mL). The solution was purged with argon for 20 min, to this was added oxalyl chloride (0.15 mL, 1.72 mmol). The reaction was allowed to stir for 45 min and the excess oxalyl chloride was evaporated off under reduced pressure. The reaction was kept under argon and compound **3** (69.3 mg, 0.43 mmol) dissolved in benzene was added. The reaction continued for 12 h, then the solvent was evaporated under reduced pressure. The mixture was dissolved in ethyl acetate and extracted with water. The organic phase was dried over sodium sulfate, filtered, and concentrated under reduced pressure. The product was purified by silica gel column chromatography (DCM/ethyl acetate 1:1). The final product was a purple solid (61 mg, 0.057 mmol, yield 66.3%). ^{1}H-NMR δ ppm ($CDCl_3$): 8.92 (m, 6H), 8.50 (d, 2H), 8.21 (d, 2H), 7.91, (d, 2H), 4.53 (d, 4H), 3.88 (d, 6H), -2.86 (s, 2H). MALDI-TOF: *m/z* obsd 1071.31 calc for $C_{51}H_{24}F_{15}N_5O_5$ 1071.15.

5-(4-(2,2'-(Formylazanediyl)diacetic acid)phenyl)-10,15,20-tris(pentafluorophenyl)porphyrin (**1d**). Compound **1d** was prepared by dissolving compound **9** (50 mg, 0.0442 mmol) in dioxane (50 mL). Separately, KOH (7.5 mg, 0.133 mmol) was dissolved in water (1 mL) and added to the porphyrin solution. The reaction was allowed to stir vigorously for 12 h at room temperature. The dioxane was removed under reduced pressure and the product was extracted using ethyl acetate and water acidified with citric acid. The organic layer was dried over sodium sulfate, filtered, and concentrated under reduced pressure. The product was purified by silica gel column chromatography (acetic acid/methanol/acetone 1:5:44) resulting in a pink solid (46.1 mg, 0.0442 mmol, yield 100%). MALDI-TOF: *m/z* obsd 1043.90 calc for $C_{49}H_{20}F_{15}N_5O_5$ 1043.12.

SnO_2 Nanoparticles. The synthesis of 2.5 nm SnO_2 nanoparticles was done by dissolving $SnCl_4$ (0.18 g, 0.69 mmol) in distilled ethyl acetate (100 mL) and stirring for 5 min.[176] Separately, $NaBH_4$ (0.08 g, 2.1 mmol) was dissolved in water, then added to the organic solution drop wise under continuous and vigorous stirring at room temperature for 120 min. The aqueous layer was removed in a seperatory funnel. The nanoparticles were centrifuged (4700 rpm/10 min) and washed with water and methanol to remove impurities, then dried with a rotary evaporator.

Porphyrin-Nanoparticle Assembly. The same procedure was followed to obtain the attachment of all the porphyrins (**1a-d**) to the SnO_2 nanoparticles. The binding was obtained by adding an aqueous solution of SnO_2 nanoparticles ([SnO_2] = ~ 0.1 mg/mL) at pH=6, to a solution of the porphyrin in a mixture composted by EtOH:water:AcOH (5:4:1 v/v) ([porphyrin] = ~ 10^{-5}mol/L. This mixture was stirred at 55°C in air for 2 h. After cooling, no other treatment was applied on the solution.

Results

Porphyrin Dyes. Four porphyrins were synthesized following Scheme 1-5, two low potential and two high potential. In each case, both carboxylic acid functionalized and imidodiacetic acid versions were synthesized to evaluate the effect of the linker on their photophysical properties. Figure 27 shows the steady-state absorption spectra of all four porphyrins (**1a-d)** in methanol. The high potential porphyrins, **1c** and **1d**, are blue-shifted in both the Soret and Q bands compared to the low-potential porphyrins, **1a** and **1b** (Table 1).

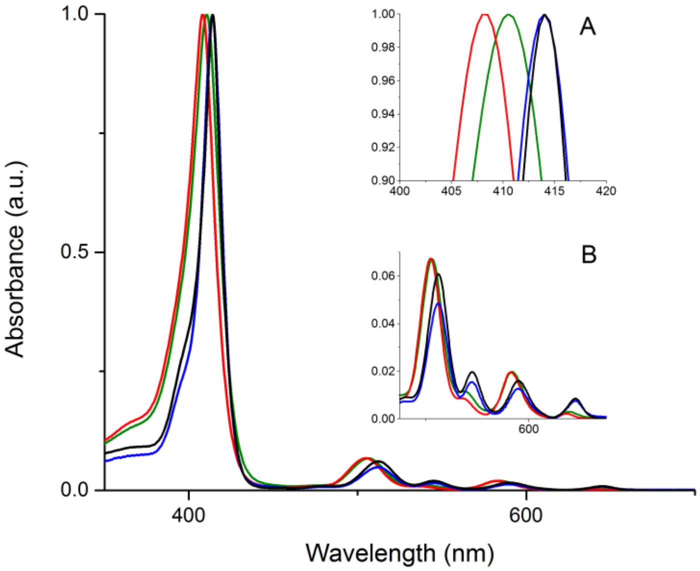

Figure 27. Absorption spectra of **1a** (black), **1b** (blue), **1c** (red), and **1d** (green). Inset A is an enlargement of the Soret band region and inset B is the Q band region.

Table 2. The maximum wavelength for each band of the four different porphyrins studied.

Compound	Soret λ_{max}, (nm)	Qy(0,1) λ_{max}, (nm)	Qy(1,1) λ_{max}, (nm)	Qx(0,0) λ_{max}, (nm)	Qx(1,0) λ_{max}, (nm)
1a	414	512	545	590	646
1b	414	512	545	589	645
1c	408	505	536	582	637
1d	410	506	537	583	640

Cyclic Voltammetry. Cyclic voltammetry was used to determine the reduction potentials of the porphyrins. The low potential trimesityl porphyrins, **1a** and **1b**, have a reversible signal corresponding to the first oxidation of the ground state at +1.2 V vs. NHE. The high potential porphyrins bearing the pentafluorophenyl groups, **1c** and **1d**, are oxidized at a much higher potential of +1.68 V vs. NHE (Figure 28).

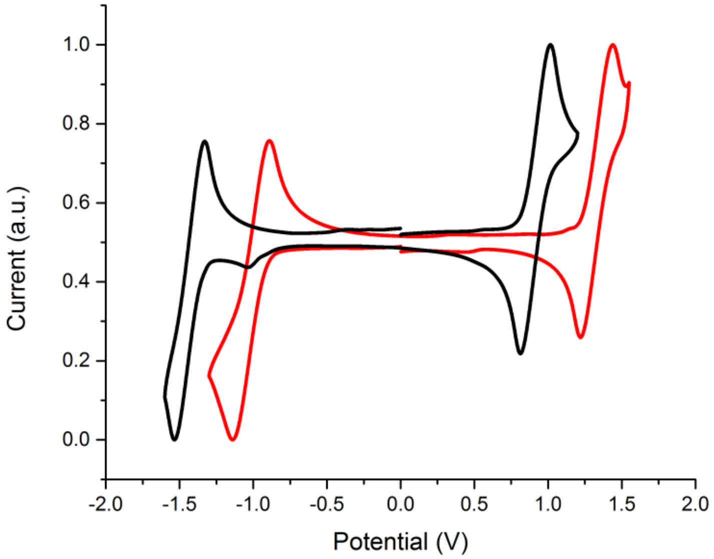

Figure 28. Cyclic voltammograms of **1a** (black) and **1c** (red) in dichloromethane with 0.1 M TBAPF. The potential on the x-axis is vs. SCE.

SnO_2 Nanoparticle Characteristics. TEM images show that the SnO_2 nanoparticles are about 2.5 nm (Figure 29). These nanoparticles disperse fairly well and have little agglomeration and hence relatively low light scattering effect into water and methanol/water. The experimental band gap in methanol calculated using Tauc plot is 4.1 eV, which corresponds to nanoparticles of 2.4 nm diameter. [177] The conduction band edge of SnO_2 is +0.05 V vs. NHE and the valence band edge is +3.85 V vs. NHE, each calculated for pH 7 from pH 1.[9]

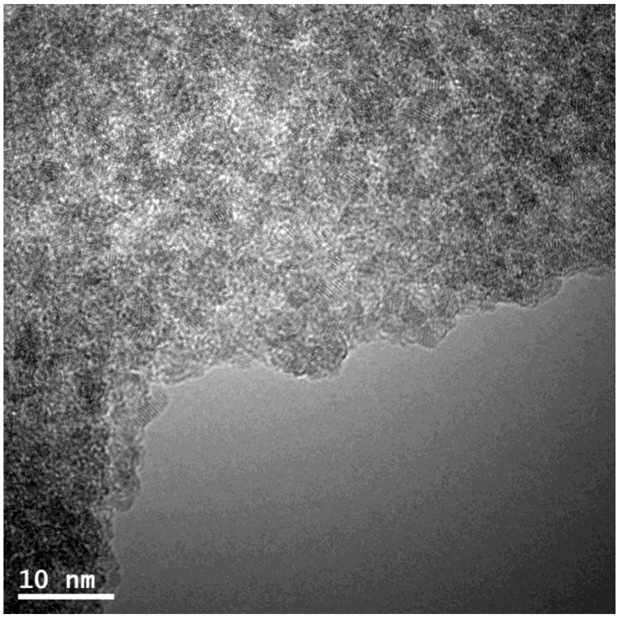

Figure 29. TEM image of the SnO_2 nanoparticles.

Porphyrin-Nanoparticle System. *UV-Vis Spectroscopy and Steady-State Fluorescence***.** Porphyrin dyes were bound to SnO_2 nanoparticles (Figure 30) to study electron injection rates. Dye attachment was confirmed using UV-vis spectroscopy. Figure 31 shows the bathochromic shift of the Soret and Q bands of **1a** attached to the SnO_2 nanoparticle surface (purple); there is a prominent increase in absorption at shorted wavelengths due to light scattering from the nanoparticles.[162]

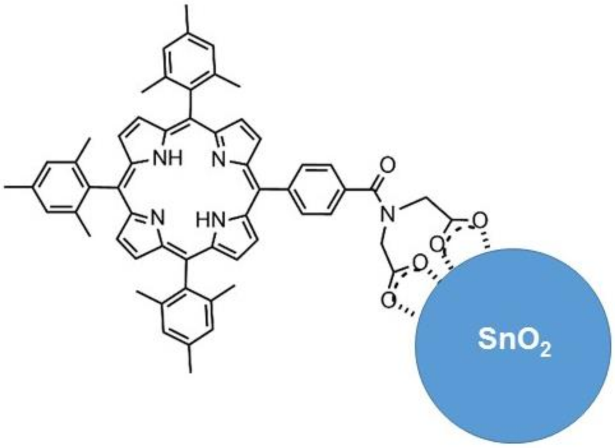

Figure 30. Proposed attachment of the porphyrin dye to the SnO_2 nanoparticle via the new anchoring group.

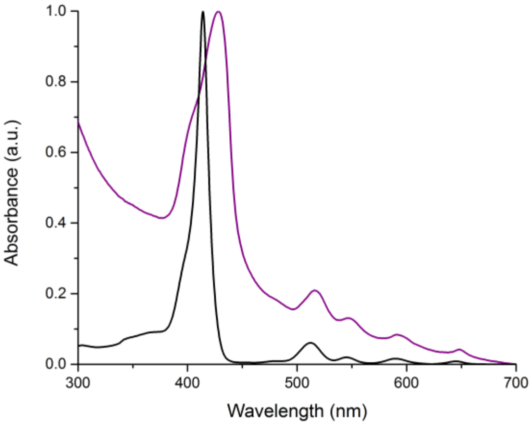

Figure 31. The absorption spectra of **1a** (black) and **1a**-SnO_2 hybrid system (purple).

Fluorescence quenching in the **1a**-SnO_2 hybrid system confirms attachment of the dye to the nanoparticle because of expected ultrafast electron injection from the dye singlet excited state to the conduction band of the nanoparticle. Figure 32 shows the absorption and emission spectra of **1a** compared to **1a**-SnO_2. Both solutions had an optical density of 0.067 at 425 nm when the emission spectra were taken. The unbound dye fluoresced strongly, as seen by the black dashed line while the fluorescence of the dye anchored to the nanoparticle is highly quenched, as seen by the purple dashed line.

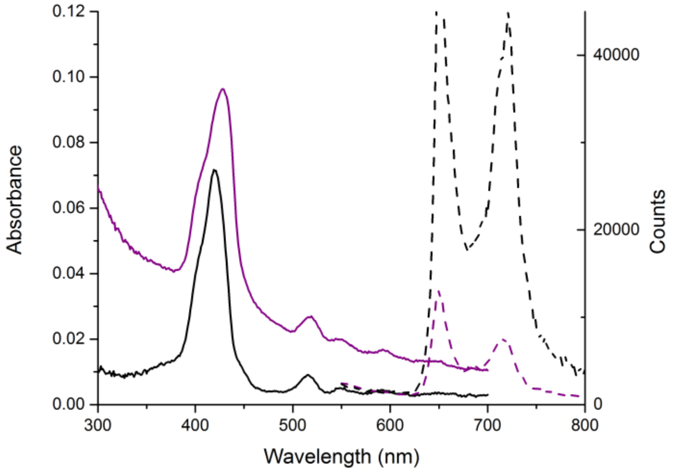

Figure 32. Absorption (solid lines) and emission (dashed lines) spectra of **1a** (black) and **1a**-SnO_2 hybrid system (purple) in a mixed solvent system of EtOH:water:AcOH (5:4:1 v/v).

Photophysics. Femtosecond pump-probe transient absorption spectroscopy measurements were taken to measure the influence of the carboxylic acid (**1a**) and the IDAA (**1b**) anchoring groups on the rate of electron injection for porphyrins attached to SnO_2 nanoparticles. It was found that porphyrin fluorescence was highly quenched for all four dyes and it was not possible to produce a readable signal in the transient absorption spectra for porphyrins **1c** and **1d** because of a very low concentration of the attached dye in the dye-nanoparticle system obtained after the attachment procedure.

The decay-associated spectra (DAS) obtained after global analysis of transient absorption data of porphyrin **1a** and **1b** attached to the SnO_2 nanoparticles are shown in Figure 33 and Figure 34. The global analysis for porphyrin **1a** attached to SnO_2 gives four DAS with lifetimes of 1.2 ps, 13 ps, 94 ps and nondecaying on the 2 ns decay time window used during the measurement. The 1.2 ps DAS can be attributed to the electron recombination from P^{+}-SnO_2^{-}. The spectroscopic fingerprints which testify to the formation of the charge separated state are the presence of a characteristic induced absorption band in the range between 670 nm and 740 nm due to the oxidized porphyrin and the ground state bleach of the Q bands at around 600 nm and 660 nm. The 13 ps DAS can be attributed to electron injection from the singlet excited state of the dye, **1a**, into the conduction band of the SnO_2. It shows the decay of stimulated emission around 730 nm. The 94 ps DAS and nondecaying DAS have blue shifted ground state bleaching bands at 590 nm and 650 nm, therefore can be attributed to aggregated and/or porphyrin not directly attached to the nanoparticles. Due to the high nonhomogeneity of the system, the obtained lifetimes do not correspond to single species but rather are effective averages of the decay of several slightly different species. For **1a**-SnO_2 there is likely some population with very fast formation of the charge separated state (<100 fs), this would explain the high amplitude of the 1.2 ps DAS which is not likely in such an inverted kinetics case.

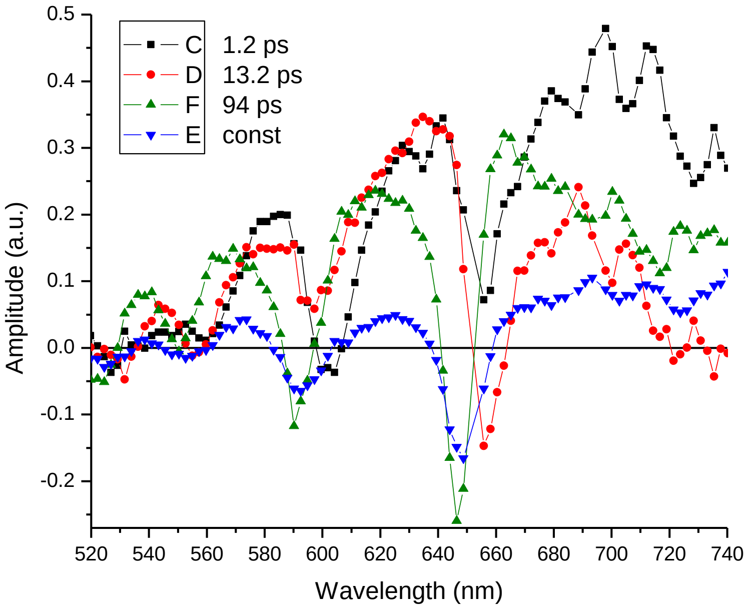

Figure 33. Decay-associated-spectra in acetonitrile solution measured by fs transient absorption upon excitation at 420 nm for **1a**–SnO_2.

The global analysis of the transient absorption data for the porphyrin **1b** attached to SnO_2 gives three DAS with lifetimes of 26 ps, 332 ps, and nondecaying component. The 26 ps DAS can be attributed to electron recombination from P^+-SnO_2^-. The spectroscopic fingerprints which testify the formation of the charge separated state are the presence of a transient absorption band in the range between 670 nm and 740 nm due to the oxidized porphyrin and the ground state bleach of the Q bands at around 600 nm and 660 nm as was observed for **1a**-SnO_2 as well. The 332 ps DAS and nondecaying DAS are due to aggregated and/or porphyrin not directly attached. The electron injection process occurs with a lifetime shorter than the detection limit of our equipment (c.a. 100 fs).

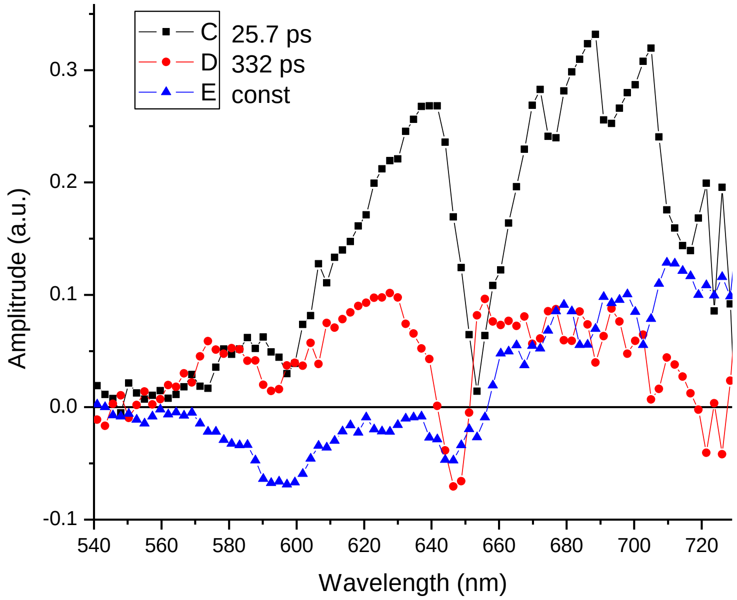

Figure 34. Decay-associated-spectra in acetonitrile solution measured by fs transient absorption upon excitation at 420 nm for **1b**–SnO_2.

Discussion

Four porphyrins have been synthesized to study the effectiveness of a new anchoring group, imidodiacetic acid (IDAA), and compare it to the commonly used carboxylic acid. The porphyrins were bound to SnO_2 to determine the effect of the anchoring group on their photoelectrochemical and photophysical properties. Porphyrins with high and low potentials were synthesized to test the electronic communication of the IDAA anchoring group with compounds of various redox potentials.

The high potential porphyrins, **1c** and **1d**, bearing three pentafluorophenyl groups, have an electron deficient macrocycle. Their redox potentials are more positive by about 480 mV than the low potential porphyrins, **1a** and **1b**, because they are more difficult to oxidize. The low potential porphyrins are electron rich due to the three mesityl groups attached to the macrocycle. They require only +1.2 V vs NHE to oxidize but are harder to reduce than the high potential porphyrins, or to add an electron to, due to the electron rich macrocycle. Using the ground-state oxidation potential, the first excited-state oxidation potentials for the porphyrins can be estimated using the Rehm-Weller approximation:[178,179]

$$E^{o}(P^{\bullet +}/{}^{1}P) \approx E^{o}(P^{\bullet +}/P) - \frac{E^{00}(P \rightarrow {}^{1}P)}{e} \qquad (1)$$

where $E^{o}(P^{\bullet +}/{}^{1}P)$ is the couple of the excited-state potential for the radical cation and the first singlet excited state of the porphyrin, $E^{o}(P^{\bullet +}/P)$ is the couple of the ground state potential for the porphyrin-radical cation and the porphyrin, $E^{00}(P \rightarrow {}^{1}P)$ is the estimated E^{00} transition energy from the porphyrin ground state to the porphyrin singlet state (S_0 – S_1), and e is the elementary charge of an electron. The estimated oxidation potentials for the singlet excited-states of each porphyrin is shown in Table 3.

Table 3. Estimation of the singlet excited-state oxidation potentials from the ground state oxidation potentials (vs. NHE).

Compound	**Ground State Oxidation Potential, $E^{o}(P^{\bullet +}/P)$**	**Singlet Excited-State Oxidation Potential, $E^{o}(P^{\bullet +}/{}^{1}P)$**
1a	+1.22 V	-0.71 V
1b	+1.23 V	-0.70 V
1c	+1.68 V	-0.25 V
1d	+1.68 V	-0.25 V

The SnO_2 nanoparticles synthesized for this study have low scattering due to their small size and can be dispersed into water and/or methanol. The TEM images show well rounded, evenly distributed nanoparticles with a diameter of about 2.5 nm on average. An estimated band gap of 4.1 eV from the steady state absorption supports the observed nanoparticle diameter. The conduction band of SnO_2 nanoparticles lies around +0.05 V vs. NHE, which allows for electron injections from both high and low potential porphyrins because their singlet excited-state oxidation potentials are -0.25 V and -0.71 V vs. NHE, respectively. Figure 35 illustrates the energy levels relevant to electron injection from the porphyrins to the nanoparticles.

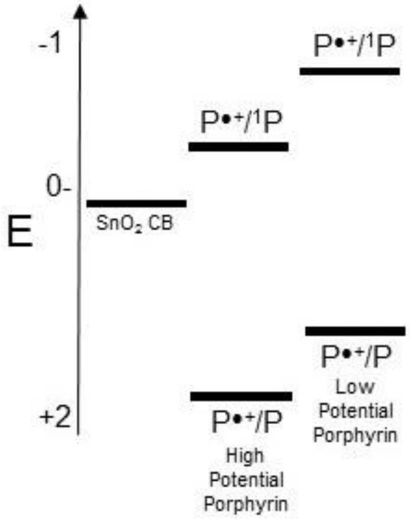

Figure 35. Energy levels relevant to electron injection from the porphyrin excited state, ^1P, into the conduction band of SnO_2 nanoparticles.

Each of the four porphyrin dyes was anchored onto the SnO_2 nanoparticles. UV-Vis spectroscopy was the initial test to confirm the attachment of the dyes to the nanoparticles. The shift and broadening of the Soret and Q bands in the absorption spectra suggests binding of the dyes to the nanoparticles.[162] Further evidence for dye attachment is the fluorescence quenching of the porphyrin. Porphyrin dyes in solution, unattached to nanoparticles, fluoresce significantly, as shown in Figure 32. After the dye was bound to the nanoparticles, the emission spectra showed nearly complete fluorescence quenching for all four porphyrins, indicating the attachment was successful. Once attached, photophysical measurements were carried out using femtosecond pump-probe transient absorption spectroscopy. These results showed very fast decay lifetime of attached dye singlet excited state which is attributed to the electron injection from the photoexcited dye into the nanoparticle.[154] This is one of the indications of dye attachment because free dye in solution would not inject an electron into the nanoparticle; its singlet excited state would decay via other relaxation pathways with slower lifetimes.[154] These results also suggest that the IDAA group is allowing electron injection into the nanoparticles.

The transient absorption analysis leads to the conclusion that both systems, **1a**-SnO_2 and **1b**-SnO_2, have very fast electron injection into the nanoparticle. In the case of IDAA attachment, the electronic coupling between the porphyrin (electron donor) and the SnO_2 (electron acceptor) is decreased as compared to the carboxylic group attachment, moreover the distance between the porphyrin moiety and the SnO_2 is increased. These effects are expected to slow down the charge recombination and are in agreement with transient absorption results showing slower charge recombination rate in the **1b**-SnO_2 system. Furthermore, the IDAA group thanks to the presence of two carboxylic functions most likely leads to a more stable linkage between the porphyrin **1b** and SnO_2 compared with the carboxylic group in **1a**; this effect possibly influences the electron transfer and recombination processes. Typically, it is believed that breaking conjugation with a CH_2 group would inhibit electron injection.[160,164] In this case, it does not seem to prevent electron injection. The distance between the macrocycle and semiconductor is short enough to allow electron injection and it is possible that the amide linkage increases the electronic coupling between the donor and acceptor.

Conclusion

In conclusion, we have demonstrated that imidodiacetic acid can be used as an efficient anchoring group to attach porphyrin dyes onto semiconducting metal oxides. The transient absorption spectroscopy measurements indicate that the IDAA anchoring group has good electron injection efficiency and shows slower electron recombination rate compared to the carboxylic acid group attachment. These are preliminary results and more experiments are needed to obtain the spectroscopy measurements for the high potential porphyrins but the results are expected to be similar. Future work would include attaching these porphyrins onto a SnO_2 electrode and determining photocurrent efficiency for each anchoring group. It would also be interesting to determine the pH dependence of the IDAA anchoring group and determine its binding mode using infrared spectroscopy. Compounds with imidodiacetic acid as an anchoring group could be used in artificial photosynthetic devices and dye-sensitized solar cells that use organic dyes on semiconducting metal oxides; that could help improve efficiency and longevity of the devices. Further studies will be done to determine the stability of the imidodiacetic acid anchoring group over time in aqueous conditions.

Acknowledgements

This work has been supported by the Center for Bio-Inspired Solar Fuel Production, an Energy Frontier Research Center funded by the U.S. Department of Energy, Office of Science, Office of Basic Energy Sciences under Award Number DE-SC0001016.

CHAPTER 3

PHTHALOCYANINE-CAROTENOID DYADS FOR TRIPLET-TRIPLET ENERGY TRANSFER STUDIES

Chelsea L. Brown, Manuel J. Llansola-Portoles, Gerdenis Kodis, Gabriela Coutinho, Ghabriel Anton, Thomas A. Moore, Devens Gust, Ana L. Moore.

A manuscript with the subject of this chapter is presently in preparation.

> My contribution to this work is the synthesis of the dyads, gathering data, writing the manuscript, and assisting with the editing process.

INTRODUCTION

In photosynthetic organisms, carotenoids and cyclic tetrapyrroles interact with each other to help drive photosynthesis.[29,30] During the first steps of the photosynthetic process, the absorption of photons by antenna pigment-protein complexes and the subsequent transfer of the excitation energy to the reaction centers are both intimately linked with the potential production of dangerous oxidative species. Production of (bacterio)chlorophyll ((B)Chl) triplet excited states by intersystem crossing from (B)Chls excited singlet states is a major source of singlet oxygen in photosynthetic organisms, one of the most dangerous chemical species for living organisms.[180] In photosynthetic pigment-protein complexes, this sensitization reaction is precluded by transfer of the triplet excited state from (B)Chls to carotenoid molecules, which has a triplet state energy below that of singlet oxygen. This quenching reaction reduces the lifetime of the (B)Chl triplet state by many orders of magnitudes.[181,182] Understanding the interchromophore coupling of these pigment systems is important for understanding the details of photoprotective mechanism.[183]

Carotenoids are known to interact with tetrapyrroles, like chlorophyll, in three important ways: as light-harvesting chromophores in antennas, in photoregulation, and in photoprotection.[28,184,185] In antennas, carotenoids help optimize light harvesting by absorbing in the blue/green region (400-550 nm), where chlorophyll absorbs little, and transferring that energy to the neighboring chlorophylls.[29] Carotenoids are also used for photoregulation by dissipating excess energy in the form of heat through non-photochemical quenching (NPQ).[184,185] Carotenoids method of photoprotection has been studied for decades.[186-196] When an excited state is formed in a tetrapyrrole, it can undergo intersystem crossing to the triplet state, which is able to sensitize singlet oxygen.[27-30] It has been determined that the interchromophore coupling between carotenoids and chlorophyll allows for the chlorophyll to do triplet-triplet (T-T) energy transfer to the triplet state on the carotenoid, which cannot sensitize singlet oxygen and instead harmlessly decays to the ground state.[28,30] It is well-known that in purple bacteria T-T energy transfer occurs in the nanosecond time scale (20-200 ns)[30] which is relatively slow. However, it is not determined yet how fast this energy transfer occurs in the light-harvesting complex II (LHCII) of green plants, and what governs their interaction.[30] To understand the role of electronic coupling and thermodynamics in controlling the rate of triplet-triplet energy transfer between the two chromophores it is essential to measure the rate constant of the T-T energy transfer as a function of electronic coupling and energy driving force for the process. This fundamental knowledge is essential for incorporating photoprotection into artificial photosynthetic systems capable of meeting humanity's need for biomass. [13,20]

In a similar manner than their natural counterparts, artificial photosynthetic devices for solar energy conversion, such as dye-sensitized photoelectrochemical cells (DSPECs),[13] are susceptible to photodegradation due to singlet oxygen being formed in the water splitting component of the device.[20] The success of artificial photosynthesis in the energy market depends on the cost-effectiveness of the device. The cost is directly related to the longevity of the device. Photoprotection will be essential for increasing the longevity of these devices and therefore decreasing their cost. Understanding how nature uses carotenoids coupled to tetrapyrroles to quench singlet oxygen is a critical to implementing photoprotection in artificial photosynthetic devices.

This work focuses on improving our understanding how carotenoids are involved in the photoprotection of the photosynthetic organism from the damaging effects of singlet oxygen.[27-30] We coupled a series of carotenoids to a phthalocyanine to form dyads through amide linkages (Figure 36). The amide linkage has been shown to provide good electronic coupling between carotenoids and phthalocyanines.[183,184,193,194] The phthalocyanine has been metallated with palladium in order to increase the triplet yield of the phthalocyanine through the heavy metal effect.[154,197] The dyads contain carotenoids of varying conjugation lengths, 9, 10, and 11 conjugated double bonds. The carotenoid and the phthalocyanine absorb in different regions of the visible spectrum so that excitation of the phthalocyanine does not overlap with the excitation of the carotenoid. That allows the selective excitation of the phthalocyanine whose singlet excited state due to the palladium decays very fast forming its triplet state with a high yield, so we are able to measure the subsequent T-T energy transfer to the carotenoid and determine the rate at which this process occurs.

METHODS

Materials. Dichloromethane (DCM), methanol, 4- hexanamidophthalonitrile, 3,6-dibutoxyphthalonitrile, $PdCl_2$, 1,8-diazabicyclo[5.4.0]undec-7-ene, potassium hydroxide, 1-ethyl-3-(3-dimethylaminopropyl)carbodiimide (EDCI), and 4-dimethylaminopyridine (4-DMAP) were purchased from Sigma-Aldrich and used without further purification. Silica gel (SiliaFlash F60 40–63 μm) used for column chromatography was purchased from SiliCycle. Dichloromethane, ethyl acetate, and methanol for synthesis and column chromatography were distilled. Toluene, chloroform, and butanol for synthesis were dried over activated 4 Å molecular sieves. Tetrahydrofuran was distilled over CaH_2 and stored over activated 4 Å molecular sieves and under argon atmosphere.

Synthesis of the compounds. The 4-hexanamidophthalonitrile was synthesized following a previously published method.[184] The ester carotenoids, methyl 8'-apo-β-caroten-8'-oate (9 double bonds), methyl 6'-apo-β-caroten-6'-oate (10 double bonds), and methyl 4'-apo-β-caroten-4'-oate (11 double bonds), were prepared as described,[198,199] and the corresponding acids were obtained by base catalyzed hydrolysis.

Palladium-8,11,15,18,22,25-hexabutoxy-2-hexanamidophthalocyanine. Portions of 4-hexanamidophthalonitrile (456 mg, 1.89 mmol), 3,6-dibutoxyphthalonitrile (1.50 g, 5.67 mmol), and $PdCl_2$ (603 mg, 3.40 mmol) were dissolved in 30 ml of butanol, heated to 45 °C, and bubbled with argon for 15 min. A portion of 1,8-diazabicyclo[5.4.0]undec-7-ene (DBU, 3.39 ml) was added, and the solution was heated to 118 °C and refluxed overnight under a blanket of argon. The green mixture was cooled to room temperature, and 100 ml of a water/chloroform mixture (1:1) was added. The organic layer was extracted, dried over $NaSO_4$, and filtered. The solvent was concentrated by rotary evaporation. The product was purified by column chromatography (silica gel, 1 % MeOH/10 % ethyl acetate/$CHCl_3$). Palladium-8,11,15,18,22,25-hexabutoxy-2-hexanamidophthalocyanine was obtained in 1.05 % yield (23 mg). ^{1}H-NMR δ ppm (20% Pyridine-d/$CDCl_3$): 1.09 (t, J = 7.4, 7.4 Hz, 3H), 1.27 (m, 18H), 1.70 (m, 4H), 2.24 (q, 2H), 2.39 (t, J = 7.5, 7.5 Hz, 2H), 3.20-5.20 (m, 36H), 6.85 (d, J = 8.7 Hz, 1H), 7.13 (d, J = 8.8 Hz, 1H), 7.38 (d, J = 9.6 Hz, 1H), 7.52 (d, J = 9.3 Hz, 1H), 7.64 (m, 2H), 8.31 (d, J = 7.8 Hz, 1H), 9.26 (d, J = 7.9 Hz, 1H), 10.03 (s, 1H), 10.84 (s, 1H). MALDI-TOF: *m/z* obsd. 1163.46 calc. for $C_{62}H_{75}N_9O_7Pd$ 1163.48. UV/vis λ_{max} (95% $CHCl_3$ / 5% MeOH): 327, 647, and 721 nm.

Palladium-2-amino-8,11,15,18,22,25-hexabutoxyphthalocyanine. The hexanamidophthalocyanine obtained in the above reaction (20.4 mg, 17.6 μmol) was dissolved in 10 ml of THF and 5 ml of a saturated methanolic solution of KOH. The solution was heated to 65 °C and stirred overnight. The reaction mixture was diluted with chloroform and washed with water (three times). The organic layer was dried over Na2SO4 and filtered, and the solvent was removed by rotary evaporation. The desired palladium 2-amino-8,11,15,18,22,25- hexabutoxyphthalocyanine (18.5 mg) was obtained in 99 % yield. MALDI-TOF: *m/z* obsd. 1065.32 calc. for $C_{56}H_{65}N_9O_6Pd$ 1065.41. UV/vis λ_{max} (95% $CHCl_3$ / 5% MeOH): 324, 647, and 721 nm.

Dyad 9. The 8'-apo-β-caroten-8'-oic acid (28.5 mg, 65.7 μmol) and palladium 2-amino-8,11,15,18,22,25-hexabutoxyphthalocyanine (35 mg, 32.9 μmol) were dissolved in 45 mL of dry chloroform. While under argon, EDCI (68.9 mg, 0.36 mmol) and DMAP (224 mg, 1.83 mmol) were added. The reaction was stirred overnight at room temperature under a blanket of argon. The solvent was removed by rotary evaporation and the product was purified by column chromatography (silica, 2 % MeOH/DCM). The product was then purified by two prepatory TLCs, the first in 1 % MeOH/5 % ethyl acetate/chloroform and the second in 2 % MeOH/DCM. Dyad 9 (5.7 mg) was obtained in 11.7% yield. MALDI-TOF: *m/z* obsd. 1479.98 calc. for $C_{86}H_{103}N_9O_7Pd$ 1479.70. UV/vis λ_{max} (95% $CHCl_3$ / 5% MeOH): 330, 454, 648, and 722 nm.

Dyad 10 was prepared by the same procedure described for **dyad 9** except using 6'-apo-β-caroten-6'-oic acid. MALDI-TOF: *m/z* obsd. 1505.70 calc. for $C_{88}H_{105}N_9O_7Pd$ 1505.72. UV/vis λ_{max} (95% $CHCl_3$ / 5% MeOH): 327, 470, 650, and 725 nm.

Dyad 11 was prepared by the same procedure described for dyad 9 except using 4'-apo-β,y-caroten-4'-oic acid. MALDI-TOF: *m/z* obsd. 1545.83 calc. for $C_{91}H_{109}N_9O_7Pd$ 1545.75. UV/vis λ_{max} (95% $CHCl_3$ / 5% MeOH): 330, 482, 649, and 723 nm.

Steady state absorption. Spectra were recorded in 1.0 cm path length cuvette with a Shimadzu UV2550 UV-visible spectrometer.

Time resolved fluorescence. Fluorescence decay measurements were performed by the time-correlated single-photon-counting method. The excitation source was a fiber supercontinuum laser based on a passive modelocked fiber laser and a high-nonlinearity photonic crystal fiber supercontinuum generator (Fianium SC450). The laser provides 6-ps pulses at a repetition rate variable between 0.1 – 40 MHz. The laser output was sent through an Acousto-Optical Tunable Filer (Fianium AOTF) to obtain excitation pulses at desired wavelength of ca. 450-900 nm. Fluorescence emission was detected at the magic angle using a double grating monochromator (Jobin Yvon Gemini-180) and a microchannel plate photomultiplier tube (Hamamatsu R3809U-50). The instrument response function was 35-55 ps. The spectrometer was controlled by software based on the LabView programming language and data acquisition was done using a single photon counting card

(Becker-Hickl, SPC-830. Data analysis of results from both systems was carried out using locally written software (ASUFIT) developed in a MATLAB environment (Mathworks Inc.). Data were fitted as a sum of exponential decays, which were reconvoluted with the appropriate instrument response function. Goodness of fit was established by examination of residuals and the reduced χ^2 value.

Time resolved absorption. Femtosecond to nanosecond transient absorption measurements were acquired with a kilohertz pulsed laser source and a pump-probe optical setup. Laser pulses at 800 nm (c.a. 100 fs) were generated from an amplified, mode-locked titanium sapphire kilohertz laser system (Millennia/Tsunami/Spitfire, Spectra Physics). Part of the laser pulse energy was sent through an optical delay line and focused onto a 3 mm sapphire plate to generate a white light continuum for the probe beam. The remainder of the pulse energy was used to pump an optical parametric amplifier (Spectra Physics) to generate excitation pulses at 700 nm, which were selected using a mechanical chopper. The white light generated was compressed by prism pairs (CVI) before passing through the sample. The polarization of the pump beam was set to the magic angle (54.7°) relative to the probe beam and its energy was adjusted to 200 nJ using a continuously variable neutral density filter. The beams were focused in a 2 mm path-length quartz cuvette to a ~200 μm diameter spot. The white light probe was dispersed by a spectrograph (300 line grating) onto a charge-coupled device (CCD) camera (DU420, Andor Tech.). The final spectral resolution was about 2.3 nm for over a nearly 300 nm spectral region. The instrument response function was ca. 100 fs. The decay-associated spectra (DAS) were obtained by fitting globally the transient absorption kinetic traces over a selected wavelength region simultaneously as described by equation (1) (parallel kinetic model).[79]

$$\Delta A(\lambda,t)=\sum_{i=1}^{n}A_i(\lambda)\exp(-t/\tau_i) \quad (1)$$

where $\Delta A(\lambda,t)$ is the observed absorption change at a given wavelength at time delay t and n is the number of kinetic components used in the fitting. A plot of $A_i(\lambda)$ versus wavelength is called a Decay Associated Spectra (DAS) and represents the amplitude spectrum of the i^{th} kinetic component, which has a lifetime of τ_i. Random errors associated with the reported lifetimes obtained from transient absorption measurements were typically ≤ 5%.

RESULTS AND DISCUSSION

Figure 36 shows the three dyads used for this work and the phthalocyanines used as standard. Through an amide linker three carotenes with 9, 10 and 11 double carbon bonds have been attached to the phthalocyanine. By changing the energy level of the carotenoid triplet by changing the number of double bonds of the polyene, we are able to assess how the thermodynamics influence the rate of T-T energy transfer.

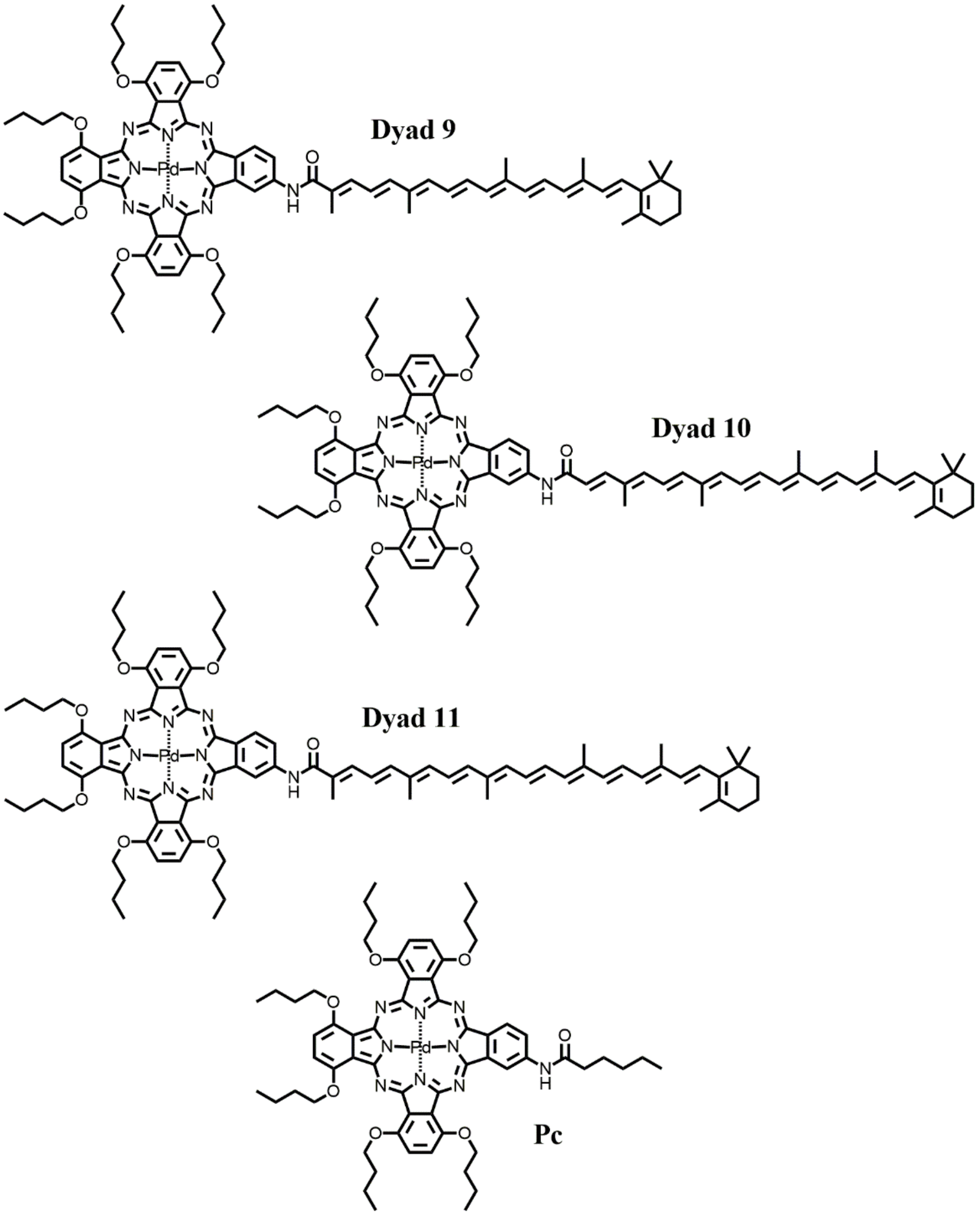

Figure 36. Molecular structures of the phthalocyanine reference and the carotenophthalocyanine dyads with 9 (**Dyad 9**), 10 (**Dyad 10**), and 11 (**Dyad 11**) double bonds.

Figure 37 shows the carotenophthalocyanine absorption spectra of **Dyad 9**, **Dyad 10**, **Dyad 11** and the reference phthalocyanine (**Pc**) in toluene. The absorption maxima at ~320 nm (Soret), 650 nm and 720 nm (Q bands) are due to the Pc, and the broad absorption around 500 nm are mostly associated with carotenoids. Because carotenoids have no absorption at >700 nm, we are able to selectively excite the phthalocyanine at those wavelengths for the transient absorption experiments. Time-resolved fluorescence measurements (Figure 38) were performed but due to the fast quenching from the singlet state of the **Pc** to the triplet state of the **Pc** (around 10 ps), no signal was detected because the detection limit of the equipment is around 40 ps.

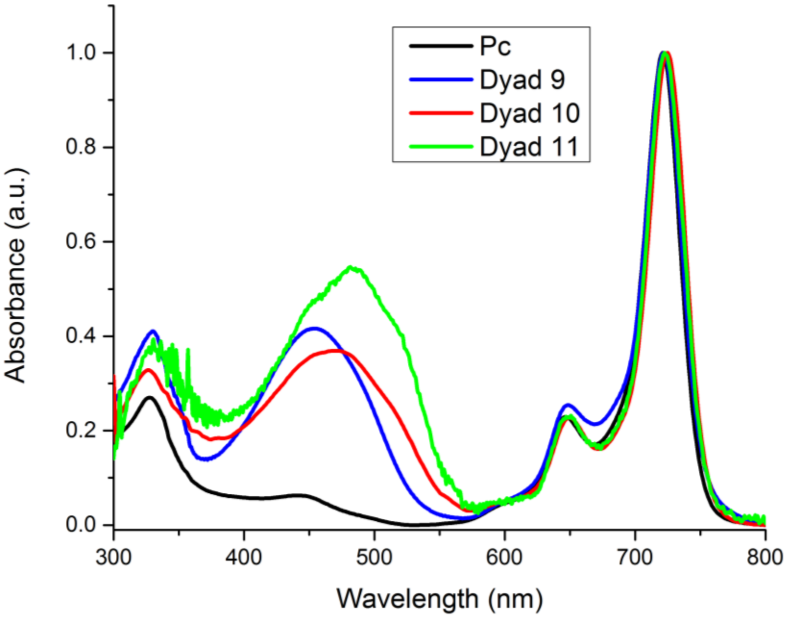

Figure 37. Absorption spectra in 95% chloroform/10% methanol of **Dyad 9**, **Dyad 10**, **Dyad 11**, and **Pc**.

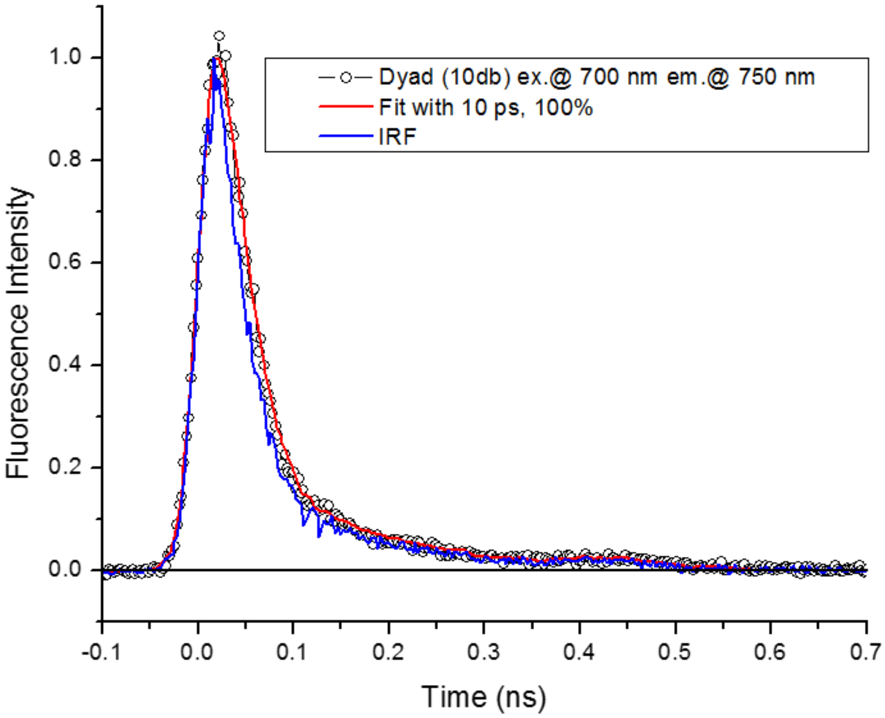

Figure 38. Fluorescence at 750 nm kinetics (symbols) and single exponential fit (red) for the model phthalocyanine (**Pc**) measured by means of the time-correlated single-photon-counting technique with excitation at 700 nm. The instrument response function is shown as the blue line.

The global analysis of the transient absorption data obtained with 700 nm excitation for each compound gives the decay-associated spectra (DAS) shown in Figure 39. The four DAS, 1 ps, 10 ps, 100 ps, and nondecaying lifetime on a 2 ns time scale (Figure 39, **Pc**), are associated with the decay of **Pc** excited states. The 10 ps DAS shows the decay of the **Pc** singlet excited state forming ^{3}**Pc** since we observe the formation of the characteristic triplet excited state induced absorption around 600 nm. The 1 ps DAS and 100 ps DAS are associated with the relaxation/solvation of the **Pc** singlet and triplet excited states, respectively; they show the characteristic feature associated with the red shift of the Q band bleaching at ~710 nm. The non-decaying DAS is associated with ^{3}**Pc** showing the characteristic induced absorption at around 600 nm and Q band bleaching.

The global analysis of the transient absorption data for **Dyad 9** gives five DAS with 1 ps, 10 ps, 126 ps, 9 ns and a nondecaying DAS (Figure 39, D9). The 10 ps DAS is associated with the decay of the singlet excited state to form ^{3}**Pc**, since we observe the rise of the induced absorption at around 600 nm. The 126 ps DAS is associated with the T-T energy transfer between ^{3}**Pc** and ^{3}**Car**, since we observe the rise of the induced absorption characteristic of the ^{3}**Car** around 550 nm, and simultaneous decay of the ground state bleaching at 720 nm associated with ^{3}**Pc**. The nondecaying DAS is associated with decay of ^{3}**Car** to the ground state; this transient is associated with the bleaching of **Pc** at 720 nm. This phenomenon is a characteristic of strongly coupled carotenoid-tetrapyrrole systems and its origin is not understood. The 9 ns DAS is most likely associated with a small amount of free/nonattached **Pc**. These results indicate that the triplet-triplet energy transfer from the ^{3}**Pc** to the triplet excited state of the 9 double bond carotenoid in **Dyad 9** occurs in 126 ps.

The global analysis of the transient absorption data for **Dyad 10** and **Dyad 11** give five DAS, 1 ps, 10 ps, 80 ps, 1.47 ns and a nondecaying DAS with 1 ps, 10 ps, 79 ps, 287 ps and a nondecaying component, respectively. Similar to **Dyad 9**, the 10 ps DAS is associated with the formation of ^{3}**Pc** as we observed in the model **Pc** and **Dyad 9** transient absorption analysis. The nondecaying DAS is associated with ^{3}**Car**. The 80 ps DAS in **Dyad 10** shows the T-T energy transfer from ^{3}**Pc** to ^{3}**Car**, since we again observe the formation of the characteristic **Car^3** induced absorption at around 550 nm, and simultaneous decay of the ground state bleaching of **^{3}Pc** at 720 nm. These results indicate that the T-T energy transfer from the **^{3}Pc** to the 10 double bond carotenoid triplet in **Dyad 10** occurs in 80 ps, which is faster than for **Dyad 9**. This is expected because of the larger driving force for the T-T energy transfer with the longer carotenoid.[198] In **Dyad 11** the picture is more complicated because we have two DAS, the 79 ps DAS and 287 ps DAS, which can both be associated with the T-T energy transfer from **^{3}Pc** to **^{3}Car**. It is possible that there are two different configurational isomers, cis and trans. When the data is fitted with only four lifetimes, we found that the T-T energy transfer between **^{3}Pc** and **^{3}Car** occurs in 122 ps, but the five exponential analysis gives a better goodness of the fit parameter and residuals. **Dyad 11** needs to be measured again after care is taken to make sure there is no cis isomer or some other impurity. If we assume that the fit with four lifetimes is correct, these results indicate that the T-T energy transfer from the **^{3}Pc** to the 11 double bond carotenoid triplet in **Dyad 11** occurs in about 122 ps, which is longer than in the case of **Dyad 10** and does not fit the expected trend for thermodynamic driving force for the T-T energy transfer process. This could be due to a reduced orbital overlap between the Pd-phthalocyanine and the 11 double bond carotenoid and therefore less coupling compared with the 10 double bond carotenoid. More work needs to be done in order to understand these results and determine why the thermodynamic driving force is not the dominate factor controlling the rate of T-T energy transfer in these dyads if that is the case.

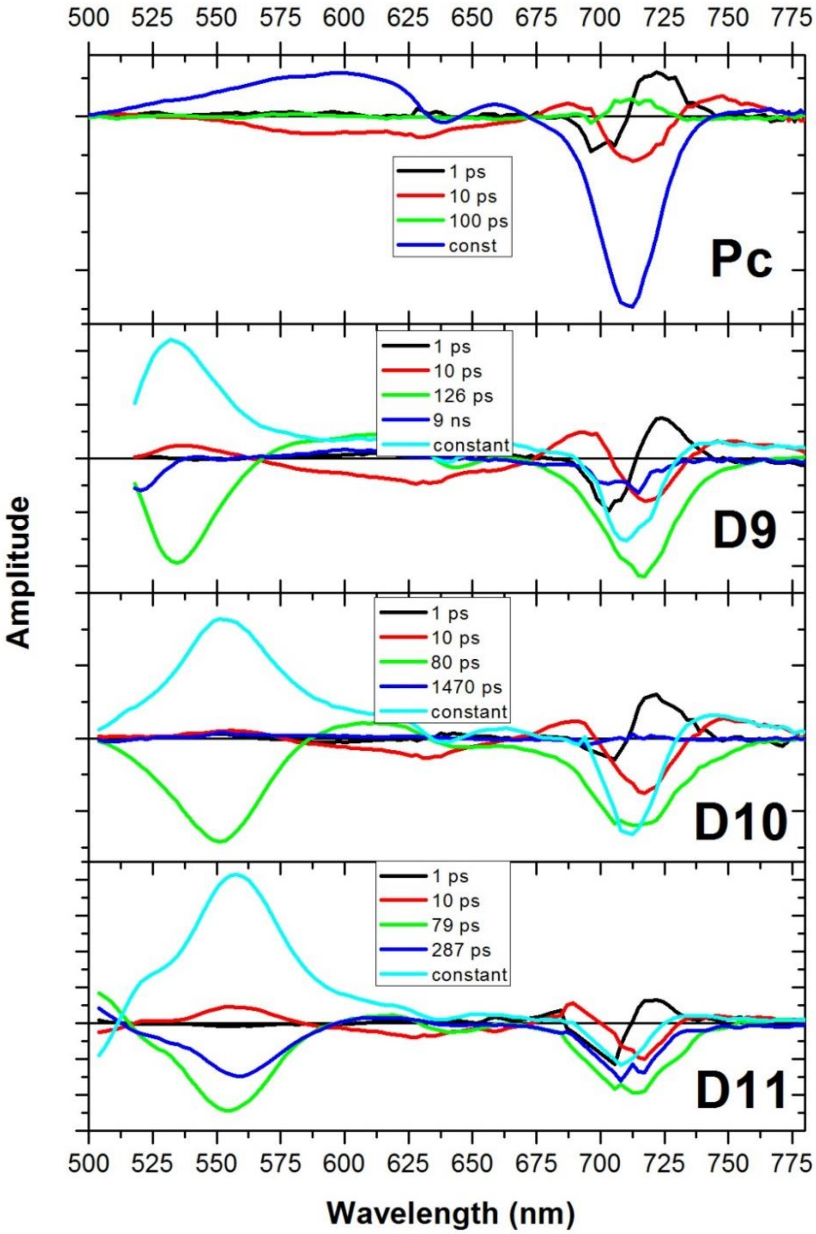

Figure 39. Decay-associated-spectra in toluene for the model phthalocyanine (**Pc**), **Dyad 9** (D9), **Dyad 10** (D10) and **Dyad 11** (D11) measured by transient absorption upon excitation at 700 nm. On the 2 ns time delay window neither the ^{3}**Pc** nor the ^{3}**Car** transient species of dyads decays and are shown as constants.

CONCLUSIONS

The intersystem crossing for the Pd-phthalocyanine occurs in 10 ps and the triplet-triplet energy transfer from the Pd-phthalocyanine to the carotenoid is between 80-290 ps, depending on the nature of the carotenoid in the dyad. Usually, the driving force correlates with the triplet-triplet (T-T) energy transfer rate and therefore we would like to believe that the longer the carotenoid chain, the faster the T-T energy transfer would occur. However, our preliminary results suggest that the T-T energy transfer for **Dyad 9** and **Dyad 11** are slower than it is for **Dyad 10**. It is possible that the wavefunction overlap for the 10 double bond carotenoid triplet excited state and the triplet excited state of the Pd-phthalocyanine is better than that for the 9 and 11 double bond carotenoids because of the methyl group adjacent to the linker in those cases. In order to confirm this hypothesis, molecular mechanics and quantum mechanics calculations are being performed. **Dyad 11** must be purified and studied again by means of transient absorption spectroscopy.

CHAPTER 4

PHOTOCHEMICAL & PHOTOBIOLOGICAL SCIENCES PAPER

Kinetic isotope effect of proton-coupled electron transfer in a hydrogen bonded phenol-pyrrolidino[60]fullerene

Authors: Janneke Ravensbergen[A], Chelsea L. Brown[B], Gary F. Moore[B], Raoul N. Frese[A], Rienk van Grondelle[A], Devens Gust[B], Thomas A. Moore[B], Ana L. Moore[B] and John T. M. Kennis[A]

[A] *Department of Physics and Astronomy, Faculty of Sciences, VU University, De Boelelaan 1081, 1081 HV, Amsterdam, The Netherlands.*

[B] *Center for Bioenergy and Photosynthesis, Department of Chemistry and Biochemistry, Arizona State University, Tempe, AZ, USA 85287-1604*

Citation:

Janneke Ravensbergen, Chelsea L. Brown, Gary F. Moore, Raoul N. Frese, Rienk van Grondelle, Devens Gust, Thomas A. Moore, Ana L. Moore and John T. M. Kennis. *Photochem. Photobiol. Sci.*, **2015**. DOI: 10.1039/C5PP00259A

My contribution to this work is the NMR exchange studies and assisting with the editing process.

ABSTRACT: Proton-coupled electron transfer (PCET) plays a central role in photosynthesis and potentially in solar-to-fuel systems. We report a spectroscopy study on a phenol–pyrrolidino[60]fullerene. Quenching of the singlet excited state from 1 ns to 250

ps is assigned to PCET. A H/D exchange study reveals a kinetic isotope effect (KIE) of 3.0, consistent with a concerted PCET mechanism.

Proton-coupled electron transfer (PCET) is of key importance in photosynthesis and various other biological processes.[200] In photosystem II, after the initial charge separation the oxidized chlorophyll is reduced in a PCET step by a tyrosine (Tyr_Z). The tyrosine phenolic proton is donated to a nearby histidine residue (His 190).[201,202] When the tyrosine is reduced by the water oxidation complex it regains a proton. By the coupling of proton movement to these redox reactions photosynthesis avoids high energy intermediates and stabilizes the charge separated state.[32,203,204]

In artificial photosynthesis one aim is to use design principles from nature to develop a solar fuel producing system. PCET is one of these principles that can play a crucial role in bridging the timescale of short-lived, reactive intermediates formed by photoinduced charge separation to that of the relative slow process of multi-electron catalysis. Various studies have been performed on artificial PCET systems with various degrees of molecular complexity.[32,157,200,205-213] In search of a minimal biomimetic construct for photoinduced PCET, Moore et al., have previously reported a fullerene-based dyad in which the fullerene fluorescence lifetime in benzonitrile is reduced to from 1.3 ns to 260 ps. This reduction of the fluorescence lifetime was not found in acidified solvent, strongly suggesting a PCET mechanism for the quenching of excited fullerene.[155] This could be either a ‘proton first’, ‘electron first’ or concerted transfer process. We will refer to both the step-wise and concerted mechanisms as PCET.

Here we report a transient absorption study of this putative PCET in the phenol-pyrrolidino[60]fullerene **1** depicted in Figure 40. In this isomer the phenol hydroxyl group is *ortho* to the pyrrolidine moiety and designed to hydrogen bond to the lone pair electrons of the nitrogen on the pyrrolidine. This internal hydrogen bond provides a well-defined structural framework for the PCET process. Reference compound **2** has a hydroxyl group at the *para* position where the internal hydrogen bond cannot be formed. Reference compound **3** lacks the hydroxyl group.

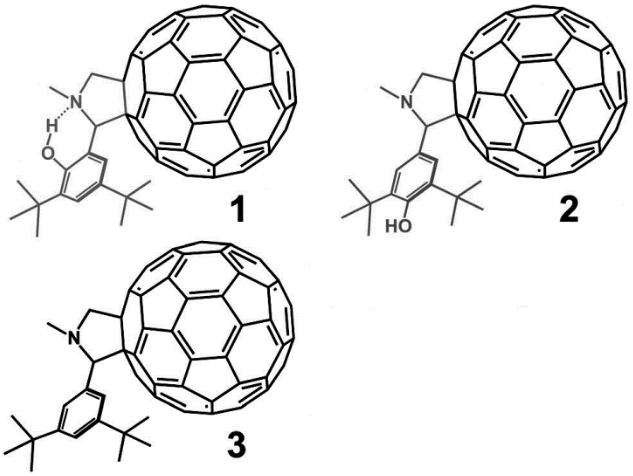

Figure 40. Phenol–pyrrolidino[60]fullerene compounds investigated in the present work.

Previously reported electrochemical measurements revealed that the phenol moiety of compound **1** is thermodynamically capable of reducing singlet excited C_{60}. The phenol moiety in compound **2** and the phenyl group in **3** are thermodynamically incapable of reducing singlet excited C_{60}. This also holds for compound **1** in acidified solvent, where the internal hydrogen bond is disrupted.[155]

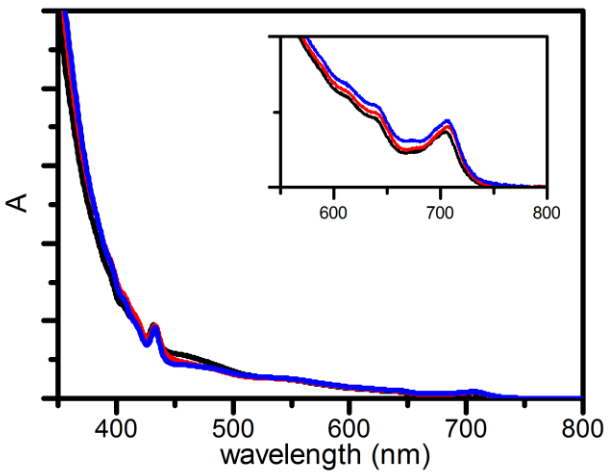

Figure 41. Normalized absorption spectra of **1** (black), **2** (red) and **3** (blue) in benzonitrile, normalized at 433 nm.

The steady-state absorption spectra in Figure 41 are dominated by features from fullerene.[214] The extinction coefficient of the compounds is largest in the UV. A small amplitude tail spans the visible part of the spectrum, where maxima are found at 433 nm and 705 nm.

For transient absorption spectroscopy the compounds were excited at 705 nm in the lowest-energy absorption band of fullerene; the instrument response time was 100 fs. Global analysis yields the Evolution Associated Difference Spectra (EADS) in Figure 42. These are the interconverting spectra that follow from analysis with a sequential model. Further details of the measurements and analysis are given in the Materials and Methods section in the SI. Raw transient absorption data is presented in Figure S2.

For compound **2** (Figure 42A) in aerated benzonitrile two lifetime components are needed for a sufficient fit of the data: 1.3 ns and 386 ns. The spectra are assigned to the singlet and triplet excited state of fullerene and are very similar to those reported for methylfulleropyrrolidine.[214] The first EADS (black) assigned to the singlet state shows excited state absorption in the full probed window. Overlapping, but with smaller amplitude we find ground state bleach. This has a negative contribution to the ΔA signal that can be recognized by the minima at 433 nm and 705 nm. The singlet excited state has a lifetime of 1.3 ns. The second EADS, assigned to the fullerene triplet, has lower amplitude at wavelengths shorter than 585 nm and higher amplitude at longer wavelengths. A maximum is found around 700 nm. The triplet decays to the ground state in 386 ns. Very similar results are found for **3** (Figure S 32).

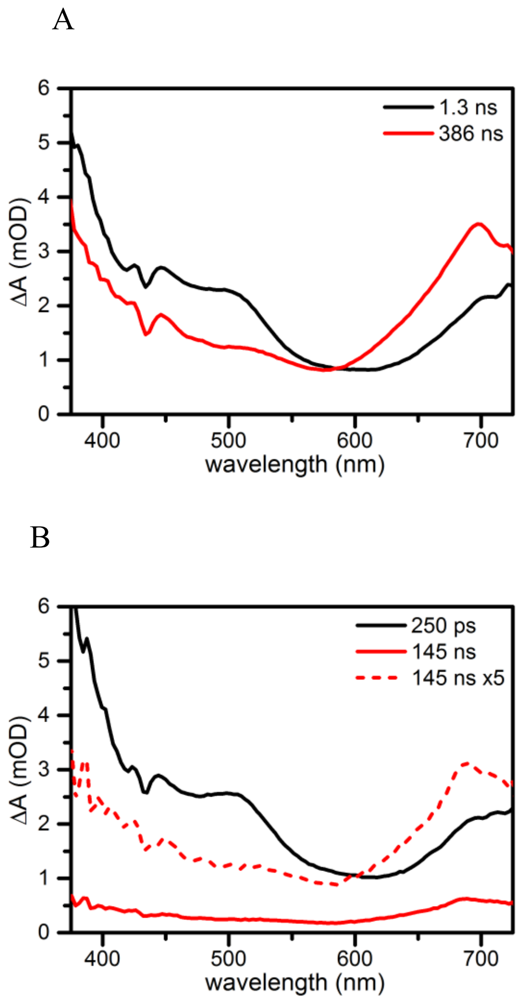

Figure 42. Evolution Associated Difference Spectra (EADS) of compounds **2** (A) and **1** (B) in aerated benzonitrile upon 705 nm excitation. The lifetimes of the interconverting spectra are given in the legend.

The singlet excited state spectrum of **1** (Figure 42B, black) closely resembles the singlet spectra of **2** and **3**. The lifetime of the singlet state is found to be 250 ps, in agreement with the reported fluorescence lifetime.[155] As a result of the shorter singlet lifetime, less triplet is formed, and the triplet spectrum (which is similar to that of **2** and **3**), is smaller in amplitude (Figure 42B, red and red dash). The reduced singlet lifetime has been assigned to a proton-coupled electron transfer process forming a neutral phenoxyl radical and a zwitterionic pyrrolidino[60]fullerene group ($PhO^{\cdot}$–$PyrH^{+}$-$C60^{\cdot -}$). The zwitterionic state could not be detected. Most probably, the rate constant for recombination is larger than that for formation of the zwitterionic state. In such 'inverted kinetics', the zwitterionic state signal would rise with the time constant of its lifetime, and its transient concentration would be low. The detection of such recombination time constants on fast timescales is further complicated by a large coherent and cross-phase modulation artefact around zero time delay.

To confirm the involvement of proton migration in the photophysical pathway we performed transient absorption spectroscopy of compound **1** in aerated benzonitrile with 2% v/v H_2O or D_2O. The protons or deuterium from H_2O or D_2O will exchange with the phenolic proton, the only exchangeable proton of compound **1**. The H/D exchange was confirmed by ^1H-NMR. The ^1H-NMR spectrum of the compound in equal parts CDCl3/CS_2 with 2% H_2O was compared to the ^1H-NMR spectrum in equal parts $CDCl_3$/CS_2 with 2% D_2O. The disappearance of the peak for the phenolic proton was observed after addition of D_2O (Figure S 33 and Figure S 34). We refer to the deuterated compound as **1-D** (**1-H** for H_2O). Figure 43 shows the time trace for the absorption of both compounds at 538 nm. For **1-H** we find a singlet lifetime of 250 ps, similar to the measurement in benzonitrile. In contrast, the singlet lifetime of **1-D** is 546 ps. Based on the lifetime for decay of **2** of 1.3 ns, we estimate the rate of PCET at 3.2×10^9 s^{-1} and 1.1×10^9 s^{-1} for **1-H** and **1-D** respectively. ‡ Thus, excited state quenching by PCET is associated with a H/D kinetic isotope effect (KIE) of 3.0. For compounds **2** and **3** in benzonitrile with 2% v/v H_2O or D_2O no kinetic isotope effect was found.

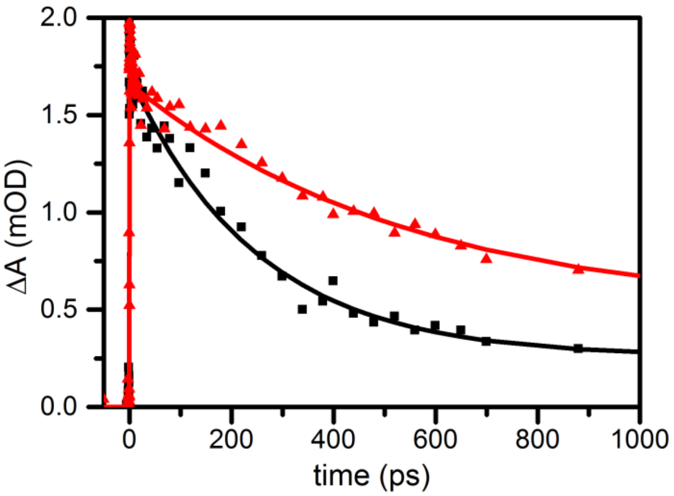

Figure 43. Transient absorption spectroscopy time trace of **1** at 538 nm in aerated benzonitrile with 2% H_2O (**1-H**, black) and 2% D_2O (**1-D**, red). The sharp peak at 0 ps is due to a coherent and cross-phase modulation artifact.

This significant kinetic isotope effect for **1** confirms the involvement of proton migration in the quenching of the singlet state. We propose that this PCET process occurs by a concerted mechanism. The size of the KIE shows that the proton is involved in the rate determining step and excludes the 'electron first' mechanism for this non-equilibrium PCET process.[205-209,215,216] The 'proton first' mechanism is excluded by the large difference in acidity. The pyrrolidine is about 10 pKa units more acidic than the phenol, based on values in acetonitrile.[217,218] Prato et al. have shown that pyrrolidine is even more acidic when attached to fullerene.[219] The pKa of pyrrolidine is not expected to change much upon excitation of fullerene, because the HOMO and LUMO do not include the atoms around the H-bond.[220] Due to the large difference in acidity, proton transfer from phenol to pyrrolidine prior to electron migration would be energetically steeply uphill. Concerted PCET avoids this high energy intermediate.

Constentin et al. reported a phenol-pyrrolidine system with an electrochemically observed KIE of 1.8.[221] A possible explanation for the larger KIE in our experiments is the lower pKa of pyrrolidinofullerene, as compared to pyrrolidine, which leads to a weaker hydrogen bond. Hammes-Schiffer and co-workers discussed the KIE dependence on hydrogen bond strength in PCET processes.[222] The trend of increasing KIE with weaker hydrogen bond is explained by the more localized wavefunction in the case of deuterium, leading to a faster decay of overlap with increasing donor-acceptor distance. However the opposite trend has been observed in some systems and explained by the role of vibronic states.[222]

To summarize, our transient absorption spectroscopy results for compound **1** show a quenching of the singlet excited fullerene, assigned to a proton coupled electron transfer process. We observe a H/D kinetic isotope effect of 3.0 consistent with a concerted PCET mechanism.

Notes and references

‡ From the measured 1.3 ns singlet lifetime of reference compound **2** it follows that the rate of singlet decay is $k_{ref} = 1/(1.3\ ns) = 7.7 \times 10^8\ s^{-1}$. This rate includes intersystem crossing and internal conversion in compound **2** and is used as estimation for these processes in **1-H** and **1-D**. For **1-H** and **1-D** the singlet decay rate is the sum of k_{ref} and the PCET rate as $k_{sum} = k_{ref} + k_{PCET}$. Here, k_{sum} corresponds to the observed singlet decay rate, which is (1/250 ps) for **1-H** and (1/546 ps) for **1-D**. From this is follows that k_{PCET} is $3.2 \times 10^9\ s^{-1}$ and $1.1 \times 10^9\ s^{-1}$ for **1-H** and **1-D** respectively.

ASSOCIATED CONTENT

Supporting Information

Transient absorption results on compound **3** and a description of used materials and methods is provided in the supplemental information. This material is available free of charge via the Internet at http://pubs.acs.org.

AUTHOR INFORMATION

Corresponding Author

John T.M. Kennis: j.t.m.kennis@vu.nl

Notes

The authors declare no competing financial interests.

ACKNOWLEDGMENT

J.R. was supported by the research programme of BioSolar Cells, co-financed by the Dutch Ministry of Economic Affairs. J.T.M.K. was supported by a VICI grant of the Chemical Sciences council of the Netherlands Organization of Scientific Research (NWO-CW). This work was supported by the Office of Basic Energy Sciences, Division of Chemical Sciences, Geosciences, and Energy Biosciences, Department of Energy under contract DE-FG02-03ER15393 and the Center for Bio-Inspired Solar Fuel Production, an Energy Frontier Research Center funded by the U.S. Department of Energy, Office of Science, Office of Basic Energy Sciences under Award Number DE-SC0001016. R. v. G. was supported by the VU University Amsterdam, the Laserlab-Europe Consortium, the advanced investigator grant (267333, PHOTPROT) from the European Research Council, and by the EU FP7 project PAPETS (GA 323901).

SUPPORTING INFORMATION

Materials and methods

The synthesis of compound **1**, **2** and **3** was described previously.[223] The ^{1}H-NMR spectra were taken on a Varian spectrometer at 400 MHz. Samples were prepared using equal parts of $CDCl_3$ and CS_2 with 2% H_2O or D_2O and with 0.03% tetramethylsilane as an internal standard. For the spectroscopic investigations the compounds were dissolved in benzonitrile, benzonitrile with 2% v/v D_2O, and benzonitrile with 2% v/v H_2O. Benzonitrile and D_2O were purchased from Sigma Aldrich and used without further purification or deoxygenation.

Room-temperature steady-state absorption spectra were recorded on a Perkin Elmer Lambda 40 UV/VIS spectrometer. Both steady-state and transient absorption spectra were recorded using a 1 mm quartz cuvette.

Transient absorption spectroscopy was performed on a setup using two electronically synchronized amplified Ti:sapphire laser systems (Legend and Libra, Coherent, Santa Clara, CA) as described previously.[224] The amplifiers were seeded by a single 80 MHz oscillator (Vitesse, Coherent) and pumped with separate pump lasers (Evolution, Coherent). Both lasers have an 800 nm output at a repetition rate of 1 kHz. The output power is 3.0 W for the Legend and 4.5 W for the Libra.

For the measurements in benzonitrile, the output of the Legend was used to drive an optical parametric amplifier (OperA SOLO, TOPAS, Coherent) with which the excitation wavelength was set to 705 nm. Excitation energies of 1 µJ were used at a spot size of ~300 µm. A broadband probe beam was generated by focusing part of the output of the Libra on a CaF_2 or sapphire plate. The transient absorption signal was acquired in a multichannel fashion by spectrally dispersing the probe through a spectrograph projecting it on a 256-element diode array detector.[225] The instrument response function had a width of 100 fs (full width at half maximum).

The time difference between pump and probe was controlled in two ways. An optical delay line was used for delays of the pump beam in the fs to 3.5 ns regime. Delay steps of 12.5 ns were generated by selection and amplification of consecutive seed pulses of the oscillator. The timing of the amplification process of the Libra was controlled by a signal delay generator (SDG Elite, Coherent). A second signal delay generator – one that synchronizes with the first – governed the timing of the Legend (SDG, Coherent). By varying the triggering of the second SDG with respect to the first, delays of the probe were achieved up to 10 μs. Both delay methods were applied simultaneously, addressing the fs to μs range in a single experiment.

For the measurements in benzonitrile with 2% v/v D_2O or H_2O the pump and probe beam were both generated from the Libra. The time difference between pump and probe was set with an optical delay line, addressing the fs to 3.5 ns regime.

Global analysis of the transient absorption data was performed using the Glotaran program.[226] In global analysis all wavelengths are analyzed simultaneously with a set of common time constants and spectra.[79,227] Here, we present the results using a sequentially interconverting model. In a sequential analysis (1 → 2 → 3 →….) the numbers indicate evolution-associated difference spectra (EADS) that interconvert with successive mono-exponential decay times, each of which can be regarded as the lifetime of each EADS. The first EADS corresponds to the time-zero difference spectrum. The first EADS evolves into the second EADS with time constant τ_1, which in turn evolves in the third EADS with time constant τ_2, etc. This procedure clearly visualizes the evolution of the excited and intermediate states of the system. In general, the EADS may well reflect mixtures of difference spectra of pure electronic states, which may arise from heterogeneous ground states or branching at any point in the photo-induced evolution.[228-230] For a more detailed description of global analysis we refer to Van Stokkum et al. 2004.[79,227]

Transient absorption spectroscopy of compound 3

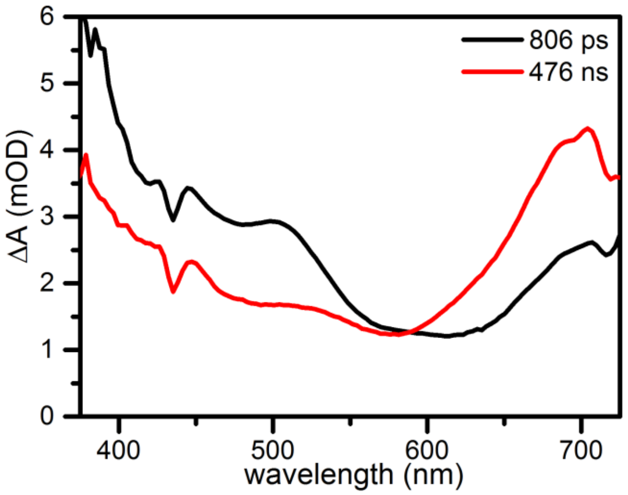

Figure S 32. EADS of **3** in benzonitrile upon 705 nm excitation.

Raw transient absorption data

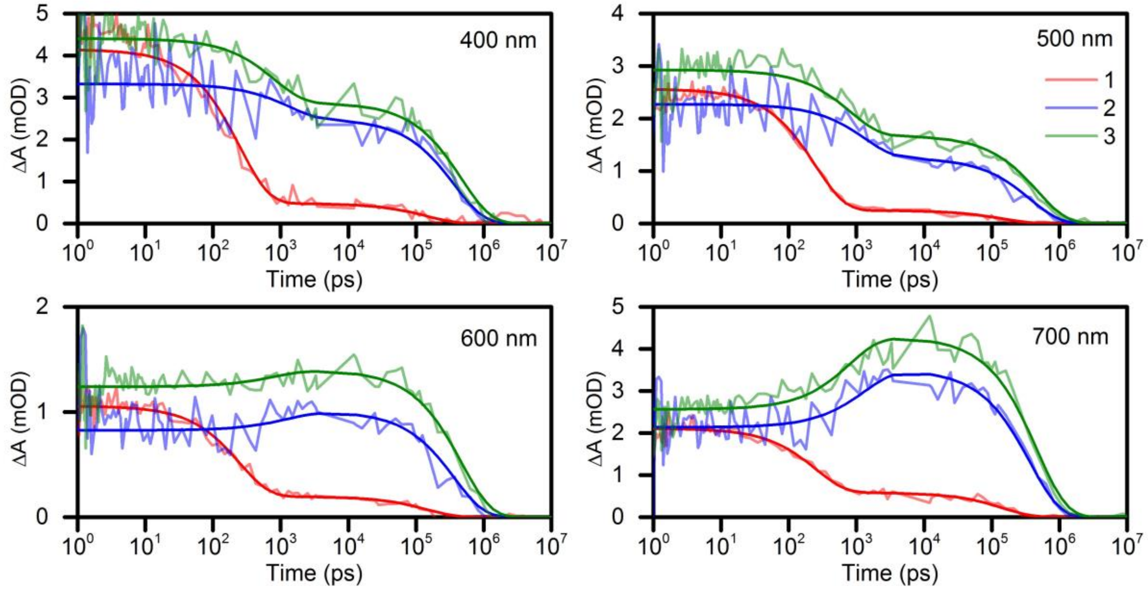

Figure S 33. Raw transient absorption data presented as time traces at 400, 500, 600 and 700 nm. The semi-transparent lines are raw data, the solid lines the fits of compound **1** (red), **2** (blue) and **3** (green).

^{1}*H-NMR of compounds 1 and 2*

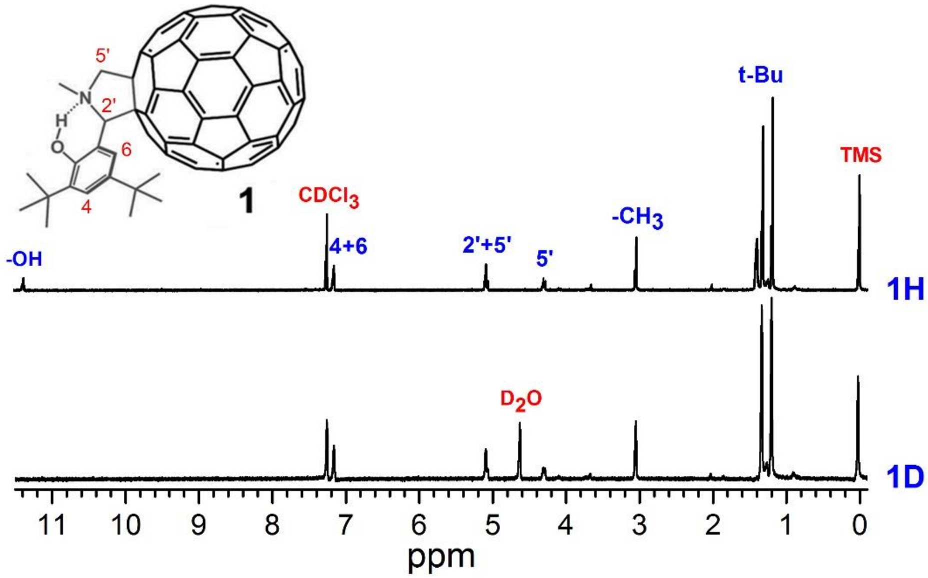

Figure S 34. ^{1}H-NMR of compound **1** in equal parts $CDCl_3/CS_2$ with 2% H_2O (**1-H**) or 2% D_2O (**1-D**).

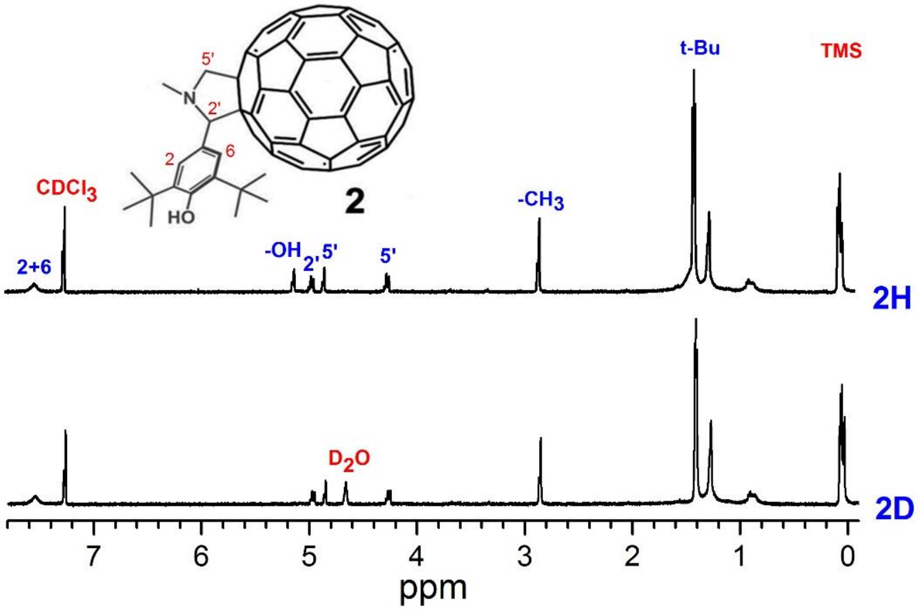

Figure S 35. *^{1}H-NMR of compound* ***2*** *in equal parts* $CDCl_3/CS_2$ *with 2%* H_2O (***2-H***) *or 2%* D_2O (***2-D***).

CHAPTER 5

QUINONES FOR MICROBIAL ELECTRO-PHOTOSYNTHESIS

INTRODUCTION

Photosynthetic microorganisms are capable of using solar energy to produce fuels but with very low efficiency and therefore cannot be used to replace fossil fuels. Artificial photosynthetic systems can efficiently product electricity but cannot yet produce complex molecules and fuels. Microbial Electro-Photosynthesis (MEPS) seeks to combine the efficiency of photovoltaics (PV) and the fuel production of microorganism to extract electrons from water and use photosynthetic organisms to capture and convert CO_2 into valuable fuels. PVs coupled with photosynthetic microorganisms can capture twice as many photons by expanding the photosynthetically active radiation (PAR) range from 400-700 nm to 400-1100 nm[26] and can be used with a water oxidation catalyst to extract electrons from water. At the start, platinum will be used to oxidize water but can be replaced as new technologies are developed.[231]

The MEPS system uses a strain of cyanobacteria lacking photosystem II (PSII)[232] and replaces the electrons usually provided by PSII with electrons delivered from a PV by redox mediators. These designed mediators will deliver electrons directly to the modified cyanobacteria's photosynthetic electron transport chain which has been designed to promote accepting external electrons (Figure 44). The cyanobacteria without PSII will grow while irradiated but without organic carbon, therefore it will accept the electrons from the redox mediators to grow and fix CO_2 and should evolve overtime to be more efficient.

The modified cyanobacteria can produce biofuels such as free fatty acids or other valuable organic compounds.[233]

The ideal mediator will be inexpensive, robust, highly-soluble, non-toxic, have a midpoint potential close to 0 mV deliver the electrons and protons to cytochrome b_6f, and allow photoelectroautotrophic growth. A pool of redox mediators were synthesized in order to screen for all of these characteristics. Mediators with too negative redox potentials may reduce other substances or generate H_2 at the cathode[234] and if the potential is too positive they may oxidize NAD(P)H and inhibit the growth. The mediator must also have the ability to cross multiple membranes, going through the outer membrane with a lipopolysaccharide layer, the peptidoglycan layer, and the cytoplasmic membrane before entering the thylakoid membrane. Then they must be able to get back out and reach the electrode again to be reduced. Duroquinone[235] and plastoquinone[236] (Figure X) have been shown to directly transfer electrons to cytochrome b_6f complex while benzoquinone has been shown to shuttle electrons from PSII or the plastoquinone pool, through the various membranes, to an electrode.[237] These results led to designing quinone-type mediators with varying alkane tails with the goal of determining what effects the mediator efficiency (Figure 45).

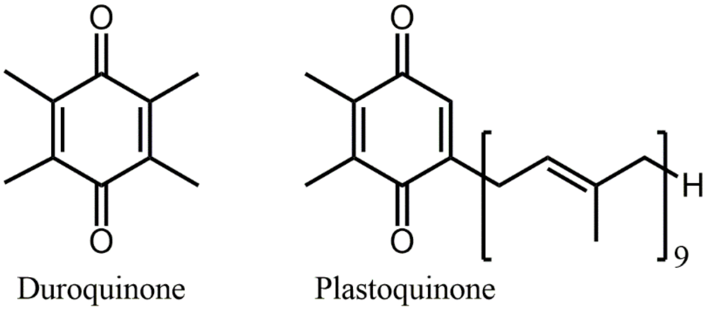

Figure 44. The structures of duroquinone and plastoquinone.

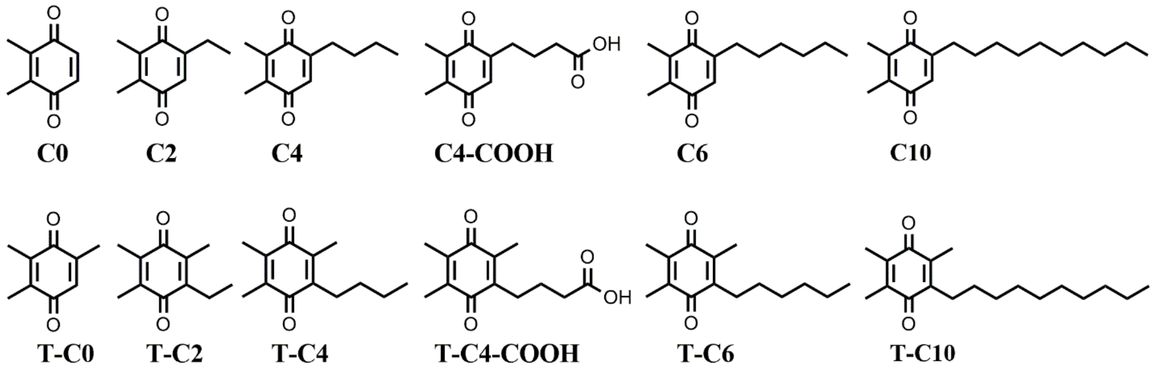

Figure 45. The structures of all the quinone mediators.

.

METHODS

Synthesis of Quinones

The synthetic scheme followed for the various quinones and hydroquinones is shown in Scheme 6. The hydroquinone starting material was oxidized using silver(I) oxide and then the desired alkyl chain was added using silver(I) nitrate and sodium persulfate. The stable quinones were kept in the fridge until they were ready to be tested. At that point, the quinones were reduced to the hydroquinones using sodium borohydride and either used immediately or stored in the -20 °C freezer until they are used.

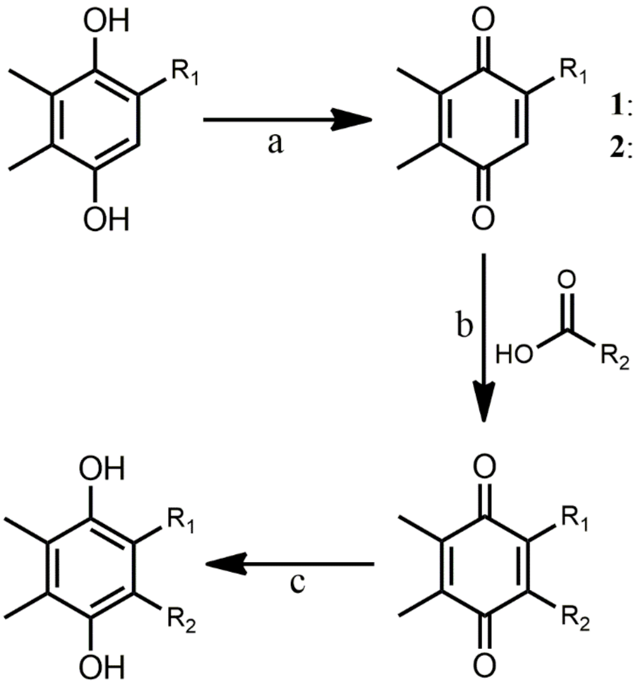

1: $R_1 = H$
2: $R_1 = CH_3$

C2 and **R-C2**: $R_1 = H, R_2 = CH_2CH_3$
C4 and **R-C4**: $R_1 = H, R_2 = CH_2CH_2CH_2CH_3$
C4-COOH: $R_1 = H, R_2 = CH_2CH_2CH_2COOH$
C6 and **R-C6**: $R_1 = H, R_2 = CH_2CH_2CH2CH_2CH_2CH_3$
C10 and **R-C10**: $R_1 = H, R_2 = CH_2CH_2CH_2CH_2CH_2CH_2CH_2CH_2CH_2CH_3$
T-C2 and **R-T-C2**: $R_1 = CH3, R_2 = CH_2CH_3$
T-C4 and **R-T-C4**: $R_1 = H, R_2 = CH_2CH_2CH_2CH_3$
T-C4-COOH: $R_1 = CH_3, R_2 = CH_2CH_2CH_2COOH$
T-C6 and **R-T-C6**: $R_1 = CH_3, R_2 = CH_2CH_2CH_2CH_2CH_2CH_3$
T-C10 and **R-T-C10**: $R_1 = CH_3, R_2 = CH_2CH_2CH_2CH_2CH_2CH_2CH_2CH_2CH_2CH_3$

Scheme 6. General synthetic route for the quinone redox mediators. a) Ag_2O, diethyl ether, 3 h; b) $AgNO_3$, $Na_2S_2O_8$, alkyl acid, acetonitrile/H_2O, 70 °C, 3 h; c) $NaBH_4$, THF/MeOH. RT→0 °C, 2 h.

Oxidation of 2,3-dimethylhydroquinone. In a 500 mL round bottom flask, 2,3-dimethylhydroquinone (10.0 g, 72.4 mmol) was dissolved in diethyl ether (300 mL). Silver oxide was added and the mixture was stirred vigorously for 3 h at room temperature. The silver oxide was removed by filtering the reaction mixture through celite and rinsing with diethyl ether. The solvent was removed by rotary evaporation to give 2,3-dimethylquinone (**1**) as a yellow solid (8.10 g, 82% yield). ^{1}H-NMR δ ppm ($CDCl_3$): 2.04 (6H, s), 6.73 (2H, s). UV/vis λ_{max} (EtOH): 335 nm.

Oxidation of trimethylhydroquinone. Trimethylhydroquinone (20.0 g, 131 mmol) was dissolved in diethyl ether (600 mL) and to that was added silver oxide (36.0 g, 157 mmol). The reaction was stirred vigorously at room temperature for 2 h and then the silver oxide was removed by filtering the reaction mixture through celite. The solvent was removed by rotary evaporation to yield trimethylquinone (**2**) as a yellow solid in a 98.0 % yield (19.7 g). ^{1}H-NMR δ ppm ($CDCl_3$): 1.99 (3H, s), 2.01 (3H, s), 2.03 (3H, s), 6.54 (1H, s). UV/vis λ_{max} (EtOH): 340 nm.

General synthesis of trisubstituted quinones. In a three-neck round bottom flask equipped with a condenser, addition flask, and a rubber stopper was placed 2,3-dimethylquinone (3.0 g, 22.0 mmol), acid (19.8 mmol), water (100 mL), and acetonitrile (100 mL). The set-up was flushed with argon and simultaneously a solution of sodium persulfate (6.29 g, 26.4 mmol) in water (60 mL) was flushed with argon. The sodium persulfate solution was added to the addition flask and the setup was flushed with argon again. Silver nitrate (3.36 g, 19.8 mmol) was quickly added to the flask and the setup was flushed again with argon. The reaction was heated to 75 °C and the sodium persulfate solution was added slowly, dropwise over 1.5 hrs. The reaction was then allowed to stir for 1 h at 75 °C. The reaction was cooled to room temperature and the acetonitrile was removed via rotary evaporation. Dichloromethane (DCM) was added and a white precipitate formed. The mixture was filtered and extracted with DCM. The organic layer was collected and dried over sodium sulfate, then filtered and concentrated. The mixture was purified by silica gel column chromatography (1:1 hexane:DCM). The first band to elute was the disubstituted side product. The second band to elute was the desired trisubstituted product. The third band to elute was the starting material.

General synthesis of tetrasubstituted quinones. The tetrasubstituted quinones were synthesized following a similar procedure as for trisubstituted quinones. In a three-neck round bottom flask equipped with a condenser, addition flask, and a rubber stopper was placed trimethylquinone (2.0 g, 13.3 mmol), alkyl carboxylic acid (13.3 mmol), water (70 mL), and acetonitrile (70 mL). The set-up was flushed with argon and simultaneously a solution of sodium persulfate (3.81 g, 16.0 mmol) in water (50 mL) was flushed with argon. The sodium persulfate solution was added to the addition flask and the setup was flushed with argon again. Silver nitrate (2.26 g, 13.3 mmol) was quickly added to the flask and the setup was flushed with argon again. The reaction was heated to 75 °C and the sodium persulfate solution was added slowly, dropwise over 1.5 hrs. The reaction was then allowed to stir for 1 h at 75 °C. The reaction was cooled to room temperature and the acetonitrile was removed via rotary evaporation. DCM was added and a white precipitate formed. The mixture was filtered then extracted with DCM. The organic layer was collected and dried over sodium sulfate, then filtered and concentrated. The mixture was purified by silica gel column chromatography (1:1 hexane:DCM). The first band to elute was the product. The second band to elute was the starting material.

General synthesis for acid hydrolysis of the quinones. Quinones bearing ester functional groups were hydrolyzed to give a carboxylic acid by dissolving the quinone-ester (100 mg, 0.4 mmol) in THF (20 mL) and H_2O (3 mL). HCl (1.0 mL, 12.0 mmol) was added dropwise and the reaction was refluxed at 65 °C for 12 h. The solvent was removed under reduced pressure, the mixture was resuspended in DCM, and washed with dionized water. The organic layer was dried over sodium sulfate and the solvent was removed under reduced pressure. The crude mixture was purified by silica gel column chromatography (20% ethyl acetate/DCM) to give a yellow solid.

5-Ethyl-2,3-dimethylquinone (C2). Prepared by the trisubstituted quinone procedure and propanoic acid. ^{1}H-NMR δ ppm ($CDCl_3$): 1.13 (3H, t, *J* = 7.4, 7.4), 2.01 (3H, s), 2.03 (3H, s), 2.46 (2H, q, *J* = 7.4, 7.4, 7.4), 6.50 (1H, s). UV/vis λ_{max} (EtOH): 339 nm.

5-Butyl-2,3-dimethylquinone (C4). Prepared by the trisubstituted quinone procedure and valeric acid. ^{1}H-NMR δ ppm ($CDCl_3$): 0.92 (3H, t, *J* = 7.2, 7.2), 1.37 (2H, m), 1.47 (2H, m), 2.00 (3H, s), 2.02 (3H, s), 2.40 (2H, t, *J* = 6.9, 6.9), 6.49 (1H, s). UV/vis λ_{max} (EtOH): 342 nm.

5-(Methyl 4-butanoate)-2,3-dimethylquinone (C4-E). Prepared by the trisubstituted quinone procedure and 5-methoxy-5-oxopentanoic acid. ^{1}H-NMR δ ppm ($CDCl_3$): 1.85 (2H, p), 2.01 (3H, s), 2.03 (3H, s), 2.40 (2H, t, *J* = 7.4, 7.4), 2.47 (2H, t, *J* = 7.6, 7.6), 3.67 (3H, s), 6.54 (1H, s). UV/vis λ_{max} (EtOH): 340 nm.

5-(4-Butanoic acid)-2,3-dimethylquinone (C4-COOH). Prepared by acid hydrolysis procedure for quinones. ^{1}H-NMR δ ppm ($CDCl_3$): 1.86 (2H, p), 2.01 (3H, s), 2.03 (3H, s), 2.43 (2H, t, *J* = 7.0, 7.0), 2.49 (2H, t, *J* = 7.6, 7.6), 6.54 (1H, s). UV/vis λ_{max} (EtOH): 337 nm.

5-Hexyl-2,3-dimethylquinone (C6). Prepared by the trisubstituted quinone procedure and heptanoic acid. . ^{1}H-NMR δ ppm ($CDCl_3$): 0.88 (3H, t, *J* = 6.9, 6.9), 1.28-1.38 (6H, m), 1.49 (2H, p), 2.01 (3H, s), 2.03 (3H, s), 2.40 (2H, t, *J* = 7.0), 6.50 (1H, s). UV/vis λ_{max} (EtOH): 338 nm.

5-Decyl-2,3-dimethylquinone (C10). Prepared by the trisubstituted quinone procedure and undecanoic acid. ^{1}H-NMR δ ppm (CDCl$_3$): 0.88 (3H, t, *J* = 6.72, 6.72), 1.22-1.40 (14H, m), 1.50 (2H, p), 2.01 (3H, s), 2.03 (3H, s), 2.41 (2H, t, *J* = 7.3), 6.50 (1H, s). UV/vis λ_{max} (EtOH): 340 nm.

2-Ethyl-3,5,6-trimethylquinone (T-C2). Prepared by the tetrasubstituted quinone procedure and propanoic. ^{1}H-NMR δ ppm (CDCl$_3$): 1.04 (3H, t, *J* = 7.55, 7.55), 2.01 (6H, s), 2.03 (3H, s), 2.50 (2H, q, *J* = 7.5, 7.5, 7.5). UV/vis λ_{max} (EtOH): 340 nm.

2-Butyl-3,5,6-trimethylquinone (T-C4). Prepared by the tetrasubstituted quinone procedure and valeric. ^{1}H-NMR δ ppm (CDCl$_3$): 0.93 (3H, t, *J* =7.0, 7.0), 1.38 (4H, m), 2.01 (6H, s), 2.02 (3H, s), 2.47 (2H, t. *J* = 7.4, 7.4). UV/vis λ_{max} (EtOH): 344 nm.

2-(Methyl 4-butanoate)-3,5,6-trimethylquinone (T-C4-E). Prepared by the tetrasubstituted quinone procedure and 5-methoxy-5-oxopentanoic acid. ^{1}H-NMR δ ppm (CDCl$_3$): 1.75 (2H, p), 2.01 (6H, s), 2.05 (3H, s), 2.38 (2H, t, *J* = 7.3, 7.3), 2.53 (2H, t, *J* = 7.9, 7.9), 3.68 (3H, s). UV/vis λ_{max} (EtOH): 335 nm.

2-(4-Butanoic acid)-3,5,6-trimethylquinone (T-C4-COOH). Prepared by the acid hydrolysis procedure for quinones. ^{1}H-NMR δ ppm (CDCl$_3$): 1.75 (2H, p, *J* = 7.4, 7.4, 15.0), 2.01 (6H, s), 2.04 (3H, s), 2.42 (2H, t, *J* = 7.3, 7.3), 2.55 (2H, t, *J* = 7.9, 7.9). UV/vis λ_{max} (EtOH): 342 nm.

2-Hexyl-3,5,6-trimethylquinone (T-C6). Prepared by the tetrasubstituted quinone procedure and heptanoic acid. ^{1}H-NMR δ ppm (CDCl$_3$): 0.88 (3H, t, *J* = 6.7, 6.7), 1.26-1.33 (4H, m), 1.34-1.42 (4H, m), 2.00 (6H, s), 2.01 (3H, s), 2.46 (2H, t, *J* = 7.3, 7.3). UV/vis λ_{max} (EtOH): 338 nm.

2-Decyl-3,5,6-trimethylquinone (T-C10). Prepared by the tetrasubstituted quinone procedure and undecanoic acid. ^{1}H-NMR δ ppm ($CDCl_3$): 0.88 (3H, t, *J* = 6.8, 6.8), 1.23-1.43 (16H, m), 2.01 (6H, s), 2.02 (3H, s), 2.46 (2H, t, *J* = 7.4, 7.4). UV/vis λ_{max} (EtOH): 341 nm.

General Procedure for Quinone Reduction. In a dry round bottom flask a sample of the quinone (0.61 mmol) was dissolved in anhydrous tetrahydrofuran (2 mL) and anhydrous methanol (0.5 mL). The mixture was flushed with argon and then sodium borohydride (4.9 mmol) was added. The reaction was flushed with argon again and then allowed to stir at room temperature for 30 min. The reaction was then placed in an ice bath and allowed to stir for an additional 1.5 h. While still on ice, cold water was added (1.5 mL) and the volatile solvents were removed by bubbling the mixture with argon. A white precipitate formed and was collected by filtration. The water was removed from the white solid and the reduced quinone was stored in the -20 °C freezer.

5-Ethyl-2,3-dimethylhydroquinone (R-C2). . ^{1}H-NMR δ ppm ($CDCl_3$): 1.22 (3H, t, *J* = 7.6, 7.6), 2.15 (3H, s), 2.18 (3H, s), 2.56 (2H, q, *J* = 7.6, 7.6, 7.6), 4.24 (1H, s), 4.25 (1H, s), 6.47 (1H, s).

5-Butyl-2,3-dimethylhydroquinone (R-C4). ^{1}H-NMR δ ppm ($CDCl_3$): 0.93 (3H, t, *J* = 7.2, 7.2), 1.32-1.61 (4H, m), 2.01 (3H, s), 2.03 (3H, s), 2.41 (2H, t, *J* = 8.2, 8.2), 4.27 (1H, s), 4.37 (1H, s), 6.50 (1H, s).

5-Hexyl-2,3-dimethylhydroquinone (R-C6). ^{1}H-NMR δ ppm ($CDCl_3$): 0.89 (3H, t, *J* = 6.9, 6.9), 1.25-1.41 (6H, m), 1.58 (2H, p), 2.15 (3H, s), 2.18 (3H, s), 2.51 (2H, t, *J* = 7.8, 7.8), 4.24 (1H, s), 4.28 (1H, s), 6.45 (1H, s).

5-Decyl-2,3-dimethylhydroquinone (R-C10). ^{1}H-NMR δ ppm ($CDCl_3$): 0.88 (3H, t, *J* = 6.8, 6.8), 1.22-1.39 (14H, m), 1.58 (2H, p), 2.15 (3H, s), 2.18 (3H, s), 2.51 (2H, t, *J* = 7.8, 7.8), 4.24 (1H, s), 4.28 (1H, s), 6.45 (1H, s).

2-Ethyl-3,5,6-trimethylhydroquinone (R-T-C2). ^{1}H-NMR δ ppm ($CDCl_3$): 1.13 (3H, t, *J* = 7.6, 7.6), 2.17 (6H, s), 2.19 (3H, s), 2.66 (2H, q, *J* = 7.6, 7.6, 7.6), 4.24 (1H, s), 4.25 (1H, s).

2-Butyl-3,5,6-trimethylhydroquinone (R-T-C4). ^{1}H-NMR δ ppm ($CDCl_3$): 0.95 (3H, t, *J* = 6.9, 6.9), 1.36-1.51 (4H, m), 2.17 (6H, s), 2.18 (3H, s), 2.62 (2H, t, *J* = 7.7, 7.7), 4.24 (1H, s), 4.25 (1H, s).

2-Hexyl-3,5,6-trimethylhydroquinone (R-T-C6). ^{1}H-NMR δ ppm ($CDCl_3$): 0.88 (3H, t, *J* = 6.9, 6.9), 1.22-1.51 (8H, m), 2.15 (6H, s), 2.17 (3H, s), 2.59 (2H, t, *J* = 7.8, 7.8), 4.22 (1H, s), 4.23 (1H, s).

2-Decyl-3,5,6-trimethylhydroquinone (R-T-C10). ^{1}H-NMR δ ppm ($CDCl_3$): 0.88 (3H, t, *J* = 6.9, 6.9), 1.22-1.52 (16H, m), 2.17 (6H, s), 2.18 (3H, s), 2.60 (2H, t, *J* = 7.9, 7.9), 4.23 (1H, s), 4.25 (1H, s).

RESULTS

The preliminary quinone pool was successfully synthesized, reduced, and some compounds were tested for water solubility. The water solubility was estimated using the absorption spectra and Beer's Law. The extinction coefficient of each quinone was determined by a calibration curve in ethanol, because it was the solvent most similar to water that the quinones were soluble in. Then, a saturated solution of the quinone in water was made and the absorption was measured. Using Beer's Law, the concentration of the quinone in water can be calculated:

$$A = \varepsilon b c \tag{1}$$

A is for the measured absorbance, ε is the determined extinction coefficient, b is the path length of the cell which was 1 cm, and c is the concentration of the solution. The water solubility of a few compounds at room temperature is shown in Table 4. This method of estimating the water solubility at 25 °C was only effective for the compounds with alkyl tails shorter than four carbons. Any quinones with longer than a four carbon tail were below the detection limit of this method.

Table 4. The water solubility of various quinones at 25 °C.

Compound	**Water Solubility**
C2	5.0 mM
T-C2	0.23 mM
C4	0.5 mM
T-C4-E	0.5 mM
C4-COOH	1.9 mM

The quinones will be tested in short-term experiments for their ability to shuttle the electrons between the cyanobacteria and electrode. They will also be tested in long-term reactors to test for toxicity and growth, as well as long term stability and current.

CONCLUSIONS

The final MEPS prototype is calculated to be 30% more efficient than the cyanobacteria wildtype and the tandem design could result in thermodynamic efficiencies nearing 40%.[26]

The PV in tandem with a bioreactor could drive our MEPS system without any additional land and our modular design could accept electricity from any renewable source, like hydro, wind, and geothermal as well as PV. The MEPS system could cohabit with a power plant to utilize the heat waste, water, CO_2 and electricity, providing bioremediation. The final goal is to develop a system that is capable of producing a renewable fuel at less than $3 per gallon which our system has the potential to do.

CHAPER 6

SYNTHESIS OF OTHER PHOTOSENSITIZERS

A variety of chromophores have been synthesized for applications in artificial photosynthesis related research. Typically either a ruthenium or porphyrin chromophore is used as the photosensitizer in the water oxidation cell.[15,25] The first porphyrin discussed is a simple, high potential porphyrin, bearing a carboxylic acid anchoring group (Figure 46). The second group of porphyrins were synthesized for the purpose of using click chemistry to attach the porphyrin to semiconductors or for attachment of heterogeneous catalysts for water oxidation such as IrO_2 to the porphyrins (see below). (Figure 47).[238-241] The third group of porphyrins are water soluble porphyrin chromophores (Figure 48). Lastly, the synthesis of a new ruthenium complex is detailed (Figure 49).

The high-potential porphyrin, compound **2**, was synthesized following Scheme 7. The synthesis starts by following the Lindsey method, first synthesizing the dipyrromethane and then condensing the porphyrin with the dipyrromethane and the two aldehydes.[242] The 5-(pentafluorophenyl)dipyrromethane was synthesized following a literature procedure[175] and then two equivalences of it were reacted with one equivalence of 4-bromobenzaldehyde and one equivalence of methyl 4-formylbenzanoate. The ester of the resulting porphyrin was hydrolyzed using HCl to give the final product, compound **2**.

The synthesis of the second groups of compounds to be used in click chemistry are outlined in Scheme 8-Scheme 10. The terminal alkyne moiety was synthesized with the purpose of attachment to nanoparticles, like IrO_2, and then covalently linking the water soluble nanoparticles to the organic soluble porphyrin chromophores bearing an azide functionality using a copper-catalyzed click reaction. The **alkyne-IDAA** compound was synthesized following Scheme 8. Iminodimethylester (IDME) was reacted with propargyl bromide in an S_N2 fashion to give **alkyne-IDME**. The **alkyne-IDME** was used for the test click reactions but the esters could also be hydrolyzed to give the di-acid, **alkyne-IDAA**, which can be used for attachment to nanoparticles.

Two porphyrins were synthesized with azide functional groups, compound **6** and compound **14**. Compound **6** was synthesized following Scheme 9. The porphyrin was condensed to give a nitro group. Zinc was inserted into the macrocycle, then the nitro group was reduced to the amine and then the amine was substituted with an azide through a diazonium intermediate. Compound **6** was reacted with **alkyne-IDME** via a click reaction to give the product, compound **7**, as a proof of concept for this type of click reaction.

Compound **14** was synthesized following a similar protocol (Scheme 10) but bearing an anchoring group as well as the azide group. The required dipyrromethanes and aldehydes were condensed to give a high-potential porphyrin with a nitro and an ester functionality. The ester was hydrolyzed using acid and then reacted with IDME using an acid-chloride coupling to give compound **10**. Zinc was then inserted to the macrocycle and then the nitro group was reduced to the amine and then substituted with an azide. Compound **13** could be used for testing the click reaction with **alkyne-IDME** for a second proof of concept. The esters of compound **13** were also hydrolyzed using mild-base hydrolysis to give compound **14** which could be attached to a semiconductor for click chemistry on the surface of an electrode.

The last group of porphyrins discussed in this chapter are the water soluble porphyrins, **tetra-COOH** and **tetra-IDAA**. **Tetra-COOH** was synthesized following Scheme 11. The porphyrin was condensed using the Adler-Longo method to give **tetra-**

COOMe and the esters were hydrolyzed using base-hydrolysis to give **tetra-COOH**, a water soluble porphyrin. **Tetra-IDAA** was synthesized following a very different protocol (Scheme 12). The aldehyde of methyl-4-formylbenzanoate was protected using p-toluenesulfonic acid. The ester was then hydrolyzed and the resulting carboxylic acid was reacted with iminodimethyl ester to give compound **17**. Compound **17** was then used in the synthesis of a symmetric porphyrin, compound **tetra-IDME**. The esters were hydrolyzed using a base-hydrolysis to give the final product, water soluble **tetra-IDAA**.

Lastly, a ruthenium dye bearing the IDAA anchoring group was synthesized because although porphyrins have been shown to have good stability over time, the photocurrent is lower than a ruthenium dye.[40,243] One of the drawbacks to ruthenium dyes is they tend to desorb from the surface quickly. The aim of this synthesis was to design a ruthenium bipyridine chromophore bearing an anchoring group that may be more stable in aqueous conditions, imidodiacetic acid. The ruthenium chromophore, **Ru-IDAA**, was synthesized following Scheme 13. The **bpy-IDME** was made with an acid chloride coupling between 2,2'-bipyridine-4,4'-dicarboxylic acid and **IDME**. The **Ru-IDME** was condensed following a literature procedure for a similar compound.[244] Finally, the esters were hydrolyzed to give the carboxylic acids using mild basic conditions.

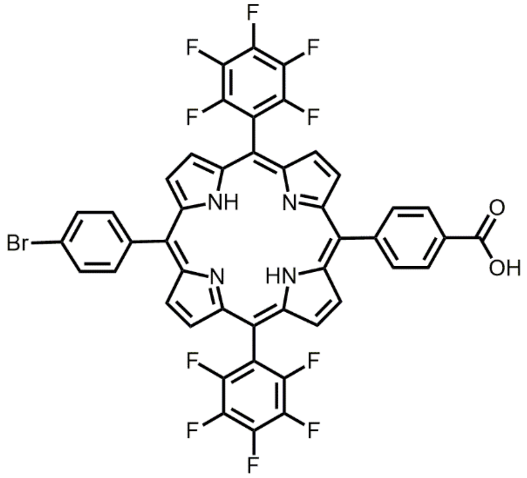

Figure 46. Structure of the simple, high-potential porphyrin, compound **2**.

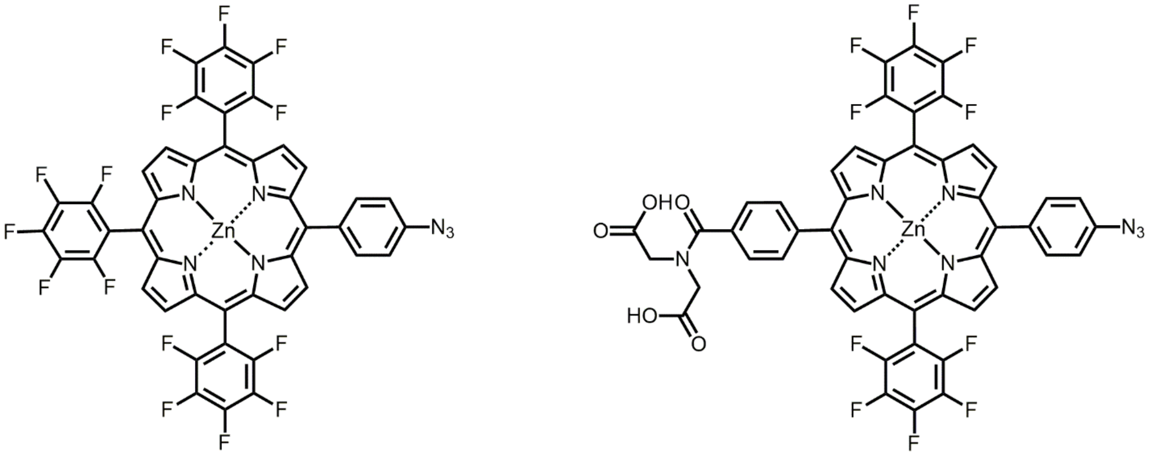

Figure 47. Structure of compounds **6** and **14**, porphyrins to be used in click chemistry.

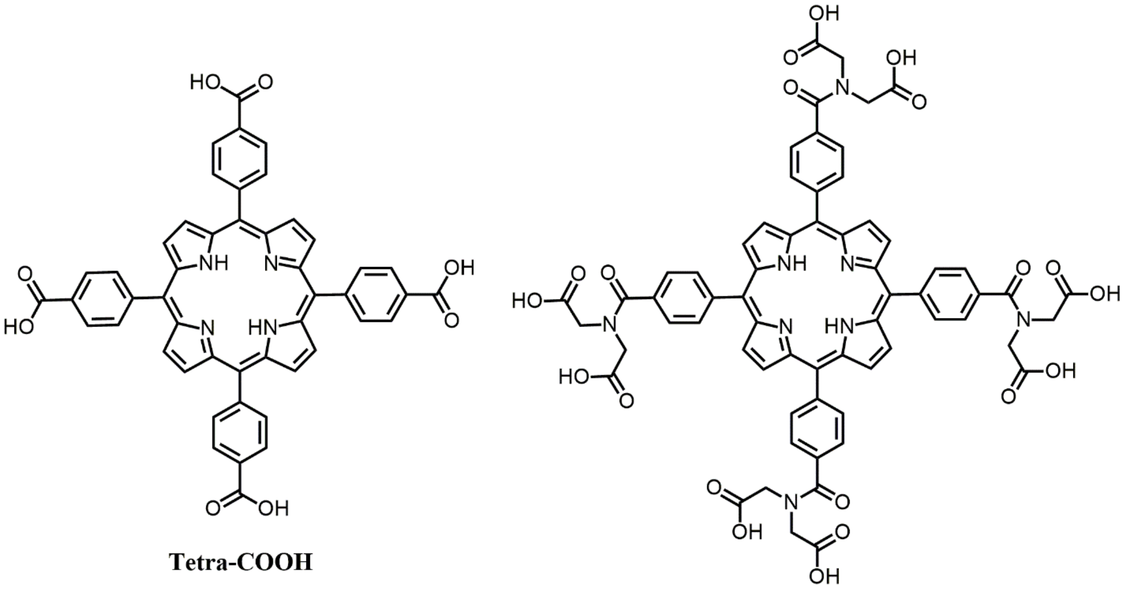

Tetra-COOH

Tetra-IDAA

Figure 48. Structure of the water soluble porphyrins, **tetra-COOH** and **tetra-IDAA**.

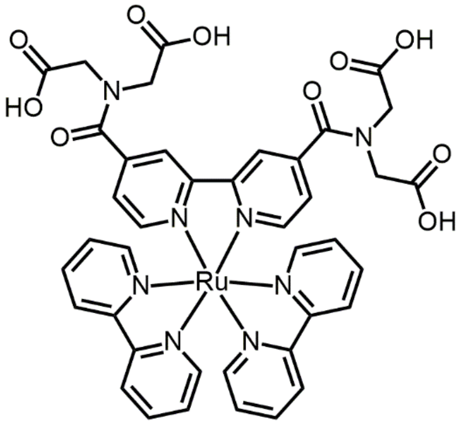

Figure 49. Structure of the ruthenium chromophore bearing the imidodiacetic acid anchoring group, **Ru-IDAA**.

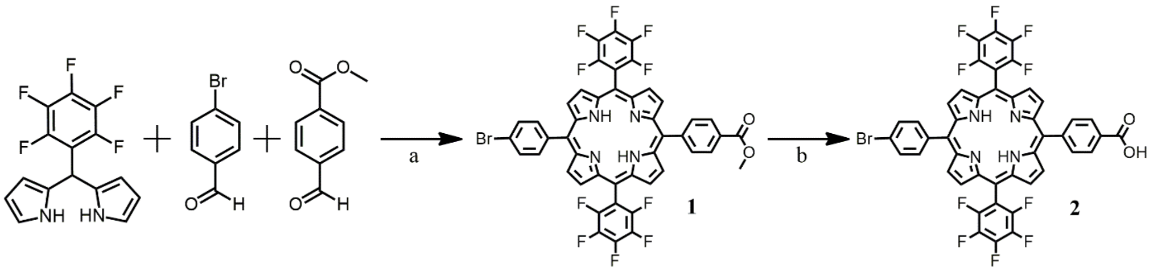

Scheme 7. Synthesis of the high potential porphyrin, **2**: a) 1. $BF_3(OEt)_2$, 2 h, 2. DDQ, 12 h, $CHCl_3$; b) HCl/TFA, 90 °C, 12 h.

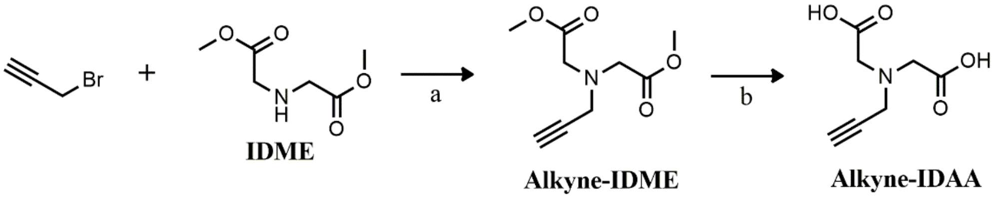

Scheme 8. Synthesis of **alkyne-IDAA**: a) DIPEA, acetone, 35 °C, 12 h; b) KOH, $THF/EtOH/H_2O$, 12 h.

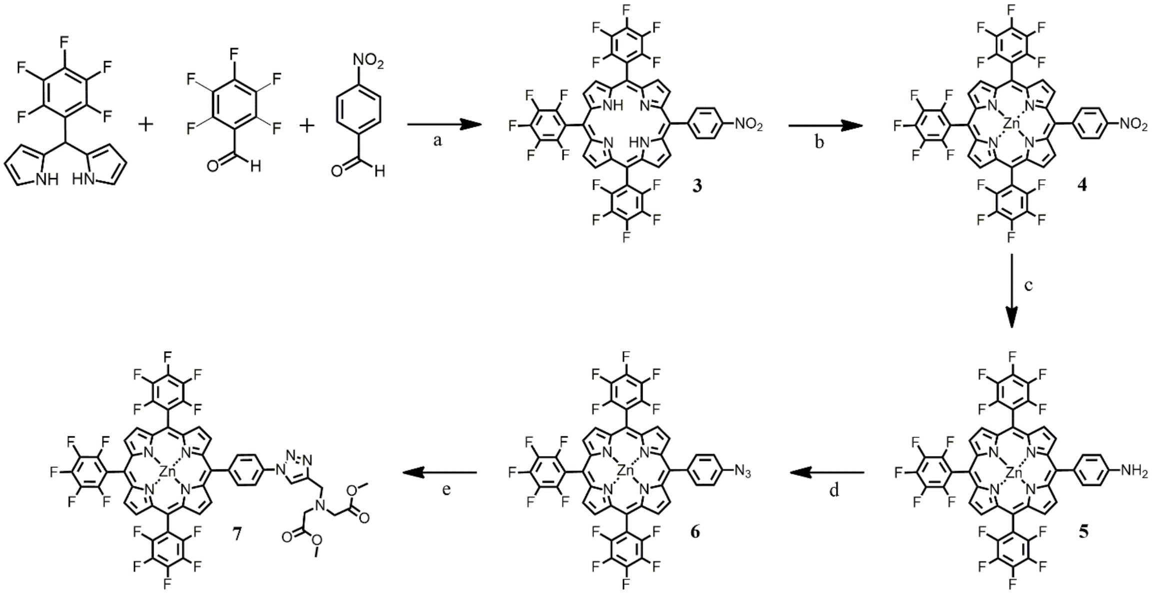

Scheme 9. Synthesis of porphyrin **6** and its click reaction product, **7**: a) 1. $BF_3(OEt)_2$, 2 h, 2. DDQ, 12 h, $CHCl_3$; b) $ZnOAc•2H_2O$, THF, 60 °C, 12 h; c) Zn dust/acetic acid, DCM, 1 h; d) $tBuNO_2/TMSN_3$, THF/ACN, 0 °C → room temperature, 2h; e) **alkyne-IDME**/$[Cu(CH_3CN)_4]PF_6$/DIPEA/TBTA, DMF, 100 °C, 12 h.

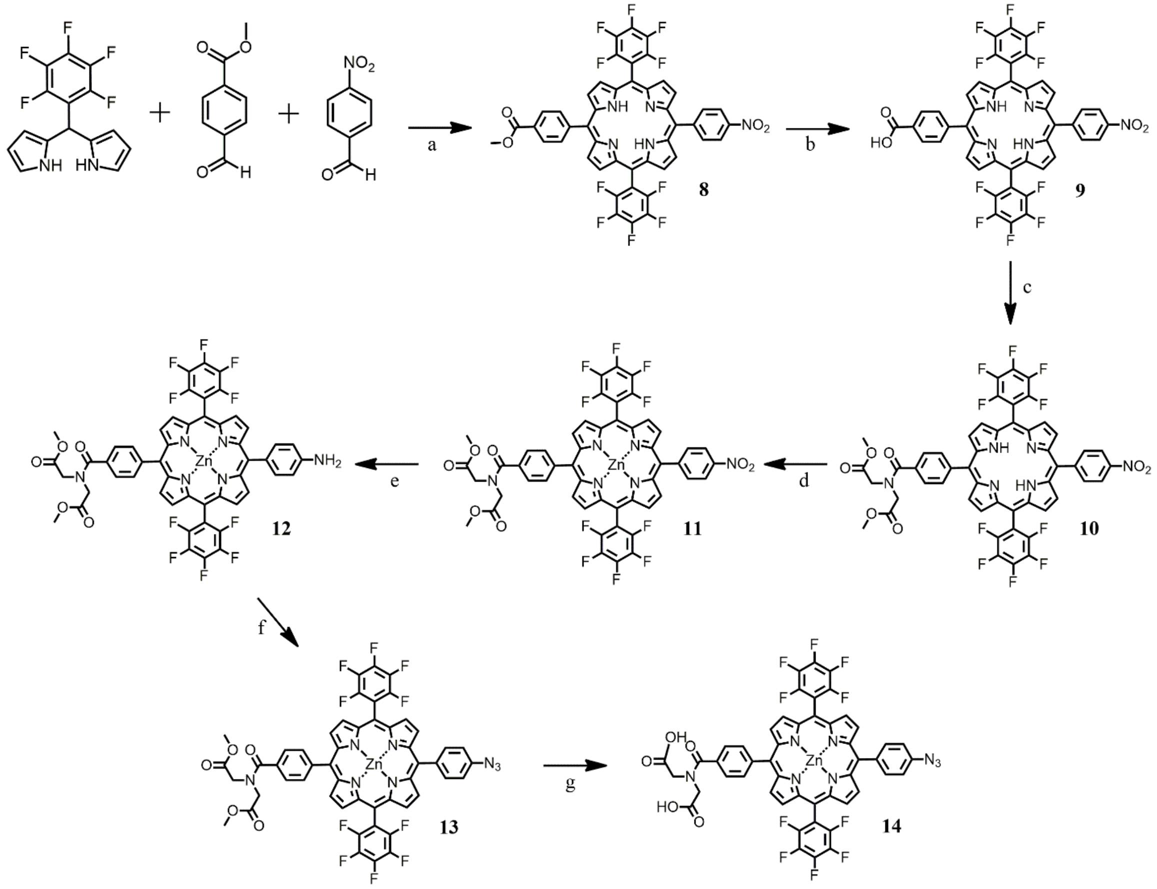

Scheme 10. Synthesis of compound **14**: a) 1. $BF_3(OEt)_2$, 2 h, 2. DDQ, 12 h, $CHCl_3$; b) 12 M HCl/TFA, 80 °C, 24 h; c) 1. Oxalyl chloride, 1 h, 2. IDME, 12 h, benzene/pyridine; d) $ZnOAc\bullet2H_2O$, THF, 60 °C, 12 h; e) Zn dust/acetic acid, DCM, 1 h; f) $tBuNO_2/TMSN_3$, THF/ACN, 0 °C → room temperature, 1 h; g) LiOH, $THF/MeOH/H_2O$, 18 h.

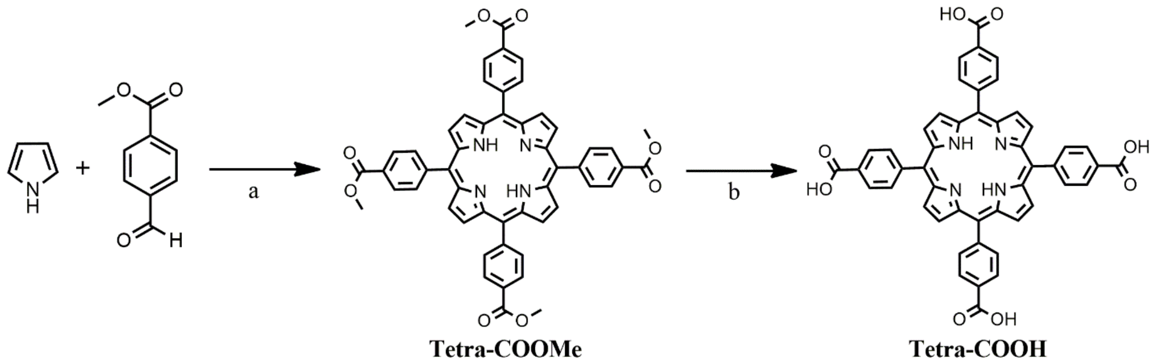

Scheme 11. Synthesis of **tetra-COOH**: a) propanoic acid, 118 °C, 1 h; b) KOH, THF/MeOH/H_2O, 18 h.

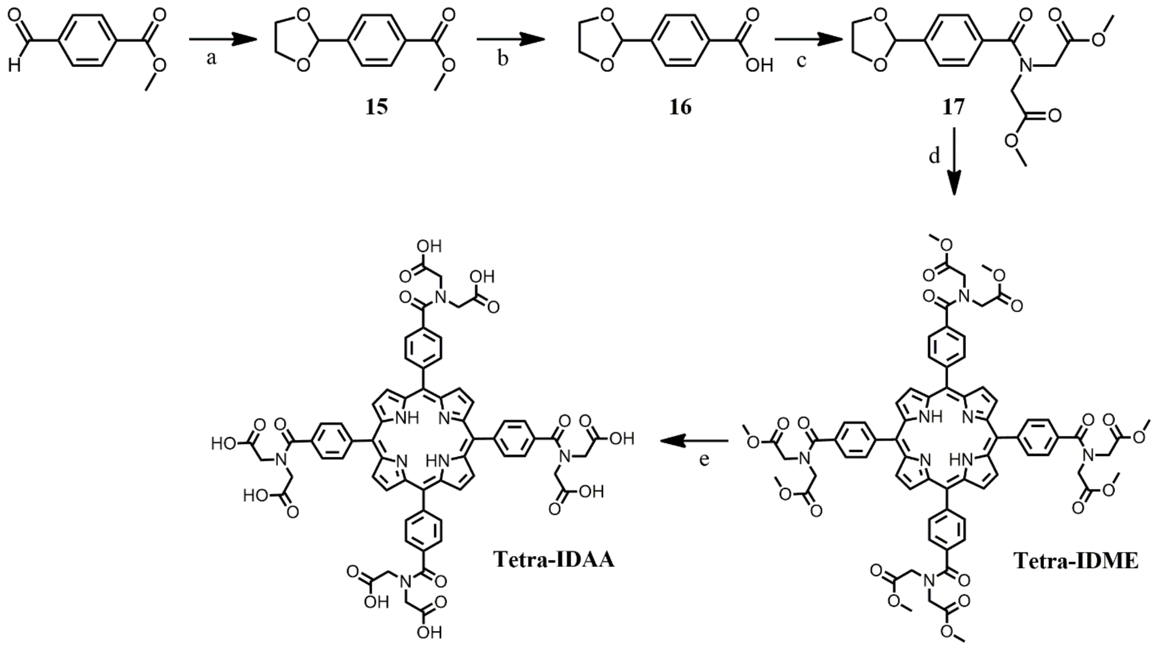

Scheme 12. Synthesis of **tetra-IDAA**: a) ethylene glycol/p-toluenesulfonic acid, benzene, 90 °C, 18 h; b) KOH, THF/EtOH, 40 °C, 12 h; c) 1. $SOCl_2$, 1 h, 2. IDME, 18 h, THF/pyridine; d) 1. pyrrole/$BF_3(OEt)_2$, 2 h, 2. DDQ, 12 h, $CHCl_3$; e) KOH, THF/EtOH/H_2O, 1 h.

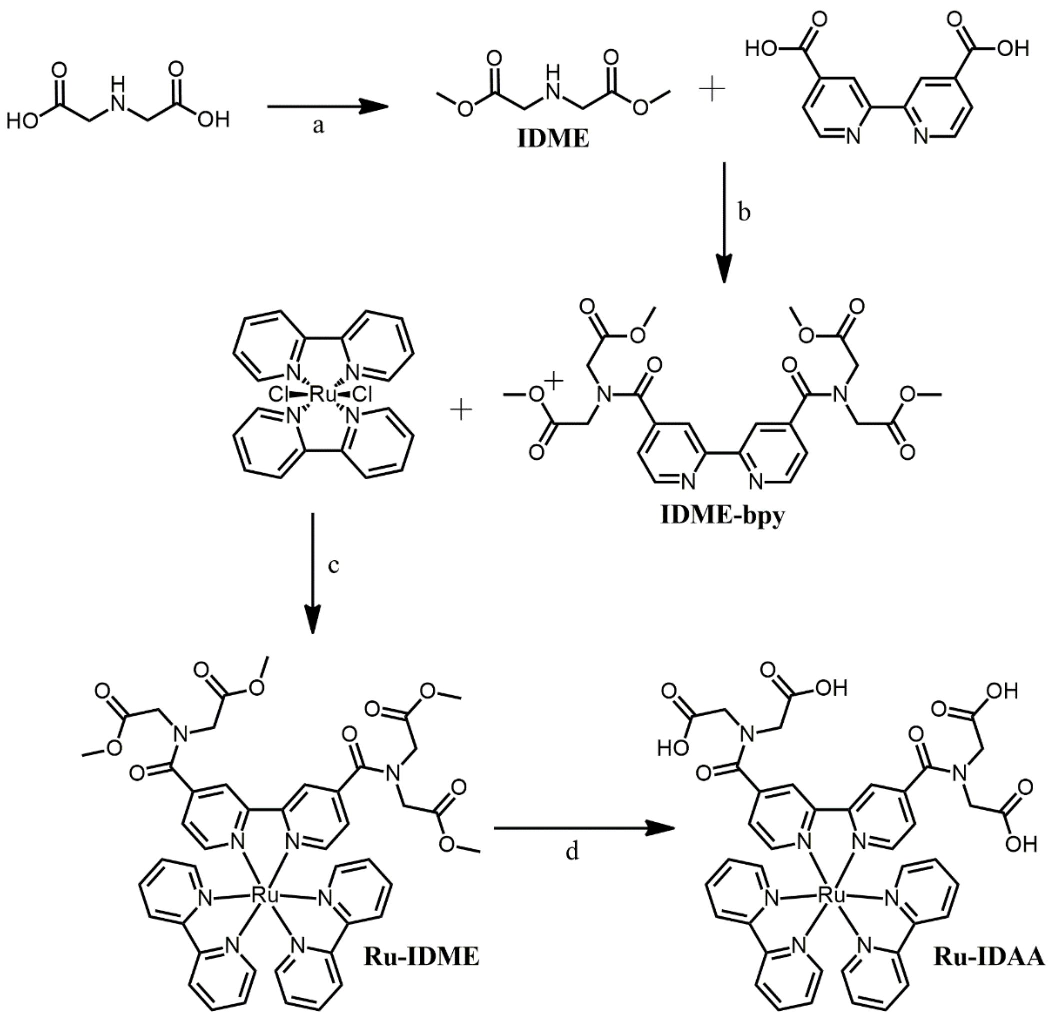

Scheme 13. Synthetic scheme for the synthesis of $[Ru(bpy)_2(4,4'\text{-}(CONH(CH_2COOH)_2)_2bpy)]Cl_2$ a) 1. $SOCl_2$/MeOH, -15 °C → RT, 12 h, 2. TEA/diethyl ether, 1h; b) $SOCl_2$/THF/pyridine, 12 h; c) EtOH/H_2O, reflux, 12 h; d) 70 mM NaOH/H_2O, RT, 1 h.

*Synthesis of 5-(4-benzoic acid)-15-(4-bromophenyl)-10,20-bis(pentafluorophenyl)porphyrin (**2**).*

5-(Methyl-4-benzoate)-15-(4-bromophenyl)-10,20-bis(pentafluorophenyl)porphyrin (1). In a 1000 mL round-bottom flask was placed 5-(pentafluorophenyl)dipyrromethane

(2.0 g, 6.4 mmol), methyl-4-formylbenzoate (0.53 g, 3.2 mmol), and 4-bromobenzaldehyde (0.59 g, 3.2 mmol). The compounds were dissolved in chloroform stabilized with 1% ethanol (750 mL) and the mixture was bubbled with argon for 30 min. Boron trifluoride diethyl etherate (0.35 mL) was added and the reaction stirred at room temperature for 2 h. Then, 2,3-dichloro-5,6-dicyano-1,4-benzoquinone (1.96 g, 8.64 mmol) was added and the reaction was stirred for 18 h. The mixture was dried down under reduced pressure and then resuspended in ethyl acetate and washed with aqueous sodium bicarbonate and then dried over sodium sulfate. The solution was concentrated and then the crude mixture was passed through a silica pad using dichloromethane (DCM) as the eluent. The crude product was then purified using silica gel column chromatography (40 % hexane:DCM) to yield a purple solid (400 mg, 0.43 mmol, 13% yield). MALDI-TOF: *m/z* obsd. 930.08 calc. 930.07 for $C_{46}H_{21}BrF_{10}N_4O_2$.

5-(4-benzoic acid)-15-(4-bromophenyl)-10,20-bis(pentafluorophenyl)porphyrin (2). Compound **1** (400 mg, 0.43 mmol) was placed in a 500 mL round bottom flask and was dissolved in trifluoroacetic acid (80 mL). Hydrochloric acid (160 mL) was slowly added through a funnel and the reaction was refluxed at 90 °C for 36 h. The acid was neutralized slowly at 0 °C with potassium carbonate and then the product was extracted using ethyl acetate. The organic layer was dried over sodium sulfate and then the solvent was removed under reduced pressure. The crude product was purified by silica gel column chromatography (30% ethyl acetate:DCM) to yield a red-wine solid (240 mg, 0.26 mmol, 61% yield). MALDI-TOF: *m/z* obsd. 916.14 calc. 916.05 for $C_{45}H_{19}BrF_{10}N_4O_2$.

*Synthesis of 2,2'-(prop-2-yn-1-ylazanediyl)diacetic acid (**alkyne-IDAA**).*

Dimethyl 2,2'-(prop-2-yn-1-ylazanediyl)diacetate (alkyne-IDME). Dimethyl 2,2'-azanediyldiacetate (1.0 g, 6.2 mmol) (iminodimethyl ester as described in chapter 2.4) was dissolved in dry acetone (250 mL) and the solution was bubbled with argon for 15 min. Diisopropylethylamine (3.24 mL, 18.6 mmol) and propargyl bromide (0.55 mL, 6.2 mmol) were added and the reaction was heated at 35 °C for 12 h. The solvent was removed under reduced pressure. The mixture was resuspended in dichloromethane and washed with deionized (DI) water acidified with acetic acid to remove unreacted dimethyl 2,2'-azanediyldiacetate. The organic layer was dried over sodium sulfate and the solvent was removed under reduced pressure. The crude product was purified using silica gel column chromatography (8% ethyl acetate:DCM) to give an orange oil (246 mg, 1.2 mmol, 20% yield). ^{1}H-NMR δ ppm ($CDCl_3$): 2.19 (t, J = 2.4, 2.4 Hz, 1H), 3.43 (s, 4H), 3.53 (d, J = 2.4 Hz, 2H), 3.60 (s, 6H).

2,2'-(Prop-2-yn-1-ylazanediyl)diacetic acid (alkyne-IDAA). Alkyne-IDME (135 mg, 0.678 mmol) was dissolved in THF (50 mL). Separately, KOH (114 mg, 2.0 mmol) was dissolved in ethanol (1.0 mL) and DI water (0.5 mL) and then the KOH solution was added to the reaction flask. The reaction was stirred vigorously at room temperature for 24 h. The mixture was neutralized with HCl and then the solvents were removed under reduced pressure to yield an orange oil in 100% yield. FT-IR-ATR: ν(spC-H) 3280 cm^{-1}, ν(COOH) 2556 cm^{-1}, ν(C=O) 1694 cm^{-1}, ν(C-O) 1240 cm^{-1}.

*Synthesis of 5-(4-azidophenyl)-10,15,20-tris(pentafluorophenyl)porphyrin(Zn) (**6**) and the product of the click reaction (**7**).*

5-(4-Nitrophenyl)-10,15,20-tris(pentafluorophenyl)porphyrin (3). In a 1000 mL round-bottom flask was placed 5-(pentafluorophenyl)dipyrromethane (4.50 g, 14.4 mmol), pentafluorobenzaldehyde (1.41 g, 7.21 mmol), and 4-nitrobenzaldehyde (1.09 g, 7.21 mmol). The compounds were dissolved in chloroform stabilized with 1% ethanol (750 mL) and the mixture was bubbled with argon for 30 min. Boron trifluoride diethyl etherate (0.8 mL) was added and the reaction stirred at room temperature for 2 h. Then, 2,3-dichloro-5,6-dicyano-1,4-benzoquinone (4.5 g, 19.5 mmol) was added and the reaction was stirred for 18 h. The mixture was dried down under reduced pressure and then resuspended in ethyl acetate and washed with aqueous sodium bicarbonate and then dried over sodium sulfate. The solution was concentrated and then the crude mixture was passed through a silica pad using 40% hexane/dichloromethane as the eluent. The crude product was then purified using silica gel column chromatography (40% DCM:hexane) to yield a purple solid (600 mg, 0.65 mmol, 9.0% yield). MALDI-TOF: *m/z* obsd. 929.13 calc. 929.09 for $C_{44}H_{14}F_{15}N_5O_2$.

5-(4-Nitrophenyl)-10,15,20-tris(pentafluorophenyl)porphyrin(Zn) (4). Compound **3** (600 mg, 0.65 mmol) was dissolved in THF (250 mL) and zinc acetate dihydrate (1.4 g, 6.46 mmol) was added. The reaction was refluxed at 60 °C for 18 h. The solvent was removed under reduced pressure, the mixture was resuspended in DCM and washed with DI water, then the organic layer was dried over sodium sulfate and the solvent was removed under reduced pressure to yield a magenta solid (600 mg, 0.61 mmol, 94% yield). MALDI-TOF: *m/z* obsd. 991.28 calc. 991.00 for $C_{44}H_{12}F_{15}N_5O_2Zn$.

5-(4-Aminophenyl)-10,15,20-tris(pentafluorophenyl)porphyrin(Zn) (5). Compound **4** (300 mg, 0.30 mmol) was dissolved in DCM (250 mL) and the solution was bubbled with argon for 15 min. Zinc dust (140 mg, 2.1 mmol) and acetic acid (10 mL) were added and the reaction was stirred at room temperature for 30 min. The mixture was decanted to remove the zinc dust and then washed with DI water. The solvent was removed under reduced pressure and the crude product was purified using silica gel column chromatography with ethyl acetate/DCM/hexane (1:3:6) as the eluent to give a pink solid (200 mg, 0.21 mmol, 69% yield). ^{1}H-NMR δ ppm (DMSO): 9.17 (d, *J* = 4.8 Hz, 2H), 9.14 (d, *J* = 4.8 Hz, 2H), 9.09 (d, *J* = 4.7 Hz, 2H), 9.01 (d, *J* = 4.6 Hz, 2H), 7.87 (d, *J* = 8.1 Hz, 2H), 7.01 (d, *J* = 8.3 Hz, 2H), 5.61 (s, 1H). MALDI-TOF: *m/z* obsd. 961.23 calc. 961.03 for $C_{44}H_{14}F_{15}N_5Zn$.

5-(4-Azidophenyl)-10,15,20-tris(pentafluorophenyl)porphyrin(Zn) (6). Compound **5** (100 mg, 0.10 mmol) was dissolved in anhydrous THF (25 mL) and anhydrous acetonitrile (25 mL). The solution was bubbled with argon for 20 min and cooled to 0 °C. Next, t-butyl nitrite (0.02 mL, 0.16 mmol) was added and the reaction stirred for 1 min. Then trimethylsilylazide (0.02 mL, 0.16 mmol) was quickly added and the reaction was allowed to warm to room temperature and stirred for 2 h. The solvent was removed under reduced pressure and the crude mixture was purified using silica gel column chromatography with ethyl acetate/DCM/hexane (1:3:6) as the eluent to give a pink solid (100 mg, 0.10 mmol, 100% yield). ^{1}H-NMR δ ppm (DMSO): 9.21 (d, *J* = 4.9 Hz, 2H), 9.19 (d, *J* = 4.8 Hz, 2H), 9.14 (d, *J* = 4.6 Hz, 2H), 8.91 (d, *J* = 4.6 Hz, 2H), 8.26 (d, *J* = 8.2 Hz, 2H), 7.58 (d, *J* = 8.2 Hz, 2H). MALDI-TOF: *m/z* obsd. 987.17 calc. 987.02 for $C_{44}H_{12}F_{15}N_7Zn$.

PF15-Clicked Product (7). The azide porphyrin compound **6** (30 mg, 30.4 μmol) and **alkyne-IDME** (12 mg, 60.8 μmol) were dissolved in anhydrous DMF. The solution was bubbled with argon for 15 min then the copper catalyst $[Cu(CH_3CN)_4]PF_6$ (1.2 mg, 3.04 μmol) was added. Next, diisopropylethylamine (22 μL, 0.12 mmol) and then tris(benzyltriazolylmethyl)amine (1.6 mg, 3.04 μmol) were added while the reaction was under argon pressure. The reaction was heated to 100 °C and allowed to stir for 24 h. The solvent was removed under reduced pressure, the mixture was resuspended in DCM and washed with water. The organic layer was dried over sodium sulfate and the solvent was removed under reduced pressure. The crude product was purified using silica gel column chromatography (15% ethyl acetate:DCM) to yield a pink solid (30 mg, 25.3 μmol, 83% yield). ^{1}H-NMR δ ppm (DMSO): 9.23 (d, *J* = 4.8 Hz, 2H), 9.21 (d, *J* = 4.8 Hz, 2H), 9.17 (d, *J* = 4.7 Hz, 2H), 9.06 (s, 1H), 8.97 (d, *J* = 4.7 Hz, 2H), 8.45 (d, *J* = 8.6 Hz, 2H), 8.39 (d, *J* = 8.6 Hz, 2H), 4.17 (s, 2H), 3.68 (s, 10H). MALDI-TOF: *m/z* obsd. 1187.17 calc. 1186.11 for $C_{53}H_{25}F_{15}N_8O_4Zn$.

Synthesis of 5-(4-azidophenyl)-15-(4- (2,2'-(formylazanediyl))diacetic acid)- 10,20-bis(pentafluorophenyl)porphyrin(Zn) ***(14)***

5-(4-Nitrophenyl)-15-(methyl-4-benzoate)-10,20-bis(pentafluorophenyl)porphyrin (8). In a 1000 mL round-bottom flask was placed 5-(pentafluorophenyl)dipyrromethane (2.0 g, 6.4 mmol), methyl-4-formylbenzoate (0.53 g, 3.2 mmol), and 4-nitrobenzaldehyde (0.48 g, 3.2 mmol). The compounds were dissolved in chloroform stabilized with 1% ethanol (750 mL) and the mixture was bubbled with argon for 30 min. Boron trifluoride diethyl etherate (0.35 mL) was added and the reaction stirred at room temperature for 2 h.

Then, 2,3-dichloro-5,6-dicyano-1,4-benzoquinone (2.5 g, 11.0 mmol) was added and the reaction was stirred for 18 h. The mixture was dried down under reduced pressure and then resuspended in ethyl acetate and washed with aqueous sodium bicarbonate and then dried over sodium sulfate. The solution was concentrated and then the crude mixture was passed through a silica pad using 10% hexane/DCM as the eluent. The crude product was then purified using silica gel column chromatography (20% hexane:DCM) to yield a purple solid (335 mg, 0.37 mmol, 12% yield). MALDI-TOF: *m/z* obsd. 897.14 calc. 897.14 for $C_{46}H_{21}F_{10}N_5O_4$.

5-(4-Benzoic acid)-15-(4-nitrophenyl)-10,20-bis(pentafluorophenyl)porphyrin (9). Compound **8** (237 mg, 0.26 mmol) was subjected to acid hydrolysis by dissolving it in trifluoroacetic acid (40 mL) and then slowly adding HCl (80 mL) through a funnel. The reaction was refluxed at 80 °C for 24 h. The acid was neutralized with potassium carbonate at 0 °C and then the product was extracted with ethyl acetate. The organic layer was dried over sodium sulfate and the solvent was removed under reduced pressure to give a purple solid (140 mg, 0.16 mmol, 62% yield). ^{1}H-NMR δ ppm (DMSO): -3.07 (s, 2H), 8.14 (d, *J* = 8.9 Hz, 2H), 8.40 (d, *J* = 7.6 Hz, 2H), 8.57 (d, *J* = 8.7 Hz, 2H), 8.69 (d, *J* = 8.7 Hz, 2H), 8.96 (t, *J* = 5.2, 5.2 Hz, 4H), 9.30 (t, *J* = 5.4, 5.4 Hz, 4H), 10.15 (s, 1H). MALDI-TOF: *m/z* obsd. 883.12 calc. 883.13 for $C_{45}H_{19}F_{10}N_5O_4$.

5-(4-(Dimethyl-2,2'-(formylazanediyl)diacetate)phenyl)-15-(4-nitrophenyl)-10,20-bis(pentafluorophenyl)porphyrin (10). Compound **9** (135 mg, 0.15 mmol) was dissolved in anhydrous benzene (140 mL) and anhydrous pyridine (35 mL) and the solution was bubbled with argon for 15 min. Oxalyl chloride (0.26 mL, 3.1 mmol) was added and the reaction was stirred at room temperature for 1 h. Then, 20 mL of the solution was removed using a rotary evaporator to remove unreacted oxalyl chloride and iminodimethyl ester (123 mg, 0.76 mmol) was added. The reaction was allowed to stir at room temperature for 12 h. The solvent was removed under reduced pressure and the mixture was resuspended in DCM, washed with water, and dried over sodium sulfate. The solvent was again removed under reduced pressure and the crude product was purified using silica gel column chromatography (8% ethyl acetate:DCM) to give a purple solid (100 mg, 0.098 mmol, 65% yield). ^{1}H-NMR δ ppm ($CDCl_3$): -2.87 (s, 2H), 3.84 (s, 6H), 4.53 (s, 4H), 7.90 (d, J = 8.1 Hz, 2H), 8.27 (d, J = 8.1 Hz, 2H), 8.37 (d, J = 8.7 Hz, 2H), 8.64 (d, J = 8.7 Hz, 2H), 8.85 (m, 6H), 8.93 (d, J = 4.8 Hz, 2H). MALDI-TOF: *m/z* obsd. 1026.44 calc. 1026.19 for $C_{51}H_{28}F_{10}N_6O_7$.

5-(4-(Dimethyl-2,2'-(formylazanediyl)diacetate)phenyl)-15-(4-nitrophenyl)-10,20-bis(pentafluorophenyl)porphyrin(Zn) (11). Zinc was inserted into the macrocycle by dissolving compound **10** (100 mg, 0.097 mmol) in THF (50 mL) and adding zinc acetate dihydrate (214 mg, 0.98 mmol). The reaction was refluxed at 60 °C for 12 h. The solvent was removed under reduced pressure, the mixture was resuspended in DCM and washed with DI water. The organic layer was dried over sodium sulfate and the solvent was removed under reduced pressure to yield a magenta solid (105 mg, 0.097 mmol, 100% yield). MALDI-TOF: *m/z* obsd. 1088.36 calc. 1088.10 for $C_{51}H_{26}F_{10}N_6O_7Zn$.

5-(4-Aminophenyl)-15-(4-(dimethyl-2,2'-(formylazanediyl)diacetate)phenyl))-10,20-bis(pentafluorophenyl)porphyrin(Zn) (12). Compound **11** (105 mg, 0.097 mmol) was dissolved in DCM (250 mL) and the solution was bubbled with argon for 15 min. Zinc dust (44.5 mg, 0.68 mmol) and acetic acid (3 mL) were added and the reaction was stirred at room temperature for 1 h. The mixture was decanted to remove the zinc dust and then washed with DI water (×3). The solvent was removed under reduced pressure and the crude product was purified using silica gel column chromatography (5% acetone/DCM) to give a pink solid (80 mg, 0.076 mmol, 78% yield). ^{1}H-NMR δ ppm (DMSO): 9.07 (d, *J* = 4.6 Hz, 2H), 9.04 (d, *J* = 4.6 Hz, 2H), 8.97 (d, *J* = 4.6 Hz, 2H), 8.82 (d, *J* = 4.6 Hz, 2H), 8.26 (d, *J* = 8.0 Hz, 2H), 7.83 (d, *J* = 8.2 Hz, 2H), 7.73 (d, *J* = 8.0 Hz, 2H), 6.97 (d, *J* = 8.2 Hz, 2H), 5.53 (s, 2H), 4.52 (s, 2H), 4.42 (s, 2H), 3.75 (s, 6H). MALDI-TOF: *m/z* obsd. 1058.19 calc. 1058.13 for $C_{51}H_{28}F_{10}N_6O_5Zn$.

5-(4-Azidophenyl)-15-(4-(dimethyl-2,2'-(formylazanediyl)diacetate)phenyl)-10,20-bis(pentafluorophenyl)porphyrin(Zn) (13). Compound **12** (20 mg, 0.019 mmol) was dissolved in anhydrous THF (10 mL) and anhydrous acetonitrile (10 mL). The solution was bubbled with argon for 10 min and cooled to 0 °C. Next, t-butyl nitrite (0.01 mL, 0.08 mmol) was added and the reaction stirred for 1 min. Then trimethylsilylazide (0.01 mL, 0.08 mmol) was quickly added and the reaction was allowed to warm to room temperature and stirred for 2 h. The solvent was removed under reduced pressure and the crude mixture was purified using silica gel column chromatography (5% ethyl acetate/DCM) to yield a magenta solid (11.9 mg, 0.011 mmol, 58% yield). ^{1}H-NMR δ ppm (DMSO): 9.13 (m, 4H), 9.99 (m, 4H), 8.31 (d, *J* = 8.0 Hz, 2H), 8.26 (d, *J* = 8.3 Hz, 2H), 7.77 (d, *J* = 8.0 Hz, 2H), 7.58 (d, *J* = 8.3 Hz, 2H), 4.56 (s, 2H), 4.45 (s, 2H), 3.78 (s, 6H). MALDI-TOF: *m/z* obsd. 1088.16 calc. 1086.17 for $C_{51}H_{26}F_{10}N_8O_5Zn$.

5-(4-azidophenyl)-15-(4-(2,2'-(formylazanediyl)diacetic acid)phenyl)-10,20-bis(pentafluorophenyl)porphyrin(Zn) (14). Compound **13** (15 mg, 0.014 mmol) was dissolved in THF (6 mL), methanol (2 mL), and DI water (2 mL). Lithium hydroxide dihydrate (3.0 mg, 0.069 mmol) was added and the reaction was stirred at room temperature for 18 h. The solvent was removed under reduced pressure, the mixture was resuspended in ethyl acetate and washed with DI water acidified with 3 M HCl and then brine. The organic layer was dried over sodium sulfate and the solvent was removed under reduced pressure. The final product was a magenta solid (9.0 mg, 8.5 μmol, 61% yield). MALDI-TOF: *m/z* obsd. 1056.39 calc. 1056.08 for $C_{49}H_{22}F_{10}N_8O_5Zn$.

*Synthesis of 5,10,15,20-tetrakis(4-benzoic acid)porphyrin (**Tetra-COOH**).*

5,10,15,20-Tetrakis(methyl-4-benzoate)porphyrin (tetra-COOMe). The porphyrin was condensed following the Adler-Longo method.[52] In a 100 mL round bottom flask was placed methyl-4-formylbenzoate (821 mg, 5.0 mmol) and propanoic acid (30 mL). The reaction was heated to 80 °C, pyrrole (0.35 mL, 5.0 mmol) was added, and then the reaction was heated to 118 °C and refluxed for 1 h. The reaction was cooled to room temperature, the precipitated porphyrin was collected by filtration, and rinsed with methanol and DI water. The final product was a purple solid (450 mg, 0.53 mmol, 42% yield). MALDI-TOF: *m/z* obsd. 846.48 calc. 846.27 for $C_{52}H_{38}N_4O_8$.

5,10,15,20-Tetrakis(methyl-4-benzoate)porphyrin (tetra-COOH). Tetra-COOMe (15 mg, 0.018 mmol) was dissolved in THF (10 mL). Separately, KOH (100 mg, 1.78 mmol) was dissolved in methanol (1 mL) and H_2O (0.5 mL) and then added to the reaction. The reaction was stirred vigorously at room temperature for 72 h. The solvent was removed under reduced pressure and the mixture was resuspended in ethyl acetate and DI water. The aqueous layer was acidified with citric acid and the organic layer was extracted. The organic layer was dried over sodium sulfate and the solvent was removed under reduced pressure to yield a purple solid (14 mg, 0.018 mmol, 100% yield). MALDI-TOF: *m/z* obsd. 790.43 calc. 790.21 for $C_{48}H_{30}N_4O_8$.

Synthesis of 5,10,15,20-tetrakis(4-(2,2'-(formylazanediyl)diacetic acid)phenyl)porphyrin ***(Tetra-IDAA)****.*

Methyl 4-(1,3-dioxolan-2-yl)benzoate (15). Methyl 4-formylbenzoate (5.0 g, 30.5 mmol) and ethylene glycol (2.17 mL, 38.9 mmol) were dissolved in benzene (135 mL) and the solution was bubbled with argon for 5 min. Then, p-toluenesulfonic acid (167 mg) was added and the solution was bubbled with argon for another 5 min. The reaction was heated to 90 °C and was allowed to reflux for 18 h. The solvent was removed under reduced pressure, the mixture was resuspended in DCM and washed with DI water, then dried over sodium sulfate. The crude product was purified using silica gel column chromatography (30% hexane:DCM) and yield a yellow oil (1.4 g, 6.73 mmol, 22% yield). ^{1}H-NMR δ ppm ($CDCl_3$): 8.06 (d, *J* = 8.3 Hz, 2H), 7.55 (d, *J* = 8.3 Hz, 2H), 5.86 (s, 1H), 4.12 (m, 2H), 4.06 (m, 2H), 3.92 (s, 3H).

4-(1,3-Dioxolan-2-yl)benzoic acid (16). Compound **15** (1.4 g, 6.73 mmol) was dissolved in THF (40 mL) and ethanol (10 mL), then KOH (0.45 g, 8.04 mmol) was added. The reaction was heated to 40 °C for 18 h. The solvent was removed under reduced pressure and the mixture was resuspended in ethyl acetate and DI water. The aqueous layer was acidified with citric acid and then the organic layer was removed and dried over sodium sulfate. The solvent was removed under reduced pressure and the yellow solid was recrystallized with DCM. The white precipitate was collected by filtration to yield 1.0 g of product (5.15 mmol, 76% yield).

Dimethyl 2,2'-((4-(1,3-dioxolan-2-yl)benzoyl)azanediyl)diacetate (17). In a dry 500 mL three-neck round bottom flask, compound **16** (1.0 g, 5.15 mmol) was dissolved in anhydrous THF (200 mL) and anhydrous pyridine (10 mL). The mixture was heated to 40 °C to help with solubility and bubbled with argon for 20 min. Thionyl chloride (0.75 mL, 10.3 mmol) was added and the reaction was cooled to room temperature and allowed to stir for 1 h. The solvent was then removed under reduced pressure to remove unreacted thionyl chloride. The reaction was kept under argon and iminodimethyl ester (1.66 g, 10.3 mmol) was added in THF (100 mL) and pyridine (10 mL). The reaction was then allowed to stir at room temperature for 18 h. The solvent was removed under reduced pressure, the mixture was resuspended in ethyl acetate and washed with DI water, then dried over sodium sulfate. The mixture was purified using silica gel column chromatography (30% ethyl acetate:DCM) to yield yellow crystals (1.5 g, 4.45 mmol, 86% yield). ^{1}H-NMR δ ppm ($CDCl_3$): 3.73 (s, 3H), 3.78 (s, 3H), 4.05 (m, 2H), 4.12 (m, 2H), 4.32 (s, 2H), 5.82 (s, 1H) 7.46 (d, *J* = 8.3 Hz, 2H), 7.53 (d, *J* = 8.1, 2H).

5,10,15,20-Tetrakis(4-(dimethyl-2,2'-(formylazanediyl)diacetate)phenyl)porphyrin (Tetra-IDME). Compound **17** (250 mg, 0.74 mmol) and pyrrole (52 μL, 0.74 mmol) was dissolved in chloroform stabilized with 1% ethanol (250 mL) and the solution was bubbled with argon for 15 min. Boron trifluoride diethyl etherate (0.01 mL) was added and the reaction stirred at room temperature for 1.5 h. Then, 2,3-dichloro-5,6-dicyano-1,4-benzoquinone (0.42 g, 1.85 mmol) was added and the reaction was stirred for 48 h. The mixture was dried down under reduced pressure and then resuspended in ethyl acetate and washed with aqueous sodium bicarbonate and then dried over sodium sulfate. The solution was concentrated and then the crude mixture was passed through a silica pad using acetone/DCM/ethyl acetate (1:1:2) as the eluent. The crude product was then purified using silica gel column chromatography (25% DCM:ethyl acetate) to yield a purple solid (20.6 mg, 0.015 mmol, 2% yield). ^{1}H-NMR δ ppm ($CDCl_3$): 8.80 (s, 8H), 8.34 (d, *J* = 7.9 Hz, 8H), 7.92 (d, *J* = 8.0 Hz, 8H), 4.52 (s, 16H), 3.86 (s, 24H), -1.24 (s, 2H). MALDI-TOF: *m/z* obsd. 1362.80 calc. 1362.44 for $C_{72}H_{66}N_8O_{20}$.

5,10,15,20-Tetrakis(4-(2,2'-(formylazanediyl)diacetic acid)phenyl)porphyrin (Tetra-IDAA). Tetra-IDME (20.6 mg, 0.015 mmol) was dissolved in THF (125 mL), methanol (5 mL), and H_2O (0.5 mL), then KOH (8.5 mg, 0.15 mmol) was added. The reaction was stirred overnight at room temperature. The solvent was removed under reduced pressure. The mixture was resuspended in H_2O and washed with ethyl acetate and DCM. The aqueous layer was collected and the solvent was removed under reduced pressure to yield a purple solid (18.8 mg, 0.015 mmol, 100% yield). MALDI-TOF: *m/z* obsd. 1251.71 calc. 1251.12 for $C_{64}H_{50}N_8O_{20}$.

Synthesis of $[Ru(bpy)_2(4,4'\text{-}(CONH(CH_2COOH)_2)_2bpy)]Cl_2$ ***(Ru-IDAA)****.*

Ligand Synthesis and Characterization. Dimethyl 2,2'-azanediyldiacetate or iminodimethylester (**IDME**) was synthesized according to chapter 2.4.

4,4'-diimidodimethyl ester-2,2'-bipyridine ***(IDME-bpy)****.* This compound was synthesized by a thionyl chloride coupling. The acid chloride was formed by dissolving 4,4'-dicarboxylic-2,2'-bipyridine (200 mg, 0.819 mmol) in anhydrous THF (35 ml) and anhydrous pyridine (5 ml). The solution was bubbled with argon and then $SOCl_2$ (0.18 ml, 2.46 mmol) was added by syringe. The reaction was allowed to stir for 1 h at room termperature. The color changed from white to yellow to pink. The solvent and unreacted

$SOCl_2$ was removed by rotary evaporator and then the flask was back-filled with argon gas. **IDME** (397 mg, 2.46 mmol) dissolved in THF (16 mL) and pyridine (4 mL) was added by syringe and the color changed from pink to yellow. The reaction was allowed to stir for 12 h at room temperature. The solvent was removed by rotary evaporator and the crude mixture was resuspended in DCM/H2O. The yellow organic layer was collected, dried over NaSO4, filtered through cotton, and then the solvent was removed by rotary evaporator. The crude product was purified by column chromatography (silica gel, 4% MeOH/50% ethyl acetate/DCM) and then crystallized in DCM/hexanes to yield a white solid. Yield: 100 mg (%). ^{1}H-NMR δ ppm ($CDCl_3$): 3.68 (s, 6H), 3.73 (s, 6H), 4.05 (s, 4H), 4.29 (s, 4H), 7.32 (d, *J* = 1.5, 4.9, 2 H), 8.36 (s, 2H), 8.67 (d, *J* = 4.9, 2H). MALDI-TOF: m/z obsd. 531.21 calc. 530.16 for $C_{24}H_{26}N_4O_{10}$.

Metal Complex Synthesis and Characterization. *[Ru(bpy)$_2$(4,4’-(CONH(CH$_2$COOCH$_3$)$_2$)$_2$bpy)]Cl$_2$ (**Ru-IDME**).* This complex was prepared by modifying a literature procedure for a similar compound.[244]The *cis*-[Ru(bpy)$_2$Cl$_2$] (45.6 mg, 0.0942 mmol) and **IDME-bpy** (50 mg, 0.0942 mmol) were dissolved in ethanol (10 mL) and H2O (10 mL). The solution was bubbled with argon for 10 min and then heated to 78 C. The reaction was allowed to reflux with stirring for 12 h. The solvent was removed by a rotary evaporator. The crude mixture was re-suspended in H2O and washed with ether. The aqueous layer was collected and the solvent was removed by rotary evaporator leaving an orange solid. Yield: 92 mg (%). ^{1}H-NMR δ ppm (D_2O): 3.67 (s, 6H), 3.83 (s, 6H), 4.31 (s, 4H), 4.45 (d, *J* = 4.65 Hz, 4H), 7.43 (dd, *J* = 6.3, 15.9 Hz, 4H), 7.48 (d, *J* = 7.3 Hz, 2H), 7.82 (d, *J* = 7.3 Hz, 4H), 8.04 (d, *J* = 5.8 Hz, 2H), 8.11 (dd, *J* = 6.7, 13.0, 4H), 8.58 (d, *J* =

8.2 Hz, 4H), 8.64 (s, 2H). UV/vis λ_{max} (H_2O): 448 nm. MALDI-TOF: *m/z* obsd. 944.53 calc. 944.21 for $C_{44}H_{42}N_8O_{10}Ru$.

[Ru(bpy)$_2$(4,4'-(CONH(CH$_2$COOH)$_2$)$_2$bpy)]Cl$_2$ ***(Ru-IDAA)****.* The hydrolysis was prepared by modifying published procedures for similar compounds.[245,246] A sample of **Ru-IDME** (80 mg, 0.0789 mmol) was dissolved in 8 mL of H2O with NaOH (22 mg, 0.552 mg). The reaction was stirred for 1 h at room temperature until the mass spectrometer showed no more of the ester. The base was neutralized by dropwise addition of 12 M HCl. The solvent was removed by rotary evaporator and the crude mixture was dissolved in methanol. Hexane was added to crystallize out a red precursor. The liquid was transferred into another flask and the solvent was removed to give an orange solid. The orange solid was dissolved in ethanol and placed on ice to crystallize out any remaining salts. A white precipitate formed and was filtered out and washed with cold ethanol. The filtrate was dried to give the final product. Yield: 73 mg (%). ^{1}H-NMR δ ppm (D_2O): 4.04 (s, 4H), 4.21 (s, 2H), 4.38 (s, 2H), 7.40 (m, 4H), 7.76 (d, J = 5.6, 2H), 7.81 (m, 4H), 8.00 (d, J = 5.7, 2H), 8.07 (m, 4H), 8.56 (d, J = 7.9, 4H), 8.98 (d, J = 17.0, 2H). UV/vis λ_{max} (H_2O): 449 nm.

CHAPTER 7

CONCLUSIONS

This thesis has discussed some of the recent results our group has produced in the area of artificial photosynthesis research. These studies are just a step in the development of a solar-to-fuel photoelectrochemical device that can provide a clean, renewable fuel to meet humanities energy needs. Studies have demonstrated that the development of a water splitting dye sensitized photoelectrochemical cell is possible with the right components. A new p-type semiconductor with a valence band more positive than the water oxidation potential and an extremely negative conduction band has been discovered. A protein was designed with the capabilities of tailoring its redox and catalytic properties within its scaffold. A new anchoring group for attaching organic dyes to semiconductors has been shown to have efficient electron injection properties and can help increase the overall efficiency of a cell. Mimics of the natural system have been studied to show the role of electronic coupling and thermodynamics on the rate of triplet-triplet energy transfer photoprotection by carotenoids and that proton-coupled electron transfer is a concerted mechanism. A series of quinones for use as redox mediators in a biological-photovoltaic tandem system have been synthesized and characterized. Lastly, a variety of novel chromophores have been designed and synthesized for their redox, photoactive, solubility and reactivity properties that could be used for future applications in an artificial photosynthetic device.

This dissertation has covered a variety of projects, ranging from organic and inorganic synthesis to electrochemical and spectroscopic measurements, with the common thread being synthetic organic chemistry. There are still many improvements that need to be made in order to develop a solar-to-fuel photoelectrochemical cell capable of solving the energy crisis. Future work will focus on improving each component and assembling them in the appropriate configuration to produce a durable, long lasting, and efficient solar fuel cell.

REFERENCES

(1) Meadows, D. H.; Potomac Associates, Universe Books: New York, NY, USA, 1972.

(2) Energy, U. S. D. o. **2014**.

(3) Corporation, E. **2014**.

(4) Solomon, S.; Qin, D.; Manning, M.; Chen, Z. *IPCC* **2007**, *Group I*.

(5) Sabine, C. L.; Feely, R. A.; Gruber, N.; Key, R. M.; Lee, K.; Bullister, J. L.; Wanninkhof, R.; Wong, C. S.; Wallace, D. W. R.; Tilbrook, B.; Millero, F. J.; Peng, T.-H.; Kozyr, A.; Ono, T.; Rios, A. F. *Science* **2004**, *305*, 367.

(6) Keeling, R. *Scripps CO_2 Program*, 2014.

(7) Lewis, N. S.; Nocera, D. G. *Proceedings of the National Academy of Sciences* **2006**, *103*, 15729.

(8) Armaroli, N.; Balzani, V. *Angewandte Chemie International Edition* **2007**, *46*, 52.

(9) Grätzel, M. *Nature* **2001**, *414*, 6.

(10) Grätzel, M. *Journal of Photochemistry and Photobiology C: Photochemistry Reviews* **2003**, *4*, 145.

(11) Imahori, H.; Umeyama, T.; Ito, S. *Acc. Chem. Res.* **2009**, *42*, 1809.

(12) Higashino, T.; Imahori, H. *Dalton Trans.* **2015**, *44*, 448.

(13) Gust, D.; Moore, T. A.; Moore, A. L. *Acc. Chem. Res.* **2009**, *42*, 1890.

(14) Song, W.; Chen, Z.; Glasson, C. R. K.; Hanson, K.; Luo, H.; Norris, M. R.; Ashford, D. L.; Concepcion, J. J.; Brennaman, M. K.; Meyer, T. J. *ChemPhysChem* **2012**, *13*, 2882.

(15) Youngblood, W. J.; Lee, S.-H. A.; Kobayashi, Y.; Hernandez-Pagan, E. A.; Hoertz, P. G.; Moore, T. A.; Moore, A. L.; Gust, D.; Mallouk, T. E. *J. Am. Chem. Soc.* **2009**, *131*, 926.

(16) Zhao, Y.; Swierk, J. R.; Megiatto, J. D.; Sherman, B.; Youngblood, W. J.; Qin, D.; Lentz, D. M.; Moore, A. L.; Moore, T. A.; Gust, D.; Mallouk, T. E. *Proceedings of the National Academy of Sciences* **2012**, *109*, 15612.

(17) Magnuson, A.; Anderlund, M.; Johansson, O.; Lindblad, P.; Lomoth, R.; Polivka, T.; Ott, S.; Stensjö, K.; Styring, S.; Sundström, V.; Hammarström, L. *Acc. Chem. Res.* **2009**, *42*, 1899.

(18) Lan, E. I.; Liao, J. C. *Metab. Eng.* **2011**, *13*, 353.

(19) Nichols, E. M.; Gallagher, J. J.; Liu, C.; Su, Y.; Resasco, J.; Yu, Y.; Sun, Y.; Yang, P.; Chang, M. C. Y.; Chang, C. J. *Proceedings of the National Academy of Sciences* **2015**, *112*, 11461.

(20) Gust, D.; Moore, T. A.; Moore, A. L. *Faraday Discuss.* **2012**, *155*, 9.

(21) Sherman, B.; Vaughn, M.; Bergkamp, J.; Gust, D.; Moore, A.; Moore, T. *Photosynth. Res.* **2013**, 1.

(22) Shockley, W.; Queisser, H. J. *J. Appl. Phys.* **1961**, *32*, 510.

(23) Mathew, S., Yella, Aswani, Geo, Peng, Humphry-Baker, Robin, CurchodBasile, F. E., Achari-Ashani, Negar, Tavernelli, Ivano, Rothlisberger, Ursula, Nazeeruddin Md., Khaja, Gratzel, Michael. *Nature Chem.* **2014**, *6*, 6.

(24) Odobel, F.; Pellegrin, Y. *The Journal of Physical Chemistry Letters* **2013**, *4*, 2551.

(25) Yella, A.; Mai, C.-L.; Zakeeruddin, S. M.; Chang, S.-N.; Hsieh, C.-H.; Yeh, C.-Y.; Grätzel, M. *Angew. Chem.* **2014**, n/a.

(26) Blankenship, R. E.; Tiede, D. M.; Barber, J.; Brudvig, G. W.; Fleming, G.; Ghirardi, M.; Gunner, M. R.; Junge, W.; Kramer, D. M.; Melis, A.; Moore, T. A.; Moser, C. C.; Nocera, D. G.; Nozik, A. J.; Ort, D. R.; Parson, W. W.; Prince, R. C.; Sayre, R. T. *Science* **2011**, *332*, 805.

(27) Frank, H.; Cua, A.; Chynwat, V.; Young, A.; Gosztola, D.; Wasielewski, M. *Photosynth. Res.* **1994**, *41*, 389.

(28) Frank, H. A.; Cogdell, R. J. *Photochem. Photobiol.* **1996**, *63*, 257.

(29) Polívka, T.; Sundström, V. *Chem. Rev. (Washington, DC, U. S.)* **2004**, *104*, 2021.

(30) Gall, A.; Berera, R.; Alexandre, Maxime T. A.; Pascal, Andrew A.; Bordes, L.; Mendes-Pinto, Maria M.; Andrianambinintsoa, S.; Stoitchkova, Katerina V.; Marin, A.; Valkunas, L.; Horton, P.; Kennis, John T. M.; van Grondelle, R.; Ruban, A.; Robert, B. *Biophys. J.* **2011**, *101*, 934.

(31) Hammes-Schiffer, S. *Acc. Chem. Res.* **2009**, *42*, 1881.

(32) Hammarstrom, L.; Styring, S. *Energy & Environmental Science* **2011**, *4*, 2379.

(33) Sherman, B. D.; Vaughn, M. D.; Bergkamp, J. J.; Gust, D.; Moore, A. L.; Moore, T. A. *Photosynth. Res.* **2014**, *120*, 59.

(34) Ort, D. R.; Merchant, S. S.; Alric, J.; Barkan, A.; Blankenship, R. E.; Bock, R.; Croce, R.; Hanson, M. R.; Hibberd, J. M.; Long, S. P.; Moore, T. A.; Moroney, J.; Niyogi,

K. K.; Parry, M. A. J.; Peralta-Yahya, P. P.; Prince, R. C.; Redding, K. E.; Spalding, M. H.; van Wijk, K. J.; Vermaas, W. F. J.; von Caemmerer, S.; Weber, A. P. M.; Yeates, T. O.; Yuan, J. S.; Zhu, X. G. *Proceedings of the National Academy of Sciences* **2015**, *112*, 8529.

(35) Bolton, J. R.; Strickler, S. J.; Connolly, J. S. *Nature* **1985**, *316*, 495.

(36) Hanna, M. C.; Nozik, A. J. *J. Appl. Phys.* **2006**, *100*, 074510.

(37) Khaselev, O.; Turner, J. A. *Science* **1998**, *280*, 425.

(38) Walter, M. G.; Warren, E. L.; McKone, J. R.; Boettcher, S. W.; Mi, Q.; Santori, E. A.; Lewis, N. S. *Chem. Rev. (Washington, DC, U. S.)* **2010**, *110*, 6446.

(39) O'Regan, B., Gratzel, Michael. *Nature* **1991**, *353*, 4.

(40) Alibabaei, L.; Sherman, B. D.; Norris, M. R.; Brennaman, M. K.; Meyer, T. J. *Proceedings of the National Academy of Sciences* **2015**, *112*, 5899.

(41) Brimblecombe, R.; Koo, A.; Dismukes, G. C.; Swiegers, G. F.; Spiccia, L. *J. Am. Chem. Soc.* **2010**, *132*, 2892.

(42) Gao, Y.; Ding, X.; Liu, J.; Wang, L.; Lu, Z.; Li, L.; Sun, L. *J. Am. Chem. Soc.* **2013**, *135*, 4219.

(43) Moore, G. F.; Blakemore, J. D.; Milot, R. L.; Hull, J. F.; Song, H.-e.; Cai, L.; Schmuttenmaer, C. A.; Crabtree, R. H.; Brudvig, G. W. *Energy & Environmental Science* **2011**, *4*, 2389.

(44) Fan, K.; Li, F.; Wang, L.; Daniel, Q.; Gabrielsson, E.; Sun, L. *Phys. Chem. Chem. Phys.* **2014**, *16*, 25234.

(45) Nattestad, A.; Mozer, A. J.; Fischer, M. K. R.; Cheng, Y. B.; Mishra, A.; Bauerle, P.; Bach, U. *Nat. Mater.* **2010**, *9*, 31.

(46) Odobel, F.; Le Pleux, L.; Pellegrin, Y.; Blart, E. *Acc. Chem. Res.* **2010**, *43*, 1063.

(47) He, J.; Lindström, H.; Hagfeldt, A.; Lindquist, S.-E. *J. Phys. Chem. B* **1999**, *103*, 8940.

(48) Sumikura, S.; Mori, S.; Shimizu, S.; Usami, H.; Suzuki, E. *Journal of Photochemistry and Photobiology A: Chemistry* **2008**, *194*, 143.

(49) Sullivan, I.; Brown, C. L.; Llansola-Portoles, M. J.; Gervaldo, M.; Kodis, G.; Moore, T. A.; Gust, D.; Moore, A. L.; Maggard, P. A. *J. Phys. Chem. C* **2015**, *119*, 21294.

(50) Dabestani, R.; Bard, A. J.; Campion, A.; Fox, M. A.; Mallouk, T. E.; Webber, S. E.; White, J. M. *J. Phys. Chem.* **1988**, *92*, 1872.

(51) de la Garza, L.; Jeong, G.; Liddell, P. A.; Sotomura, T.; Moore, T. A.; Moore, A. L.; Gust, D. *J. Phys. Chem. B* **2003**, *107*, 10252.

(52) Adler, A. D.; Longo, F. R.; Shergalis, W. *J. Am. Chem. Soc.* **1964**, *86*, 3145.

(53) Bergkamp, J. J.; Sherman, B. D.; Mariño-Ochoa, E.; Palacios, R. E.; Cosa, G.; Moore, T. A.; Gust, D.; Moore, A. L. *J. Porphyrins Phthalocyanines* **2011**, *15*, 943.

(54) Li, Z.; Lieberman, M. *Inorg. Chem.* **2001**, *40*, 932.

(55) Koyama, T.; Suzuki, T.; Hanabusa, K.; Shirai, H.; Kobayashi, N. *Inorg. Chim. Acta* **1994**, *218*, 41.

(56) Janson, T. R.; Kane, A. R.; Sullivan, J. F.; Knox, K.; Kenney, M. E. *J. Am. Chem. Soc.* **1969**, *91*, 5210.

(57) Brune, A.; Jeong, G.; Liddell, P. A.; Sotomura, T.; Moore, T. A.; Moore, A. L.; Gust, D. *Langmuir* **2004**, *20*, 8366.

(58) Hambourger, M.; Brune, A.; Gust, D.; Moore, A. L.; Moore, T. A. *Photochem. Photobiol.* **2005**, *81*, 1015.

(59) Hambourger, M.; Liddell, P. A.; Gust, D.; Moore, A. L.; Moore, T. A. *Photochem. Photobiol. Sci.* **2007**, *6*, 431.

(60) Hambourger, M.; Kodis, G.; Vaughn, M. D.; Moore, G. F.; Gust, D.; Moore, A. L.; Moore, T. A. *Dalton Trans.* **2009**, 9979.

(61) Quan, M.; Sanchez, D.; Wasylkiw, M. F.; Smith, D. K. *J. Am. Chem. Soc.* **2007**, *129*, 12847.

(62) Yella, A.; Lee, H.-W.; Tsao, H. N.; Yi, C.; Chandiran, A. K.; Nazeeruddin, M. K.; Diau, E. W.-G.; Yeh, C.-Y.; Zakeeruddin, S. M.; Grätzel, M. *Science* **2011**, *334*, 629.

(63) Kang, M. G.; Park, N.-G.; Park, Y. J.; Ryu, K. S.; Chang, S. H. *Sol. Energy Mater. Sol. Cells* **2003**, *75*, 475.

(64) Chappel, S.; Zaban, A. *Sol. Energy Mater. Sol. Cells* **2002**, *71*, 141.

(65) Snaith, H. J.; Ducati, C. *Nano Lett.* **2010**, *10*, 1259.

(66) Rockstrom, J.; Steffen, W.; Noone, K.; Persson, A.; Chapin, F. S.; Lambin, E. F.; Lenton, T. M.; Scheffer, M.; Folke, C.; Schellnhuber, H. J.; Nykvist, B.; de Wit, C. A.; Hughes, T.; van der Leeuw, S.; Rodhe, H.; Sorlin, S.; Snyder, P. K.; Costanza, R.; Svedin, U.; Falkenmark, M.; Karlberg, L.; Corell, R. W.; Fabry, V. J.; Hansen, J.; Walker, B.; Liverman, D.; Richardson, K.; Crutzen, P.; Foley, J. A. *Nature* **2009**, *461*, 472.

(67) O'Regan, B.; Grätzel, M. *Nature* **1991**, *353*, 737.

(68) Mathew, S.; Yella, A.; Gao, P.; Humphry-Baker, R.; CurchodBasile, F. E.; Ashari-Astani, N.; Tavernelli, I.; Rothlisberger, U.; NazeeruddinMd, K.; Grätzel, M. *Nature Chem.* **2014**, *6*, 242.

(69) Tachibana, Y.; Vayssieres, L.; Durrant, J. R. *Nat. Photonics* **2012**, *6*, 511.

(70) Kalyanasundaram, K.; Graetzel, M. *Curr. Opin. Biotechnol.* **2010**, *21*, 298.

(71) Henry, C. H. *J. Appl. Phys.* **1980**, *51*, 4494.

(72) Odobel, F.; Pellegrin, Y.; Gibson, E. A.; Hagfeldt, A.; Smeigh, A. L.; Hammarström, L. *Coord. Chem. Rev.* **2012**, *256*, 2414.

(73) Liao, L.; Yan, B.; Hao, Y. F.; Xing, G. Z.; Liu, J. P.; Zhao, B. C.; Shen, Z. X.; Wu, T.; Wang, L.; Thong, J. T. L.; Li, C. M.; Huang, W.; Yu, T. *Appl. Phys. Lett.* **2009**, *94*.

(74) Joshi, U. A.; Maggard, P. A. *The Journal of Physical Chemistry Letters* **2012**, *3*, 1577.

(75) Flynn, C. J.; Oh, E. E.; McCullough, S. M.; Call, R. W.; Donley, C. L.; Lopez, R.; Cahoon, J. F. *J. Phys. Chem. C* **2014**, *118*, 14177.

(76) Gryko, D.; Lindsey, J. S. *J. Org. Chem.* **2000**, *65*, 2249.

(77) Mitchell, D. R.; Schaffer, B. *Ultramicroscopy* **2005**, *103*, 319.

(78) Malerba, C.; Biccari, F.; Leonor Azanza Ricardo, C.; D’Incau, M.; Scardi, P.; Mittiga, A. *Sol. Energy Mater. Sol. Cells* **2011**, *95*, 2848.

(79) van Stokkum, I. H. M.; Larsen, D. S.; van Grondelle, R. *Biochimica et Biophysica Acta (BBA) - Bioenergetics* **2004**, *1657*, 82.

(80) Choi, J.; King, N.; Maggard, P. A. *ACS Nano* **2013**, *7*, 1699.

(81) Ullah, R.; Sun, H.; Ang, H. M.; Tadé, M. O.; Wang, S. *Ind. Eng. Chem. Res.* **2013**, *52*, 3320.

(82) Zhang, X.; Song, J.; Jiao, J.; Mei, X. *Solid State Sci.* **2010**, *12*, 1215.

(83) Boltersdorf, J.; King, N.; Maggard, P. A. *CrystEngComm* **2015**.

(84) *Light Scattering from Polymer Solutions and Nanoparticle Dispersions*; Schärtl, W., Ed.; Springer Berlin, 2006.

(85) Sartor, M. *Dinamic Light Scattering*, University of California, 2010.

(86) Johnson, E. J. In *Optical Properties of III-V Compounds, Semiconductors and Semimetals*; R.K. Willardson, A. C. B., Ed.; Academic Press: New York, 1967; Vol. 3, p 153.

(87) Fuoco, L.; Joshi, U. A.; Maggard, P. A. *J. Phys. Chem. C* **2012**, *116*, 10490.

(88) Gomes, W. P.; Cardon, F. *Prog. Surf. Sci.* **1982**, *12*, 155.

(89) Williams, R. F. X.; Hambright, P. *Bioinorganic Chemistry* **1978**, *9*, 537.

(90) Worthington, P.; Hambright, P.; Williams, R. F. X.; Reid, J.; Burnham, C.; Shamim, A.; Turay, J.; Bell, D. M.; Kirkland, R.; Little, R. G.; Datta-Gupta, N.; Eisner, U. *J. Inorg. Biochem.* **1980**, *12*, 281.

(91) Yu, M.; Natu, G.; Ji, Z.; Wu, Y. *The Journal of Physical Chemistry Letters* **2012**, *3*, 1074.

(92) Powar, S.; Xiong, D.; Daeneke, T.; Ma, M. T.; Gupta, A.; Lee, G.; Makuta, S.; Tachibana, Y.; Chen, W.; Spiccia, L.; Cheng, Y.-B.; Götz, G.; Bäuerle, P.; Bach, U. *J. Phys. Chem. C* **2014**, *118*, 16375.

(93) Wang, H.; Zeng, X.; Huang, Z.; Zhang, W.; Qiao, X.; Hu, B.; Zou, X.; Wang, M.; Cheng, Y.-B.; Chen, W. *ACS Appl. Mater. Interfaces* **2014**, *6*, 12609.

(94) Han, G. W.; Yang, X.-L.; McMullan, D.; Chong, Y. E.; Krishna, S. S.; Rife, C. L.; Weekes, D.; Brittain, S. M.; Abdubek, P.; Ambing, E.; Astakhova, T.; Axelrod, H. L.; Carlton, D.; Caruthers, J.; Chiu, H.-J.; Clayton, T.; Duan, L.; Feuerhelm, J.; Grant, J. C.; Grzechnik, S. K.; Jaroszewski, L.; Jin, K. K.; Klock, H. E.; Knuth, M. W.; Kumar, A.; Marciano, D.; Miller, M. D.; Morse, A. T.; Nigoghossian, E.; Okach, L.; Paulsen, J.; Reyes, R.; van den Bedem, H.; White, A.; Wolf, G.; Xu, Q.; Hodgson, K. O.; Wooley, J.; Deacon, A. M.; Godzik, A.; Lesley, S. A.; Elsliger, M.-A.; Schimmel, P.; Wilson, I. A. *Acta Crystallographica Section F* **2010**, *66*, 1326.

(95) Lill, R. *Nature* **2009**, *460*, 831.

(96) Beinert, H.; Holm, R. H.; Münck, E. *Science* **1997**, *277*, 653.

(97) Meyer, J. *JBIC Journal of Biological Inorganic Chemistry* **2008**, *13*, 157.

(98) Stephens, P. J.; Jollie, D. R.; Warshel, A. *Chem. Rev. (Washington, DC, U. S.)* **1996**, *96*, 2491.

(99) Durrant, J. D.; de Oliveira, C. A. F.; McCammon, J. A. *J. Mol. Graphics Modell.* **2011**, *29*, 773.

(100) Antonkine, M. L.; Maes, E. M.; Czernuszewicz, R. S.; Breitenstein, C.; Bill, E.; Falzone, C. J.; Balasubramanian, R.; Lubner, C.; Bryant, D. A.; Golbeck, J. H. *Biochimica et Biophysica Acta (BBA) - Bioenergetics* **2007**, *1767*, 712.

(101) Fontecilla-Camps, J. C.; Volbeda, A.; Cavazza, C.; Nicolet, Y. *Chem. Rev. (Washington, DC, U. S.)* **2007**, *107*, 4273.

(102) Johnson, D. C.; Dean, D. R.; Smith, A. D.; Johnson, M. K. *Annu. Rev. Biochem.* **2005**, *74*, 247.

(103) W V Sweeney, a.; Rabinowitz, J. C. *Annu. Rev. Biochem.* **1980**, *49*, 139.

(104) Vignais, P. M.; Billoud, B.; Meyer, J. *FEMS Microbiol. Rev.* **2001**, *25*, 455.

(105) Jin, Z.; Heinnickel, M.; Krebs, C.; Shen, G.; Golbeck, J. H.; Bryant, D. A. *J. Biol. Chem.* **2008**, *283*, 28426.

(106) Dubini, A.; Mus, F.; Seibert, M.; Grossman, A. R.; Posewitz, M. C. *J. Biol. Chem.* **2009**, *284*, 7201.

(107) Mulder, David W.; Shepard, Eric M.; Meuser, Jonathan E.; Joshi, N.; King, Paul W.; Posewitz, Matthew C.; Broderick, Joan B.; Peters, John W. *Structure* **2011**, *19*, 1038.

(108) Peters, J. W.; Lanzilotta, W. N.; Lemon, B. J.; Seefeldt, L. C. *Science* **1998**, *282*, 1853.

(109) Jordan, P.; Fromme, P.; Witt, H. T.; Klukas, O.; Saenger, W.; Krausz, N. *Nature* **2001**, *411*, 909.

(110) Scott, M. P.; Biggins, J. *Protein Sci.* **1997**, *6*, 340.

(111) Antonkine, M. L.; Koay, M. S.; Epel, B.; Breitenstein, C.; Gopta, O.; Gärtner, W.; Bill, E.; Lubitz, W. *Biochimica et Biophysica Acta (BBA) - Bioenergetics* **2009**, *1787*, 995.

(112) Kennedy, M. L.; Gibney, B. R. *J. Am. Chem. Soc.* **2002**, *124*, 6826.

(113) Grzyb, J.; Xu, F.; Weiner, L.; Reijerse, E. J.; Lubitz, W.; Nanda, V.; Noy, D. *Biochimica et Biophysica Acta (BBA) - Bioenergetics* **2010**, *1797*, 406.

(114) Grzyb, J.; Xu, F.; Nanda, V.; Łuczkowska, R.; Reijerse, E.; Lubitz, W.; Noy, D. *Biochimica et Biophysica Acta (BBA) - Bioenergetics* **2012**, *1817*, 1256.

(115) Coldren, C. D.; Hellinga, H. W.; Caradonna, J. P. *Proceedings of the National Academy of Sciences* **1997**, *94*, 6635.

(116) Laplaza, C. E.; Holm, R. H. *J. Am. Chem. Soc.* **2001**, *123*, 10255.

(117) Gibney, B. R.; Mulholland, S. E.; Rabanal, F.; Dutton, P. L. *Proceedings of the National Academy of Sciences* **1996**, *93*, 15041.

(118) Roy, A.; Sarrou, I.; Vaughn, M. D.; Astashkin, A. V.; Ghirlanda, G. *Biochemistry* **2013**, *52*, 7586.

(119) Ogihara, N. L.; Ghirlanda, G.; Bryson, J. W.; Gingery, M.; DeGrado, W. F.; Eisenberg, D. *Proceedings of the National Academy of Sciences* **2001**, *98*, 1404.

(120) Mathews, R.; Charlton, S.; Sands, R. H.; Palmer, G. J. *Biol. Chem.* **1974**, *249*, 4326.

(121) Carter, P. *Anal. Biochem.* **1971**, *40*, 450.

(122) Sherman, B. D.; Pillai, S.; Kodis, G.; Bergkamp, J.; Mallouk, T. E.; Gust, D.; Moore, T. A.; Moore, A. L. *Can. J. Chem.* **2011**, *89*, 152.

(123) Torres, R. A.; Lovell, T.; Noodleman, L.; Case, D. A. *J. Am. Chem. Soc.* **2003**, *125*, 1923.

(124) Loewe, R. S.; Ambroise, A.; Muthukumaran, K.; Padmaja, K.; Lysenko, A. B.; Mathur, G.; Li, Q.; Bocian, D. F.; Misra, V.; Lindsey, J. S. *J. Org. Chem.* **2004**, *69*, 1453.

(125) Bencini, A.; Gatteschi, D. *Springer* **2011**.

(126) Guldi, D. M.; Zilbermann, I.; Anderson, G.; Li, A.; Balbinot, D.; Jux, N.; Hatzimarinaki, M.; Hirsch, A.; Prato, M. *Chem. Commun. (Cambridge, U. K.)* **2004**, 726.

(127) Smith, E. T.; Feinberg, B. A. *J. Biol. Chem.* **1990**, *265*, 14371.

(128) Eisenstein, K. K.; Wang, J. H. *J. Biol. Chem.* **1969**, *244*, 1720.

(129) Kyritsis, P.; Hatzfeld, O. M.; Link, T. A.; Moulis, J.-M. *J. Biol. Chem.* **1998**, *273*, 15404.

(130) Kathan-Galipeau, K.; Nanayakkara, S.; O’Brian, P. A.; Nikiforov, M.; Discher, B. M.; Bonnell, D. A. *ACS Nano* **2011**, *5*, 4835.

(131) Topoglidis, E.; Discher, B. M.; Moser, C. C.; Dutton, P. L.; Durrant, J. R. *ChemBioChem* **2003**, *4*, 1332.

(132) Lichtenstein, B. R.; Farid, T. A.; Kodali, G.; Solomon, L. A.; Anderson, J. L. R.; Sheehan, M. M.; Ennist, N. M.; Fry, B. A.; Chobot, S. E.; Bialas, C.; Mancini, J. A.; Armstrong, C. T.; Zhao, Z.; Esipova, T. V.; Snell, D.; Vinogradov, S. A.; Discher, B. M.; Moser, C. C.; Dutton, P. L. *Biochem. Soc. Trans.* **2012**, *40*, 561.

(133) McAllister, K. A.; Zou, H.; Cochran, F. V.; Bender, G. M.; Senes, A.; Fry, H. C.; Nanda, V.; Keenan, P. A.; Lear, J. D.; Saven, J. G.; Therien, M. J.; Blasie, J. K.; DeGrado, W. F. *J. Am. Chem. Soc.* **2008**, *130*, 11921.

(134) Strzalka, J.; Xu, T.; Tronin, A.; Wu, S. P.; Miloradovic, I.; Kuzmenko, I.; Gog, T.; Therien, M. J.; Blasie, J. K. *Nano Lett.* **2006**, *6*, 2395.

(135) Harriman, A. *Journal of the Chemical Society, Faraday Transactions 1: Physical Chemistry in Condensed Phases* **1980**, *76*, 1978.

(136) Zastrow, M. L.; PeacockAnna, F. A.; Stuckey, J. A.; Pecoraro, V. L. *Nat Chem* **2012**, *4*, 118.

(137) Zastrow, M. L.; Pecoraro, V. L. *J. Am. Chem. Soc.* **2013**, *135*, 5895.

(138) Dutton, P. L.; Moser, C. C. *Faraday Discuss.* **2011**, *148*, 443.

(139) Ghirlanda, G.; Lear, J. D.; Ogihara, N. L.; Eisenberg, D.; DeGrado, W. F. *J. Mol. Biol.* **2002**, *319*, 243.

(140) Boyle, A. L.; Woolfson, D. N. *Chem. Soc. Rev.* **2011**, *40*, 4295.

(141) Brodin, J. D.; Carr, J. R.; Sontz, P. A.; Tezcan, F. A. *Proceedings of the National Academy of Sciences* **2014**, *111*, 2897.

(142) Brodin, J. D.; Ambroggio, X. I.; Tang, C.; Parent, K. N.; Baker, T. S.; Tezcan, F. A. *Nat Chem* **2012**, *4*, 375.

(143) Huard, D. J. E.; Kane, K. M.; Tezcan, F. A. *Nat. Chem. Biol.* **2013**, *9*, 169.

(144) Mills, J. H.; Khare, S. D.; Bolduc, J. M.; Forouhar, F.; Mulligan, V. K.; Lew, S.; Seetharaman, J.; Tong, L.; Stoddard, B. L.; Baker, D. *J. Am. Chem. Soc.* **2013**, *135*, 13393.

(145) King, N. P.; Bale, J. B.; Sheffler, W.; McNamara, D. E.; Gonen, S.; Gonen, T.; Yeates, T. O.; Baker, D. *Nature* **2014**, *510*, 103.

(146) Tinberg, C. E.; Khare, S. D.; Dou, J.; Doyle, L.; Nelson, J. W.; Schena, A.; Jankowski, W.; Kalodimos, C. G.; Johnsson, K.; Stoddard, B. L.; Baker, D. *Nature* **2013**, *501*, 212.

(147) Lewis, N. S. *Science* **2007**, *315*, 798.

(148) Youngblood, W. J.; Lee, S.-H. A.; Maeda, K.; Mallouk, T. E. *Acc. Chem. Res.* **2009**, *42*, 1966.

(149) Nazeeruddin, M. K.; Kay, A.; Rodicio, I.; Humphry-Baker, R.; Mueller, E.; Liska, P.; Vlachopoulos, N.; Graetzel, M. *J. Am. Chem. Soc.* **1993**, *115*, 6382.

(150) Chen, C.-Y.; Wang, M.; Li, J.-Y.; Pootrakulchote, N.; Alibabaei, L.; Ngoc-le, C.-h.; Decoppet, J.-D.; Tsai, J.-H.; Grätzel, C.; Wu, C.-G.; Zakeeruddin, S. M.; Grätzel, M. *ACS Nano* **2009**, *3*, 3103.

(151) Grätzel, M. *Journal of Photochemistry and Photobiology A: Chemistry* **2004**, *164*, 3.

(152) Kalyanasundaram, K.; Grätzel, M. *Coord. Chem. Rev.* **1998**, *177*, 347.

(153) Pérez León, C.; Kador, L.; Peng, B.; Thelakkat, M. *J. Phys. Chem. B* **2006**, *110*, 8723.

(154) Milot, R. L.; Moore, G. F.; Crabtree, R. H.; Brudvig, G. W.; Schmuttenmaer, C. A. *J. Phys. Chem. C* **2013**, *117*, 21662.

(155) Moore, G. F.; Konezny, S. J.; Song, H.-e.; Milot, R. L.; Blakemore, J. D.; Lee, M. L.; Batista, V. S.; Schmuttenmaer, C. A.; Crabtree, R. H.; Brudvig, G. W. *J. Phys. Chem. C* **2012**, *116*, 4892.

(156) Brillet, J. Y., Jun-Ho; Cornuz, Maurin; Hisatomi, Takashi; Solarska, Renata; Augustynski, Jan; Graetzel, Michael; Sivula, Kevin *Nat. Photonics* **2012**, *6*, 4.

(157) Megiatto Jr, J. D., Mendez-Hernandez, Dalvin D., Tejeda-Ferrari, Marely E., Teillout, Anne-Lucie, Llansola-Portoles, Manuel J., Kodis, Gerdenis, Poluektov, Oleg G., Rajh, Tijana; Mujica, Vladimiro, Groy, Thomas L., Gust, Devens, Moore, Thomas A., Moore, Ana L. *Nature Chem.* **2014**.

(158) Rochford, J.; Chu, D.; Hagfeldt, A.; Galoppini, E. *J. Am. Chem. Soc.* **2007**, *129*, 4655.

(159) Kathiravan, A.; Renganathan, R. *J. Colloid Interface Sci.* **2009**, *331*, 401.

(160) Young, K. J.; Martini, L. A.; Milot, R. L.; Snoeberger Iii, R. C.; Batista, V. S.; Schmuttenmaer, C. A.; Crabtree, R. H.; Brudvig, G. W. *Coord. Chem. Rev.* **2012**, *256*, 2503.

(161) Galoppini, E. *Coord. Chem. Rev.* **2004**, *248*, 1283.

(162) Rochford, J.; Galoppini, E. *Langmuir* **2008**, *24*, 5366.

(163) Hoertz, P. G.; Kim, Y.-I.; Youngblood, W. J.; Mallouk, T. E. *J. Phys. Chem. B* **2007**, *111*, 6845.

(164) Sharma, D.; Steen, G.; Korterik, J. P.; García-Iglesias, M.; Vázquez, P.; Torres, T.; Herek, J. L.; Huijser, A. *J. Phys. Chem. C* **2013**, *117*, 25397.

(165) Bae, E.; Choi, W.; Park, J.; Shin, H. S.; Kim, S. B.; Lee, J. S. *J. Phys. Chem. B* **2004**, *108*, 14093.

(166) Brewster, T. P.; Konezny, S. J.; Sheehan, S. W.; Martini, L. A.; Schmuttenmaer, C. A.; Batista, V. S.; Crabtree, R. H. *Inorg. Chem.* **2013**, *52*, 6752.

(167) Li, J.; Nilsing, M.; Kondov, I.; Wang, H.; Persson, P.; Lunell, S.; Thoss, M. *J. Phys. Chem. C* **2008**, *112*, 12326.

(168) Llansola-Portolés, M. J.; Palacios, R. E.; Gust, D.; Moore, T. A.; Moore, A. L. In *From Molecules to Materials - Pathways to Artificial Photosynthesis*; Rozhkova, E., Ariga, K., Eds.; Springer: 2015.

(169) Saitoh, T.; Satoh, F.; Hiraide, M. *Talanta* **2003**, *61*, 811.

(170) Kusakabe, K.; Nishida, H.; Morooka, S.; Kato, Y. *J. Appl. Electrochem.* **1986**, *16*, 121.

(171) Wijeratne, S.; Bruening, M. L.; Baker, G. L. *Langmuir* **2013**, *29*, 12720.

(172) Zhu, J.; Sun, G. *ACS Appl. Mater. Interfaces* **2013**, *6*, 925.

(173) Asapu, S.; Pant, S.; Gruden, C. L.; Escobar, I. C. *Desalination* **2014**, *338*, 17.

(174) Liu, J.-W.; Yang, T.; Chen, S.; Chen, X.-W.; Wang, J.-H. *Journal of Materials Chemistry B* **2013**, *1*, 810.

(175) Laha, J. K.; Dhanalekshmi, S.; Taniguchi, M.; Ambroise, A.; Lindsey, J. S. *Organic Process Research & Development* **2003**, *7*, 799.

(176) Zhang, H.; Du, N.; Chen, B.; Cui, T.; Yang, D. *Mater. Res. Bull.* **2008**, *43*, 3164.

(177) Lee, E. J. H.; Ribeiro, C.; Giraldi, T. R.; Longo, E.; Leite, E. R.; Varela, J. A. *Appl. Phys. Lett.* **2004**, *84*, 1745.

(178) Rehm, D.; Weller, A. *Isr. J. Chem.* **1970**, *8*, 259.

(179) Rehm, D.; Weller, A. *Ber. Bunsenges. Phys. Chem.* **1969**, *73*, 834.

(180) Foote, C. S. In *Free Radicals in Biology*; Pryor, W. A., Ed.; Academic Press: New York, 1976; Vol. 2.

(181) Monger, T. G.; Cogdell, R. J.; Parson, W. W. *Biochimica et Biophysica Acta (BBA) - Bioenergetics* **1976**, *449*, 136.

(182) Mathis, P.; Butler, W. L.; Satoh, K. *Photochem. Photobiol.* **1979**, *30*, 603.

(183) Berera, R.; van Stokkum, I. H. M.; Kodis, G.; Keirstead, A. E.; Pillai, S.; Herrero, C.; Palacios, R. E.; Vengris, M.; van Grondelle, R.; Gust, D.; Moore, T. A.; Moore, A. L.; Kennis, J. T. M. *J. Phys. Chem. B* **2007**, *111*, 6868.

(184) Berera, R.; Herrero, C.; van Stokkum, I. H. M.; Vengris, M.; Kodis, G.; Palacios, R. E.; van Amerongen, H.; van Grondelle, R.; Gust, D.; Moore, T. A.; Moore, A. L.; Kennis, J. T. M. *Proceedings of the National Academy of Sciences* **2006**, *103*, 5343.

(185) Holt, N. E.; Zigmantas, D.; Valkunas, L.; Li, X.-P.; Niyogi, K. K.; Fleming, G. R. *Science* **2005**, *307*, 433.

(186) Bensasson, R. V., Land, Edward J., Moore, Ana L., Crouch, Robert L., Dirks, Gary, Moore, Thomas A., Gust, Devens *Nature* **1981**, *290*.

(187) Moore, A. L.; Joy, A.; Tom, R.; Gust, D.; Moore, T. A.; Bensasson, R. V.; Land, E. J. *Science* **1982**, *216*, 982.

(188) Gust, D.; Moore, T. A.; Bensasson, R. V.; Mathis, P.; Land, E. J.; Chachaty, C.; Moore, A. L.; Liddell, P. A.; Nemeth, G. A. *J. Am. Chem. Soc.* **1985**, *107*, 3631.

(189) Gust, D.; Moore, T. A.; Liddell, P. A.; Nemeth, G. A.; Makings, L. R.; Moore, A. L.; Barrett, D.; Pessiki, P. J.; Bensasson, R. V. *J. Am. Chem. Soc.* **1987**, *109*, 846.

(190) Gust, D.; Moore, T. A.; Moore, A. L.; Gao, F.; Luttrull, D.; DeGraziano, J. M.; Ma, X. C.; Makings, L. R.; Lee, S. J. *J. Am. Chem. Soc.* **1991**, *113*, 3638.

(191) Gust, D.; Moore, T. A.; Moore, A. L.; Devadoss, C.; Liddell, P. A.; Hermant, R.; Nieman, R. A.; Demanche, L. J.; DeGraziano, J. M.; Gouni, I. *J. Am. Chem. Soc.* **1992**, *114*, 3590.

(192) Land, E. J.; Lexa, D.; Bensasson, R. V.; Gust, D.; Moore, T. A.; Moore, A. L.; Liddell, P. A.; Nemeth, G. A. *J. Phys. Chem.* **1987**, *91*, 4831.

(193) Kloz, M.; Pillai, S.; Kodis, G.; Gust, D.; Moore, T. A.; Moore, A. L.; van Grondelle, R.; Kennis, J. T. M. *J. Am. Chem. Soc.* **2011**, *133*, 7007.

(194) Liao, P.-N.; Pillai, S.; Gust, D.; Moore, T. A.; Moore, A. L.; Walla, P. J. *J. Phys. Chem. A* **2011**, *115*, 4082.

(195) Mani, T.; Niedzwiedzki, D. M.; Vinogradov, S. A. *J. Phys. Chem. A* **2012**, *116*, 3598.

(196) Liao, P.-N.; Pillai, S.; Kloz, M.; Gust, D.; Moore, A.; Moore, T.; Kennis, J. M.; Grondelle, R.; Walla, P. *Photosynth. Res.* **2012**, *111*, 237.

(197) Robinson, G. W.; Frosch, R. P. *J. Chem. Phys.* **1963**, *38*, 1187.

(198) Cardoso, S. L.; Nicodem, D. E.; Moore, T. A.; Moore, A. L.; Gust, D. *J. Braz. Chem. Soc* **1996**, *7*, 19.

(199) Fungo, F.; Otero, L.; Durantini, E.; Thompson, W. J.; Silber, J. J.; Moore, T. A.; Moore, A. L.; Gust, D.; Sereno, L. *Phys. Chem. Chem. Phys.* **2003**, *5*, 469.

(200) Barry, B. A. *Biochimica et Biophysica Acta (BBA) - Bioenergetics* **2015**, *1847*, 46.

(201) Nakamura, S.; Nagao, R.; Takahashi, R.; Noguchi, T. *Biochemistry* **2014**, *53*, 3131.

(202) Noguchi, T. *Biochimica et Biophysica Acta (BBA) - Bioenergetics* **2015**, *1847*, 35.

(203) Hambourger, M.; Moore, G. F.; Kramer, D. M.; Gust, D.; Moore, A. L.; Moore, T. A. *Chem. Soc. Rev.* **2009**, *38*.

(204) Huynh, M. H. V.; Meyer, T. J. *Chem. Rev. (Washington, DC, U. S.)* **2007**, *107*, 5004.

(205) Rhile, I. J.; Markle, T. F.; Nagao, H.; DiPasquale, A. G.; Lam, O. P.; Lockwood, M. A.; Rotter, K.; Mayer, J. M. *J. Am. Chem. Soc.* **2006**, *128*, 6075.

(206) Mayer, J. M.; Rhile, I. J.; Larsen, F. B.; Mader, E. A.; Markle, T. F.; DiPasquale, A. G. *Photosynth. Res.* **2006**, *87*, 3.

(207) Concepcion, J. J.; Brennaman, M. K.; Deyton, J. R.; Lebedeva, N. V.; Forbes, M. D. E.; Papanikolas, J. M.; Meyer, T. J. *J. Am. Chem. Soc.* **2007**, *129*, 6968.

(208) Irebo, T.; Johansson, O.; Hammarström, L. *J. Am. Chem. Soc.* **2008**, *130*, 9194.

(209) Bronner, C.; Wenger, O. S. *The Journal of Physical Chemistry Letters* **2011**, *3*, 70.

(210) Lachaud, F.; Quaranta, A.; Pellegrin, Y.; Dorlet, P.; Charlot, M.-F.; Un, S.; Leibl, W.; Aukauloo, A. *Angewandte Chemie International Edition* **2005**, *44*, 1536.

(211) Reece, S. Y.; Hodgkiss, J. M.; Stubbe, J.; Nocera, D. G. *Philosophical Transactions of the Royal Society B: Biological Sciences* **2006**, *361*, 1351.

(212) Weinberg, D. R.; Gagliardi, C. J.; Hull, J. F.; Murphy, C. F.; Kent, C. A.; Westlake, B. C.; Paul, A.; Ess, D. H.; McCafferty, D. G.; Meyer, T. J. *Chem. Rev. (Washington, DC, U. S.)* **2012**, *112*, 4016.

(213) Chen, J.; Kuss-Petermann, M.; Wenger, O. S. *Chemistry – A European Journal* **2014**, *20*, 4098.

(214) Guldi, D. M.; Prato, M. *Acc. Chem. Res.* **2000**, *33*, 695.

(215) Hammes-Schiffer, S.; Stuchebrukhov, A. A. *Chem. Rev. (Washington, DC, U. S.)* **2010**, *110*, 6939.

(216) Hazra, A.; Soudackov, A. V.; Hammes-Schiffer, S. *The Journal of Physical Chemistry Letters* **2011**, *2*, 36.

(217) Kütt, A.; Movchun, V.; Rodima, T.; Dansauer, T.; Rusanov, E. B.; Leito, I.; Kaljurand, I.; Koppel, J.; Pihl, V.; Koppel, I.; Ovsjannikov, G.; Toom, L.; Mishima, M.; Medebielle, M.; Lork, E.; Röschenthaler, G.-V.; Koppel, I. A.; Kolomeitsev, A. A. *J. Org. Chem.* **2008**, *73*, 2607.

(218) Kaljurand, I.; Kütt, A.; Sooväli, L.; Rodima, T.; Mäemets, V.; Leito, I.; Koppel, I. A. *J. Org. Chem.* **2005**, *70*, 1019.

(219) Prato, M.; Maggini, M. *Acc. Chem. Res.* **1998**, *31*, 519.

(220) Petsalakis, I. D.; Tagmatarchis, N.; Theodorakopoulos, G. *J. Phys. Chem. C* **2007**, *111*, 14139.

(221) Costentin, C.; Robert, M.; Savéant, J.-M. *J. Am. Chem. Soc.* **2006**, *128*, 4552.

(222) Edwards, S. J.; Soudackov, A. V.; Hammes-Schiffer, S. *J. Phys. Chem. A* **2009**, *113*, 2117.

(223) Moore, G. F.; Megiatto, J. D.; Hambourger, M.; Gervaldo, M.; Kodis, G.; Moore, T. A.; Gust, D.; Moore, A. L. *Photochem. Photobiol. Sci.* **2012**, *11*, 1018.

(224) Ravensbergen, J.; Abdi, F. F.; van Santen, J. H.; Frese, R. N.; Dam, B.; van de Krol, R.; Kennis, J. T. M. *J. Phys. Chem. C* **2014**, *118*, 27793.

(225) Berera, R.; van Grondelle, R.; Kennis, J. T. M. *Photosynth. Res.* **2009**, *101*, 105.

(226) Snellenburg, J. J.; Laptenok, S.; Seger, R.; Mullen, K. M.; van Stokkum, I. H. M. *Journal of Statistical Software* **2012**, *49*, 22.

(227) van Stokkum, I. H. M.; Larsen, D. S.; van Grondelle, R. *Biochimica et Biophysica Acta (BBA) - Bioenergetics* **2004**, *1658*.

(228) Kennis, J. T. M.; Groot, M.-L. *Curr. Opin. Struct. Biol.* **2007**, *17*, 623.

(229) Papagiannakis, E.; Kennis, J. T. M.; van Stokkum, I. H. M.; Cogdell, R. J.; van Grondelle, R. *Proceedings of the National Academy of Sciences of the United States of America* **2002**, *99*, 6017.

(230) Bonetti, C.; Alexandre, M. T. A.; van Stokkum, I. H. M.; Hiller, R. G.; Groot, M. L.; van Grondelle, R.; Kennis, J. T. M. *Phys. Chem. Chem. Phys.* **2010**, *12*, 9256.

(231) Artero, V.; Fontecave, M. *Chem. Soc. Rev.* **2013**, *42*, 2338.

(232) Vermaas, W. J.; Williams, J. K.; Arntzen, C. *Plant Mol. Biol.* **1987**, *8*, 317.

(233) Chavez-Santoscoy, A.; Benavides, J.; Vermaas, W.; Rito-Palomares, M. *Chem. Eng. Technol.* **2010**, *33*, 177.

(234) Villano, M.; Aulenta, F.; Ciucci, C.; Ferri, T.; Giuliano, A.; Majone, M. *Bioresour. Technol.* **2010**, *101*, 3085.

(235) Rich, P.; Madgwick, S.; Moss, D. *Biochim. Biophys. Acta* **1991**, *1058*, 312.

(236) Wood, P. M.; Bendall, D. S. *Eur. J. Biochem.* **1976**, *61*, 337.

(237) Sekar, N.; Umasankar, Y.; Ramasamy, R. P. *Phys. Chem. Chem. Phys.* **2014**, *16*, 7862.

(238) Huisgen, R. *Angewandte Chemie International Edition in English* **1963**, *2*, 565.

(239) Dumoulin, F.; Ahsen, V. *J. Porphyrins Phthalocyanines* **2011**, *15*, 481.

(240) Palomaki, P. K. B.; Krawicz, A.; Dinolfo, P. H. *Langmuir* **2011**, *27*, 4613.

(241) Baier, G.; Siebert, J. M.; Landfester, K.; Musyanovych, A. *Macromolecules* **2012**, *45*, 3419.

(242) Geier Iii, G. R.; Lindsey, J. S. *Tetrahedron* **2004**, *60*, 11435.

(243) Swierk, J. R.; Méndez-Hernández, D. D.; McCool, N. S.; Liddell, P.; Terazono, Y.; Pahk, I.; Tomlin, J. J.; Oster, N. V.; Moore, T. A.; Moore, A. L.; Gust, D.; Mallouk, T. E. *Proceedings of the National Academy of Sciences* **2015**, *112*, 1681.

(244) Norris, M. R.; Concepcion, J. J.; Glasson, C. R. K.; Fang, Z.; Lapides, A. M.; Ashford, D. L.; Templeton, J. L.; Meyer, T. J. *Inorg. Chem.* **2013**, *52*, 12492.

(245) Myers, C. P.; Miller, J. R.; Williams, M. E. *J. Am. Chem. Soc.* **2009**, *131*, 15291.

(246) Schwalbe, M.; Schäfer, B.; Görls, H.; Rau, S.; Tschierlei, S.; Schmitt, M.; Popp, J.; Vaughan, G.; Henry, W.; Vos, J. G. *Eur. J. Inorg. Chem.* **2008**, *2008*, 3310.

APPENDIX A

COPYRIGHTS AND PERMISSIONS

Chapter 2.2

Reprinted with permission from Ian Sullivan, Chelsea L. Brown, Manuel J. Llansola-Portoles, Miguel Gervaldo, Gerdenis Kodis, Thomas A. Moore, Devens Gust, Ana L. Moore, and Paul A. Maggard. *The Journal of Physical Chemistry C* **2015**, *119*, 21294-21303. Copyright 2015 American Chemical Society.

Chapter 2.3

Reprinted with permission from Anindya Roy, Dayn Joseph Sommer, Robert Arthur Schmitz, Chelsea Lynn Brown, Devens Gust, Andrei Astashkin, and Giovanna Ghirlanda. *Journal of the American Chemical Society* **2014**, *136*, 17343-17349. Copyright 2014 American Chemical Society.

Chapter 4

J. Ravensbergen, C. L. Brown, G. F. Moore, R. N. Frese, R. van Grondelle, D. Gust, T. A. Moore, A. L. Moore and J. T. M. Kennis, *Photochem. Photobiol. Sci.*, **2015**, Advance Article, DOI: 10.1039/C5PP00259A - Published by The Royal Society of Chemistry (RSC) on behalf of the European Society for Photobiology, the European Photochemistry Association, and RSC.